Full Spectral Fitting of Stellar Population Models for Studies of Galaxy Evolution

David Mark Wilkinson

The thesis is submitted in partial fulfilment of the requirements for
the award of the degree of
Doctor of Philosophy
of the
University of Portsmouth

August 2015

To my family,
who have always been there for me.

Declaration

The work of this Ph.D. thesis was carried out at the Institute of Cosmology and Gravitation, University of Portsmouth, United Kingdom, under the supervision of Professor Claudia Maraston and Dr. Daniel Thomas.

Whilst registered as a candidate for the above degree, I have not been registered for any other research award. The results and conclusions embodied in this thesis are the work of the named candidate and have not been submitted for any other academic award.

The work in this thesis is my own unless otherwise stated.

Chapters 3 and 4 contain work from Wilkinson & Maraston 2015, submitted.

Chapters 3 and 5 contain work from Wilkinson et al. 2015, MNRAS 449 (1): 328-360. Sections 5.2 and 5.3 are based on 'common text' between this paper and 2 others: Belfiore et al. (2015) and Li et al. (2015), written primarily by the architects of the MaNGA collaboration: Bundy et al. (2015).

I have contributed stellar population properties and maps using the codes outlined in this thesis to the following works to date:

Bundy et al. (2015).

Belfiore et al. (2015).

Li et al. (2015).

Word Count: 39,258.

David Mark Wilkinson
August 2015

Abstract

In this work we present a new full spectral fitting code called FIREFLY. It is a χ^2-minimisation code that obtains thousands of spectral fits in order to build probability distribution functions of stellar population properties, and includes an innovative method to treat dust attenuation. We use the code to determine galaxy properties, including age, metallicity, stellar mass and dust extinction, of over 2 million galaxy spectra, both from point-source and from resolved galaxy surveys, using modern high-resolution stellar population models. We analyse the results to assess the redshift evolution of galaxy properties, and the importance of their internal processes. We test a set of stellar population models based on three stellar libraries to assess the systematic effects of changing model ingredients and provide a detailed assessment of degeneracies in the models, in all stages of the thesis.

After introducing the central concepts in galaxy evolution and astrophysics, we describe the advancements of stellar population models and their use in the derivation of galaxy properties. We then give a detailed overview of the landscape of full spectral fitting and its application to observational data. We describe the motivation, features and function of FIREFLY, performing careful calibration on a set of mock galaxies and globular clusters. We also very carefully assess the degeneracies in model spectra and measure the uncertainties from applying a full spectral fitting approach to optical data.

We apply FIREFLY to two observation point-source surveys with millions of galaxy members: the Sloan Digital Sky Survey (SDSS) Data Release 7 (DR7), and SDSS Data Release 9, the galaxy data of which is called the Baryon Oscillation Spectroscopic Survey (BOSS). We present the full star formation histories of all of the galaxies in the surveys and important subsamples within them. We use the derived galaxy properties as the calibrator for combining these surveys into one large survey across redshifts $0.0 < z < 0.8$. This enables us to assess the redshift evolution of the most luminous and passive galaxies across both samples.

Significantly, we use FIREFLY in the first scientific publication of SDSS-IV, for the MaNGA

Integral Field Unit survey. We retrieve stellar population maps and radial profiles from high spatial resolution prototype observations of 18 galaxies, encompassing thousands of individual spectra. Our analysis gives detailed measurements of the precision to which one can recover stellar population gradients and resolved maps as a function of observational conditions and stellar population model ingredients, paving the way for future work both in MaNGA and other spatial galaxy surveys.

Acknowledgements

Firstly I would like to thank my supervisors, Professor Claudia Maraston and Dr. Daniel Thomas, for their support, encouragement, ideas and guidance during my PhD. I would also like to thank the Institute of Cosmology and Gravitation and the University of Portsmouth for welcoming me as a PhD student in the first place.

There are so many people that I've met at Portsmouth who I feel very grateful to be able to call my friends, but I would like to express my particular gratitude towards Claire, Tom, Emma, Cullan, James, Adam, Bridget, Jon, Tim, Kat, Andreas, Xan, Dan, Kyle, Hana, Yuting, Jen, and Matt. Outside of Portsmouth, I am especially grateful to Louise, Arpine and Zach for their long-term friendship and support.

I would like to give particular thanks to Janine, Amanda, and Kate from the University Well-being service for their compassion and empathy, and whose words I hope to continue to find valuable in the future.

I also wish to express heartfelt thanks and gratitude to Mum, Dad, Matthew and Catherine for all their love and encouragement over the years.

Finally, thanks to Joey, for his love and kindness.

The author acknowledges support from a University of Portsmouth PhD bursary.

Numerical computations were carried out on the Sciama High Performance Compute (HPC) cluster which is supported by the ICG, SEPNet and the University of Portsmouth.

Funding for SDSS-III and SDSS-IV has been provided by the Alfred P. Sloan Foundation and Participating Institutions. Additional funding for SDSS-III comes from the National Science Foundation and the U.S. Department of Energy Office of Science. Further information about both projects is available at `www.sdss3.org`.

Acronyms and Abbreviations

AAO	Australian Astronomical Observatory
AGB	Asymptotic Giant Branch
AGN	Active Galactic Nuclei
APO	Apache Point Observatory
ATLAS^{3D}	Multi-wavelength IFU galaxy survey (Cappellari et al., 2011)
BC03	Bruzual & Charlot (2003)
BIC	Bayesian Information Criterion
BOSS	Baryon Oscillation Spectroscopic Survey
BPT	Baldwin, Phillips & Terlevich (1981) diagnostic diagram
CALIFA	Calar Alto Legacy Integral Field Area Survey
(Λ)CDM	(Λ) Cold Dark Matter
CMASS	'Constant-Mass' subsample of *BOSS*
CMBR	Cosmic Microwave Background Radiation
CMD	Colour-Magnitude Diagram
CSP	Composite Stellar Population
DAP	Data Analysis Pipeline
DRP	Data Reduction Pipeline
DR[Number]	Data Release [Number]
ELODIE	Stellar library named after the spectrograph used to take its data
ETG	Early-Type Galaxy
EW	Equivalent Width
E(B-V)	Extinction in the Blue (minus) Visual bands
FIREFLY	Fitting IteRativEly For Likelihood analYsis
FOV	Field Of View
FWHM	Full Width Half Maximum
GAMA	Galaxy And Mass Assembly

GANDALF	Gas AND Absorption Line Fitting
GC	Globular Cluster
HB	Horizontal Branch
HPF	High-Pass Filter
HR	Hertzsprung-Russell (diagram)
IFU	Integral Field Unit
IMF	Initial Mass Function
IR	Infra-Red
LHS	Left-Hand Side
LINER	Low-Ionisation Nuclear Emission-line Region
LOSVD	Line Of Sight Velocity Dispersion
LOWZ	Low-Redshift subsample of *BOSS*
LRG	Luminous Red Galaxy
LTG	Late-Type Galaxy
MaNGA	Mapping Nearby Galaxies at *APO*
MARCS	Stellar library named after the code used to produce its model atmospheres
MILES	a Medium resolution Isaac Newton Telescope Library of Empirical Spectra
MPA-JHU	Max-Planck institut für Astrophysik/Johns Hopkins University
MS	Main Sequence
M05	Maraston (2005)
M11	Maraston & Strömbäck (2011)
M67	Globular cluster Messier 67
N_{19} / N_{61} / N_{127}	Fiber bundle with 19/61/127 fibers respectively
pc / kpc / Mpc	parsec / kiloparsec / megaparsec
PCA	Principle Component Analysis, in this thesis in reference to Chen et al. (2012)
PDAP	Prototype Data Analysis Pipeline
PDRP	Prototype Data Reduction Pipeline
PMS	Post-Main Sequence
pPXF/PPXF	Penalised PiXel Fitting
P-MaNGA	Prototype version of the *MaNGA* survey
RGB	Red Giant Branch
RHS	Right-Hand Side
SAMI	Galaxy survey using the Sydney-*AAO* Multi-object Integral field spectrograph
SAURON	Spectroscopic Area Unit for Research on Optical Nebulae
SDSS	Sloan Digital Sky Survey

SED	Spectral Energy Distribution
SFR	Star Formation Rate
SGB	Sub-Giant Branch
SN(e)	Supernova(e)
SSFR	Specific Star Formation Rate
SSP	Simple Stellar Population
STARLIGHT	A fitting code
STECKMAP	STEllar Content and Kinematics via Maximum A Posteriori
STELIB	Contraction of 'Stellar Libary'
S/N	Signal/Noise
TP-AGB	Thermally Pulsating - Asymptotic Giant Branch
urgiz	5 *SDSS* bands, increasing in wavelength respectively
VENGA	The *VIRUS-P* Exploration of Nearby Galaxies
VESPA	VErsatile SPectral Analysis
VIRUS-P	Visible Integral-field Replicable Unit Spectrograph - Prototype
Yr / Myr / Gyr	Year(s) / Megayear(s) / Gigayear(s)
z	Redshift
[Z/H]	Metallicity
2dFGRS	Two-degree-Field Galaxy Redshift Survey

Contents

List of Figures

List of Tables

Chapter 1

Introduction

1.1 The Big Picture

Looking deeper and deeper into the night sky, it becomes apparent that the visible Universe is composed primarily of galaxies, each containing an abundance of stars, gas, and dust. The field of galaxy formation and evolution provides us with understanding of these systems, and through that, understanding of the Universe they exist in.

Cosmological studies have built up a wealth of evidence that the Universe started 13.8 billion years ago with a hot 'Big Bang'. Since then it has expanded and cooled in order to form the stars and galaxies that we see today. Evaluating the fundamental properties of the Universe, such as its age, can only be answered with any degree of certainty if we have detailed knowledge of the nuclear processes that take place in stars.

Collections of stars such as those within galaxies are known as stellar populations. Major advances in the field of the stellar population analysis, both from the theoretical treatment and from observational data, has allowed for a huge increase in the amount of information into the evolutionary history of galaxies that can be obtained. To analyse this information we can use a technique called stellar population modelling. This technique uses the principles of stellar evolution in order to build model galaxies, thus enabling the transformation of observed quantities into the physical properties of galaxies and the stellar populations within them, such as their ages and chemical composition.

Modern stellar population models cover an increasingly large range of stellar population prop-

erties to an increasing resolution, and are becoming more sophisticated in their treatment of rare and short-lived stellar evolutionary states. As a complement to this, more comprehensive catalogues of observational galaxy data are now becoming available, in some cases boasting data from millions of galaxies, and in other cases providing observational galaxy data as a function of position.

In order to combine these models and data, analysis tools must also continue to be developed to exploit these advances. In this thesis, I shall be presenting original work based on the development of such a new analysis tool. I will describe the tool in detail, apply it to both large statistical samples and spatial samples of galaxy data, and assess how the ingredients used in stellar population modelling can affect the interpretation of galaxy properties and thus galaxy evolution as a whole.

Going back to our initial idea of assessing the age of the Universe, it is important to realise the extent to which the first precise methods of doing so relied on detailed knowledge of galaxy astrophysics. We list here a few ways in which cosmological measurements such as this question depend on galaxy evolution:

- Measurements of the Hubble constant by Sandage (1958) depend on the understanding of the brightest stars in galaxy clusters.
- Bringing the measurements of the cosmic microwave background radiation anisotropies (first detected in Smoot et al. (1992)) together with measurements of large scale structure requires a very firm grasp of how galaxies populate the underlying dark matter distribution of the Universe, known as galaxy bias (White & Rees (1978)).
- Direct gravitational lensing methods (Brainerd, Blandford & Smail, 1996) to measure the mass density contrast of the Universe require understanding of galaxy shape and morphology across cosmic time.
- Measurements of the ages of the oldest globular clusters such as by Sandage & Cacciari (1990) require highly accurate knowledge of star cluster formation and hence their component stellar properties.

Galaxies are complex systems and the study of them still contains many unsolved problems that draw from a very wide range of topics. Our knowledge of cosmology relies upon the understanding of the processes above and how they affect the constituents of the galaxy, since it is only in the analysis of the galaxies' light that we can infer the composition of the Universe. For example, weighing the dark matter halos in which galaxies are thought to exist (see

section 1.2) requires combining galaxy lensing methods to deduce the gravitational potential of the galaxy and halo, and subtracting off the stellar and baryonic mass using observations and models of the visible material. Age-dating stars and galaxies also provide an independent check of the timescales deduced from cosmological models. This is not a simple task, as galaxies as a population are extremely diverse. It therefore needs to be understood why different aspects of galaxy processes are important for the formation and evolution of different types of galaxies. In this introduction, we will describe and explain the diversity of galaxy properties and important concepts in galaxy evolution.

1.2 Galaxy Formation

The current paradigm for galaxy formation is the ΛCDM model. The CDM (Cold Dark Matter) part of the model was theorised by White & Rees (1978) and established observationally from galaxy dynamics in clusters (Zwicky, 1937), individual galaxy dynamics (Rubin et al., 1985), large scale structure (Percival et al., 2001), and the cosmic microwave background radiation (CMBR) (Spergel et al., 2003). Recent studies of the CMBR by the Planck satellite (Planck Collaboration et al., 2015) estimate that less than 5 % of the total mass density of the Universe is contained within the baryonic matter that we are most familiar with. $\sim$ 25 % is composed of invisible 'dark matter' which is thought to act only through gravity. The remaining mass density of the Universe, ($\sim$ 70 %) is thought to be in the form of 'dark energy' (Λ), responsible for the acceleration of the expansion of the Universe, as first observed from measurements of Type 1a Supernovae (Perlmutter et al., 1999). The ΛCDM model has been extremely successful in providing a framework to understand the formation of galaxies.

Two processes must occur in order to form a galaxy: mass assembly and star formation. First, a sufficient overdensity of matter in the Universe must undergo gravitational collapse. If the matter involved is collisional, *i.e.* baryonic matter such as gas, we expect the system to continue to cool and collapse. Current models of structure formation suggest that there is also a dominant dark matter component in this process that is non-collisional, which is required in order to form the distribution of structure observed in the Universe. This component then collapses to a relaxed state called a dark matter halo, in which the baryonic matter is then embedded.

The baryonic matter continues to cool and collapse further inside the dark matter halo. At some point, the gas begins to fragment until some of the gas reaches sufficient densities to ignite their cores through nuclear fusion, providing radiation pressure to balance the inwards

gravitational pressure (i.e. to reach hydrostatic equilibrium) and form stars. These stars can inject energy into the remaining gas in a process known as feedback, heating gas up and regulating further star formation. In addition to this, matter at the centre of the galaxies reaches a high enough density to form a super-massive black hole, although the physics of this formation is still very unclear.

Further internal evolution of this galaxy is then described by processes that affect the baryonic matter. This includes further cooling of hot gas, further star formation from the cold gas, feedback processes from the stars, recycling of gas and dust from dying stars, and accretion and feedback processes from the supermassive black hole. External processes also occur, such as inflow of new baryonic material onto the galaxy, and outflow of material out of the galaxy from strong feedback processes. Interactions also happen between galaxies, such as merging.

1.3 Galaxy Evolution

The ΛCDM model predicts that larger dark matter structures form over time through gravitational attraction to overdense regions in the Universe (Press & Schechter, 1974), described as 'hierarchical clustering'. The galaxies that form within these dark matter haloes may naively be thought to grow hierarchically as well, growing in size and mass over time. However, observations at high redshift find old massive galaxies already in place at $z \sim 2$ and above (e.g. Moustakas et al. (2004)). Observations furthermore find that there is 'downsizing' trend (Thomas et al., 2005, 2010) whereby galaxies that form at high redshift are more massive compared to galaxies forming more recently. Recent observations have found these massive high redshift galaxies to be more compact than those of the same mass at lower redshift. A proposed physical mechanism for this result is that gas-poor minor mergers 'puff up' the stellar orbits of the main galaxy (Newman et al. (2012), Hilz, Naab & Ostriker (2013), van der Wel et al. (2014)), at apparent odds with the major-merger style hierarchical clustering scenario produced by the ΛCDM model.

For clues as to how this discrepancy could be resolved, one needs to look at other observable properties of galaxies. In general there are two types of observations one can make. Firstly, one can make direct observations of the galaxies, in which their colours, features in their spectra (see 1.6) or dynamical properties are measured and compared to each other as a function of their redshift. This has the benefit of directly observing redshift evolution without requiring detailed modelling to interpret the observations. However, this does not inform us of the physical processes that could relate different types galaxies to each other, describing how they

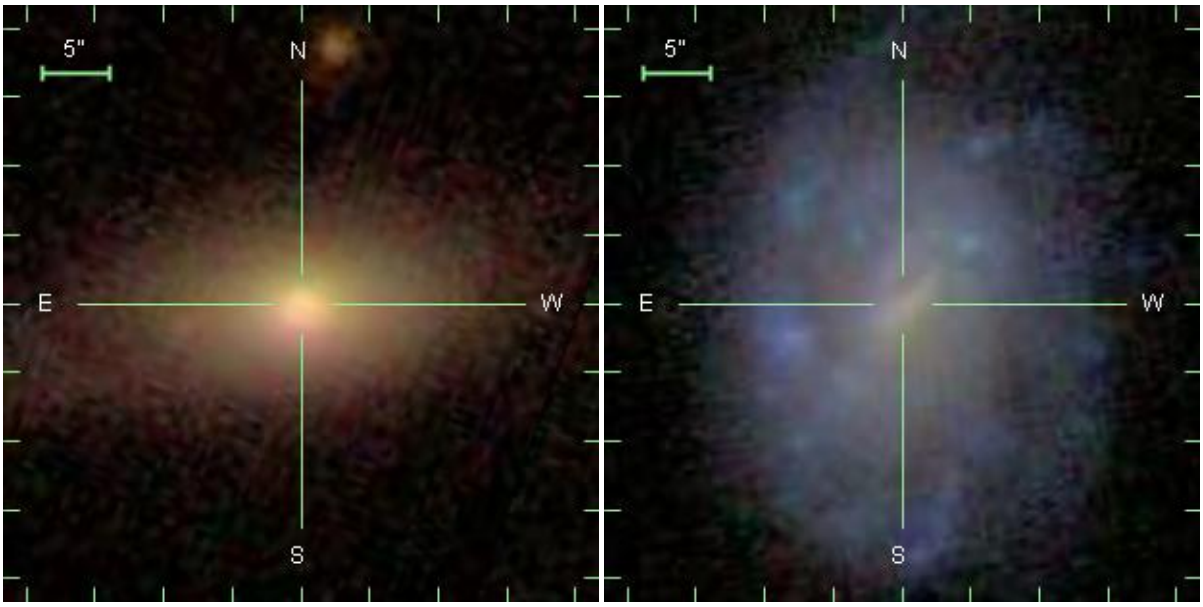

Fig. 1.1 Optical images of an early-type galaxy, left panel, and a late-type galaxy, right panel. Both images are from the Sloan Digital Sky Survey and have also been analysed in detail in this thesis using data from the P-MaNGA survey.

change as they evolve. For this, one is required to measure the imprint on each galaxy made by its evolutionary history. This is termed measuring a 'fossil record' of a galaxy, and involves using models that include evolution with time in order to interpret. This is the main type of observation analysed in this thesis, specifically combining full spectral fitting techniques with evolutionary stellar population models. Before this is described, we now give an overview of the observational results underpinning our current understanding of galaxy evolution.

Historically the vast array of galaxies we observe have been classified into 'ellipticals', 'spirals', and 'irregulars' (reviewed in Sandage (2005)) based on their morphology. This classification method has lasted through to today, since galaxies within each of these groups differ distinctly in their observed properties. For example, the morphologies of galaxies seem to correlate with their stellar content, with spirals being typically bluer in their stellar light, and ellipticals and the bulges of spirals (known as spheroids) showing redder colours. Spheroids are particularly important objects as they are estimated to account for > 73 % of the stellar mass in galaxies despite representing a fraction in number of < 40 % (Fukugita, Hogan & Peebles, 1998).

The morphological study by Hubble (1926) found that galaxies fall into two main groups: early-type galaxies and late-type galaxies (e.g. Meneux et al. (2006); Pannella et al. (2009)). We show an example of an early-type and late-type galaxy both analysed in this thesis in

Figure 1.1. Early-types such as in the left panel are generally morphologically classified as elliptical or spheroid, and contain old, metal-enriched stars that formed in a relatively short period early on in the Universe's history, i.e. at high redshift (Thomas et al., 2005, 2010). They tend to be massive (Kauffmann et al., 2003b) and supported by their own velocity dispersion, and are more common in denser environments. Late-types as in the right panel, conversely, are generally morphologically disk or spiral galaxies and show a more continuous star formation history across the history of the Universe, with less metal-enriched stars. These prefer less dense environments, are supported by rotation, and are not generally as massive as early-types.

One may reasonably ask why the most massive, early-type galaxies contain mainly old stars, and generally low amounts of ongoing star-formation (*i.e.* passive), compared to lower-mass, late-type galaxies. Combining this with the downsizing evidence as described at the beginning of this section means that we require an explanation for how galaxies stop forming stars in order to become passive. This process is described as star formation quenching. Currently the physical mechanisms for quenching are unclear and a currently very active research area, but possible mechanisms include the effects of feedback from active galactic nuclei (AGN) (Tremonti, Moustakas & Diamond-Stanic, 2007) or supernovae (Coil et al., 2011), major mergers (Hung et al., 2013), and/or the displacement or depletion of cold gas from gravitationally dense regions (Behroozi et al., 2015).

The luminosities of galaxies span many orders of magnitude, from just 100s of $L_{\odot}$ in the case of the smallest dwarf galaxies seen in the Milky Way (Belokurov et al., 2007), to 10^{13} $L_{\odot}$ starburst galaxies, whose star formation is so intense that most of the light in the optical and UV is obscured by dust and re-emitted in the IR (Chapman et al., 2005). Similarly the stellar mass of galaxies varies across a number of orders of magnitude, again from the dwarf galaxies observed in the Milky Way of 10^3 $M_{\odot}$ (Kirby et al., 2013). However, differently from the most luminous galaxies, the most massive galaxies observed are giant elliptical galaxies (up to $\sim 10^{12}$ $M_{\odot}$), with the fraction of elliptical galaxies becoming higher at high stellar masses (Bundy, Ellis & Conselice, 2005). In fact, there is significant scatter all along the luminosity-stellar mass relation for the Universal population of galaxies.

The luminosity evolution of each galaxy with age is a product of its internal and external processes, the former of which can be assessed using stellar population models and the latter through studies of cosmology. Thus, one would expect different types of galaxies to have a different relationship between mass and luminosity. Figure 1.2 (reprinted from Tollerud et al. (2011)) shows such an assessment. In that figure Tollerud et al. (2011) show that relationships in a plane with mass, luminosity, and size can be made between groups, but overall there is

still large scatter between any two of the properties shown and no simple relation between all three properties for all galaxy types.

Within these classifications are some clear trends for how the timescales of star formation change as a function of galaxy properties. For example, archaeological downsizing trends have been detected observationally in the last decade (Nelan et al., 2005; Thomas et al., 2005), where early-type galaxies with higher dynamical masses form their stars at high redshift in a rapid episode of star formation, with early-type galaxies with lower dynamical masses forming stars at lower redshifts in more extended star formation episodes. In both cases their evolution is then mostly passive though environmental effects, such as accretion, can modify their star formation histories somewhat.

Separating out these different timescales is difficult through measuring the galaxy light and total mass alone, since these properties are degenerate with star formation history. However, certain chemical signatures can reduce this degeneracy. So-called α elements (O, Ne, Mg, Si, S, Ar, Ca, Ti), known as such since they are made by successive capture of α particles (i.e. Helium nuclei), are ejected into the interstellar medium of a galaxy predominantly from the explosion of massive stars into Type II supernovae (SNe). On the other hand, Iron (Fe) can be produced through both Type II SNe and Type Ia SNe (Matteucci & Greggio, 1986; Nomoto, Thielemann & Wheeler, 1984; Nomoto, Thielemann & Yokoi, 1984). Massive stars quickly use up their fuel and explode into Type II SNe, whereas Type 1a SNe are produced from binary interactions with one or more white dwarf stars, which originate from lower-mass (and hence longer-living) stars (Yoshii, Tsujimoto & Nomoto, 1996). This enriched interstellar medium then gets recycled into new stars, with the amount of α and Fe elements dependent on the time since the onset of star formation. Hence measuring the [α/Fe] ratio in a galaxy allows us to assess how rapid star formation has been in that galaxy, since high [α/Fe] indicates bursty star formation and low [α/Fe] indicates a more continuous star formation history (Matteucci (1994); Thomas, Greggio & Bender (1998)).

Another important proxy for understanding a galaxy's evolutionary history is the metallicity of its stars, which throughout this thesis we define as [Z/H] = $log_{10}\frac{Z/H}{Z_\odot/H_\odot}$, where Z are all the elements heavier than Helium. The metallicity of a stellar population is determined by how enriched the interstellar medium from which it formed is, either from stellar explosions or supernovae enrichment. A galaxy may contain multiple populations with different metallicities, reflecting the chemical environments from which they formed. Again there are important relations with other galaxy properties. Older, more massive early-type galaxies tend to have high metallicities (Gallazzi et al., 2006; Thomas et al., 2005), especially in the core, reflecting

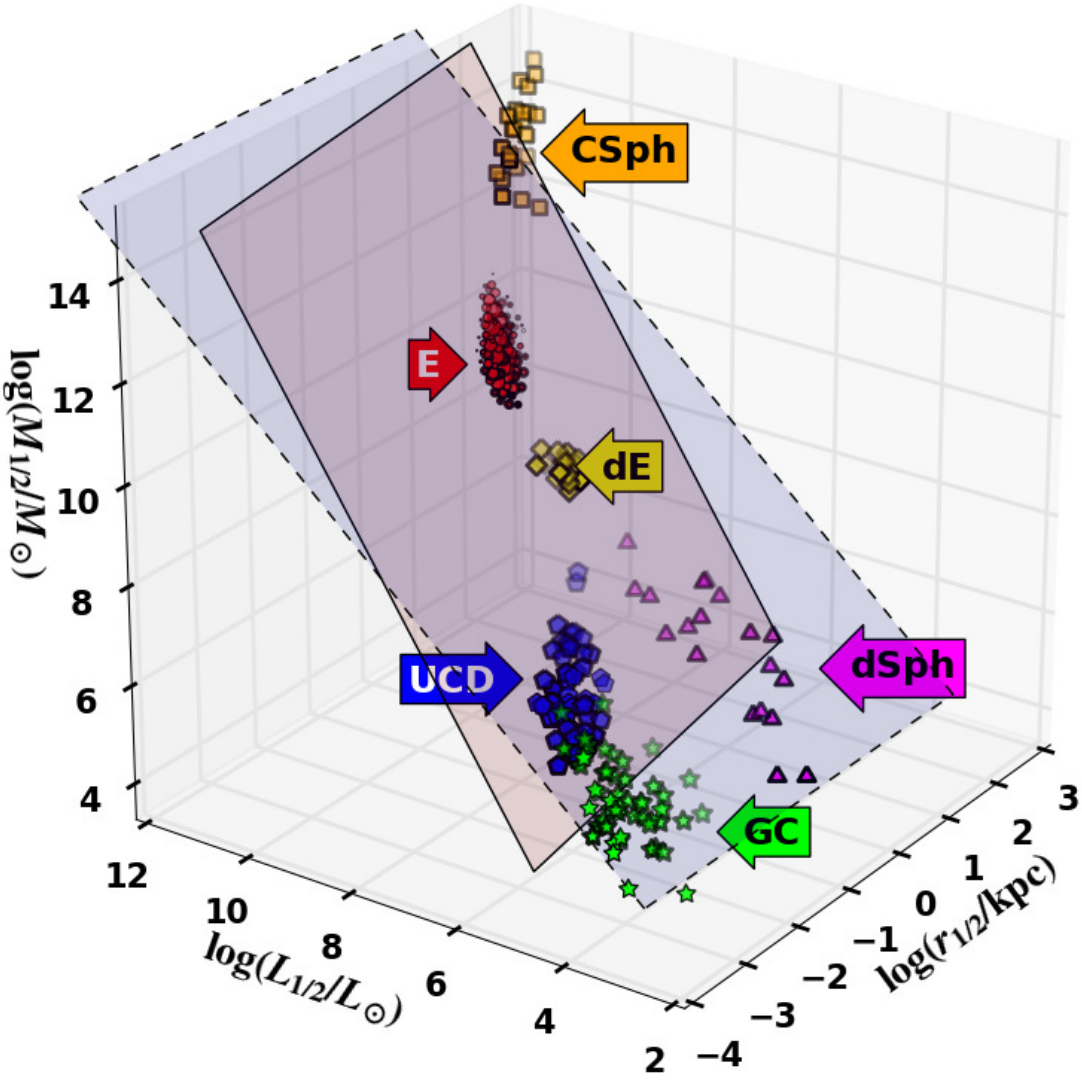

Fig. 1.2 Reprint of Figure 3 from Tollerud et al. (2011).The figure shows the mass, size, and luminosity properties of galaxies as a function of type. The key corresponds to cluster spheroids (CSphs), elliptical galaxies (E), dwarf ellipticals (dEs), Milky Way dwarf spheroidals (dSphs), Galactic globular clusters (GCs), and ultra-compact dwarfs (UCDs). Two planes show that although there are some relationships between the different groups, there does not seem to be a universal relation for relating the three properties simply.

their rapid and efficient recycling of stars and gas near their epoch of formation. Late-type galaxies will have lower but fairly uniform metallicities, reflecting the accretionary / inflow and outflow processes that drive their evolution (Tremonti et al., 2004).

These accretion processes in late-type galaxies have collectively been termed 'inside-out' galaxy formation, whereby the central core of the galaxy is formed first, and is therefore older, with younger material accreting on the outer parts of the galaxy at some later time. This theory is well-established and continuing to be backed by a range of observational evidence (e.g. Ryder & Dopita (1994), Bullock & Johnston (2005), and Nelson et al. (2012)), and theory and simulations (e.g. Fall & Efstathiou (1980), van den Bosch (2001), and Roškar et al. (2008)).

The assembly history of early-type galaxies is much less clear, however, since these early-type galaxies tend to be passive and so exhibit very little change in their stellar ages as a function of radius (though some very recent work in the UV may be starting to detect this, e.g. Petty et al. (2013)). Intriguingly, direct observations of early-type galaxies at high-redshift show that there is a size evolution with redshift, whereby luminous red galaxies (LRGs) at lower redshift tend to be larger than their high redshift equivalents ('progenitors') (Daddi et al. (2005), Trujillo et al. (2007), van Dokkum et al. (2008)). Aside from making direct high-redshift observations, one can attempt to carefully examine the fossil record of more local early-type galaxies to try and investigate what processes cause this size evolution. LRGs are also particularly interesting for this investigation since they are the most massive galaxies in the Universe, and thus understanding their evolution is crucial for understanding the growth of structure in the Universe. Hence in Chapter 4 we devote much of our analysis specifically to the fossil record of LRG stellar populations across a large redshift range.

We can also assess the assembly histories by measuring the gradients of both metallicity and age with radius. These are increasingly important quantities for galaxy evolution models assessing the relative importance of internal and external physical processes, and are very recently becoming measured in a statistically significant way with the rise of integral field spectroscopy surveys. These surveys are described in section 1.5, and will be addressed in detail in Chapter 5.

Large observational surveys have also revealed the extent to which the baryonic mass is distributed as a function of galaxy properties in terms of mass in gas (cold and hot), dust, and stars. The fractional contributions of gas, dust, and stars can tell us about how efficiently star formation has occurred in those systems. Early-type galaxies tend to have very low amounts

of dust and gas (Knapp et al., 1989) suggesting a highly efficient star formation mechanism. Conversely, late-type galaxies have a distribution of fractional mass in gas, with lower surface brightness (luminosity per unit area) galaxies having higher fractional gas mass. Late-type galaxies also have a wide distribution in dust, with actively starforming systems in particular being highly obscured by dust (Draine, 2003). It is important to control for these effects when deducing galaxy properties, since dust can heavily obscure starlight (Trumpler, 1930), significantly reducing the total galaxy's apparent luminosity. Since dust absorbs optical and ultra-violet light, typically more so in the redder wavelengths (depending on grain size), and re-emits in the far infra-red, it will also cause the galaxy to appear redder. Additionally, the effect of dust on a given galaxy's light appears to change as a function of its shape and bulge to disk ratio (Wild et al., 2011). A substantial fraction of the Universe's light has been absorbed and re-emitted by dust (Dole et al., 2006), and not taking account of this will introduce very large systematic errors when measuring relations with other properties (e.g. Cimatti et al. (1997)), so in this thesis we pay special attention to the treatment of dust, as detailed in Chapter 3.1.

It is clear that for studying galaxy formation and evolution we need to derive the physical properties of galaxies described above. Many of these are obtained via stellar population models.

1.4 Stellar Population Models

One of the best ways to get the maximum amount of information about a galaxy or stellar cluster is to take its spectral energy distribution (SED, or spectrum). Through taking an observation of SEDs of different galaxies and fitting them to models we can deduce a variety of physical properties of the object in question, including its star formation history, metallicity, gas/dust content and chemical abundance ratios, initial mass function (IMF), and kinematic parameters such as the velocity dispersions / circular velocities of elliptical / spiral galaxies respectively (see Tinsley (1972)).

For the vast majority of galaxies we cannot use individual stars to derive the properties of the whole galaxy. This means that the evolution of whole populations of stars with similar properties need to be considered to derive the galaxies' SEDs, and for this we require stellar population synthesis tools in order to 'build up' the integrated light from a galaxy. Evolutionary population synthesis tools (first developed by Tinsley & Gunn (1976), Tinsley (1980), Gunn, Stryker & Tinsley (1981) and Maraston (1998) through to the modern models of Bruzual &

Charlot (2003), Fioc & Rocca-Volmerange (1997), Leitherer et al. (1999), González Delgado et al. (2005), Thomas, Maraston & Bender (2003), Vazdekis et al. (1996), Vazdekis et al. (2010), Conroy, Gunn & White (2009), Thomas, Maraston & Johansson (2011) and Maraston & Strömbäck (2011)) have quickly evolved to take account of more complicated processes. Recent advancements include models based on more complete stellar libraries, wavelengths outside the optical, effects of non-solar metallicities, and advanced stages of stellar evolution such as the Asymptotic Giant Branch (AGB), to name a few examples. As the models grow in complexity and precision we are increasingly able to derive complex stellar evolution histories of galaxies that are independent of assumptions on cosmological parameters, by paying close attention to the observations of galactic spectra in order to guide the growth of the modelling techniques.

To model a galaxy we need to firstly deduce the spectra of individual simple stellar populations (SSPs), each a coeval population of stars with the same age and chemical composition, and then build a galaxy spectrum through some combination of these SSPs in order to construct a star formation history. To do this we need to sample a wide range of stars that take into account their energetics, gravitational and atmospheric physics. In practice this means having good coverage of the key stellar atmosphere parameters: effective temperature (T_{eff}), surface gravity ($log\ g$), and metallicity (Z) (see for example, Bressan et al. (1993), Marigo et al. (2008), and Girardi et al. (1996)) and accurate stellar tracks that describe the evolution of these properties.

The next step is to build up these libraries to form simple stellar populations (SSPs). In order to do this, we need to know how a star with particular properties evolves with time, so we take what is called a stellar evolution prescription to model this. This is usually done with a technique known as 'isochrone synthesis', which takes the comparatively well-understood processes of stellar evolution to compute stellar tracks along a colour-magnitude diagram for given mass bins, which are then populated with stars of a given age with some age dispersion to compute each isochrone, from which we can take their contribution to the spectral flux (e.g. in Bruzual & Charlot (2003)). This method suffers in cases where there are short-lived stellar evolutionary phases (where stars can jump abruptly along the colour-magnitude diagram) although this is somewhat mitigated by sophisticated interpolation methods. Often these isochrones are also used for the post-main sequence (PMS) stages of stellar evolution, and simply integrated over all the mass bins (Maraston, 1998; Renzini & Voli, 1981).

An alternative method is to use the 'fuel consumption theorem' for these PMS stages (Renzini & Buzzoni, 1986), which calculates the amount that each stage contributes by stating that a

star's contribution to luminosity is proportional to the amount of nuclear fuel that is burnt in that stage, from what is available for that particular turnoff mass. One then integrates over the amount of fuel available to determine the contribution to the spectral flux.

We now need to sample stellar spectra in order to build up a model, and this can be done in two ways:

1. Empirical stellar libraries (using the observed spectra of stars) - this has the advantage of not requiring potentially incorrect assumptions about how different stellar atmospheres contribute to the stellar spectra. The main disadvantage to this method is that many different types of stars can be measured but all are in the solar neighbourhood, so assumptions regarding chemical content (for example, the degree of alpha enhancement) need to be made for stars outside this neighbourhood in different chemical conditions (Thomas, Maraston & Bender, 2003). The libraries also require careful flux calibration to obtain reasonable accuracy.

2. Theoretical stellar libraries (using theories of model atmospheres, e.g. Kurucz (1979)) - unlike the empirical methods, are not limited by resolution and flux calibration methods, but certain stellar phases (those with low T_{eff}, such as M stars and dwarfs) are not well modelled, suggesting that large discrepancies may exist in a considerable portion of stellar atmosphere parameter space. Additionally, detailed molecular lines are often incomplete. See for an example, Coelho et al. (2005).

In order to explore all these variables, Maraston & Strömbäck (2011), hereafter M11, calculate models for a variety of stellar libraries, both empirical and theoretical. In this thesis we have used three semi-empirical models using the evolutionary stellar population model of M11 based on three corresponding stellar libraries (MILES (Sánchez-Blázquez et al., 2006), STELIB (Le Borgne et al., 2003), and ELODIE (Prugniel et al., 2007)). Figure 12 of M11 shows the flux of each of the models as a function of wavelength for comparison. We vary the input stellar libraries used in order to test the effect of model ingredients rather than the stellar population models themselves. We have plotted the direct SSP spectra for this model at various ages as a function of stellar library for a visual comparison in figure 1.3.

We are therefore also able to analyse the effect of these models on derived galaxy evolution and investigate conclusions made by previous studies in more detail - for example, as noted in M11, M11 models based on the MILES library (especially at solar metallicity) tend to have bluer spectra compared to STELIB-based models. Assessing the effect of using differing model ingredients is important to do, since the differences in the spectra of the models could propagate to recovered galaxy properties, potentially altering conclusions made in work that

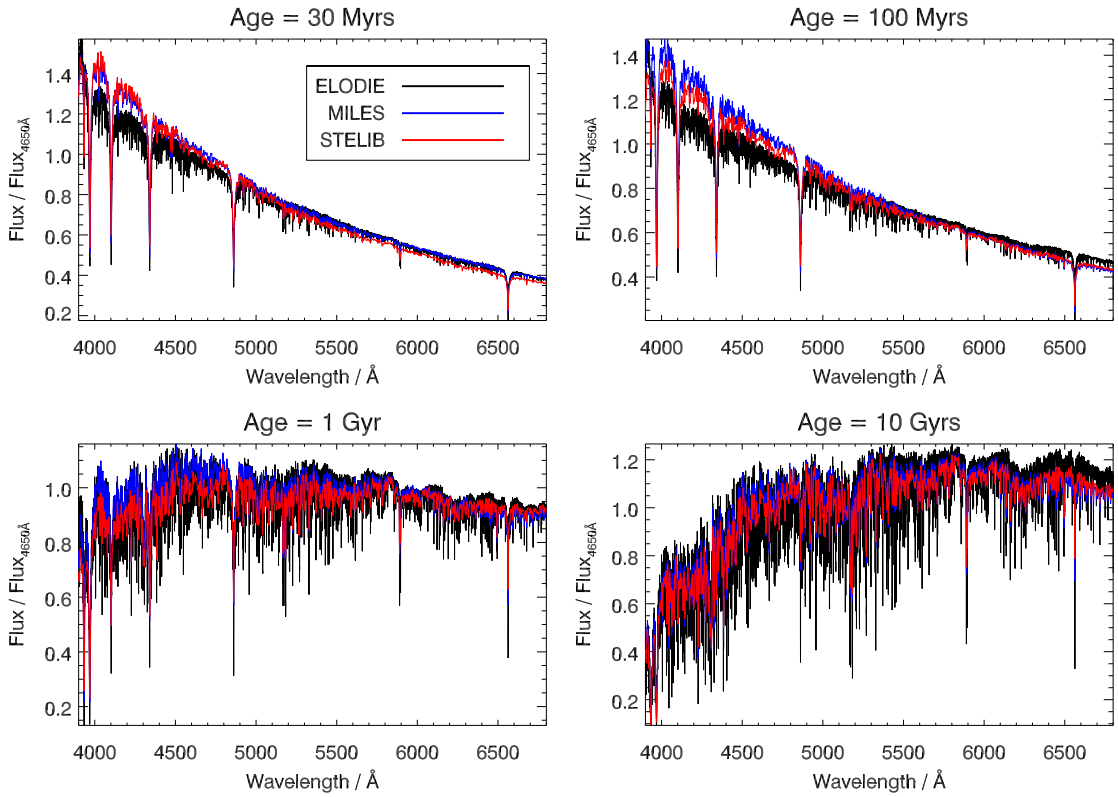

Fig. 1.3 Comparison of stellar population model spectra for different age templates: 30 Myr, 100 Myr, 1 Gyr, 10 Gyr respectively. All with a Kroupa initial mass function (Kroupa (2001)) and solar metallicity from the stellar population models of Maraston & Strömbäck (2011). Note that the different models have different resolutions that depend on the stellar library, see Chapter 2.

chooses to use a particular model.

In this thesis, we pay particular attention to analysing light from globular clusters in the Milky Way. Nearby globular clusters are essential for calibration with stellar population models, since their individual stars are able to be resolved, allowing for precise and independent age determination from colour-magnitude diagram fitting (Renzini & Fusi Pecci, 1988). They provide the 'simplest' form of stellar populations in nature, i.e. approximately a single coeval population of stars. Many of these globular clusters are therefore well fit by a single SSP, making them ideal case studies for measuring uncertainty when going on to fit unresolved stellar populations such as in galaxies. This will be explained in detail as part of the calibration of our SED analysis and presented in Chapter 3.1.

1.5 The Observational Landscape

Statistically large spectroscopic surveys in the past 15 years (e.g. SDSS (York et al., 2000), GAMA (Driver et al., 2011), 2dFGRS (Folkes et al., 1999)) have proved tremendously successful in deriving the physical properties of galaxies with high accuracy. Data across a range of redshift slices have been able to provide significant insight into the evolution of galaxy properties. Their sample sizes offer a range of environmental and morphological types, including those typically under-represented in the Universe such as galaxies in voids and galaxy major mergers.

However, these large galaxy surveys - in order to collect large samples - could only perform single aperture observations per galaxy, typically across their central regions. Therefore galaxy evolution properties as a function of internal structures, such as stellar population profiles across the core, disk or halo, cannot be measured, and the global properties are very sensitive to the aperture position and coverage (Iglesias-Páramo et al. (2013)). Physical processes such as radial migration, higher level structure such as dust structure and clumped star-formation, and signatures of merging and interactions cannot be easily constrained by single-aperture observations (Gerssen, Wilman & Christensen (2012), Wuyts et al. (2012)).

In order to surpass these limitations, many modern galaxy surveys use integral field spectroscopy (IFS) (SAURON (Bacon et al., 2001), ATLAS^{3D} (Cappellari et al., 2011), CALIFA (Sánchez et al., 2012), SAMI (Croom et al., 2012), VENGA (Blanc et al., 2013), DiskMass (Bershady et al., 2010)). This is a method by which multiple spectra of the same galaxy covering many 2D positions in the sky are obtained. This allows detailed internal information of

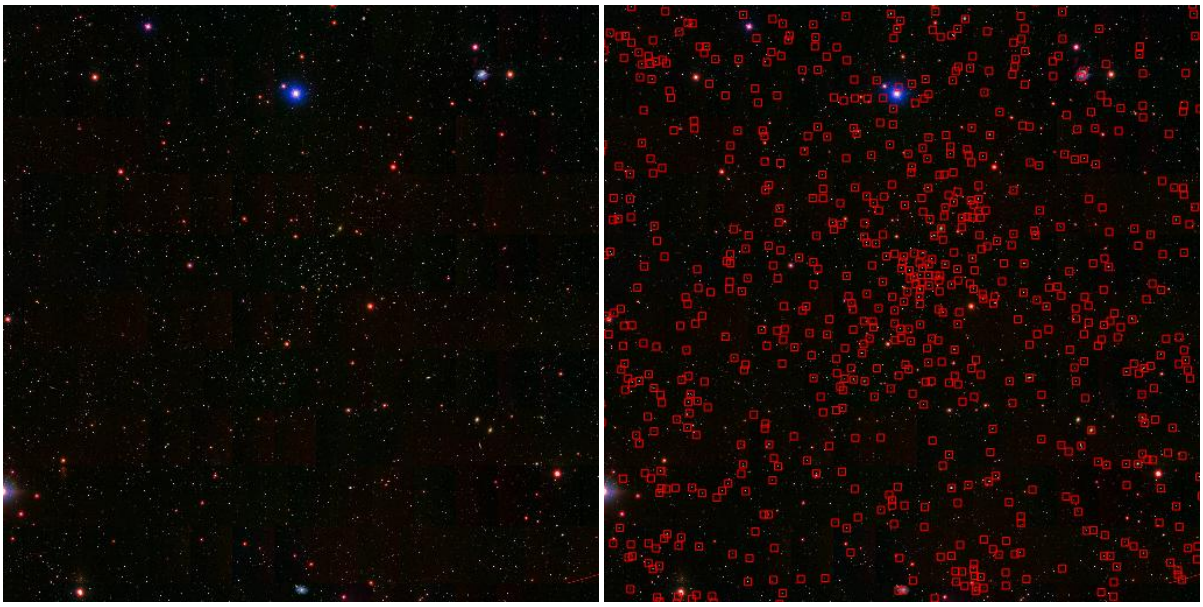

Fig. 1.4 In the left panel, a 4.55 square degree image showing a small portion of the SDSS DR7 spectroscopic area. The right panel shows the same image overlaid with the positions on the sky of the optical fibers used to obtain spectra from galaxies, stars and quasars. Most of these points are galaxy spectra and are analysed as part of the statistical samples in this thesis.

each observed galaxy to be obtained. Though, in doing so, they are more than a couple orders of magnitude lower in the sheer statistical number of galaxies observed from previous large surveys.

In this thesis we will mainly cover two cases of observational survey: a large single-aperture statistical survey, and a new IFU survey.

The observed galaxy spectra from a statistical sample that we have used in this work come from the Sloan Digital Sky Survey (SDSS) II Data Release 7 (DR7) (Abazajian et al., 2009), which gives $\sim$ 1 million galaxy object SEDs, and covers 9380 square degrees of sky at 3800 - 9200 Å. DR7 provides galaxies with a redshift range of $\sim 0 - 0.5$. We focus on spectra from the SDSS because of the very large sample available. Figure 1.4 shows a 4.55 square degree region of the sky observed in SDSS as an example, covering just 0.05 per cent of the total spectroscopic area of DR7. The right panel shows the same image overlaid with the positions on the sky of the optical fibers from which the spectra of astronomical objects are obtained. These are mainly galaxies, all of which are analysed as part of the statistical analysis in this thesis, but also include some quasars and stars. We mainly use DR7 for its wide range of galaxy types and its extensive coverage in the SED fitting literature, see section 1.6.

We have also used the SDSS-III Baryon Oscillation Spectroscopic Survey Data Release 9 (BOSS-DR9) (Schlegel, White & Eisenstein, 2009), which provides a well-defined catalogue of $\sim$ 1 million massive (and therefore more generally passive) galaxies. Therefore crucially, these galaxies provide an anchor to which to assess stellar population models, since their internal, passive processes dominate over external, cosmological processes. Combining this survey with others needs careful calibration of model ingredients, which will be assessed in this thesis.

From the IFU side of observations, we analyse the first data from the MaNGA survey (called P-MaNGA) and produce the first science publication based on the results. The P-MaNGA dataset contains 3D spectra (x position, y position, and wavelength) for 18 galaxies observed with a variety of IFU sizes and observational conditions. These data are described in detail in Bundy et al. (submitted). The analysis of the P-MaNGA observations are also used to understand and quantify the capabilities of MaNGA and help predict the results we should expect from the full dataset, and from future statistical IFU surveys.

1.6 The Full Spectral Fitting Technique: Introducing a New Code

Analysing the SEDs from galaxies allows us to deduce several of their properties, including their star formation history, metallicity, gas/dust content, chemical abundance ratios, initial mass function (IMF), and kinematic parameters such as the velocity dispersions / circular velocities of elliptical / spiral galaxies respectively. By taking a large sample of galaxies across cosmic time, investigating their properties, and classifying them, we can build up a picture of what processes drive their formation and evolution as a function of their physical properties and morphology.

The primary focus of this thesis is analysing the results obtained by fitting stellar population models to galaxy data via a full spectral fitting method. Full spectral fitting takes every available flux point in wavelength space from both the spectroscopic models and data and compares them, encompassing both absorption features in the SEDs and the overall continuum shape. This is in contrast to fitting photometric data, known as broad-band SED fitting, which integrates light over just a few wavelength 'bands'. This is a much cheaper approach in terms of integration time of telescope observations, and thus the galaxy surveys using photometry have a wider wavelength and redshift coverage, and higher signal-to-noise. However, the much coarser wavelength sampling results in much stronger degeneracies in stellar population parameters, often requiring strong priors to be placed on the star formation histories attempting

to be recovered. Another alternative approach is to use selected absorption lines (Thomas et al. (2005), Thomas et al. (2010)) of an SED. This approach is particularly useful for assessing element abundance ratios. However, it requires careful modelling of the 'pseudo-continuum' around the features, and some features can be insensitive to certain stellar population parameters, particularly dust attenuation.

Full spectral fitting over a wide wavelength range is therefore an expensive method relative to taking SEDs over a short wavelength range or broadband fitting, but one that gives a very high amount of information. Using this information effectively is important not only to derive accurate properties of galaxies, but also to understand the limitations, uncertainties, and choices that can be made in stellar population modelling.

A problem that particularly pervades the study of SEDs in the optical wavelengths is that of degeneracies. Three main parameters are particularly degenerate with respect to each other: age, dust, and metallicity. A spectrum may be redder (higher fraction of flux in higher wavelengths but lower fraction of flux at lower wavelengths) than another spectrum because of one or more of these effects:

- Higher age: as a stellar population ages, its bluer, brighter main sequence stars turn off the main sequence and evolve into red-giant-branch stars, reducing the amount of blue flux in the spectrum.
- Higher metallicity: if stellar populations have more chemical enrichment, then their stellar atmospheres have a higher opacity due to absorption by these heavier elements; this therefore reduces the effective temperature of the stars and so their surface flux is shifted towards the cooler, redder end.
- Higher reddening: Interstellar dust and gas tends to attenuate blue light more than red light, since bluer light is preferentially absorbed, so starlight appears redder overall.

All of these effects are difficult to disentangle since they can act on the SEDs in a similar way, which can be a particular difficult problem when modelling complex star formation histories. We can attempt to separate these effects by using features that become more apparent at high-resolution in the optical, for example, using the molecular lines that become more pronounced with increasing metallicity. An alternative is to use the near-infra-red or ultra-violet, but this is currently lacking in the detail that the optical wavelengths give in both the accuracy (or quality of calibration) of the models, and the size of the observational surveys. Those regions also come with their own complications (e.g. asymptotic giant branch stars' contributions to

the NIR flux, and blue stragglers / blue horizontal branch contributions in the NUV). However, since many models use optical-only model stellar libraries (especially at high resolution), and most detailed spectroscopic galaxy surveys are in optical wavelengths, most of the progress in this field to date has been in the optical.

Motivated by the wealth of galaxy properties that can be obtained with modern galaxy surveys, but also the inherent degeneracies that plague SED fitting, we set out to produce a sophisticated new method of full spectral fitting that can both assess model uncertainties, and at the same time measure galaxy properties to a high precision. In this thesis we introduce this new code, called FIREFLY(**F**itting **I**te**r**ativ**e**ly **F**or **L**ikelihood Anal**y**sis). In addition to the main motivation described above, it has been designed with the following requirements in mind:

- Be able to map out the inherent degeneracies in the model spectra, and how they propagate into degeneracies in physical properties.
- Be fast enough to analyze millions of galaxy spectra at high resolution spanning a large wavelength range in a reasonable timeframe.
- Allow a comparison of the different stellar libraries to be conducted easily.
- Have a method that visualises the parameters obtained easily so that improvements can be made incrementally.
- Can work relatively well under low signal-to-noise conditions.
- Makes as few assumptions regarding star formation history and other parameters as possible, within the constraints of the available models.

Many other fitting codes are available for full spectral fitting (e.g. PPXF by Cappellari & Emsellem (2004), VESPA by Tojeiro et al. (2007), fitting after using a PCA-based technique, by Chen et al. (2012), STARLIGHT by Cid Fernandes et al. (2005), STECKMAP by Ocvirk et al. (2006b)), all of which address the problems of degeneracies in different ways according to their purposes. In chapter 3.1 we will provide details of our approach and explain how our method compares with these full spectral fitting methods and complements the wider literature. We will also show how we have calibrated FIREFLY, and show results from example datasets, globular clusters and mock galaxies.

1.7 Outline of the Thesis

In Chapter 1 we have described the observational differences between different types of galaxies and the physical processes that are theorised to explain their properties. We have explained how the use of stellar population models combined with a full spectral fitting approach on large observational datasets can be used to obtain large datasets of galaxy properties that may shed light on the importance of these various processes. We have highlighted some important caveats and uncertainties in each part of this process. Lastly, we have motivated the production of a new full spectral fitting code, FIREFLY.

We will follow with Chapter 2, which describes stellar population modelling in detail, beginning with its historical significance through to the modern models used in this thesis. We explain how the base components of the models, simple stellar populations (SSPs), can be combined to give a full SED of a galaxy.

Chapter 3 will then describe FIREFLY. We will pay much attention to the calibration of the method through the use of tests on globular clusters and mock galaxies. We describe the motivations for the features of FIREFLY with many example datasets to illustrate the applications of the code to scientific problems. We will show the systematic effects of changing the stellar population model ingredients, such as stellar library, and the effects of changing the parameters used in the SED fit.

In Chapter 4, we apply FIREFLY to large observational datasets from the Sloan Digital Sky Survey (SDSS). We will analyse subsamples of the datasets in order to find patterns in the properties of particular galaxies. We will then show how multiple datasets can be combined consistently to assess galaxy properties as a function of redshift.

Chapter 5 shows the application of FIREFLY to a prototype Integral Field Unit (IFU) survey called MaNGA. We produce detailed maps and radial profiles of stellar population properties of this sample of galaxies. We also show how levels of data quality in IFU surveys affect errors in stellar population gradients, and show how the analysis can be extended to future large IFU surveys.

Lastly in Chapter 6 we provide conclusions on combining full spectral fitting methods with modern stellar population models, explaining their relevance in assessing current problems in galaxy evolution.

Chapter 2

Stellar Population Modelling

Stellar population models are required to convert the observed light from a galaxy into physical properties such as its age, metallicity and chemical content, stellar mass, and star formation history. In order to do this, it must predict the distribution of the physical properties of stars within galaxies, through use of a theoretical HR diagram which is described in section 2.1. This set of stars must be converted into observable properties by predicting their energy contribution to the overall galaxy light and the form that that light takes (*i.e.* a spectral energy distribution (SED). Then, all of these stars must be integrated to give a prediction of an SED for a stellar population, as described in section 2.2. The base units of these stellar populations are simple stellar populations (SSPs), in other words a co-eval cluster of stars with a given age and chemical composition. Then, a galaxy SED may be built up through integrating these SSPs over the star formation history of that galaxy, the method of which will be described in the next chapter.

In nature, globular clusters are well-represented by a single SSP. There is evidence that some globular clusters may have had more than one episode of star formation (Piotto et al., 2012), but generally these are very minor secondary episodes. Hence globular clusters are regarded as the 'simplest' stellar populations found in nature, and provide a good sanity check on the output of any stellar population model. In comparison, galaxies are very often not well-represented by a single SSP, with much more continuous star formation histories across cosmic time.

Given a fine enough grid of SSPs, one may build up any given star formation history, such as in a galaxy, by combining these SSPs by given amounts corresponding to the star formation

rate at that age. Concretely, we can recover the light from a complex stellar population as

$$L_{\text{complex}} = \int_{\text{t}} L_{\text{t}}^{\text{SSP}} \cdot \Psi(\text{t})\text{dt}, \tag{2.1}$$

where the L represents the amount of light, either as a total bolometric quantity or as a function of wavelength as an SED, $\Psi(t)$ is the star formation history, and L_t^{SSP} represents the light from a coeval stellar generation with age t. This may be represented by some discrete number of SSP components with weights approximating the star formation history as

$$L_{complex} \approx \sum_{i}^{n_{SSPs}} w_i L_i^{SSP}, \tag{2.2}$$

where w_i are the weights of each SSP component with light L_i. This then enables us to use model SSP SEDs to fit complex stellar populations, in other words fitting a stellar population model to data.

In this chapter we will discuss in detail the evolutionary population synthesis (EPS) technique, which is used to model the integrated properties, for example the SED, of a stellar population. The results of this technique is a stellar population model, and the foundation of this modelling is stellar evolution theory. We firstly give a brief outline of stellar evolution theory, describing these evolutionary phases. We then detail how this theoretical knowledge must be combined with certain model ingredients using the EPS technique in order to build up a stellar population model. Finally, we describe how these models can be used to assess the stellar population properties of observed galaxies.

2.1 Stellar Evolution

2.1.1 Hertzsprung-Russell Diagrams

The precise basic equations of stellar structure tells us that the physical properties of stars, i.e. their luminosity, effective temperature, and radius, are directly determined by their masses and their chemical composition. Stellar evolution theory then tells us how their structure evolves with time, passing through different evolutionary states. These evolutionary states can be easily separated and identified from Hertzsprung-Russell (HR) diagrams, in which one plots the luminosity of stars against their effective temperatures. Globular clusters, as described later in this chapter, represent a near-coeval population of stars with a given age and

chemical composition and so are perfect objects to identify separate evolutionary phases on a HR diagram, an example of which is shown in Figure 2.1.

In that figure one can see the prominent 'Main Sequence' (MS) stage as a nearly linear relation between luminosity and temperature. Once these MS stars have exhausted Hydrogen in their cores, the cores contract until they begin to fuse Hydrogen in a shell around the core. This transition is marked on the HR diagram in Figure 2.1 as a curve away from the main sequence known as the 'turnoff'. Later evolutionary phases described collectively as 'Post-Main Sequence' (PMS), and are described in detail in the next section.

2.1.2 Main Sequence

As stated in the introduction, star formation begins once regions of a molecular gas cloud become very dense. Once a region of the gas cloud is dense enough, it can provide radiative pressure, sourced from the gravitational contraction, to counter continued gravitational collapse. The protostars that result from this process are thought to continue to grow through steady accretion of gas in the cloud until the radiative feedback from the gas collapse onto the protostar is strong enough to prevent (or at least reduce) further accretion. This process is still poorly understood, though new observations of protostellar disks (e.g. Zapata et al. (2015)) are beginning to assess this understanding. The evolution of the protostar will depend on its mass, with higher mass protostars initiating nuclear fusion through Hydrogen burning during this accretion process, whereas lower mass stars evolve as a 'pre-main sequence' star, developing a dense enough core until nuclear fusion can then start. In either case, the timescale for the protostar and pre-main sequence phases are typically less than $\sim 10^5$ years in lifetime (Palla & Stahler, 1992), and low in brightness, and so contribute very little to the total luminosity of galaxies. Pre-main sequence stars with masses $M < 0.08\ M_\odot$ do not have cores dense enough to initiate fusion, and so do not go on to form main sequence stars. The stars with masses greater than this can move onto the main sequence, where stellar evolution processes begin to unfold.

The fractalisation (Bate, 2011) of the initial gas cloud into regions of higher density is a complex and poorly understood process, but gives rise to the mass distribution of the resulting main sequence stars. The distribution of masses of the main sequence stars in a given stellar generation is known as the initial mass function (IMF), and although there are uncertainties at the high and low extremes of this distribution (see Section 2.2.3), the IMF seems to be constant across the mass range in several regions of our Galaxy (Salpeter (1955), Zoccali et al.

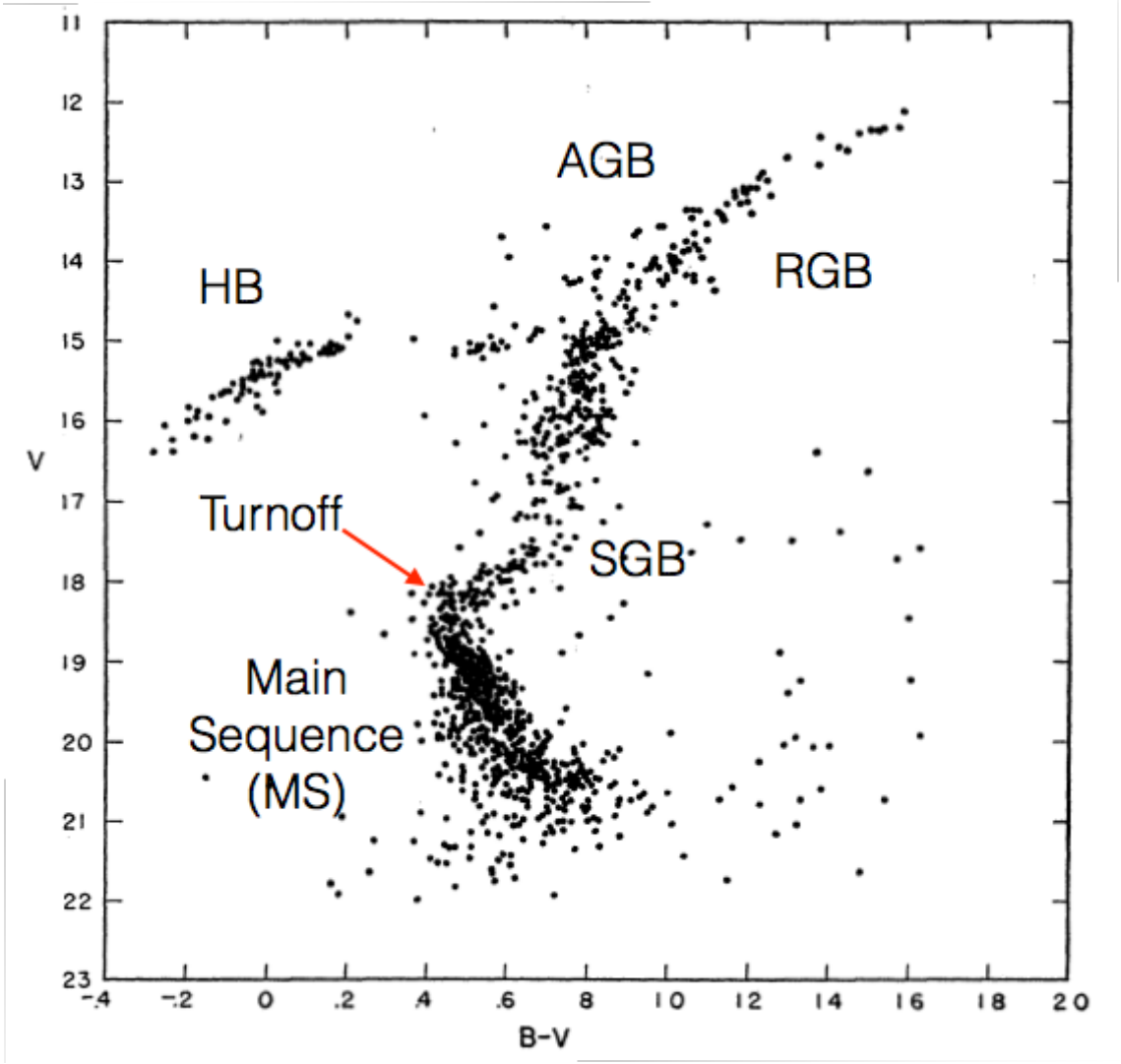

Fig. 2.1 Hertzsprung-Russell diagram of globular cluster M5, as plotted in Figure 3 of Arp (1962). The absolute V magnitude and the B-V colour relates directly to the luminosity and effective temperature respectively. We overlay labels for the stellar evolutionary states as described in this chapter: Main Sequence, Turnoff, Sub-Giant Branch (SGB), Red Giant Branch (AGB), Horizontal Branch (HB) and Asymptotic Giant Branch (AGB).

(2000), Kroupa (2001), Chabrier (2003)).

Main sequence evolution then proceeds as a function of the mass of the star, with more massive stars burning through their Hydrogen fuel more quickly. The lifetimes of this process are modelled in very high detail (e.g. Schaller et al. (1992)). During this phase, the main sequence stars move very little on the HR diagram, up until their cores are exhausted of Hydrogen and they turnoff the main sequence. Their subsequent evolution is known as post-main sequence (PMS), and the evolutionary stages within the PMS stage varies depending on the mass of the star.

2.1.3 Post-Main Sequence

Low and intermediate-mass stars ($M < 8$ M$_\odot$) move off the main sequence when all the Hydrogen fuel in the core of the star has been converted into Helium and is exhausted, known as 'turnoff'. The core does not immediately reach a hot enough temperature to fuse Helium, so once this occurs, the radiation pressure from the star reduces and the star begins to contract. A 'shell' of Hydrogen outside the Helium core then becomes hot enough to continue Hydrogen burning, injecting radiative pressure into the outer layers of the star, which causes the star to expand. At this point, the star is said to be on the 'sub-giant branch' (SGB, see Figure 2.1). As the temperature gradient between the core and outer layers increases it is said to be evolving as a 'red giant' star, growing in luminosity in a path along the HR diagram known as the 'red giant branch' (RGB, see Figure 2.1). The Helium core continues to increase in temperature as it contracts, until Helium burning starts. The injection of radiative pressure into the Hydrogen-burning shell causes the density of the shell to reduce, switching off Hydrogen shell burning. The central fusion of Helium into Carbon and Oxygen is known as the Helium burning stage, which places the star on the 'horizontal branch' (HB, see Figure 2.1). As the Helium supply is depleted, the star again begins to contract, allowing Helium burning to occur in a shell around the Carbon and Oxygen core, and Hydrogen burning in a shell around the Helium-burning shell, moving the star back into a similar position as the RGB known as the 'Asymptotic Giant Branch' (AGB, see Figure 2.1). Once the star reaches sufficient luminosity on the AGB, it ejects its hydrogen outer layers, leaving behind a planetary nebula before becoming a white dwarf star. Taking account of each of these stellar phases is important, as shown in Figure 2.2, since these phases, particularly AGB and RGB stars, can dominate the light of the whole stellar population at certain ages.

High mass stars ($M > 8$ M$_\odot$) are able to hold onto their material through phases beyond

Helium burning, successively building up layers of heavier elements all the way to Iron in the core. The PMS stage of high-mass stars is much shorter in duration than in lower mass stars, taking just 30 Myr or less. As the Iron core builds up more pressure, photodisintegration of the inner core takes place. The resulting contraction results in a powerful supernova explosion that can contribute a significant amount of a whole galaxy's light.

2.1.4 Stellar Evolution Uncertainties

The evolutionary mechanism described in Section 2.1.3 is very well understood and constrained. However, there are some uncertainties remaining in the PMS phases that can affect the interpretation of the light from a stellar population. These uncertainties particularly affect the AGB phase, where the stellar evolution is very complex. We now briefly describe some of these uncertainties. We note that we could also include the effects of stellar rotation and binary systems as introducing systematic uncertainties, and although these effects have been investigated somewhat in the literature (e.g. Vazquez 2007, Eldridge 2012), typically these are not implemented in current stellar population models.

Convective regions in stars allow for efficient energy transfer, resulting in changes to the temperature and size of the stars affected. At $M > 1$ $M_{\odot}$, the cores of stars are highly convective. The boundaries between convective regions and radiative regions are not determined theoretically, and are not sharply defined since the velocities of stellar material can cause it to be carried outside of convective regions, in a process known as 'overshooting'. More overshooting increases the size of the core of main sequence stars and thus increases their lifetime, which then propagates to a delay in forming RGB stars, changing their calibration of ages of PMS stars in the HR diagram (Girardi et al., 2000). This process results in uncertainties on the luminosities of these phases (Yi (2003), Ferraro et al. (2004), Maraston (2005), Conroy & Gunn (2010)). It is still unclear whether overshooting is important and what the size of its effect is (Stothers (1991), Nordstroem, Andersen & Andersen (1997), VandenBerg & Stetson (2004), Keller & Wood (2006), Sandberg Lacy et al. (2010)).

Mass loss is another systematic uncertainty in stellar evolution, particularly at the tip of the RGB where the radiative pressure of the star grows strong enough to begin pushing outer layers of the star away, which can then affect the later evolutionary phases. Since the physics of mass loss is not able to be constrained from purely theoretical principles, and there is a limit to the detail available from radiative models for mass-loss events such as stellar winds (Willson, 2000), mass loss is currently applied in stellar population models as an empirical

parameter (e.g. Dotter (2008)). Reimers (1977) derived the following empirical equation to describe mass loss of the form

$$\dot{M} = -\eta \frac{L}{gR}, \tag{2.3}$$

in units of $M_{\odot}$/yr, where L is the luminosity, g the surface gravity, and R the radius, of the star, all in solar units. η is an empirical parameters whose value is determined from observations of RGB stars to be $\sim 4 \times 10^{-13}$ (Reimers (1975), Fusi-Pecci & Renzini (1976)).

It is important to include this effect since mass-loss affects the luminosities and lifetimes of AGB stars and HB stars contributing to the overall population (Bedijn (1988), Bryan, Volk & Kwok (1990), Bloecker (1995)). Consider Figure 2.2, reprinted from Maraston (1998), which shows the luminosity contributions of stellar phases with age. At 0.3 – 1 Gyr, light from AGB stars dominate and above 1 Gyr, RGB stars dominate the light. Hence, modelling the mass-loss from AGB stars is critical for stellar population models at these ages. HB stars also contribute a sizeable amount of light across all ages. Higher amounts of mass-loss will cause the temperatures of HB stars to reach higher values, creating 'blue' HB evolution, thus mass loss in this phase also needs to be carefully taken account of. The analytical prescriptions used to assess the effect of mass loss in these phases are again motivated by empirical prescriptions as above, presenting an uncertainty for the luminosity contributions of these phases.

Finally, the effect of thermally-pulsating AGB stars (TP-AGB) has been discussed extensively in the literature (e.g. Maraston (1998, 2005), Marigo et al. (2008), Conroy, Gunn & White (2009)). This phase alternates Hydrogen and Helium shell burning and Carbon and Oxygen core burning for stars of mass $M = 2-3\ M_{\odot}$, and can cause a considerable change in the near-IR luminosities of $\sim$1 Gyr stellar populations. Since this process is very difficult to model numerically due to the double-shell burning and strong mass loss in this phase, empirical prescriptions need to be used.

2.2 Components of the modelling

As introduced in Chapter 1, building a stellar population model requires the following techniques: a stellar evolution prescription to tell us how stars evolve along the HR diagram, a stellar library to convert the physical properties of a stellar population into an SED, and an initial mass function to tell us the mass distribution of stars at their birth. In this section, we

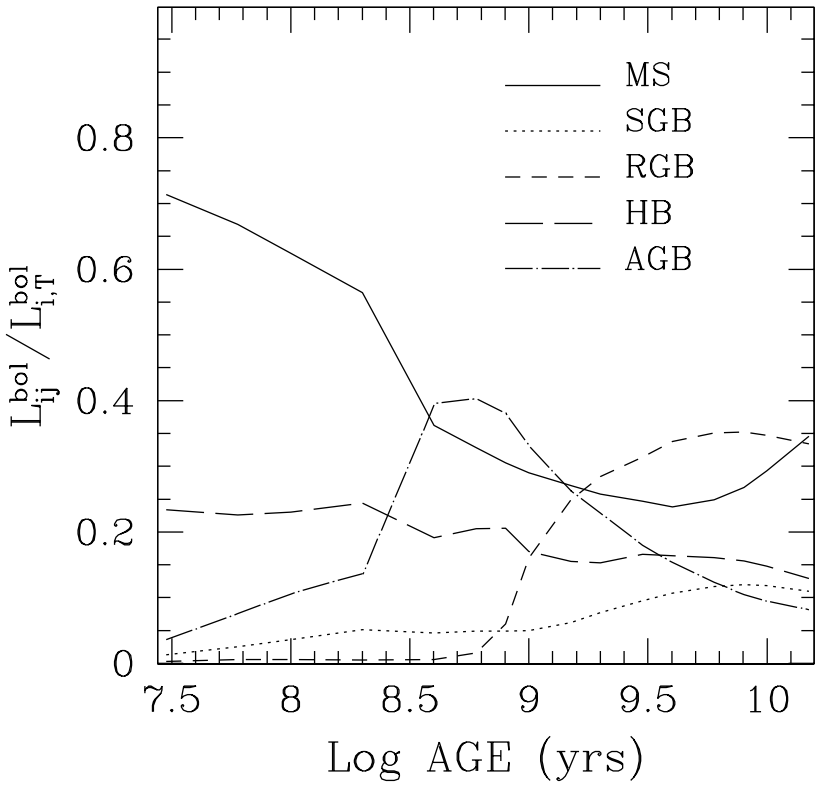

Fig. 2.2 Luminosity contributions of stellar phases as a function of age. Acronyms for the stellar phases match those from Figure 2.1. This Figure is a reprint of Figure 7 from Maraston (1998).

describe each of these aspects.

2.2.1 Stellar models

Stellar models, known as 'tracks' (such as Girardi et al. (2000), Yi, Kim & Demarque (2003), Cassisi et al. (2006)) tell us about the energetics of the stellar phases and how stars in positions on the HR diagram change with time. The relationship between the mass and luminosity is typically given as isochrones as a function of a set of mass bins. This works particularly well for main sequence stars and stars beginning to turn-off, since these are well-modeled and calibrated well with globular clusters. However, the post-main sequence stellar phases are typically not as well calibrated due to a small sample size of local globular clusters in these phases. Additionally, different sets of tracks will tackle the PMS stage problems of stellar evolution, as described above, differently depending on the empirical prescriptions used. Interpolation methods can go some way to address some of the problems associated with low-number stellar phases to give a smoothly-evolving stellar population, but the systematic errors remain.

2.2.2 Stellar spectra

Following the computation of the energetics above, we then need to convert the luminosities of each of the positions on the HR diagram into an SED, which will then be able to be compared with observations. As explained in the introduction, there is a choice to be made between empirical and theoretical stellar spectral libraries for this purpose.

Empirical libraries contain hundreds, or thousands, of observed stars with a well-determined temperature, surface gravity, luminosity and metallicity. This provides a grid of stars in the HR diagram, which can then be interpolated to return an SED for any value of temperature or gravity. Conversely, theoretical libraries of stellar spectra are based on models on stellar atmospheres modelling using detailed radiative transfer methods (Mihalas, Auer & Mihalas (1978), Kurucz (1979)).

Using different stellar libraries has an effect on the derived integrated SED. For the empirical libraries this is because the selection of stars used and the observational conditions they are observed under is different. We have plotted a sample of SSP spectra directly from the models used in this thesis as a function of age in Chapter 1. Each model clearly gives different SEDs, the differences of which change as a function of age and metallicity.

Model library	Wavelength coverage (min – max) / Å	Age coverage (min – max) / Myr	Metallicity coverage (Z/H)
MILES	3500 – 7429	6.5 – 15000	[0.0001, 0.001, 0.01, 0.02, 0.04]
STELIB	3201 – 7900	30 – 15000	[0.01,0.02,0.04]
ELODIE	3900 – 6800	3 – 15000	[0.0001, 0.01, 0.02, 0.04]

Table 2.1 Parameter coverage of the Maraston & Strömbäck (2011) stellar population models as a function of input stellar library, available at www.maraston.eu/M11/README_M11.txt

A key theme of this thesis is testing for the effect of varying the stellar spectral library as input to a fixed stellar population model on the galaxy properties obtained through SED fitting. This develops the work contained in Maraston & Strömbäck (2011) (hereafter, M11), who produce and test three semi-empirical models based on the corresponding three stellar libraries (MILES (Sánchez-Blázquez et al., 2006), STELIB (Le Borgne et al., 2003), and ELODIE (Prugniel et al., 2007)). We summarise the differences between the models based on the stellar libraries in Table 2.1.

Models based on the MILES stellar library (Sánchez-Blázquez et al., 2006) have the largest range and sampling of the stellar population parameter grid (in terms of age and metallicity), of all three of models, and a high spectral resolution of 2.54 Å (Beifiori et al., 2011). In particular, it has coverage of both low and ultra-low metallicity populations ([Z/H] = 0.05 and 0.005 respectively), albeit only to old ages (due to the chemical composition of Milky Way stars), in total comprising of five available metallicities up to twice-solar. The wavelength coverage of MILES-based models is somewhat limited, 3500 – 7429 Å, and as discussed in M11 and Maraston et al. (2009), have a somewhat lower flux upwards of 6400 Å compared to STELIB and ELODIE-based models due to the differences in the assumed temperature scales for a class of RGB stars called the RGB-bump.

Models based on the STELIB stellar library (Le Borgne et al., 2003) have the smallest age and metallicity coverage of the three models used. The stellar library only has a reasonable sample of stars for a more limited metallicity range compared to MILES, and so their corresponding models contain just three metallicities: half-solar, solar, and twice-solar. They also lack some of the younger ages present in the other models. However, they boast the largest wavelength range of 3200 – 7900 Å, and for solar metallicity 3200 – 9300 Å, with a resolution of ~ 3 Å. To keep the wavelength range consistent when fitting the SEDs of STELIB model spectra with multiple metallicities, we limit the wavelength range to 3200 – 7900 Å.

Lastly, models based on the ELODIE (v3.1) stellar library (Prugniel et al., 2007) have a fair age and metallicity coverage, extending down to ultra-low metallicities but lacking the low-

metallicity (Z/H = 0.001) stellar populations compared to MILES. They contain the youngest stellar populations of the models we use, down to just 3 Myr for solar metallicities, though higher for non-solar metallicities. The models have an exceptionally high resolution of 0.55 Å, but in exchange have a fairly low wavelength coverage of 3900 – 6800 Å. In addition, Figure 12 of M11 shows that the flux calibration may also not be optimal.

We note that we only use empirical libraries to keep comparisons equivalent. The use of empirical libraries comes with some drawbacks. Specifically, there are a lack of M dwarf stars, limiting the temperature and surface gravity coverage in the Main Sequence in that region. To mitigate this, M11 use theoretical dwarf spectra from the MARCS library (Gustafsson et al., 2008), smoothed to match the resolution of the observed stars. In addition, there are a lack of Carbon and Oxygen-rich stars, necessary to cover the TP-AGB stellar phase. To represent this phase, M11 use interpolated versions of low-resolution spectra from Lançon & Wood (2000), as was used in Maraston (2005), which still provides enough resolution to identify the broad features from the component AGB-stars in the resulting SEDs.

2.2.3 Integration Method

Finally, the energetics and physical observables (i.e. SEDs and the conversion of light to stellar mass) must be integrated across all the relevant evolutionary phases in a stellar population. For the main sequence, one is able to integrate all the flux contributions along an initial mass function (IMF), using time as the integration variable. This integration in time is known as isochrone synthesis.

Further integration using such isochrones up to PMS stages is possible for RGB stars but becomes very difficult for AGB stars and later phases due to the lack of observed stars in these states (Maraston (1998, 2005)). Instead of trying to integrate over time, as in an isochrone, to get a total luminosity, one can instead integrate over the 'fuel' available in each of those late stellar phases, where fuel is the amount of mass in Hydrogen or Helium available to undergo fusion. This is known as the 'fuel consumption theorem' (Renzini & Buzzoni 1986), which explains that the total luminosity contributed by any given late stellar phase is directly proportional to the amount of fuel available to burn in that phase. This allows MS stars and PMS stars to be analytically related in their luminosity contributions, including very short-lived stages of evolution such as TP-AGB stars. The M11 models used in this thesis use this approach for PMS phases, following the prescriptions of Maraston (2005).

2.3 Interstellar Dust

Both AGB stars and supernovae lose stellar material, known as dust, to their surroundings, *i.e.* the interstellar medium (ISM). Light from stars passing through dust becomes extincted - absorbed in optical and UV wavelengths and scattered in the far IR (Mathis, 1990). The amount of extinction as a function of wavelength is known as an 'extinction law', and can be used in modelling the passage of light through a dust region, *e.g.* a dust screen between a star and the observer, such as in the Milky Way (Fitzpatrick, 1999). In observing an external galaxy, many stars will pass through different amounts and properties of dust depending on the geometry of the galaxies' stellar and dust content. This in total affects the light by 'attenuating' it in the optical - reducing the total observed light in bluer wavelengths more than the red, because of this it is often known as 'reddening'. This can be derived theoretically by modelling the passage of all the stars' light, all of which will be extincted differently depending on their positions in the galaxy, or empirically derived, predominantly by comparing the SED shape across many galaxies with otherwise similar properties (Calzetti et al., 2000), typically measured as a 'colour excess' between regions of the spectrum.

The overall attenuation law used gives a relation between this colour excess parameter, typically the excess in green relative to blue light ('E(B-V)'), and the attenuation on the SED, in other words the multiplicative factor that one applies to the SED as a function of wavelength. In this thesis, when giving E(B-V) values we always use the Calzetti et al. (2000) attenuation law but this choice can be changed by the user easily. So, one can simply add this in as an additional parameter to fit. However, this attenuation law (and many others in general) varies smoothly with wavelength, and in Chapter 3 we show that we can exploit this feature to derive attenuation as a function of wavelength using stellar population models.

2.4 Model fitting

We can fit these derived model SEDs to data SEDs using model fitting. This is useful in cases where we have independent measurements about the object being observed, since we can calibrate the models to ensure sensible recovery of physical properties. From there, we can use model fitting on measurements of unresolved stellar populations of galaxies to measure their physical parameters, such as age, metallicity, dust, star formation history, and stellar mass, which is ultimately the goal of stellar population modelling. The importance of this is demonstrated in Figure 2.3, where we show how the relationship between mass and light is

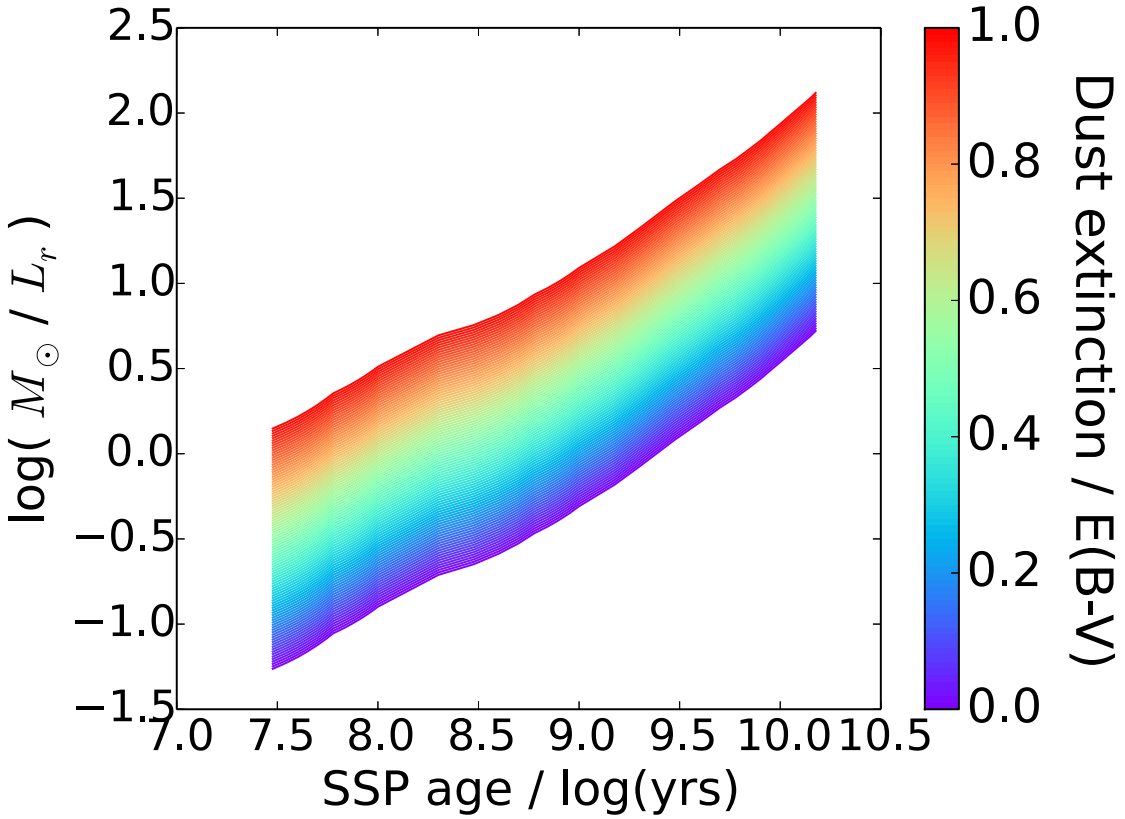

Fig. 2.3 Stellar mass-to-light ratio as a function of dust and stellar population model age, where we take the age as a simple stellar population (SSP) model, which corresponds to a single coeval population of stars. Models used are Maraston & Strömbäck (2011) models based on the STELIB stellar library with a Kroupa IMF, and dust is applied using a Calzetti law prescription. See Section 1.4 for information about the models and SSPs. Light is calculated over a red part of the SED called the SDSS r-band.

very dependent on the star formation history that one derives from stellar population model fitting.

Figure 2.3 shows the mass-to-light ratio for a set of stellar population models, computed over a particular observed window in the red part of the SED called the SDSS r-band (see Chapter 4), as a function of model age and amount of dust. The range of mass-to-light ratios shown is over orders of magnitude. The reason for this scatter is those galaxies with younger stellar populations will have brighter main sequence stars with higher amounts of luminosity per unit stellar mass. In other words, the more recent the star formation, the lower the stellar mass-to-light ratio. In addition, luminosity-obscuring dust, as described in Chapter 1, will increase the stellar mass-to-light ratio and can vary from galaxy to galaxy, further increasing the scatter in the luminosity-stellar mass relation. Late-type galaxies, which have extended star formation

histories and hence more young stars, will tend to have a lower stellar mass-to-light ratio than the early-type galaxies, which have a passive star formation history, of the same formation age. Hence deducing a galaxy's star formation history is vital for relating key physical properties, but to do this accurately requires careful calibration of the stellar population model.

The best example in nature of calibrating the stellar population models comes from observations of Milky Way globular clusters. These objects are close enough to have their stars be individually resolved, which means we can plot them on a colour-magnitude diagram and assess their ages from colour-magnitude diagram fitting (Renzini & Fusi Pecci, 1988), using exactly the same stellar tracks as are input to the models. Since globular clusters are mostly well-fit by a single coeval stellar population, their measurements also allow detailed assessment of the errors in the model fitting. We carry out this assessment in Chapter 3.1 for many different clusters.

There are many different methods for model fitting. Absorption index fitting for example, is the technique in which the 'strength' of individual absorption lines in a narrow wavelength portion of a spectrum are calculated by measuring the difference in flux from the background continuum (e.g. Worthey et al. (1994)). This has the advantage of many of the features being insensitive to dust, so long as the continuum and absorption lines come from the same type of star, and only require observing a narrow wavelength range. However, in this thesis we instead focus on using a 'full spectral fitting' approach over absorption index methods, since using the full spectrum exploits the full amount of information available to us from many optical surveys and models.

Full spectral fitting is the technique of fitting every available flux point across a large wavelength range. Modern observational surveys and models have such a high resolution that this often encompasses several thousand flux points, including both absorption features and the long-wavelength continuum shape. As will be described in Chapter 3, many codes use the minimisation of the χ^2 value, defined generally as $\chi^2 = \sum_{\text{wavelength}} \frac{(\text{Data}-\text{Model})^2}{(\text{Error})^2}$, as the algorithm for selecting better model fits to the data. How this algorithm is implemented varies depending on the full spectral fitting code, and we will compare various methods devised in the literature for implementing χ^2 minimisation.

The large amount of information available means that we can assess the stellar population properties of galaxies to a high degree of accuracy, motivating a very thorough treatment of the assumptions that go into the fitting code. In particular, spectral degeneracies inherent in the models can cause uncertainties in the physical properties obtained from full spectral

fitting codes. Hence we are motivated to present a new code that, in addition to providing accurate physical properties of galaxies for general use in the astrophysics community, takes into account the detailed treatment of these degeneracies in order to give reliable model errors.

Chapter 3

A New Code for Full Spectral Fitting

The main project of my PhD thesis has been to write a new full spectral fitting code and apply it to many different types of galaxy types and surveys. We also use it to map out the effect of spectral energy distribution (SED) degeneracies on galaxy properties, and quantify the effect of varying input model ingredients on the galaxy properties recovered. The code is a high-resolution full spectroscopic fitting code based on χ^2-minimisation with treatment of the inherent spectra degeneracies and uncertainties in the data, called FIREFLY (**F**itting **I**te**R**ativ**E**ly **F**or **L**ikelihood anal**Y**sis).

FIREFLY is unique among full spectral fitting codes in that it provides probability distributions of *star formation histories*, which may then be marginalised over other properties to give age and metallicity and mass probability distributions that some other codes provide. This gives the user an incredibly detailed view of the often diverse set of star formation histories that adequately fit to any given data SED. This means for example that one can exclude certain sets of star formation histories after fitting, rather than re-fitting with a large amount of possible permutations of star formation history form. The user can decide whether a particular star formation history is realistic, or justified given its statistical significance on a fit-by-fit bases

The second major unique feature of FIREFLY is its treatment of dust. As described in detail in section 3.4, we use a Fourier filter to fit for the long-scale features of a spectrum to derive the attenuation curve of each individual galaxy SED. This method is particularly useful when one does not wish avoid oversimplification or complication of the dust attenuation since the only input for this method in the wavelength scale that one wishes to study.

We have applied this code using three different input stellar libraries to quantify the systematic

effects of varying the model ingredients on the galaxy properties obtained, such as their age, metallicity, and star formation history. To calibrate the fitting procedure, we have used a comprehensive suite of mock galaxies and a sample of Milky Way globular clusters. In Chapter 4, we then show applications of FIREFLY to galaxies in the Sloan Digital Sky Survey, and explain how changes in the parameters used in SED fitting and stellar population models alter the derived picture of galaxy evolution.

The details of FIREFLY are described in section 3.1, with a detailed analysis of tests done using mock galaxies and globular clusters in order to calibrate our code and fitting properties. Finally we provide a comparison to other codes existing in the literature.

3.1 Introducing FIREFLY

To compare the results of fitting stellar population models to observations, FIREFLY finds physical parameters, such as age, dust, metallicity and star formation history, by minimising the χ^2 values of models with respect to the data. In addition to the 'best fit' we also output many other solutions and their associated values of χ^2. Thus, it gives a likelihood surface with many maxima across a large amount of parameter space. Full details of the algorithm are given in Section 3.3.

The reasons for writing our own code is to focus on these requirements:

- Be able to map out the inherent degeneracies in the spectra, and how they propagate into degeneracies in physical properties.
- Be fast enough to analyze millions of galaxy spectra at high resolution spanning a large wavelength range in a reasonable timeframe.
- Allow a comparison of the different stellar libraries to be conducted easily.
- Have a method that visualises the parameters obtained easily so that improvements can be made incrementally.
- Can work relatively well under low signal-to-noise, hereafter "S/N", objects.
- Makes as few assumptions regarding star formation history and other parameters as possible, within the constraints of the available models.

In section 3.2, we explain the rationale for the first requirement in this list with an example

case of the globular cluster M67. In section 3.3 to 3.6 we then detail the generalised method, with descriptions of how we treat additional complications in the spectra, including dust, complex star formation histories, emission lines, and variable wavelength ranges. In section 3.7 we discuss how we obtain overall galaxy properties such as the average age, metallicity and total stellar mass, and in section 3.7.1 we describe the statistics of the fits obtained and how these lead to visualisation of physical properties. In Section 3.9 to 3.11 we calibrate our procedure with mock galaxies and globular clusters. Lastly in section 3.12 we compare out fitting procedure with other popular procedures in the literature.

3.2 Rationale: case study of M67

For an initial comparison and test of our fitting code we developed the work shown in Figure 29 of Maraston & Strömbäck (2011), hereafter M11, in which they show that the 'best fits' in terms of minimum χ^2 of single SSP solutions to the globular cluster M67 for MILES- and STELIB-based models, finding that they give very different ages and metallicities. We also fit the globular cluster M67, but using all three of M11s semi-empirical models, i.e. with the addition of the ELODIE-based models. For this test, we select only single SSP solutions and use only the best fits (minimum χ^2), plotting the results in figure 3.1. M67 is an ideal object for the purposes of calibrating our code to extend this method because as a resolved stellar population its age and metallicity have been independently determined from colour-magnitude diagram fitting (see Sarajedini, Dotter & Kirkpatrick (2009) for a recent measurement of 3.5 – 4 Gyrs from fitting isochrones to its individual turnoff-mass stars). It is also a desirable object to calibrate with because it is approximately solar in metallicity and not alpha-enhanced, which matches with the models (which have solar-scaled abundance ratios at solar metallicities; see M11). We therefore expect the models and our fitting code to give excellent fits. The wavelength range used for the best fits is the maximum used by the data (3650 - 5350 Å) or the models, and the spectra in this case are normalised to 4600-4700 Å because this region is relatively free of absorption lines and matches the work of M11. By normalising the spectra, rather than fitting for the normalisation factor, we ensure every SSP can contribute equally in terms of flux to the fit, which will be important when building combinations of SSPs later in this Chapter. Note that after this analysis, we will normalise to as large a wavelength range as possible so that we do not need to worry about absorption features in particular regions, and so that this method still works when we are missing data from portions of the wavelength region.

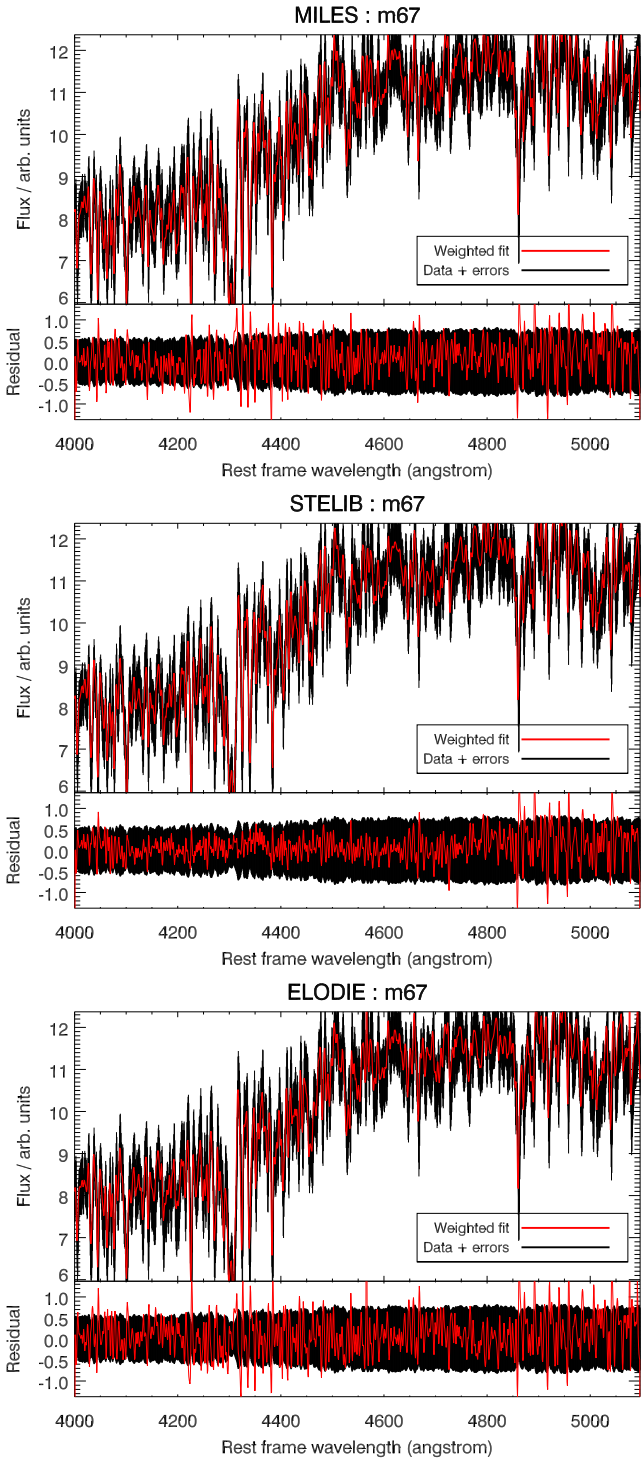

Fig. 3.1 Best fits of globular cluster M67, all of which are visually excellent. Residuals shown in red are the model minus the data, and the black shows the error spectrum minus the data.

The results from fitting M67 demonstrates clearly a common problem with simply taking the minimum chi-squared value fit of all the possible parameter combinations - the properties identified varied considerably between model used, painting a very different picture of the globular cluster's current properties and star formation history, despite their fits looking so similar. MILES-, STELIB-, and ELODIE-based models give ages of 9, 3, and 10 Gyrs at half-solar, solar, and half-solar metallicities respectively. In other words, STELIB-based models seem to match the CMD-derived results well, but MILES- and ELODIE-based models seem to suffer from age-metallicity degeneracy effects that place their lowest chi-squared values at a correspondingly higher age but a lower metallicity. This is particularly problematic because it is very easy to find combinations of age and metallicity that give very similar chi-squared values; indeed, these solutions are all within 0.1 percent of each other. Hence, we are motivated to produce a more sophisticated algorithm that takes these degeneracies into account.

3.3 Algorithm

When using a χ^2-minimisation technique, it has been demonstrated in the previous section for M67 and in M11 that, depending on input model ingredients, the 'best' solution (in terms of minimising the chi-squared value between the model and data) may not correspond to the most realistic or precise galaxy properties. Clearly, this method of finding the physical parameters of a galaxy is inadequate, especially given the close proximity of the chi-squared values of many combinations of parameters. With this in mind we have developed our fitting code to give the additional information of not only the minimal chi-squared solution, but also a good sample of other solutions. This approach requires that these solutions, which may have very different galaxy properties, adequately cover the parameter space near the minimum χ^2 solution.

Figure 3.2 shows our general procedure for fitting an object spectrum with a single set of model spectra[1]. A step-by-step diagram of the fitting process of the full spectrum of an example SDSS galaxy (see Chapter 4) is shown in Figure 3.3. By using this parallel fitting approach we can obtain many combinations of simple stellar populations (SSPs), often giving on order 1000 solutions. The assumptions in this approach are:

- we are able to find good solutions by working in the basis of the SSPs (i.e. assuming the *individual* solutions can be modelled with a bursty star formation history). However, if

[1]Examples are applications to SDSS and M11 models but this can be applied to any set of data and models

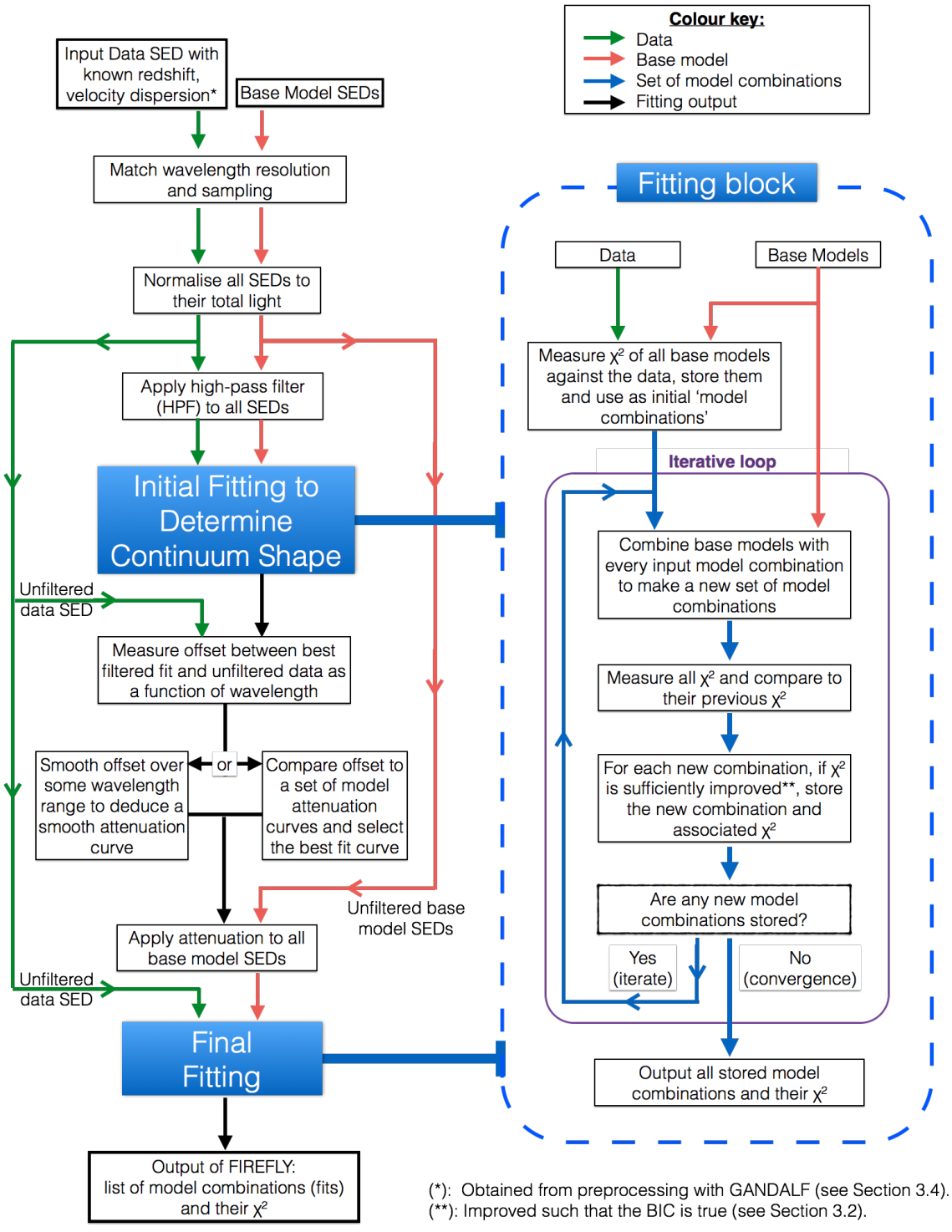

Fig. 3.2 Schematic description of FIREFLY.

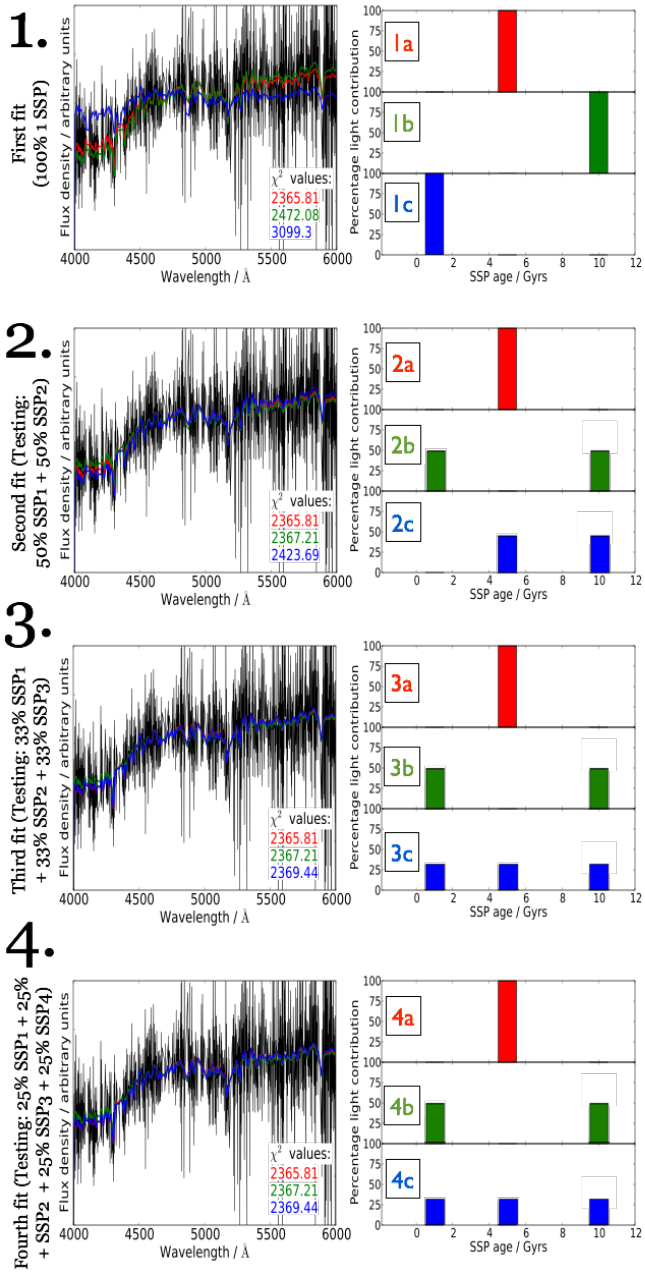

Step One: Initially each of the SSPs are fit to the data. In this example fitting process to a sample galaxy we only use 3 SSPs:
1 Gyr, 5 Gyrs, and 10 Gyrs, all at solar metallicity.
1a = 5 Gyr SSP, **1b** = 10 Gyr SSP, **1c** = 1 Gyr SSP.

Step Two: For each SSP fit in step one, we add all possible combinations of an additional SSPs such that both SSPs contribute 50% of the total light each.
i.e. New fit = 50% new SSP + 50% initial (step one) SSP.
Each combination must improve the BIC to be included, otherwise only the fit from the previous step is included. All combinations are saved and the top three plotted (left). This is an explanation of each of the fits in order:

- **2a** is the same as **1a**, where any further SSPs added to the initial 5 Gyr SSP did not improve the BIC. **100% 5 Gyr.**
- **2b** came from **1b** with the addition of a 1 Gyr SSP to the initial 10 Gyr SSP. **50% 1 Gyr + 50% 10 Gyr.**
- **2c** came from **1b** with the addition of a 5 Gyr SSP to the initial 10 Gyr SSP. **50% 5 Gyr + 50% 10 Gyr.**

Step Three: The previous step is repeated, adding another SSP if the BIC is improved.
i.e. New fit = 33% new SSP + 33% step two SSP
+ 33% step one SSP
This is an explanation of each of the fits in order:

- **3a** is the same as **2a**, again where any further SSPs added to the initial 5 Gyr SSP did not improve the BIC. **100% 5 Gyr.**
- **3b** is the same as **2b**, where any further SSPs added to the previous SSP combination did not improve the BIC. **50% 1 Gyr + 50% 10 Gyr.**
- **3c** came from **2c**, with the addition of a 1 Gyr SSP with the total light of the initial SSP. **33% 1 Gyr + 33% 5 Gyr + 33% 10 Gyr.**

Step Four: Each of the top three combinations remain unchanged, due to every possible SSP contribution not improving their BIC values. Generally, solutions tend to converge like this at around steps three to five. We save each new model combination (i.e. SSP weights) and their associated χ^2 values at every step, **including the step one 100% SSP weights.** For the full set of model SSPs, this can be on the order 1000 solutions, all of which are then output.

Fig. 3.3 Step-by-step example of running the FIREFLY fitting block on an SDSS galaxy (see Chapter 4), using a reduced set of model SSPs for clarity.

we use a finely sampled in time grid of SSPs then we are able to obtain star formation histories that are effectively continuous.

- we are able to first find a suitable SSP-based fit and then hone our overall composite star formation history by adding smaller proportions of other SSPs to this fit.
- combinations of these solutions can be combined via χ^2 likelihoods to give a physically realistic sum star formation history.

Before fitting we first match the wavelength sampling of the models and data using integration of the linearly interpolated highest sampled spectra (models or data) over the lowest sampled spectra, and normalise all input data and models across the wavelength range used such that their total flux sums to 1. Therefore, when computing the weights of SSPs to the fits we are calculating the contributions by light. Then, the main component of this code, the 'Fitting Block' in Figure 3.2, is the iterative loop over equal-light weights of all the base model SSPs. At each iteration of the loop, we progressively increase the size of the linear combinations used in the fits. To give a concrete example, suppose a 10 Gyr, solar metallicity SSP ($Fit_1 = F_{10Gyr,Z_\odot}$, where F is the SED flux) has a χ^2 value that may be reduced by adding a 3 Gyr, half-solar metallicity component, thus creating a linear combination of SSPs as a fit to the data as $Fit_2 = \frac{1}{2}\, F_{10Gyr,Z_\odot} + \frac{1}{2}\, F_{3Gyr,0.5Z_\odot}$. Each of the possible combinations of two SSPs are checked for improvement on the one-SSP fits, and all fits from both one- and two-SSP fits are saved for the next iteration. This continues until convergence, see below. The minimum weight of any given SSP in the output using this approach is therefore 1 / (number of iterations), typically around 5 for spectral with signal-to-noise of 5. Given that we save typically 1000s of base model combinations, this allows for a detailed star formation history to be recovered.

In order to avoid over-fitting and allow for convergence of solutions, we employ the Bayesian Information Criterion (BIC). The BIC quantifies the likelihood of the set of parameter values found given the goodness of the spectral fit (in our case, the χ^2 value) and includes a penalty term that increases as the number of parameters used increases; see Liddle (2007) for a discussion on the BIC and other information criteria. In order to iteratively improve our fits, we require that the BIC must be improved (reduced) at each iteration of the fit in order for a new SSP contribution to be added. The BIC is defined as follows:

$$\mathrm{BIC} = \chi^2 + k\, ln\, n, \tag{3.1}$$

where k is number of fitting parameters used (in our case, the number of SSPs added in com-

bination to make a fit), and n is the number of observations (in our case, the number of flux points used in the fit). Therefore at each iteration step the Δ_iBIC must be less than zero (where we take $\Delta_i x$ to mean the value of x at step i minus the value at step $i-1$, hence $\Delta_i k = 1$), which means that for a single iteration

$$\Delta_i \chi^2 < ln\ n \tag{3.2}$$

must hold in order to contribute to the fit. This prevents unimportant contributions (~ 1 % SSP contribution by light, estimated from observing typical $\Delta_i \chi^2$ excluded) to the star formation history from extending the fitting process, and hence prevents wasting CPU time for no measurable benefit to any of the physical properties obtained. The BIC depends on the number of pixels since the $\Delta_i \chi^2$ value will be increased by the same factor in log likelihood, hence the $ln\ n$ takes this into account. The BIC method is more appropriate for adding new models to the linear combinations than a likelihood ratio test, the use of which is only appropriate for nested models which does not hold in this case.

We ensure that we cover adequate parameter space in order to avoid over-investigating local minima in χ^2 at each iteration by allowing any combination that improves the fit beyond the median value of χ^2 computed at the previous stage. This means that as more solutions get more precise, this median value converges as a function of all the other investigations.

For the vast majority of SDSS DR7 galaxies, see Chapter 4, we find that solutions converge between the third and fifth iterative step with the BIC employed. From this procedure we thus obtain a set of ~ 1000 fits, each of which has a record of the linear combination of their SSP contribution, the flux of which is given by

$$F(\lambda) = \sum_{i}^{n_{SSPs}} a_i m_i(\lambda), \tag{3.3}$$

where a_i are our mass-weights to the base models m_i.

3.4 Interstellar Reddening

FIREFLY takes into account both interstellar reddening of the object observed, and foreground reddening due to the Milky Way's interstellar material. We take account of the foreground reddening due to dust in the Milky Way by applying the attenuation law of Fitzpatrick (1999) and using the E(B-V) values, see Chapter 2, from the Schlegal maps (Schlegel, Finkbeiner & Davis, 1998) using the input right ascension and declination of each object.

As shown in the flow chart of Figure 3.2 we use two methods to fit for dust attenuation of observed objects. Both methods involve pre-processing the data and base models with a 'high-pass filter'. As discussed in Chapter 5, where we analyse prototype MaNGA data, uncertainties in the flux calibration of data can cause long-scale offsets in their SEDs that are degenerate with a dust attenuation curve. The flux calibration issues discussed in Chapter 5 required us to develop a more sophisticated approach to dealing with the large-scale wavelength feature of a dust attenuation curve, the measurement of which would otherwise become degenerate with the similarly large-scale feature of an unknown flux calibration curve. We will now discuss how visual inspection of the SDSS images corresponding to the prototype MaNGA (P-MaNGA) objects allowed us to provide a sanity check on the results.

For this section we will use 2D maps of galaxy properties as we will use extensively in Chapter 5. Each grid point in these maps correspond to properties derived from analysed SEDs corresponding to that position. Data are binned to cover an area such that we reach the required signal-to-noise, see Chapter 5 for details as to how this is done. Consider the galaxy in figure 3.4a, where a dust lane clearly covers the top of the P-MaNGA footprint.

One could attempt to fold in dust extinction into the fitting code by treating it as an additional free parameter to the models. However in practice the dust-age-metallicity degeneracy together with flux calibration issues become so strong as to conspire to produce unphysical solutions, such as a galaxy age that varies many times by an order or magnitude between pixels. This is shown in figure 3.4b, where the E(B-V) values correspond to the value of the single parameter Calzetti law (Calzetti et al., 2000) to derive attenuation curves[2]. The E(B-V) values have a high degree of scatter, are high in general, and the band of higher values that could be identified as a dust lane is clumpy and difficult to interpret.

The problem with this approach is that the large-scale shape of a spectrum is the product of both the stellar population components, the flux calibration factor, and also dust attenuation. On the other hand, the flux values of a spectrum at small-scales is a result of only the stellar population components and are not sensitive to dust or flux calibration. Typically fits to galaxy SEDs are driven by the continuum, due to it having better signal-to-noise and less noise correlation compared to individual features. Therefore these fits are very susceptible to dust, which can become particularly problematic. If there are (even small) offsets in the continuum shape (i.e. if the continuum is flux-calibrated incorrectly or badly modelled), it can be difficult to separate out the degeneracy between dust and other stellar population properties, since both

[2]In this paper we shall use this form of the Calzetti law, with $R_V = 4.05$, as default in all of our derivations.

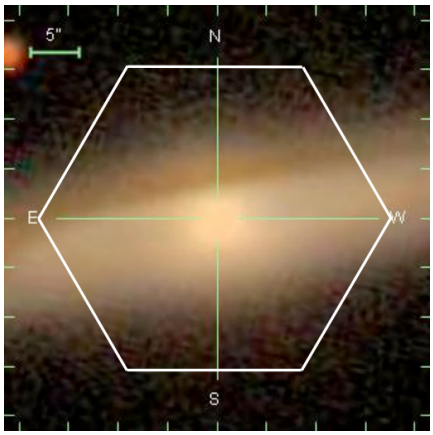

(a) SDSS imaging data with the P-MaNGA footprint in white.

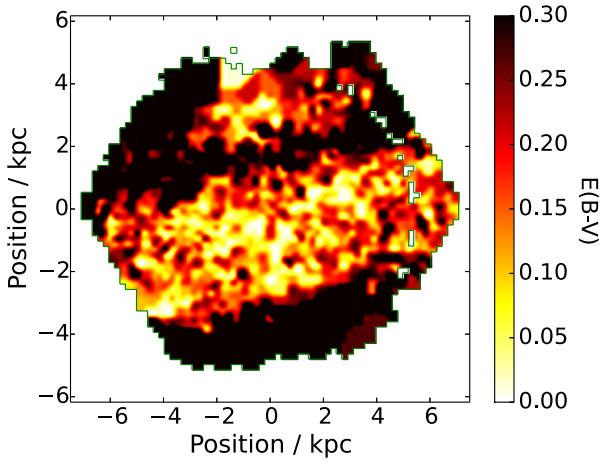

(b) Dust values obtained when folding dust in as an additional parameter to the fitting code.

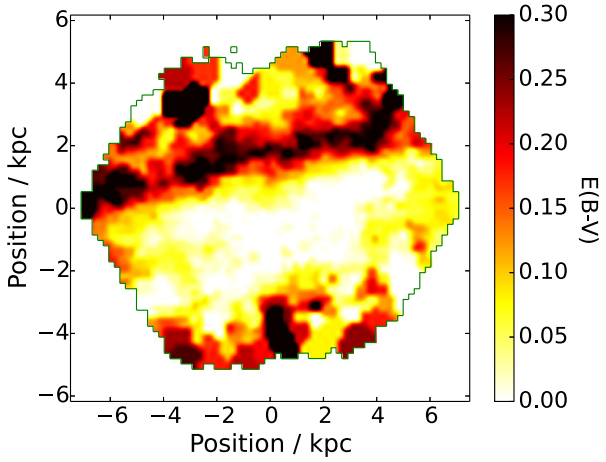

(c) Dust values obtained when using a filter to measure the dust attenuation curves before fitting the stellar population properties.

Fig. 3.4 The effect of different methods for dealing with dust attenuation in fitting codes with an example P-MaNGA galaxy, analyzed using MILES-based M11 models with its full parameter range.

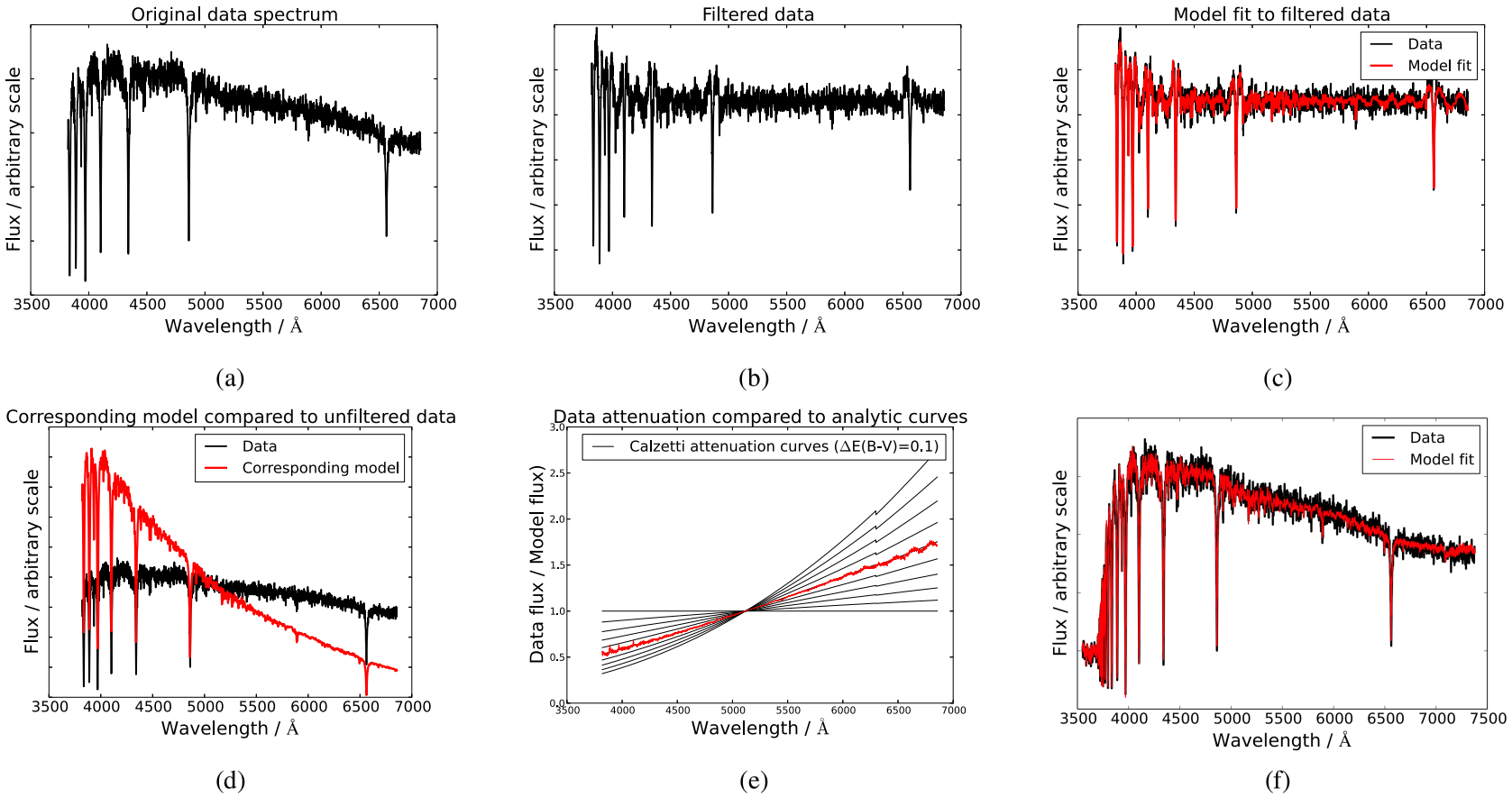

Fig. 3.5 Example of fitting a spectrum for dust using a high-pass filter. Starting top-left and moving horizontally, the panels describe each stage of the filter and fitting process. Panel a) shows the input model spectrum corresponding to a 30 Myr, [Z/H] = 0 SSP with a signal-to-noise applied at each flux point of 50. Panel b) shows that data processed through a high-pass filter that removes large-scale features such as continuum shape and dust extinction. Panel c) shows the fit to the filtered spectrum using models that are filtered in the same way. All models used to make this fit have E(B-V) = 0 since we would be removing the effect of dust attenuation on the models anyway. Using the same parameters determined through the fit in c), panel d) shows the corresponding parameters in the unfiltered model case. We expect to see a systematic tilt between the data and models, corresponding to a dust attenuation curve. In panel e) we find the best value for E(B-V) by calculating the [data / model] spectrum and fitting this to a range of attenuation curves across the whole spectrum. In practice we used ΔE(B-V) of 0.01, but intervals of 0.10 are shown here for clarity. The best fitting E(B-V) for this case is 0.50, exactly matching our input value of 0.50. Lastly we use the value of E(B-V) obtained to re-fit the original data using unfiltered attenuated models. Panel f) shows the final fit obtained across the whole wavelength range.

affect the overall continuum shape.

Our solution is to use an analytical function across all wavelengths to rectify the continuum before deriving the stellar population parameters. We use a functional form called a high-pass filter (HPF). A HPF removes the large-scale features of a spectrum, such as continuum shape and dust extinction, through the use of a window function applied to the Fourier transform of the spectra as follows:

$$\mathrm{Flux}_{\lambda}^{\mathrm{output}} = \mathrm{Flux}_{\lambda}^{\mathrm{input}} \otimes \mathrm{W}_{\lambda}, \tag{3.4}$$

where this is the convolution in real space, and the window function $\mathrm{W}_{\lambda} = \mathscr{F}^{-1}\mathrm{W}_{k}$ describes which modes are removed by the Fourier filter, where k are the modes of the spectra. Roughly these modes can be thought of as corresponding to features of the spectrum with wavelength size given by $\sim$ number of wavelength points in the spectrum divided by k. Since we remove the long modes of the spectrum, we want a window function that only allows small modes. By testing the results with mock galaxies made from simple stellar populations we find that the following step function gives good results, with the derived properties being stable to small changes in the function:

$$\mathrm{W}_{k} = \begin{cases} 0 & k \leq k_{crit} \\ 1 & \text{otherwise,} \end{cases} \tag{3.5}$$

where we set $k_{crit} = 40$ in this paper. To avoid edge effects in the spectra, which can be difficult to represent with long-scale modes, we find excluding the top and bottom 1 percent of the wavelength range by default enables stable results for all k assessed.

For example, a spectrum with regular wavelength intervals of 1 Å between 3000 Å and 9000 Å will be completely represented by 6000 modes. A filter that excludes the first 40 modes of a spectrum will therefore ignore all features in the spectrum that are larger than 6000 / 40 = 150 Å. The choice of modes excluded by the window function is chosen to remove potentially badly modelled or badly calibrated modes.

The step-by-step process of obtaining a dust attenuation curve is described in figure 3.5.

1. In figure 3.5a we show an example spectrum. This corresponds to a 30 Myr SSP from the MILES-based M11 models with a known E(B-V) of 0.5, applied using the Calzetti

law. We apply a Gaussian displacement on each point corresponding to signal to noise of 50 for clarity, although this process works as well down to S/N of 5, which is the lowest value for the P-MaNGA data outputs that we will be using in this paper. This spectrum is chosen to represent what the stellar populations of a portion of the dust lane in the galaxy in figure 3.4a might contain, using a known set of properties such that we can test their recovery. We apply random errors at each flux point assuming a signal-to-noise of 50.

2. We apply equation 3.4 to the data, giving the output shown in figure 3.5b. This equation is also applied to all of the models, which are not attenuated by dust.

3. These filtered models are then fit to the filtered data in Figure 3.5c.

4. We then use the parameters measured from this fit in the unfiltered models and data (shown in figure 3.5d), dividing the best model fit by the data to give a residual attenuation curve. This is then smoothed over a wavelength range of at least 100 Ådepending on the features one wishes to try to capture.

5. As shown in figure 3.5e, we then use the dust attenuation models of Calzetti et al. (2000) to find the best matching E(B-V) value that fits the recovered curve. The best fit model in this case returns E(B-V) = 0.5, exactly as input. Down to a signal-to-noise of 5, we can recover dust in mock galaxies to within 0.05 in E(B-V).

6. The best fitting curve is then applied to the models, which are then fit to the full unfiltered data spectrum to give the final fit in figure 3.5f.[3]

The reason for re-applying the fitting procedure to determine stellar population properties rather than using the results obtained from fitting the filtered data is that we are adding in the additional prior that we assume a smooth attenuation curve, as deduced in the fourth step of the process above. In figure 3.6 we show a representative example that demonstrates that without this requirement, we typically fit a wider range of stellar population properties since we have lost the constraint that the attenuation curve varies smoothly. This then translates to lower errors (by about a factor between 1 and 2 in most cases) in the re-fit stellar population distribution, but a set of values that are within the range of values derived from the stellar population distributions deduced from the initial fit.

[3]Errors on the dust extinction measured are evaluated separately to other stellar population properties since we fit this separately, and so consequently errors on age, metallicity and stellar mass do not include errors arising from their degeneracies with dust.

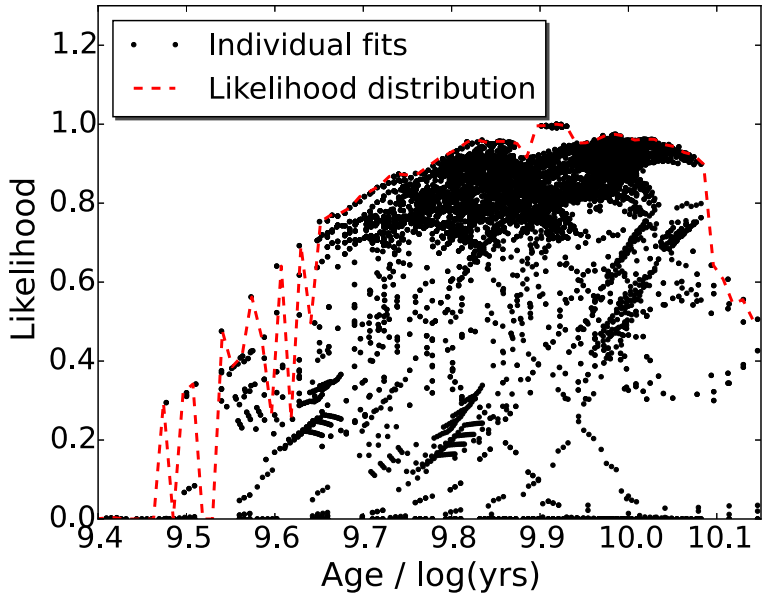

(a) High-pass filter fitting only.

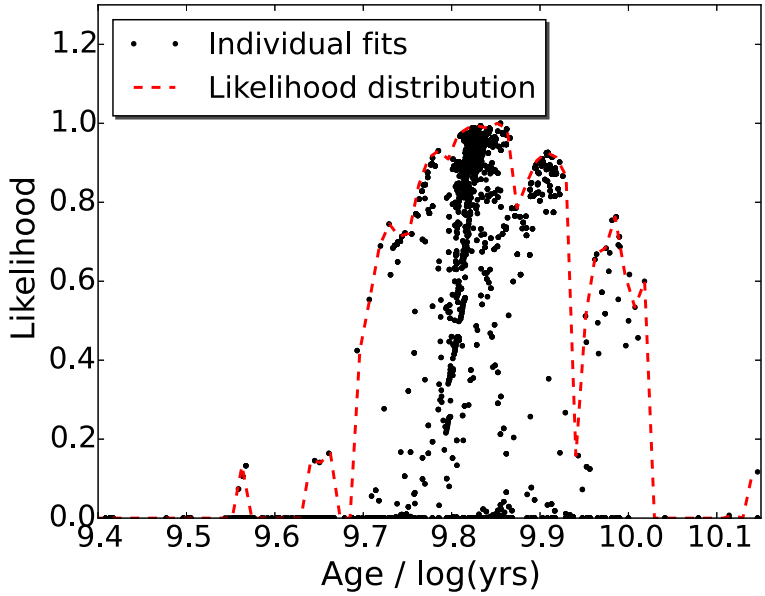

(b) Re-fitting with a derived attenuation curve.

Fig. 3.6 Complete set of solutions (black points) from FIREFLY, showing the likelihood of fits as a function of age obtained using high-pass filtered data (upper panel) compared to solutions obtained by re-fitting with a derived smooth attenuation curve (lower panel). Overplotted in red is the derived probability distribution that takes into account multiple similar solutions used to obtained best-fit properties and errors.

This number of large-scale modes excluded in the fit, selected by k_{crit}, has been tested empirically on a range of mock galaxy spectra based on SSPs. Figure 3.7 shows the dust recovery, in terms of extinction in B-V, as a function of input age, metallicity and extinction. Each of these properties are marginalised over the other two, meaning that, for example, the bottom plot shows the recovery of dust as a function of k_{crit} and dust input summed over all possible values of SSP age and metallicity input.

The plots show some dependance on dust recovered with age, visible as red or blue structure in the top plot, coming from age-dust degeneracy. However the E(B-V) values are recovered generally within a 0.03 margin within a large range of k_{crit} around the value of 40 used in Chapter 5. The metallicity plot shows that dust is recovered very well except when excluding modes $k_{crit} > 60$, where some small dependencies (< 0.02 in E(B-V)) start to become apparent. The input dust plot, bottom, similarly shows that dust recovery is excellent. We some edge effects where we are not able to fit below or above the dust parameter range we allow, but otherwise dust is recovered to within 0.01 in E(B-V).

From these plots we also conclude that our method gives stable solutions with small changes in the window function around the $k_{crit} = 40$ value used in this paper. At around $k_{crit} < 15$ we see that we almost always underestimate the amount of dust, except for low values of input dust where we cannot construct an attenuation curve to remove. Conversely, at $k_{crit} > 90$ we see increasing instability in the age plot (top) as we are removing more information from our data in terms of wavelength modes used. It is of note that FIREFLY does allow this wavelength scale to be changed by the user, uniquely among spectral fitting codes, should they have knowledge about the wavelength scale of the dust attenuation or flux calibration.

To properly compare with the P-MaNGA analysis, Chapter 5, we have downgraded the wavelength sampling of the P-MaNGA spectra to match that of the wavelength sampling of the model spectra mock spectra, using linear interpolation. In these tests we have used MILES-based models, which have been interpolated to give a constant resolution of $R = \lambda/\Delta\lambda = 4343$. The P-MaNGA spectra, with sampling of $R = 10000$ are therefore downgraded to the model sampling. Changing the wavelength sampling by a constant factor will change the k_{crit} values by that same factor accordingly. Hence the value of the number of modes excluded is an effective k_{crit}, written as k_{crit}^{eff}, that applies to the P-MaNGA wavelength sampling.

Mock spectra were made by taking input model SSPs and perturbing each of their flux points by an amount drawn randomly from a Gaussian probability distribution on each point given an input signal-to-noise. See the tests on mock galaxies carried out later in this chapter for

details as to how these are produced. For these tests we use a signal-to-noise of 10, since these represent the typical values for P-MaNGA data in the outer regions of most of the sample galaxies. We note that lowering signal-to-noise to 5 increases the errors by approximately factor 2, whereas increasing the signal-to-noise to 20 reduces the errors by approximately a factor 2, but show very similar patterns to the plots shown in Figure 3.7 otherwise.

It is important to note that the particular window function used remains self-consistent as it is applied in exactly the same way to both the data and model SEDs[4].

Using this method we derive the dust map shown in figure 3.4c. This is a clear improvement, as dust values are lower and more consistent in regions where high dust is not expected, and a clear band of higher dust values that matches the position of the observed dust lane in figure 3.4a that is more clearly defined than in figure 3.4b.

This example case shows that the functions described in equations 3.4 and 3.5 can recover dust values well despite potential flux calibration problems in at least this galaxy. We also find sensible spatially confined dust determinations for other P-MaNGA galaxies, and hence use this approach as standard in this thesis.

In Chapter 5 we used a fixed value of k_{crit} since the data always had the same wavelength range and sampling, but for a general application we set k_{crit} to the number of flux points / 100, which masks any modes greater than 100 Å in size for linearly binned spectra. This approximately corresponds to that used in Chapter 5, and the tests done on the consistency of solutions when varying k_{crit} are the same. For fitting to 500 or less flux points, k_{crit} should be set to a correspondingly smaller value, such that the scale masked covers at most a fifth of the spectrum. For fitting very small spectral regions, less than 50 points, the first method of looping over dust values mentioned at the beginning of the section is the only available option since we would no longer be able represent a spectra in terms of its long-scale modes with such a small wavelength range.

[4]We apply the filter directly to the model SSPs, and fit combinations of these to the filtered models. This takes considerably less CPU time than applying the filter to each of the model combinations, and makes only an extremely small difference to the fluxes at each point (< 0.5 percent on any given flux point, most considerably less than this). This is because the filtering process tends towards a distributive operation at the large number of flux points on any given spectrum that we analyse.

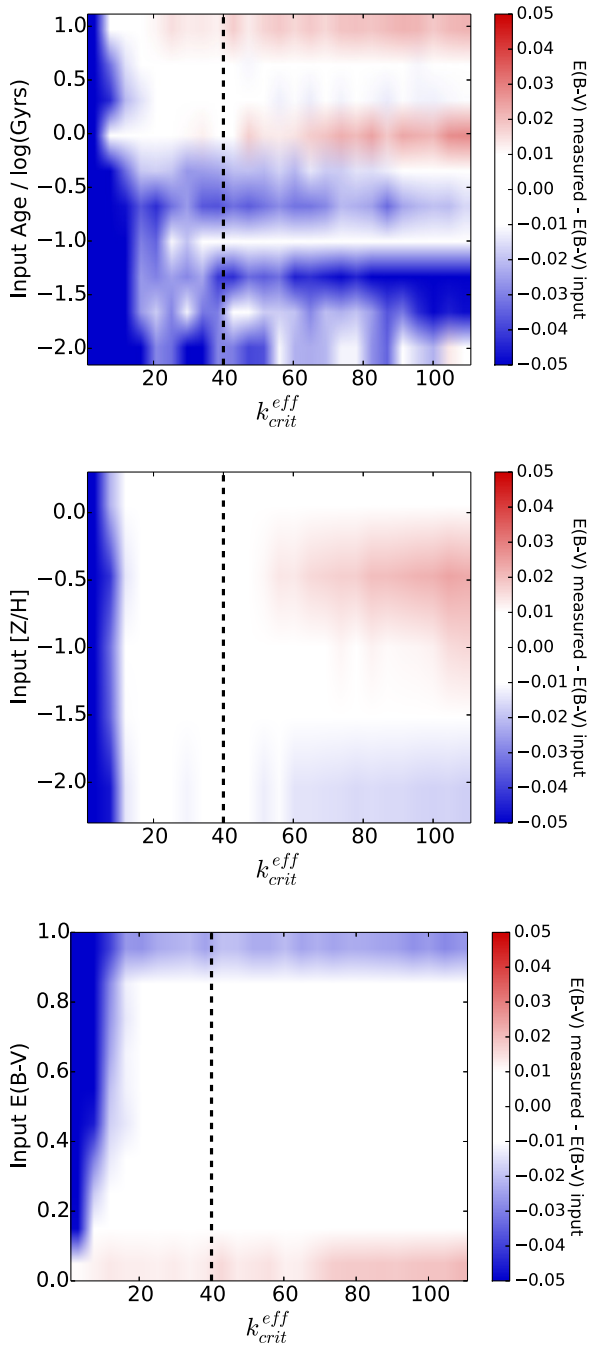

Fig. 3.7 Tests showing the recovery of dust values (in terms of difference between E(B-V) recovered to input E(B-V)) from mock galaxy spectra from MILES-based models as a function of the number of large-scale modes excluded in the fit. The number of modes excluded is described by an effective k_{crit} parameter (in equation 3.5). The three plots show recovery of dust as a function of the following input properties: age, metallicity and extinction respectively. In each case, the values plotted are marginalised over the other two input properties. The black dashed line marks the value of k_{crit} used in Chapter 5 for the analysis of P-MaNGA galaxies. Each mock galaxy spectra is constructed by perturbing each flux point of an input model SSP by a Gaussian probability distribution on each point, assuming a flat signal to noise of 10 across the whole wavelength range. A signal-to-noise of ten was chosen as it is typical of the outer regions of most P-MaNGA galaxies.

3.4.1 Producing Attenuation Curves from the Data

Once one has fit the filtered model SEDs to the filtered data SED, the fitting block returns a measured attenuation array, which is smoothed over the wavelength scales one is trying to assess, i.e. 100 Å in our application. Then, in our default approach we measure the closest fit to a set of model attenuation curves to obtain an estimate of the extinction that is output by the code as a singe number (E(B-V)), but apply the full derived attenuation array to all model SEDs and the data is refit assuming this attenuation.

In Figure 3.8 we show 3 examples of fitting SEDs using this method, returning the attenuation arrays shown. We also plot the model Calzetti et al. (2000) (see next subsection) attenuation curves for comparison from -0.1 to 1.0 in E(B-V), where the zero value of extinction corresponds to a constant value of 1.0. In the top panel, we have constructed a mock galaxy with a Calzetti attenuation law (see next subsection) applied to it with E(B-V) = 0.5, from a 10 Gyr, solar metallicity SSP with S/N of 50, which we use as an illustrative example. As can be seen, the recovery of the input Calzetti curve is excellent. In the middle panel we show an example SDSS DR7 galaxy (see Chapter 4) with moderate amounts of dust and a median S/N of ~ 5, the noise of which is clearly seen in the raw attenuation array in red. Once smoothed however, in blue, we can see that the Calzetti law represents this curve reasonably well, suggesting that it models the data well. In this case, the method described here and in the next section are equivalent. Lastly, in the bottom panel of Figure 3.8 is a P-MaNGA galaxy (see Chapter 5) with known flux calibration problems below about 4300 Å. In this case, despite having a better S/N of about 10 compared to the DR7 galaxy, the derived attenuation law is not well-represented by the Calzetti law, especially below about 4500 Å. This means that using the method described in this section will take account of this offset and effectively apply a 'correction' to the models in the refitting process, mitigating the effect of poor flux calibration.

3.4.2 Alternative Method: Fitting Attenuation Using Model Curves

The other method to take account of the effects of dust extinction is to use a model attenuation curve, which are generally well-characterised by the B (445 nm)- V (551 nm) band difference. In this method we have used the Calzetti attenuation law as in Calzetti et al. (2000), using a range of values between E(B-V) = 0.0 and 1.0 for the interstellar material of the galaxy being observed. This law has been shown to be generally applicable to good accuracy to many different types of galaxies such as those from the SDSS surveys used in this work (though

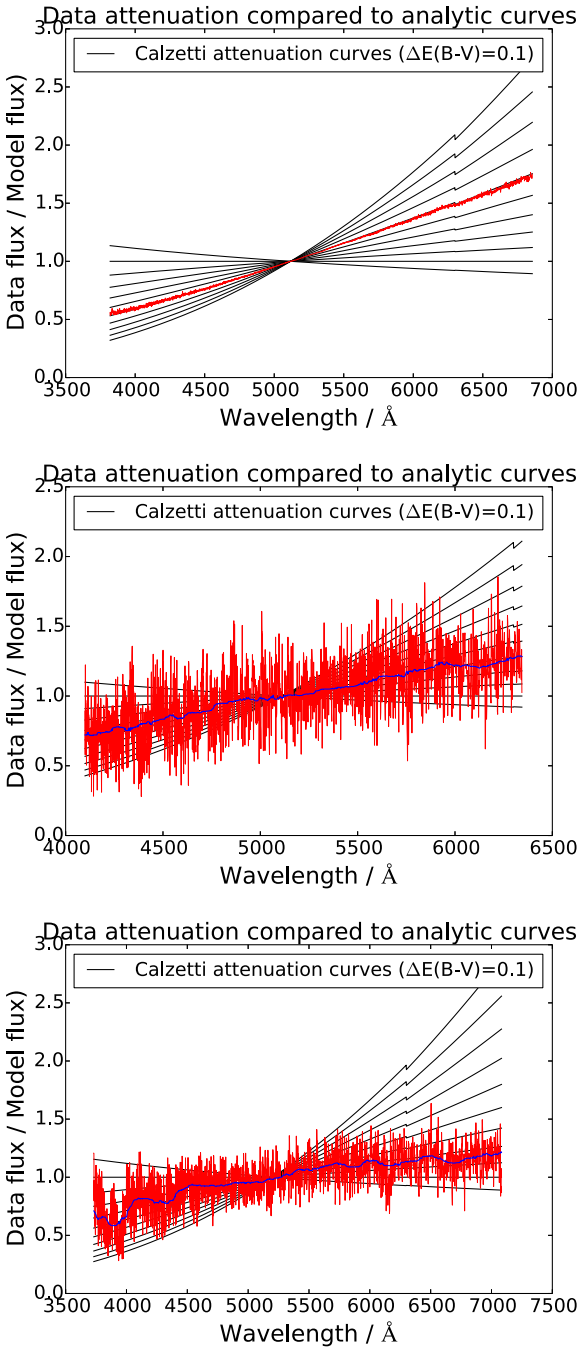

Fig. 3.8 Measured attenuation arrays from FIREFLY's fitting method of filtered data, as described in Section 3.4. In red is the raw attenuation array deduced, in blue is the smoothed attenuation array which are applied to the models for refitting, see Section 3.4.1, and in black are model Calzetti et al. (2000) law curves from E(B-V) = - 0.1 to 1.0. The top panel shows the method applied to a mock galaxy with S/N of 50 and an extinction of 0.5 in (B-V), the middle panel shows the method applied to an example SDSS DR7 galaxy (see Chapter 4) with S/N $\sim$ 5, and the bottom panel shows the method applied to a P-MaNGA galaxy (see Chapter 5) with S/N $\sim$ 10 and with known flux calibration problems.

Chevallard et al. (2013) finds a slightly steeper law than the Calzetti law, but as FIREFLY can accept any Calzetti law as input this can be investigated in the future). This method assumes that this attenuation law affects SSP combinations equally, though one could build a similar method without this assumption that would be much more computationally expensive. This method may be used over the default method of returning an unconstrained attenuation curve when one wishes to assume an attenuation law such as the Calzetti law, and in both cases the attenuated SEDs are then refit to the data. Should any user of our code in the future wish to use a different attenuation law for reddening, or use different parameters, the attenuation law can be easily changed in our code via swapping out the attenuation module.

Both dust methods give equivalent results to 0.02 dex in average age, metallicity and stellar mass when applied to mock galaxies and the signal-to-noise is above 5. However, since the former method can be applied more generally, see Figure 3.8, when the attenuation law is unknown or the flux calibration is uncertain, we use that method as default in this thesis.

3.5 Emission lines

Galaxies with emissionlines, due to ongoing star formation and ionisation of hot gas, need to be treated carefully since stellar population models in general do not include emission lines. Therefore to compare late-type galaxies to the models we must either mask out regions of emission lines, or find the strength of these emission features and remove them first. Although our fitting code can work under both circumstances, the latter method is preferable because including as much of the SED is thought to allow increased precision in the fits, except for cases of poor wavelength calibration (Koleva et al., 2008). This hypothesis is tested in section 3.9.

For emission-line removal we used an emission- and absorption-line fitting code called Gas AND Absorption Line Fitting (GANDALF; Sarzi et al. (2006), a locally adapted version used in Thomas et al. (2013)) to extract stellar kinematics and emission line statistics and output emission-free absorption spectra (also known as 'cleaned' spectra), which we were then able to use models to fit to. Thomas et al. (2013) used as input the same M11 models used in this thesis, enabling a self-consistent approach. GANDALF, when fitting to emission lines, also has the added benefit of releasing accurate measurements of the Doppler broadening of the SEDs due to the velocity dispersion of the stars in the object. This broadening effect essentially 'downgrades' the resolution to which we can identify absorption features in that SED, often below that of the instrumental resolution of the observation, and very often below

that of the model spectra that we have used. Therefore one needs to downgrade the model SSP resolution to match this effective resolution. In all of our analyses this is done based on the measurement of this broadening from GANDALF.

3.6 Velocity Dispersion

After removing for the effects of emission, the intrinsic velocity dispersion of a galaxy still has the effect of broadening its absorption features. In Figure 3.9 we construct a 'mock' galaxy consisting of a 10 Gyr, solar metallicity SSP from MILES-based M11 models with three different velocity dispersions. In the middle panel, a 170 km/s dispersion is applied to the model SSP, a value which is typical of the SDSS DR7 galaxies that we will be analysing in Chapter 4. In the top panel is the same mock galaxy with much less broadening, at 70 km/s, such as one may observe in dwarf elliptical galaxies. Lastly in the bottom panel is the same mock galaxy broadened to a dispersion of 270 km/s, as one may observe in large elliptical galaxies. There are some visual differences in these spectra, most noticeable in the 70 km/s panel compared to the two others, but the larger velocity dispersion differences are more difficult to tell. This could suggest that the effect of velocity dispersion is a small effect. In Panter et al. (2007), they argue that with 3 Å models and data, there is only negligible effects of velocity dispersions on their model fitting. However, our models use somewhat higher wavelength resolution and we may in the future apply our code to higher wavelength resolution data, so this should be carefully tested.

To test this, we fit to the mock galaxy in the middle panel, with the stellar population of 10 Gyr, solar metallicity, and 170 km/s dispersion. However, we run FIREFLY using 21 sets of models that assume velocity dispersions of 70 km/s to 270 km/s, in 10 km/s intervals. Figure 3.10 shows the corresponding age and metallicity recovered when using each of these sets of models. The effect in age is somewhat small in a $\pm$ 50 km/s range around the correct value, since here we recover the correct value, but beyond this varies by about 0.1 dex for every 20 km/s offset, going some way to support the argument of Panter et al. (2007). However, the effect on metallicity is much more pronounced, with no clear stable region of correct metallicity recovery and instead a $\sim$ 0.1 dex displacement for every 30 km/s offset from the true input value. From this, we conclude that measuring and taking account of velocity dispersion, as our method does by processing with GANDALF (Section 3.5), is required to within 10 km/s velocity dispersion accuracy in order to avoid a $\sim$0.03 dex systematic error in metallicity, although this requirement is less strict for accurate age determination. This result makes intu-

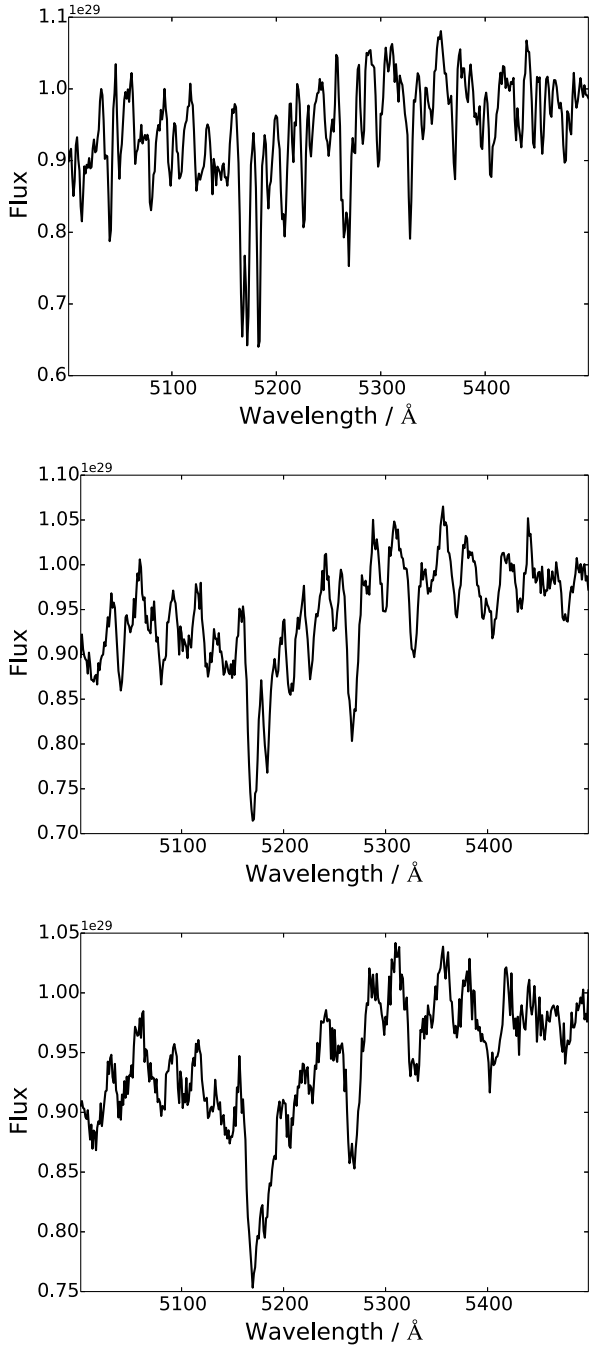

Fig. 3.9 SEDs of mock galaxies constructed from 10 Gyr, solar metallicity SSPs with velocity dispersions of 70 km/s, 170 km/s, and 270 km/s respectively. Note the change in scale results in the higher velocity dispersion spectra appearing slightly noisier.

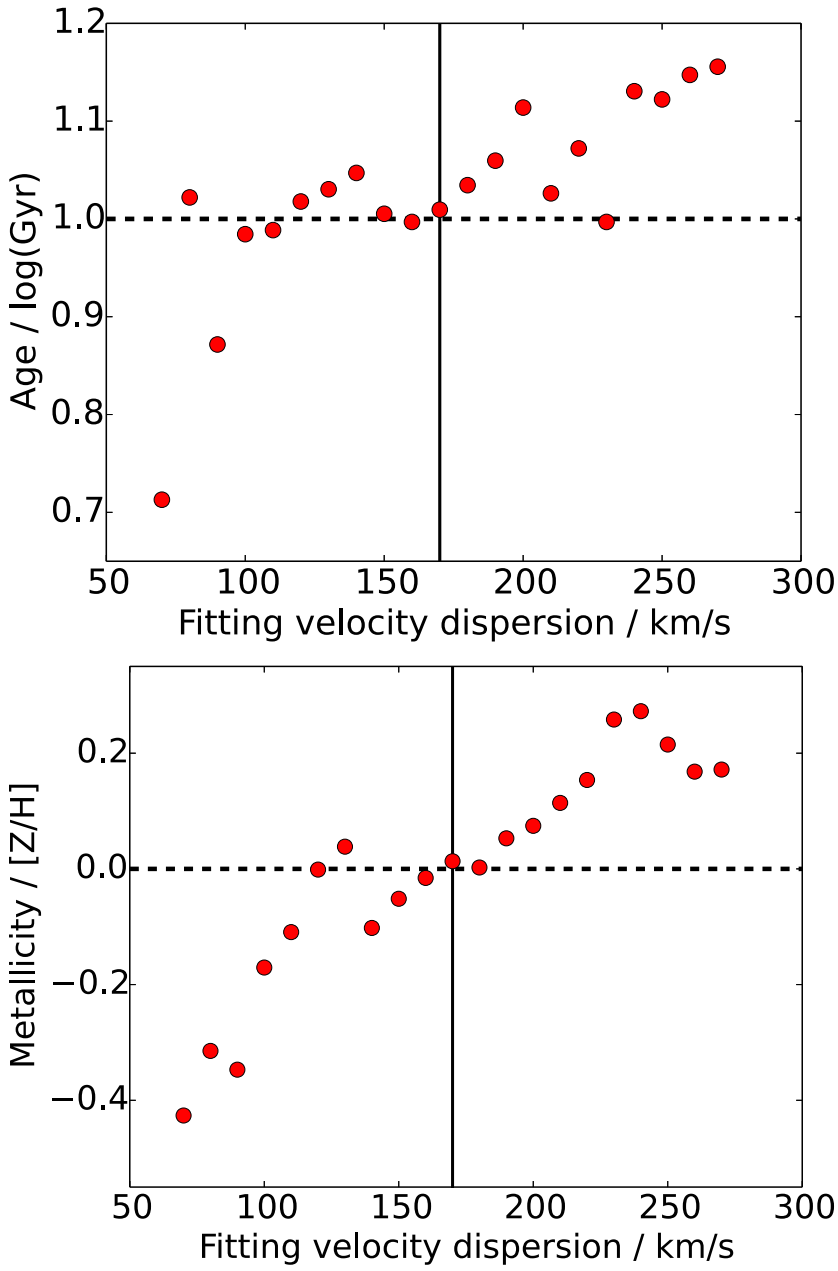

Fig. 3.10 Recovery of the ages and metallicities of a 10 Gyr, solar metallicity SSP mock galaxy with 170 km/s velocity dispersion, using a range of input model velocity dispersions.

itive sense, as one of the main effects of velocity dispersion is broadening metallic absorption lines.

3.7 Comparing the solutions

To test the goodness of each of the model fits to the data at each stage of our fitting procedure we use a chi-squared test, given by

$$\chi^2(model_i, data) = \sum_{\lambda} \frac{(\phi_{data}(\lambda) - \phi_{model_i}(\lambda))^2}{\sigma(\lambda)^2}, \tag{3.6}$$

where the ϕ represent the flux of the data and model, and σ represents the one-dimensional error, at the wavelength point λ. This method relies on the assumption that each of the errors on the fluxes are independent. This is not true for most spectroscopic surveys, such as SDSS, since neighbouring pixels will have some overlapping sensitivity and so their errors are somewhat correlated (known as 'spectral covariance'). However, since our method does not fit very narrow features (on the order of less than a few pixels) such as emission lines, and instead uses relatively wide absorption features and the continuum, the effect of the correlated errors is small.[5]

We note that FIREFLY can indeed optionally take a covariance matrix instead of a simple one-dimensional error spectrum as input in order to compute the χ^2, should spectral covariances be able to be accurately modelled and provided in future surveys. This modifies the χ^2 formula from equation 3.6 to

$$\chi^2(model_i|data) = \sum_{\lambda} \frac{(\phi_{data}(\lambda) - \phi_{model_i}(\lambda))\dot{\Sigma}^{-1}\dot{(}\phi_{data}(\lambda) - \phi_{model_i}(\lambda))}{,} \tag{3.7}$$

where Σ is the input correlation matrix. This method increases CPU time fairly significantly since the matrix calculation is more computationally expensive than a vector calculation, but

[5] In real data, the errors of nearby flux points and their errors are somewhat correlated, however this effect is small, on the order of the full-width at half-maximum of the instrument plus detector (see Bolton & Schlegel (2010), who also show how modern calibration methods could reduce this effect further). This means that the χ^2 values computed from model fitting are approximately statistically correct. In any case, in FIREFLY we will only output the *relative* probabilities, which will be affected much less than the absolute χ^2 values. Therefore, it is safe to neglect this effect when using a full spectrum.

allows for much more accurate computation once a future survey data product includes these correlation matrices.

In addition to the spectral covariance mentioned here, we also note that for integral field unit surveys (see Chapter 5), there will be spatial covariance between pixels covering different regions of the galaxy. This would then propagate to an error on the individual SEDs, which due to the prototype nature of the observations of the P-MaNGA survey analysed in chapter 5 were not taken account of. However, in the full MaNGA survey, these effects will be propagated to give a measure of spatial covariance.

Using our method we obtain a range of fits with chi-squared values that are usually close to each other (typically within a few percent of the minimum chi-squared value), which are represented by the bottom set of fits in the schematic of Figure 3.3. For our set of models we typically have of order 1000 of these fits, all expressed as a linear combination of SSPs, as in equation 3.3.

To compare the properties obtained from these fits in a meaningful way for individual galaxies we must compute each of the respective fits' relative probabilities. To do this we use the probability density function of the chi-squared probability distribution, given by

$$\rho(X=\chi^2) = \frac{1}{2^{(k/2)}\Gamma(\frac{k}{2})} X^{(k/2)-1} e^{-X/2}, \tag{3.8}$$

where Γ is the Gamma function, χ^2 is the value of chi-squared we are using to find the probability density. k is the degrees of freedom, which can be expressed as $k = N - \nu - 1$, where N is the number of (independent) observations and ν is the number of fitting parameters. For our method, N is the number of data flux points that we are fitting model fluxes to (of order 1000 for typical resolution and wavelength coverage of SDSS observations), and ν is the number of SSPs used in linear combination to obtain our fit (which will vary by model library and any priors on which SSPs to include, typically around 5) plus the number of additional parameters used (such as the E(B-V) parameter for our model of reddening, which remains constant for each SSP fit).

For typical full spectral fits, the degrees of freedom is very large ($k > 1000$), which means that the probability density function is approximated very well by the Normal distribution (Wilson & Hilferty, 1931), where $\rho(X=\chi^2_o) = \frac{1}{\sigma\sqrt{2\pi}} e^{-X/2}$, where σ is the standard deviation of the underlying probability distribution. This is a fixed value for all model fits to a given data SED.

Thus we can compute the relative likelihoods to the best fit solution, i.e. the likelihood ratio; how many times more likely the data are under one model than the best fit, as

$$P(\chi_i^2) = \frac{\rho(\chi_i^2)}{\rho(\chi_0^2)} = \frac{e^{-\chi_i^2/2}}{e^{-\chi_0^2/2}}, \tag{3.9}$$

where χ_0^2 is the minimum χ^2 value found. This provides a simple method of calculation of the relative likelihoods of all solutions obtained from the parameter exploration described in the previous sections. Thus FIREFLY produces a probability distribution of full star formation histories which are output to the user should they wish, which is not available through any other (published) fitting code.

3.7.1 Visualising the Fits

Summarising from the previous section, we can simply express the flux of the final solution of the spectral fit of the galaxy as the sum of all the fluxes of the solutions weighted by their relative likelihoods as

$$F(\lambda) = \sum_i^{\text{fits}} \frac{P(\chi^2(i))F_i(\lambda)}{\sum_i P(\chi^2(i))}, \tag{3.10}$$

where $F_i(\lambda)$ is the fluxes of an individual solution as described in Equation 3.3. This can then be plotted as a complete spectral fit. By obtaining the properties of all of the component SSP contributions from these fits (for example, age and metallicity), and again weighting the contributions by their relative likelihoods we can display a contour plot of the sum of the solutions.

Using figures 3.11 as an example, one can see the data in black over-plotted with the total weighted fits to a P-MaNGA galaxy SED (see Chapter 5) in red, which includes all possible solutions using the method described. In this case, there are $\sim$ 2000 solutions contributing to this total fit. In the bottom panel of figure 3.11 one sees a contour plot that shows an interpolated grid of all of these solutions, with the specific age and metallicity contributions shown in histograms below and to the right of the contour grid. Each contour contains the relative light-weight of SSP contributions as shown by the colour-bar. In this plot, we can see a dominant region of very old ages ($\sim$ 13 Gyrs) at approximately solar metallicity, spreading

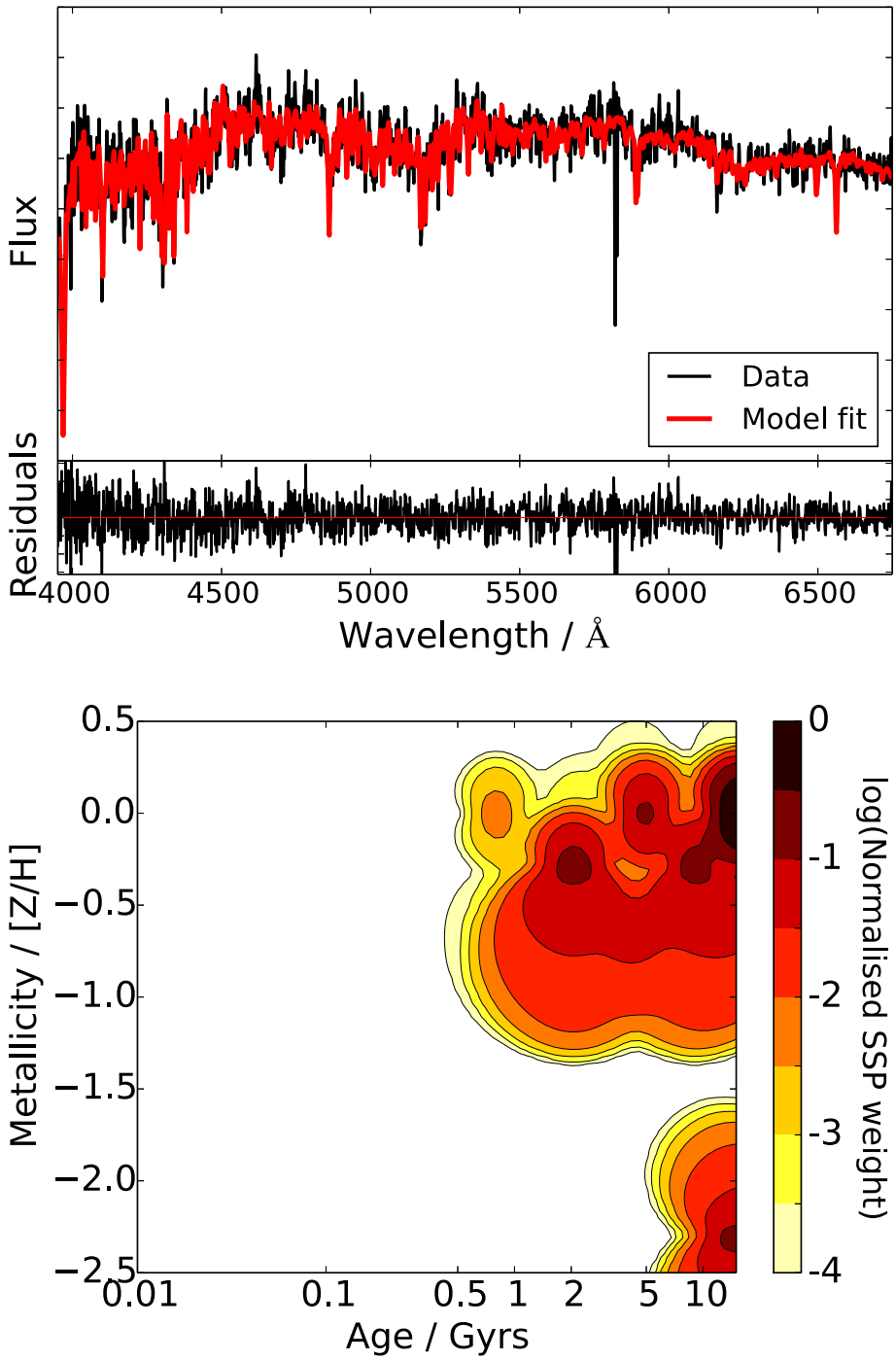

Fig. 3.11 Example fit (red) of a P-MaNGA galaxy SED (black), see Chapter 5, in the top panel corresponding to the light-weighted age-metallicity map on the bottom panel. The map is made from the likelihood-weighted sum of all fits found by FIREFLY, which darker regions corresponding to areas in parameter space with higher SSP weight, thus a reasonable model fit may combine SSPs from any region plotted, so long as their weights correspond to the weights shown by the colour scale. The map shows signs of age-metallicity degeneracy as shown by the spread of the SSP weight contours values that extend the solution contour, particularly visible as the islands of lower age, higher metallicity solutions away from the main area of SSP weight at half-solar metallicity. Models used are MILES-based M11 models with a Kroupa IMF.

to younger ages ($\sim$ 2 Gyrs) at half-solar metallicities. There is also considerable spread due to the age-metallicity degeneracy towards younger, higher metallicity solutions, and a small contribution from a ultra-low-metallicity, old ($\sim$ 13 Gyrs) population. Additionally some of the spread could come from degeneracies or inadequacies of the models, for example the lack of non-solar abundance ratios. To test which degeneracies are inherent to the modelling and which could come from the complications involved in the data we map out these degeneracies for each SSP and a range of CSPs in section 3.9.

3.8 Obtaining galaxy properties

We can simplify the complex visualisations described in section 3.7.1 by providing average physical properties of each object. For each SED analysed we recover the likelihood distributions of light- and mass-weighted age and metallicity, and stellar mass. Therefore the best fit for each property is the peak of their distributions, with confidence intervals determined by measuring the range of property values within a given likelihood value. For example, 68% confidence intervals in age are extracted by finding the minimum and maximum values of age that have at least 68% likelihood, relative to the best solution. Consider for example, the lower plot of Figure 3.6, in which we show likelihood as a function of age. The 68% confidence interval in this case would enclose all ages with that likelihood or higher, which in this case is about 9.7 to 10.0 in log(years). We provide the best fit, 68%, 95%, and 99.7% confidence intervals for all stellar population properties as default in FIREFLY's output.

We note that the error estimated is based on a single SED rather than a Monte Carlo error estimation based on many realisations of the SED, which is much more computationally expensive. Our method thus provides a fast way of measuring of the spectral degeneracies between the stellar population properties based on the input data SED errors, in addition to the best fit set of properties based on this single SED. The exception to this method of evaluating model degeneracies is the dust calculation, hence the E(B-V) value as computed in Section 3.4 are not folded into these error estimates.

3.8.1 Light- and mass-weighted properties

In the process of finding the contributions of SSPs to an overall galaxy spectral fit, we normalise both the data flux and all possible SSP fluxes before fitting, and therefore we obtain a contribution of SSP fluxes to the data. This is so that only the spectral shape and features

are fit for the SSPs used rather than the contribution to the flux - this is not specific to our fitting method; see the methods of STARLIGHT; Cid Fernandes et al. (2005) and STECMAP; Ocvirk et al. (2006b). Since these are normalised to 1 across the wavelength range chosen, such contributions are known as "luminosity-weighted contributions", which we shall identify as w_i^L, where i is the i'th SSP contribution (a typical galaxy fit will have multiple contributions). Light-weighted contributions may be converted to mass-weighted contributions *after* fitting by knowing the relative fluxes of the models (in units of flux per stellar mass) compared to the data.

Throughout this thesis we show both mass- and light-weighted properties since they can complement each other well to identify certain processes more clearly. For example, recent star formation will dramatically reduce the light-weighted stellar age deduced due to the high luminosity it contributes, despite perhaps being a very small mass component. Conversely, small or negligible differences in light- and mass-weighted properties come from having star formation histories that are well represented by a single-burst of star formation at its formation. Moderate differences can therefore be interpreted as having extended episode(s) of star formation. We note that FIREFLY fits stellar population components using their light contributed, and thus mass-weighted properties are decoded from the light-weighted properties by calculating the mass-to-light ratio of each stellar population component, as we will describe here.

We may calculate the mass contributions from the SSPs in any dataset, so we explain the process generally here. The data fluxes are measured in units proportional to [erg/s/Å/cm^2], whereas the model luminosities are measured in [erg/s/Å/M$_\odot$], i.e. scaled to 1 solar mass. This scaling includes the effects of stellar remnants (mostly white dwarfs, but also black holes and neutron stars), whose contribution to the mass depend on the initial mass function (see next Section) and analytical prescriptions relating the mass at the advanced stages of evolution and their product remnants and recycled material.

Hence to retrieve a contribution of each of the SSP fits in terms of stellar mass, we must calculate the factors of normalisation for both the data and SSPs before fitting, see figure 3.2. We save the values of the normalisation in FIREFLY for each SSP in the model library, which we shall henceforth call "N$_{M/D}$":

$$N_{M/D}^{SSPi} = \frac{\Sigma_\lambda L[SSPi]}{\Sigma_\lambda \phi[Data]} \tag{3.11}$$

where $L[SSPi]$ is the luminosity of the SSP for which we are finding the normalisation factor,

and $\phi[Data]$ is the flux of the object we are observing. The units of $N_{M/D}$ are therefore [cm^2 / $M_\odot$]. For example, in Chapter 4 the specific units for SDSS are [$10^{17} cm^2$ / $M_\odot$].

Note that the summation corresponds to adding up the fluxes or luminosities for all available wavelength data points between a defined upper and lower limit. Where possible, these wavelength limits should also be consistent when comparing models such that any systematic effect of changing the wavelength range on the stellar mass determination is reduced (see Pforr, Maraston & Tonini (2012)). The mass-weighted contribution of each SSP will then be

$$w_i^M = \frac{w_i^L}{N_{M/D}^{SSPi}} = w_i^L \times \frac{\Sigma_\lambda \phi[Data]}{\Sigma_\lambda L[SSPi]}, \tag{3.12}$$

where the w_i^M and w_i^L are the mass-weights and light-weights respectively. This expression will therefore be in units of [$M_\odot$ / cm^2]. We save these mass-weighted contributions when deriving other properties such as the mass-weighted age, mass-weighted metallicity, etc.

At this point it is useful to note that the flux from the data can be converted to a luminosity if we know that object's redshift (and hence, given a cosmological model, its luminosity distance D_L in units of centimetres),via $L = 4\pi D_L^2 \times \phi$. Hence we can now convert the luminosity-weighted contributions into mass-weighted contributions as

$$\begin{aligned} M_{SSPi} &= w_i^M \times 4\pi D_L^2 \\ &= 4\pi D_L^2 \times w_i^L \frac{\Sigma_\lambda \phi[Data]}{\Sigma_\lambda L[SSPi]} \end{aligned} \tag{3.13}$$

which is in units of [$M_\odot$].

Hence the total stellar mass is simply given by the sum of all the SSP weightings:

$$\begin{aligned} M_{stellar}^{tot} &= \Sigma_i M_{SSPi} \\ &= \Sigma(w_i^M) \times 4\pi D_L^2 \\ &= 4\pi D_L^2 \sum_i (w_i^L \frac{\Sigma_\lambda \phi[Data]}{\Sigma_\lambda L[SSPi]}) \end{aligned} \tag{3.14}$$

These values can then be used to retrieve the total stellar mass of the object. Thus, since each SSP contribution gives a mass contribution and a light contribution, for each SED fit we can retrieve a mass-weighted age and metallicity and a light-weighted age and metallicity. Since

each model SSP relates its luminosity to its mass, we can use this information to calculate average mass-to-light ratios for the SED fits. An example of using the results of FIREFLY for mass-to-light ratio analysis is shown in Chapter 5.

3.8.2 Summary of properties recovered

In addition to these light- and mass-averaged properties, FIREFLY by default outputs the E(B-V) used in each fit, the χ^2 values of each fit, and the wavelength bounds used in the fitting process. Multiple stellar population models may be used, in which case all the above properties are recorded for each model. We summarise the full set of properties obtained from FIREFLY for each galaxy here:

- Input model and fitting parameters, such as stellar library, IMF, wavelength range, etc.
- Light-weights of each SSP for each solution.
- Mass-weights of each SSP for each solution.
- χ^2 value of each solution and their associated relative likelihoods.
- Degrees of freedom.
- Light- and mass-weighted averaged age of each solution.
- Light- and mass-weighted averaged metallicity of each solution.
- E(B-V) recovered.
- Mass-to-light ratio of each solution.
- Total stellar mass.

This full set of properties allows complete recovery of the spectral fits, the properties used in the visualisation of the fits, a probability distribution of star formation histories, and the best-fit global properties with confidence intervals.

3.8.3 The effect of the Initial Mass Function

In the M11 models used in this thesis, there are three Initial Mass Functions (IMFs) available for each model library; 'Salpeter' (Salpeter, 1955), 'Kroupa' (Kroupa, 2001), and 'Chabrier'

(Chabrier, 2003), which describe the mass distribution of main sequence stars in the models. Since Kroupa and Chabrier IMFs have lower amounts of low-mass stars compared to Salpeter, they have lower mass-to-light ratios by a factor $\sim$0.6 and $\sim$0.55 respectively (in the 'i'-band: see Chapter 5) compared to Salpeter. However, other than the scaling factor the impact on the SED is restricted to only some small changes in certain absorption features. Hence in tests of multiple sets of IMFs and models we did not see any difference on the recovered SED fits greater than 0.1 % in any of the properties.

Kroupa IMFs are most often used in the literature that we will be comparing to in this Chapter, and Chapters 4 and 5. Hence for all our results in this thesis, we only show results from using models with a Kroupa IMF.

3.9 Calibration of the fitting method

3.9.1 Mock galaxies

To test the validity and stability of the results obtained from FIREFLY we run a comprehensive set of tests on two types of mock galaxies, based on model spectra. We additionally use these mock galaxies to test the effect of wavelength range on the properties obtained to directly probe the degeneracies of the model components and calibrate the fitting setup.

Perturbed simple stellar populations

In the first set of tests we use mock galaxies made from the same simple stellar population templates used to fit to them. We describe these tests carried out using models based on the MILES stellar library, since it has the largest metallicity coverage, initially using the full wavelength range available (see table 1 in Chapter 2). Tests including dust are carried out in the next section on composite populations. Each of these mock galaxies has a Gaussian perturbation applied to each of the flux points with a flat signal-to-noise, as described by

$$F_{Mock}(\lambda_i) = N(F_{SSP}(\lambda_i), (\frac{\phi_{SSP}}{S/N})^2), \tag{3.15}$$

where $F_{Mock}(\lambda_i)$ is a single flux point i of the mock galaxy and $F_{SSP}(\lambda_i)$ is the flux point i of the input SSP, both corresponding to a wavelength point $\lambda_i, N(x, \sigma^2)$ is the normal distribution

with mean x and variance σ^2, and S/N is the input signal-to-noise. For these tests, we use the following signal-to-noise values: 1, 3, 5, 10, 15, 20, 50 and 100. The 1 to 100 range covers the vast majority SDSS galaxies with higher values usually corresponding to stacked spectra. The high signal-to-noise value case allows us to measure the degeneracies of the models directly, and other values allow us to investigate perturbations from this case in real observations.

We create a Monte Carlo simulation of 100 realisations by applying these Gaussian perturbations 100 times to each SSP for each signal-to-noise bin. In Figures 3.12, 3.13 and 3.14 we plot the age, metallicity and stellar mass recovered as a function of SSP age for each S/N bin. Each point represents the average value obtained from 1000 realisations of that SSP, with the errors measured from the standard deviation of the fitted ages of the realisations. Since by design we know that each SSP has been normalised to one stellar mass, and we know the input ages and metallicities, we draw a line of where the correct solutions are so that we can see their displacement from this.

From figure 3.12 to Figure 3.14 we can see some systematic trends for many of the input signal-to-noise values. Most notably, even up to S/N of 100, is the overestimation of stellar mass at young ages (1 – 1.5 in log(Myr)); these correspond to when ultra-low metallicity solutions with much high ages, which have vastly higher mass-to-light ratios in the models, are strongly degenerate with the true values. Another systematic trend is the higher stellar masses derived at 1.5 - 3 Gyr (3 in log(Myr)) (i.e. about the age in which the TP-AGB phase dominates, see Chapter 2). This effect is much less pronounced and is not easily visible above S/N of 20 in the mass plot, but visible as 0.2 dex offsets in the age, and 0.1 dex offsets in the metallicity. These solutions correspond to degeneracies with half-solar, intermediate age (3 - 5 Gyr) solutions which have somewhat higher mass-to-light ratios. For both of these cases we note that the 1-sigma error seems to underestimate the errors fairly regularly, suggesting that quoting 2-sigma errors for Monte Carlo simulation errors would be more reasonable.

We now use these tests to give estimates of relationships between the S/N and the degeneracies' effect on derived properties. These empirically derived results will be useful for knowing the key systematic errors that one needs to be wary of when analysing properties from full spectral fitting.

Generally, offsets in age, metallicity and mass for input ages $\lesssim$ 100 Myr as a function of signal-to-noise, where offset means recovered value – input value, go as:

Age offset / dex = +1.5 / (S/N),

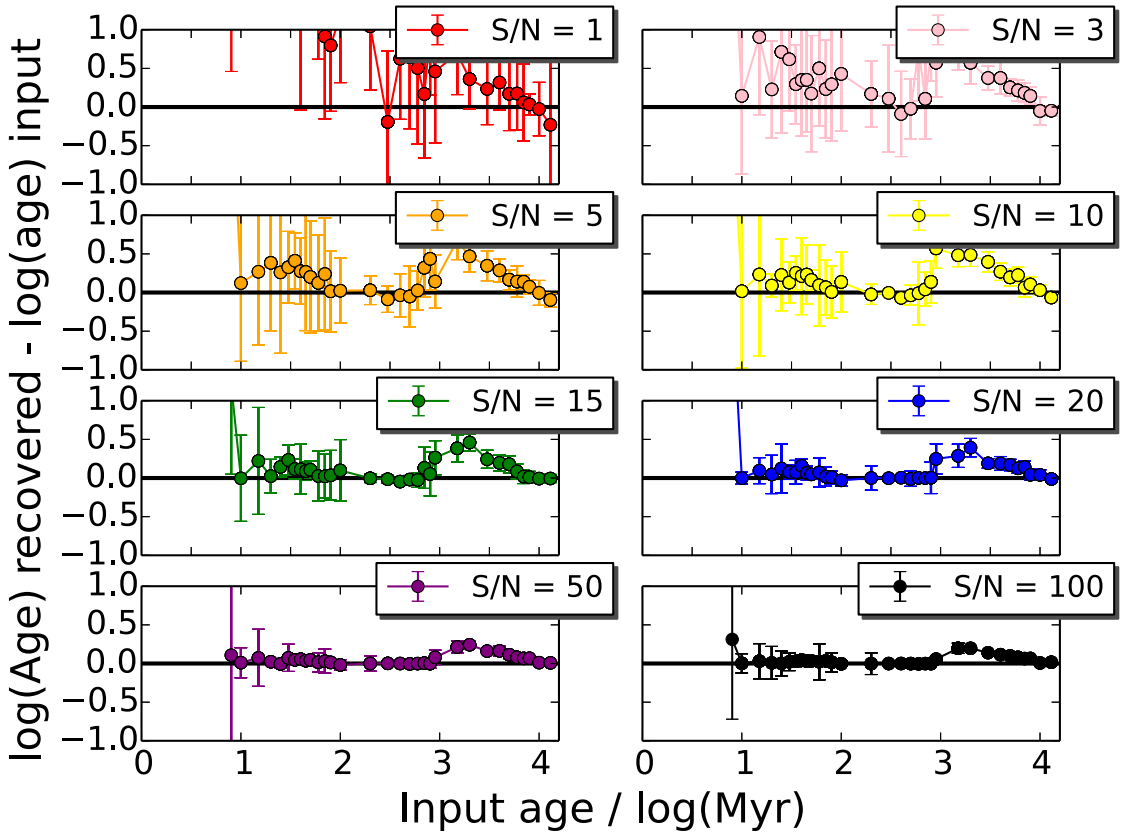

Fig. 3.12 Recovery of light-weighted age when using SSPs directly as mock galaxies, with independently applied Gaussian errors corresponding to 8 different signal-to-noise values. Each point is the median fitted value for the 100 Monte Carlo realisations, with errors plotted as the 68 percentile either side of the median of the values recovered (i.e. 1 σ). In these tests we use MILES-based model SSPs at the full wavelength range available, at solar metallicity, with no dust component, but the main conclusions hold for other test choices.

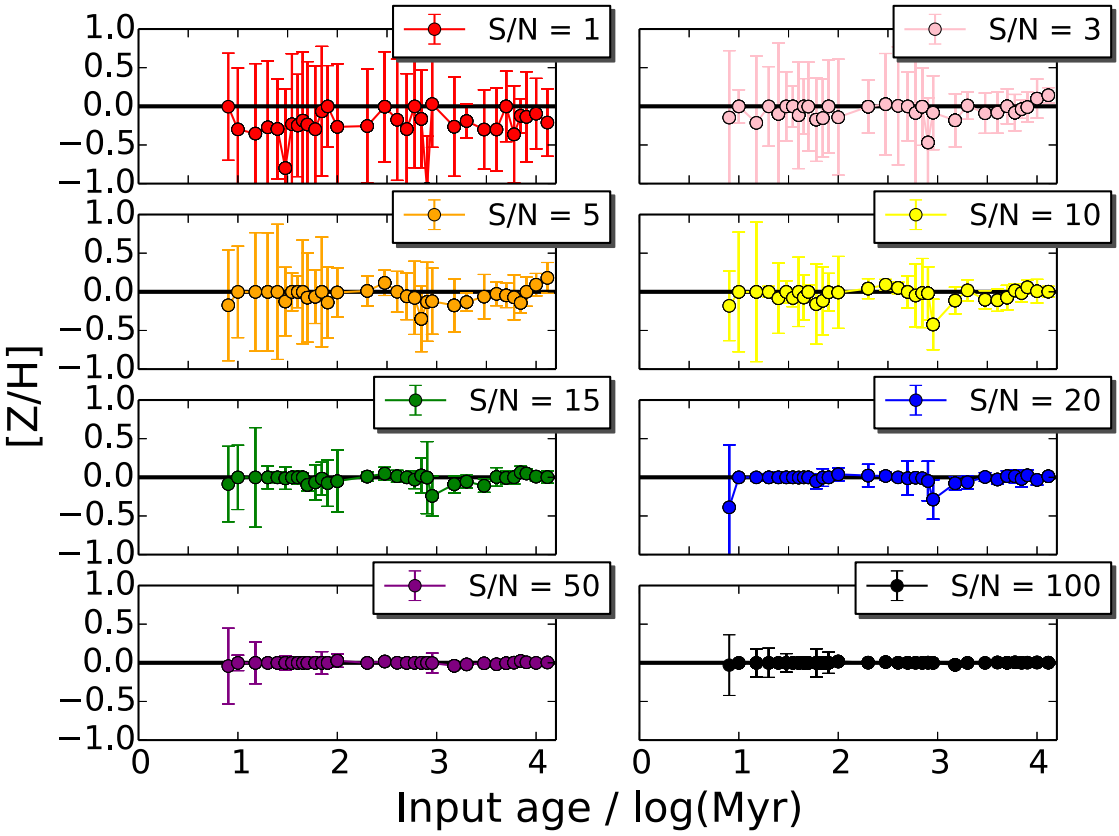

Fig. 3.13 As Figure 3.12, for metallicity.

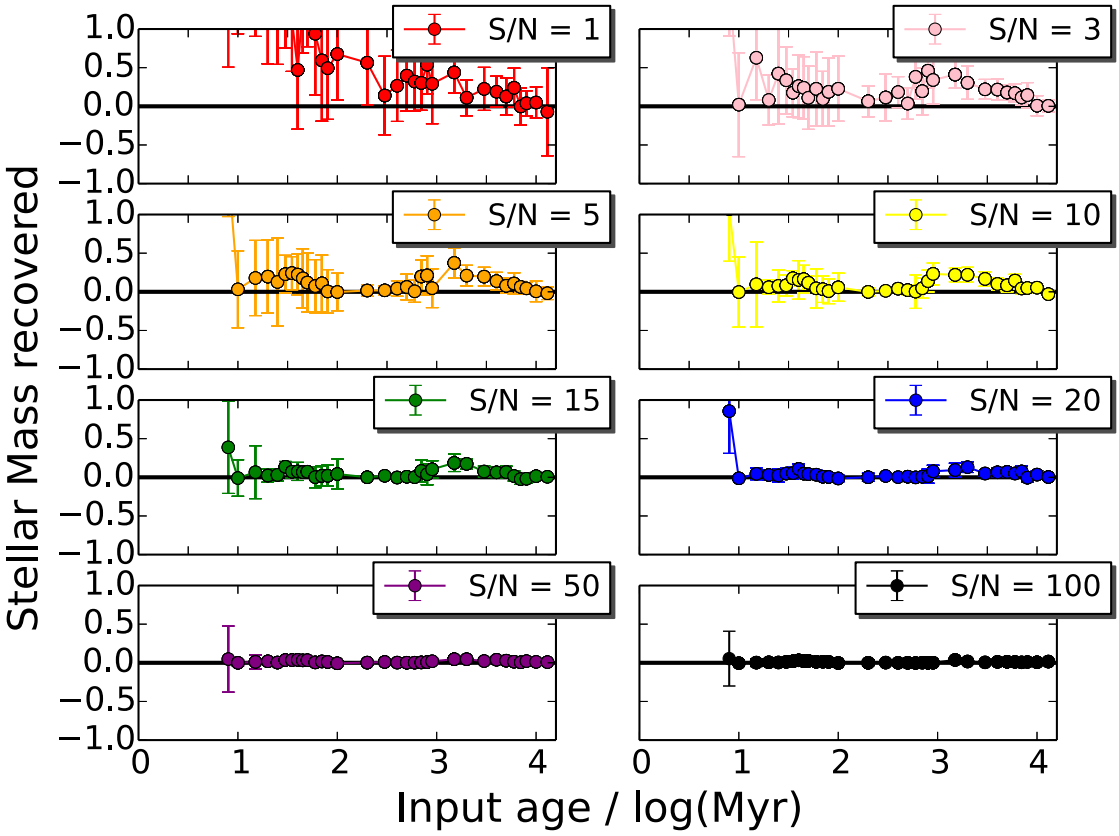

Fig. 3.14 As Figure 3.12, for stellar mass.

[Z/H] offset = –0.5 / (S/N),
Stellar mass offset / dex = +1.0 / (S/N).

Degeneracies at input ages in 1 – 3 Gyr region go as:

Age offset / dex = +0.7 / (S/N) + 0.1,
[Z/H] offset = –0.3 / (S/N),
Stellar mass offset / dex = +0.3 / (S/N).

Lastly, offsets from other ages are less significant, going as:

Age offset / dex = +0.2 / (S/N),
[Z/H] offset = –0.2 / (S/N),
Stellar mass offset / dex = +0.1 / (S/N).

Composite stellar populations

In the second set of tests we use composite models (from Claudia Maraston, private communication) obtained with a range of exponentially-declining star formation histories (known as τ models) commonly used in the literature for fitting to a variety of galaxy surveys (e.g. Longhetti & Saracco (2009), Lee et al. (2010)) as a realistic mode of star formation. We investigate these models for every combination of: a range of decay times; $\tau = 0.1$, 1, 10 Gyrs, a range of ages for the beginning of the onset of star formation; $t_s = 0.01$, 0.1, 1, 3, 5, 10 Gyrs, and a range of dust extinction values; $A_v = 0$, 0.4, 1, 3. To limit the number of combinations we take an arbitrarily high signal-to-noise since we have already computed the effect of signal-to-noise in section 3.9.1.

To test the accuracy of the fits we can show the stellar mass recovered compared to the input stellar mass (normalised to 1 as before). We show this as a grid of solutions in input τ – input t_s space, with a coloured scale showing the stellar mass obtained for two realisations; median S/N $\sim$ 20 and median S/N $\sim$ 5, in Figure 3.17 .

Firstly, we repeat the Monte Carlo simulation approach in the previous section, but applied to the CSPs with the 2 different S/N: 5 and 20. Plots 3.15 and 3.16 show the results of this analysis for all CSPs used for these S/N respectively.

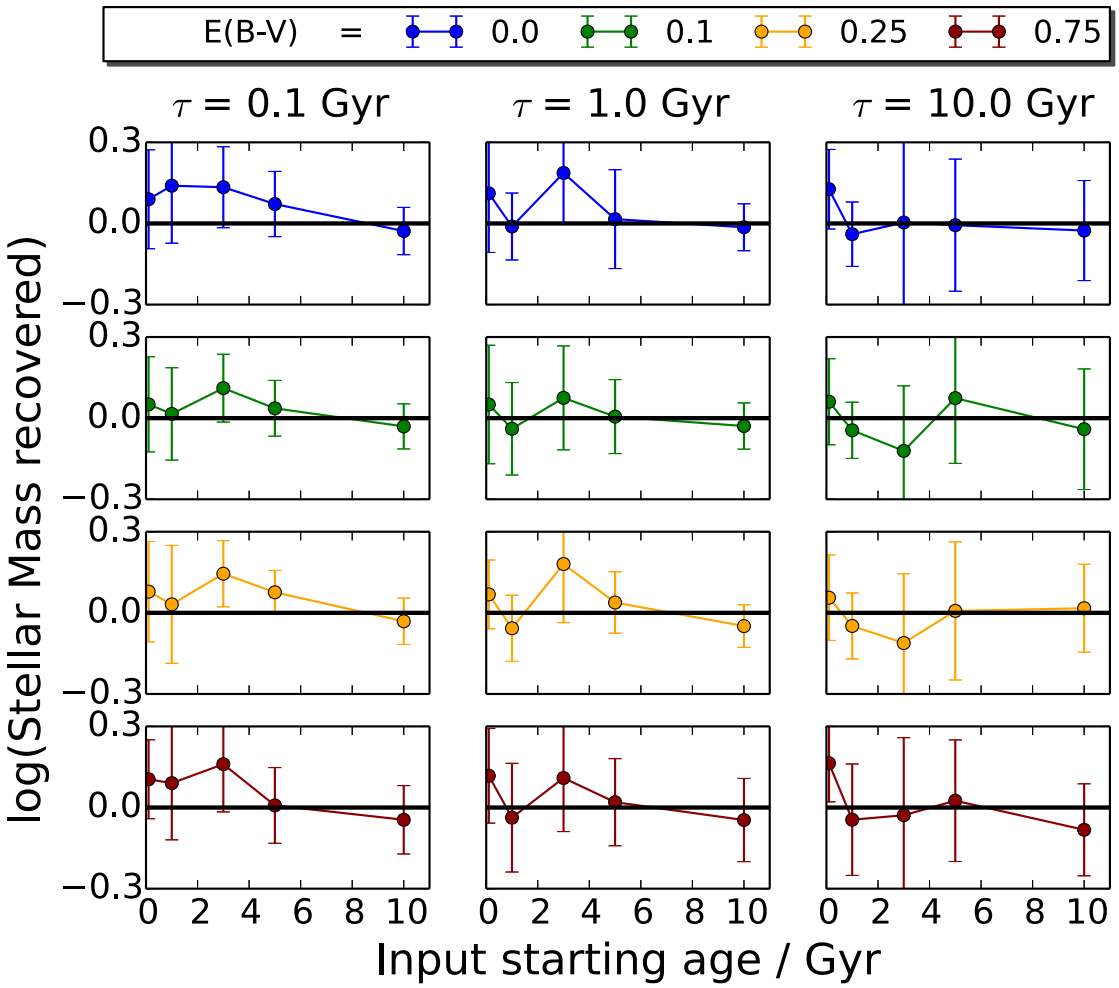

Fig. 3.15 Recovery of light-weighted age when using CSPs as mock galaxies, which have exponentially declining star formation histories with a variety of characteristic decay times (τ) and starting age (t), as $\Phi(t,\tau) \propto e^{-(t)/\tau}$, for $t > 0$. As with the SSP tests, we have applied Gaussian perturbations and errors corresponding to a S/N of 5. Each point is the median fitted value for the 100 Monte Carlo realisations, with errors plotted as the 68 percentile either side of the median of the values recovered (i.e. 1 σ). In these tests we use MILES-based model CSPs at the full wavelength range available, at solar metallicity, with no dust component, but the main conclusions hold for other test choices.

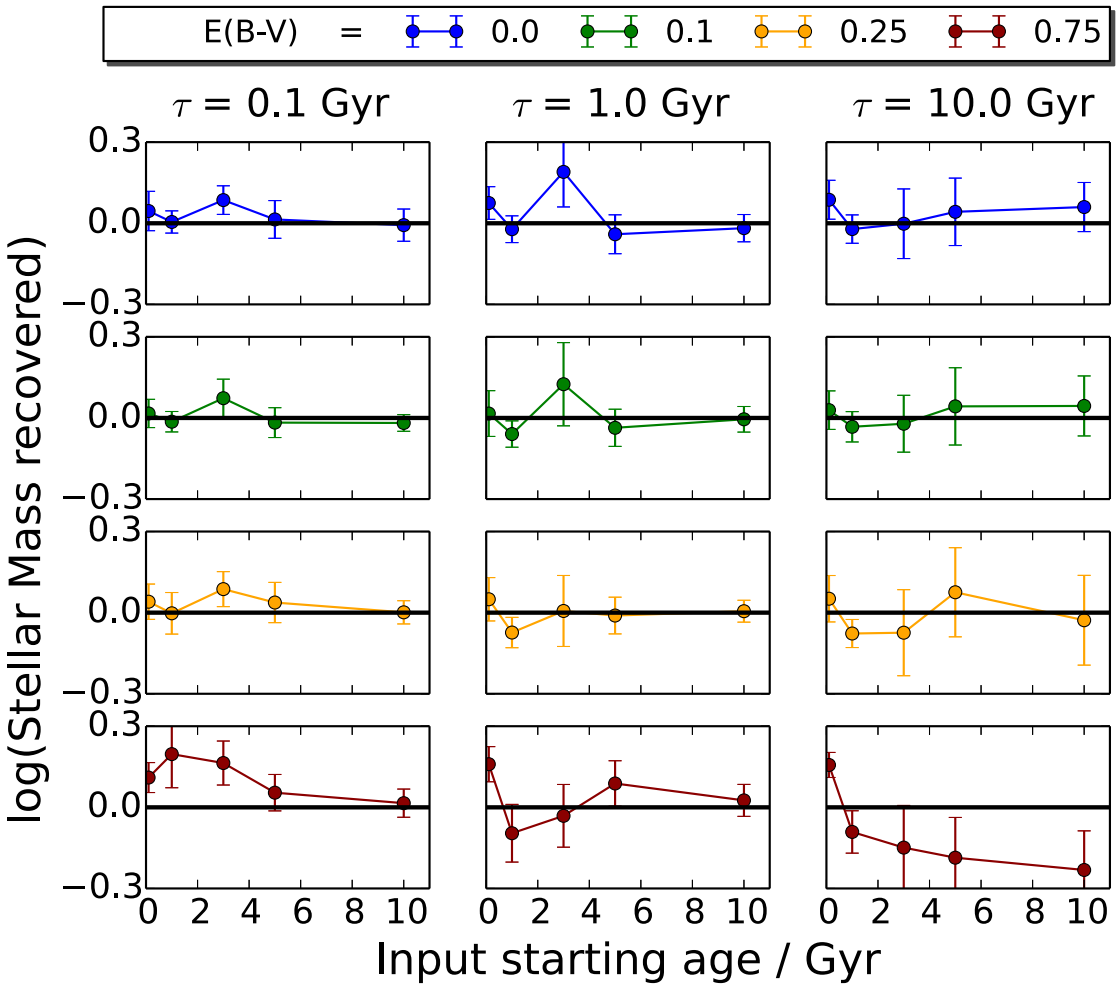

Fig. 3.16 As Figure 3.15, for mock galaxies with S/N of 20.

In this case we first note the change in scale; pleasingly for both cases the offsets of stellar mass are always less than 0.3 dex in size. Again there are some common regions in age where full spectral fitting of these solutions meets a degeneracy, corresponding to an offset in the mass recovered. However, we note that for the majority of cases within Monte Carlo errors we find the correct solutions. The errors on properties recovered generally decrease with S/N, as we should expect. The main offset seen for all τ and S/N is the input starting age of 3 Gyr, again corresponding to the TP-AGB region offset as discussed in the previous section. This effect, again, is somewhat more pronounced at lower S/N, but is still present up to S/N of 20.

These plots are also a function of attenuation. Encouragingly, the differing amounts of dust do not drastically effect the offsets for the first three low to high values of dust. However, in the case of very high dust extinction (E(B-V) = 0.75) we can see the offsets approximately doubling in size for the high S/N case. In these cases, the dust algorithm has some difficulty in fitting precisely the size of absorption features once they have been filtered, as the attenuation has reduced the size of them. This serves as a notice for checking extremely dust regions, but fortunately such high values of extinction are rare in nature. Nonetheless, solutions are still consistent within 2 sigma errors and are always below 0.3 dex in size.

We cannot do a full Monte Carlo analysis on every observed galaxy SED, since the time taken to do so would make it unsuitable for application to large surveys. However, the model errors produced by FIREFLY are still useful, so in figure 3.17 we again plot offsets in stellar mass but this time for one single run of the fitting code applied to one realisation of each mock SED for S/N of 5 and 20. The errors plotted here are the upper and lower limits of the 1 sigma confidence intervals output by FIREFLY.

First to note is that the offsets of the median points are generally larger than the Monte Carlo medians as one would expect from statistical fluctuation. Importantly however, for practically every point plotted the sensibly sized errors enclose the correct solutions. Errors are typically 0.2 dex in size for S/N of 20 and 0.5 dex in size for S/N of 5. This demonstrates the power of FIREFLY for enclosing the correct solutions in a single run, and shows that the errors derived are reliable.

From figure 3.17 we observe some systematic features of fitting to CSPs. The first is that at high τ and moderately high t_s we see underestimates of the stellar mass for all dust values (by about 0 – 15 %). Investigating these solutions further, we find that this is due to the overestimate of the light-weighted SSP contributions from young ages due to the 'overshining' problem (Maraston et al. (2010), Pforr, Maraston & Tonini (2012)), where small amounts of

mass in star formation can slightly mask other populations in their light-weighted properties. In these cases we find that our solutions enclose stellar mass fits that do not suffer this problem, and so these systematic errors are within the statistical errors of our sample of fits. However, statistically one is not able to separate the 'good' solutions from the 'bad' ones.

Secondly we also see some overestimates of the stellar masses at very low onset ages, $t_s = 10$ Myrs, in the S/N of 5 case, which is on the order of 10 percent except in the very high dust case of $A_v = 3.0$. In this case the spectral degeneracies are causing the addition of high age, metal-poor solutions that boost our stellar mass estimates; in the very high dust case the degeneracy with these solutions is so severe that we cannot statistically separate these high age solutions from the correct ones, thus boosting our average stellar masses by ~ 0.3 dex.

We also see consistent ~ 0.15 dex overestimates of the stellar mass at 1 - 3 Gyrs at very low τ, suggesting that we are still seeing the SSP-like degeneracies, boosting our age estimates higher at these input ages, as discussed in section 3.9.1. For high age and moderate τ solutions however, we find excellent agreement between input and recovered stellar mass and other physical properties. This regime is particularly important for galaxies that have a mostly passive star formation history since their relatively brief period of star formation, such as massive elliptical galaxies.

From these plots we conclude that a single run of FIREFLY encloses the correct solutions, but median values for a single galaxy can be as much as 0.2 dex offset for intermediate ages at S/N of 20 (similar to galaxy SEDs in SDSS DR7, see Chapter 4), and 0.5 dex offset for S/N of 5 (similar to galaxy SEDs in SDSS BOSS, see Chapter 4). However, we have shown using Monte Carlo simulations that for a sufficiently large sample of 100 or more galaxies, these effects become much smaller, about 0.1 dex or less on average.

3.10 Testing the effect of wavelength range

3.10.1 M67

M67 is an ideal object for the purposes of calibrating our code to extend this method, primarily because as a resolved stellar population its age and metallicity have been independently determined precisely from colour-magnitude diagram fitting (see Sarajedini, Dotter & Kirkpatrick (2009) for a recent measurement of 3.5 – 4 Gyrs from fitting isochrones to its individual turnoff-mass stars). It is also a desirable object to calibrate with because it is approximately

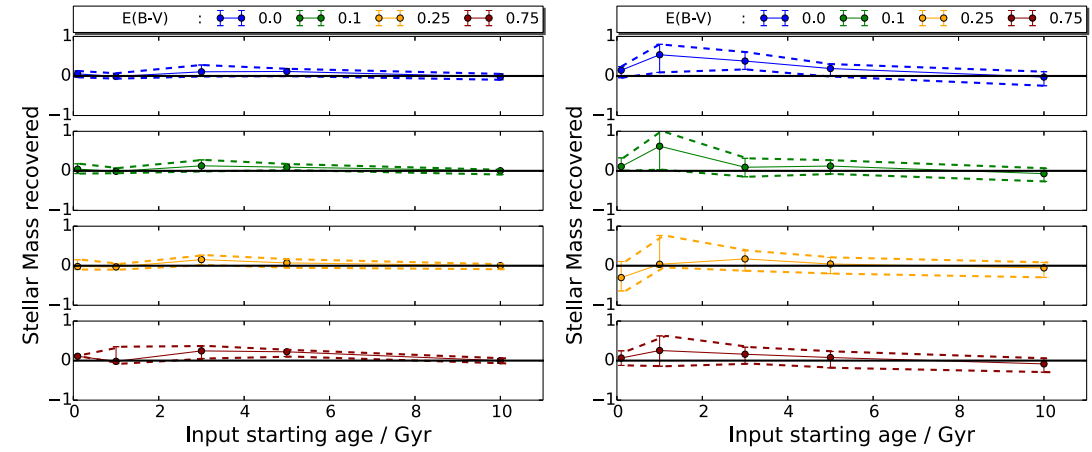

(a) S/N = 20, $\tau = 0.1$ Gyr.

(b) S/N = 5, $\tau = 0.1$ Gyr.

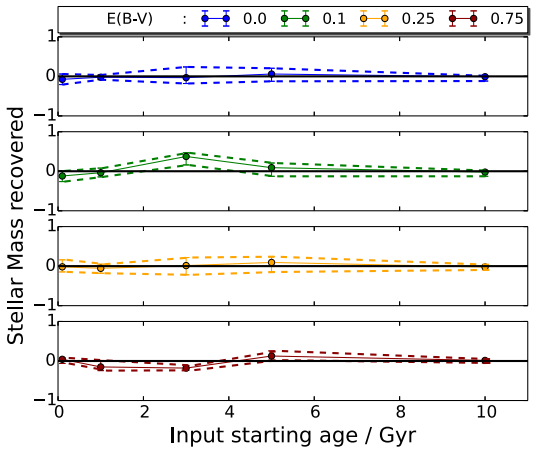

(c) S/N = 20, $\tau = 1$ Gyr.

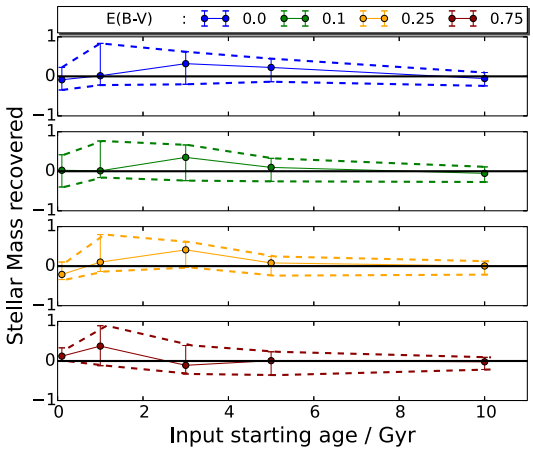

(d) S/N = 5, $\tau = 1$ Gyr.

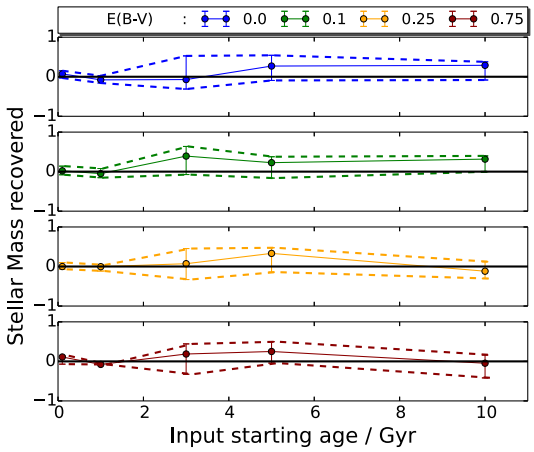

(e) S/N = 20, $\tau = 10$ Gyr.

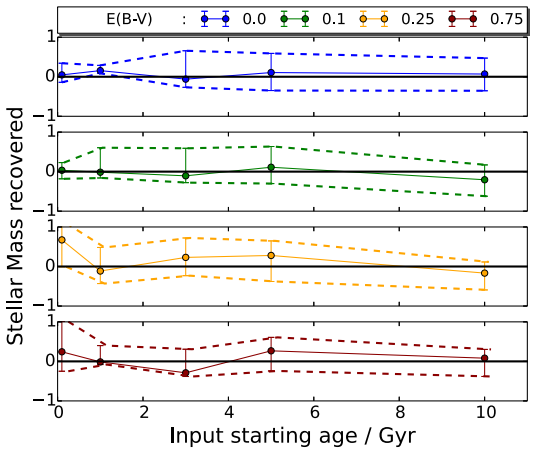

(f) S/N = 5, $\tau = 10$ Gyr.

Fig. 3.17 Recovered stellar masses from fitting mock spectra based on composite stellar populations with median signal-to-noise of 20 (LHS) and 5 (RHS). All normalised to 1 stellar mass and so the recovered stellar masses is also the fractional recovery of stellar mass. Their input star formation histories have exponentially declining star formation rates and are plotted on a grid in $\tau - t_s$-space for 4 different dust values, where the star formation history is given by $\Phi(t,\tau) \propto e^{-(t)/\tau}$, for $t > 0$. t is the time since the onset of star formation at a lookback time of t_s, and τ is the star formation decay time.

solar in metallicity and has solar-scaled element abundance ratios, which matches with the models (see M11). We therefore expect the models and our fitting code to give excellent fits. The wavelength range used for the best fits in figure 3.1 was the maximum used by the data (3650 - 5350 Å) or the models, but we can also test the effect on the age derived when choosing a smaller wavelength as a function of empirical stellar model. The results of this is shown in figure 3.18, where we have fitted with full freedom of SSPs and combinations of fits.

We note that MILES-based models most often gives the most accurate solutions, finding that for many regions of the Figure the age determined is exactly correct, with about 0.1 dex spread in values for large wavelength regions. STELIB-based models have more variance in the ages recovered, about 0.2 dex, but generally finds accurate solutions. ELODIE-based models generally overestimate the age by about +0.2 dex, though is fairly consistent with wavelength with about 0.1 dex spread.

The following wavelength features of the plots are noted: - STELIB releases the most consistent fits that are also CMD-consistent when using a relatively small, blue wavelength range (around 3900 to 4300 Å); well-known as the 4000 Åbreak.
- MILES and ELODIE release CMD-consistent ages when a large wavelength range is used but fails to do so when not taking account of the lower wavelength ranges (approximately below 4300 Å).
- All the model libraries release ages that are too high (which correspond to metal-poor solutions) when cutting out the blue part of the spectrum (up to $\sim$ 4300 Å). In general the models are more sensitive to the minimum wavelength range set, clearly showing that the models discriminate between ages fitted much more clearly in the lower wavelength regions plotted, for M67.

The dominant effects on the results are due to the well-understood effect of the 'D(4000)' (or the 4000Å break, defined and described in Bruzual A. (1983)), which is a spectral discontinuity that is related to the evolution of blue stars, which in turn evolve on timescales comparable to the whole population age. Therefore including this region in the analysis explains why this is a necessary wavelength region to fit in order to accurately determine the age of M67. This shows that in order to accurately trace the age of intermediate-age stellar populations, we must use this wavelength region in any spectral fit where these stars are dominant. These plots also serve as a warning about ELODIE's age recovery at these ages, as it generally seems to give 0.2 dex higher ages for M67.

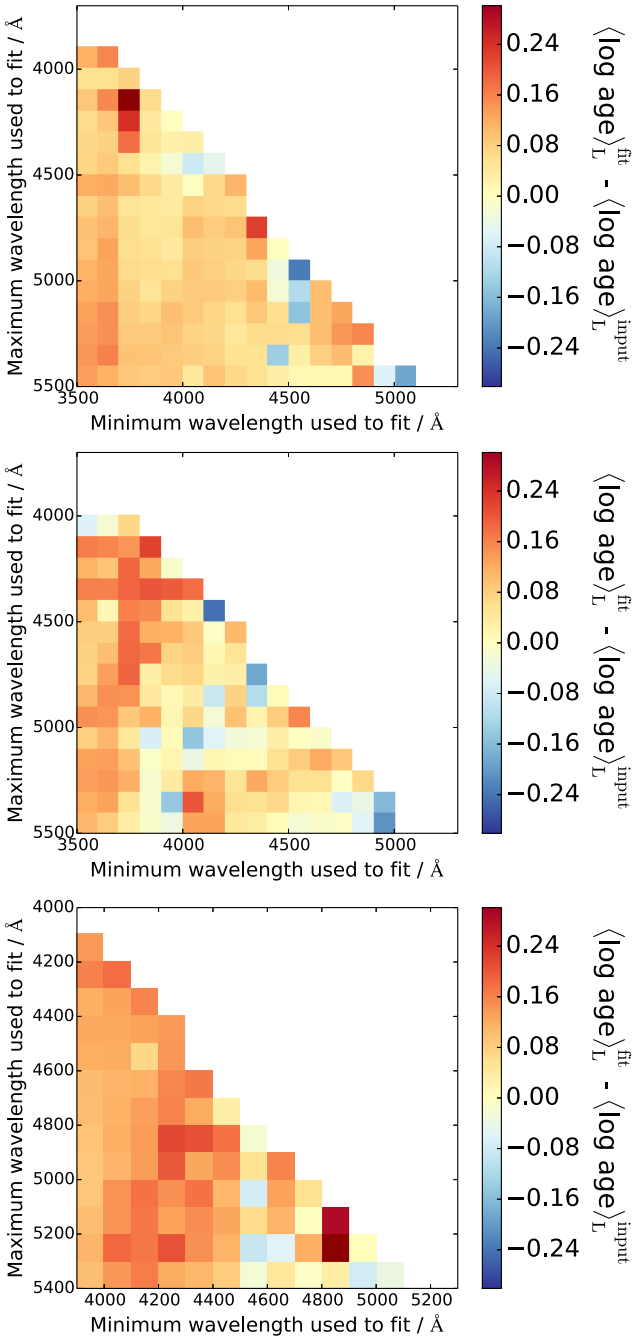

Fig. 3.18 How determination of ages of M67 for MILES/STELIB/ELODIE-based models respectively depends on the wavelength range fitted over. The coloured squares show the best-fit age determination for that range of wavelengths fitted across. CMD-consistent ages are shown in colour close to yellow, which from Chaboyer (1999) and Sarajedini, Dotter & Kirkpatrick (2009) is found to be 4 Gyrs. The top-right of the plots are empty since those regions cover a negative, and hence non-existent, wavelength range.

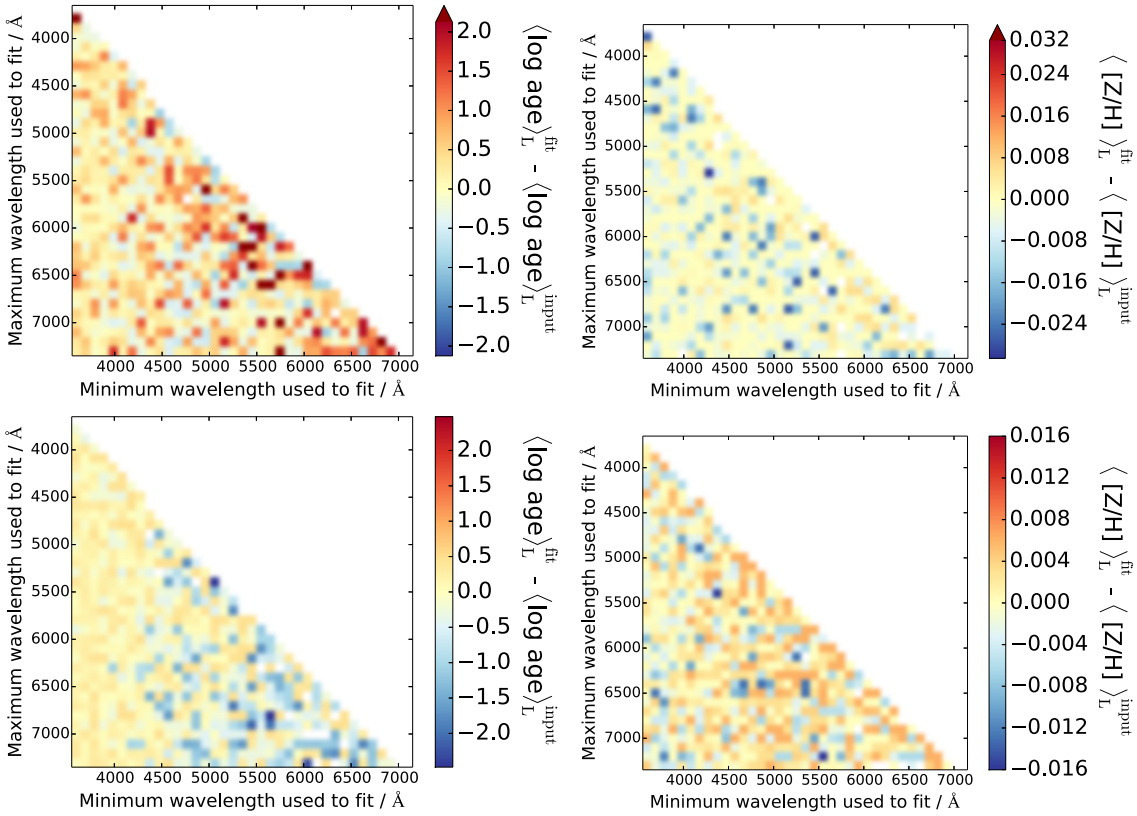

Fig. 3.19 Light-weighted age (LHS) and metallicity (RHS) recovery of SSP-based mock galaxies as a function of wavelength range used. The top panel shows results for a 55 Myr, solar metallicity SSP and the bottom panel shows results for a 5 Gyr, solar metallicity SSP. All use MILES-based models to fit to MILES-based mocks. The top-right of the plots are empty since those regions cover a negative, and hence non-existent, wavelength range.

3.10.2 Mock galaxies

To complement the above tests on M67 we carry out an investigation of the effect of varying the wavelength range used to fit to the data on the properties obtained, both as a function of input model SSP age and signal to noise. For brevity we display the ages and metallicities obtained from fitting solar metallicity-only SSPs with no dust component, using a signal-to-noise of 5 and MILES-based models. Two representative cases are shown in figures 3.19 for SSP mocks, the top panels with input age 55 Myr and bottom panels with 7 Gyr.

From Figure 3.19 we see two different cases of age-metallicity degeneracy. For the 55 Myr mock, we see that in general the recovered ages are overestimated ($\sim$ 0.3 dex) and the metallicities are slightly underestimated ($\sim$ 0.01 in [Z/H], or 0.01 dex in Z); an effect which gets worse with smaller wavelength ranges. Conversely, the 7 Gyr mock shows that as long as one

includes a wavelength fitting region below 4100 Å, ages and metallicities are well estimated. However, once the region is removed then the solutions tend towards younger (by up to 0.5 dex), generally more metal-rich (∼0.01 dex) solutions, in the same way that the M67 solutions behaved. Together, these plots show that wider wavelength ranges give more ability to overcome the effects of age-metallicity degeneracy, and confirms that for intermediate to old age solutions, the 4000 Å region is essential for precise age solutions.

3.11 Calibration with Globular Clusters

As stated throughout this thesis, globular clusters are invaluable for calibration with stellar population models, since we can achieve precise and independent age determination from colour-magnitude diagram fitting (Renzini & Fusi Pecci, 1988) and compare with our fitting results. They provide the 'simplest' form of stellar populations in nature, i.e. approximately a single coeval population of stars, something we can assess with FIREFLY. In this section we use globular cluster data from Schiavon et al. (2005). In Figure 3.20 we show two examples of FIREFLY's fits and properties to a metal-poor and metal-rich globular cluster respectively.

We see that the metal poor globular cluster NGC 5286 is well-represented by nearly a single group of SSP at high age (with a CMD-derived age of 12 – 13 Gyr) and low metallicity (about –1.5 in [Z/H]), whereas NGC 6528, a more metal-rich cluster, has evidence for having two sets of old components, a ultra-low metallicity component and an metal-enriched component, perhaps as a result of merging processes, with an overall CMD age of 9 – 12 Gyr and about solar metallicity. The latter case is rare, applying to only 3 of the full set of globular clusters.

In Figure 3.21 we compare all of our light-weighted ages and metallicities from those derived in the literature, as tabulated by Koleva et al. (2008). In cases where a CMD age has been measured, we use this value, and for others we use the value derived in Koleva et al. (2008) from their full spectral fitting using a code called NBURSTS (Chilingarian et al., 2007) with the Pegase-HR models (Le Borgne et al., 2004). Since the models and code are different, we focus on only the qualitative comparisons for these galaxies.

We see that the ages derived from CMD fitting are close to FIREFLY's, within 0.1 dex for the vast majority of values. Unfortunately, the small dynamic range of globular cluster ages means that we are not able to derive a statistically significant correlation with age within the errors as output from the code. Thus, we can only discuss the results qualitatively and with specific examples, and refer to our tests on mock galaxies for statistical results. The values

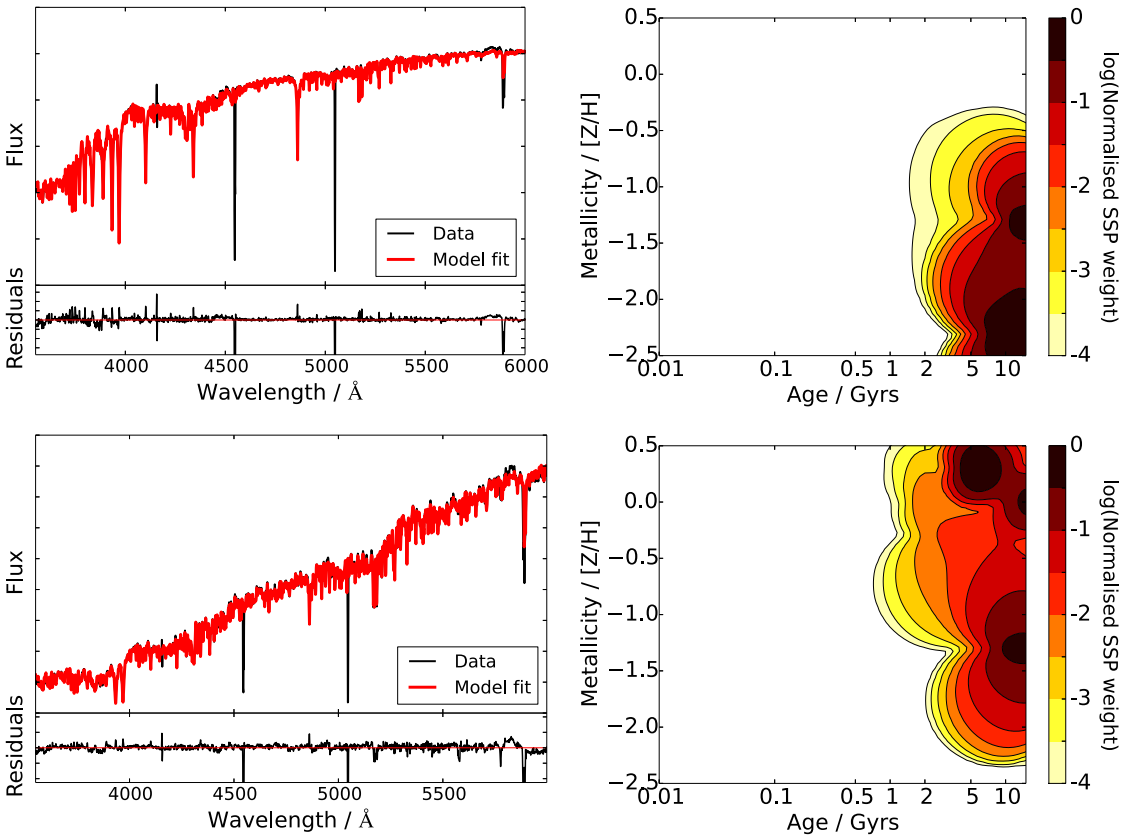

Fig. 3.20 Fits and stellar population contours of 2 example globular clusters; NGC 5286 and NGC 6528 from Schiavon et al. (2005). Measurements from colour-magnitude diagram fitting show NGC 5286 is very metal-poor, whereas NGC 6528 is approximately solar in [Z/H]. The corresponding colour-magnitude diagram fitted properties are NGC 5286: 12 – 13 Gyr, – 1.5 dex; NGC 6528: 9 – 12 Gyr, – 0.1 dex, consistent with the average of the contours shown.

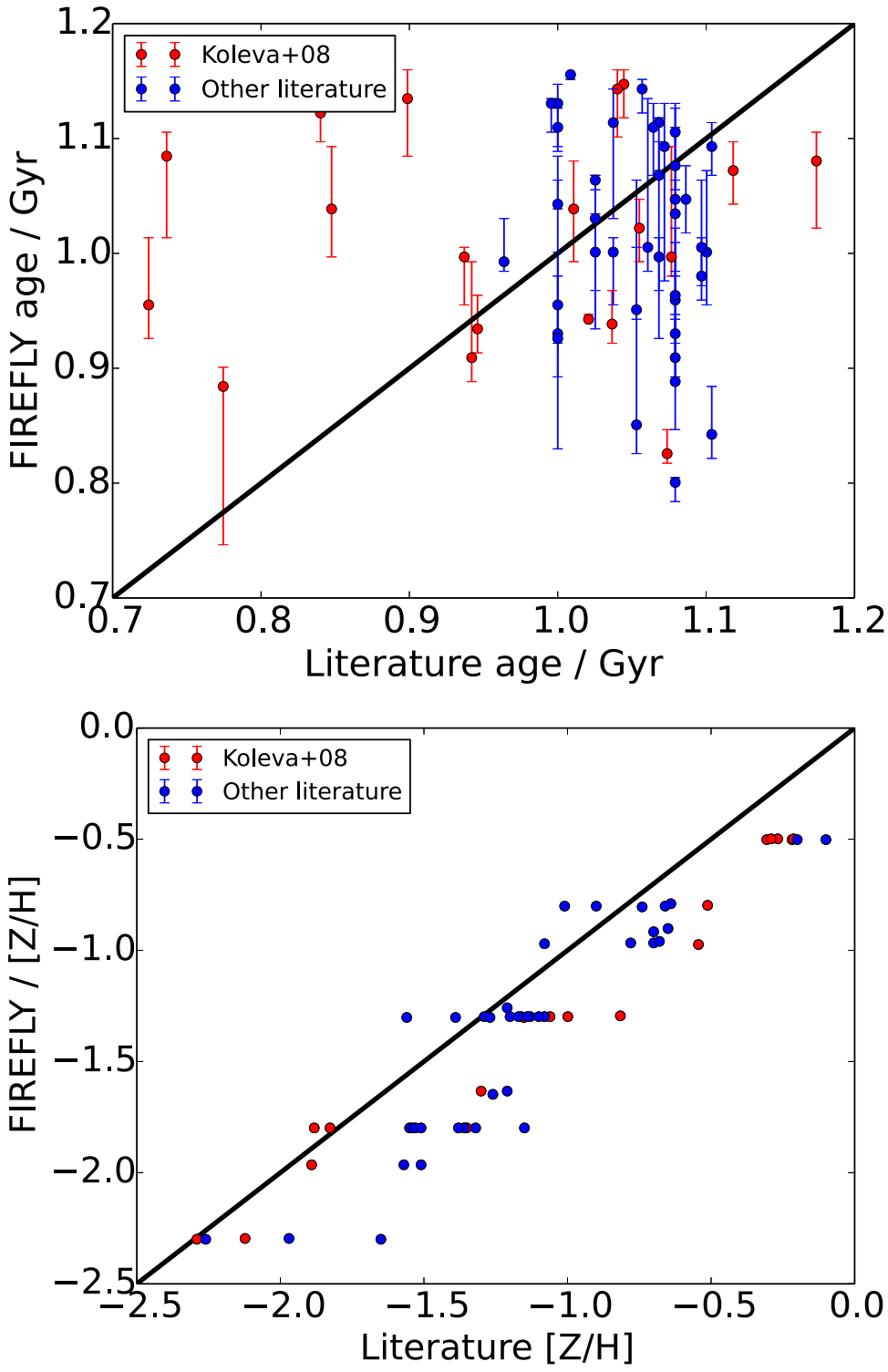

Fig. 3.21 Light-weighted age and metallicity derived from FIREFLY compared to literature values, which come from a mixture of colour-magnitude diagram fitting, and SED fitting from Koleva et al. (2008) where CMD-derived properties are unavailable.

in which we are not within 0.1 dex come from globular clusters in which we find a bimodal population, such as that of NGC 6528 in Figure 3.20. Similarly for metallicity recovery is generally excellent, though because of our model spacing at the low-metallicity end we seem to be systematically $\sim$ 0.3 dex lower for ultra-low metallicity solutions. These solutions are much more in agreement with FIREFLY than the values derived from fitting in Koleva et al. (2008), where they seem to give much lower ages that from FIREFLY, an unexpected result for globular clusters. Overall, the comparisons show that FIREFLY is capable of correctly matching with CMD fitting of globular clusters in which there is a well-defined simple population of stars, though for the ages we cannot state this conclusion with significance due to the small range of globular cluster ages available to test against.

3.12 Comparisons with other spectral fitting codes

In this section we compare the methodology of FIREFLY to that of many other popular SED fitting codes that have been used in similar work on large datasets. We reserve a comparison of results to Chapter 4.

STARLIGHT

STARLIGHT by Cid Fernandes et al. (2005) is a χ^2-minimisation full spectral fitting code that, as with FIREFLY, uses a base of SSPs as its input. However rather than iteratively adding SSP contributions directly as FIREFLY, STARLIGHT explores the parameter space by finding an approximation to the minimum χ^2 solution, further fine-tunes the result, and then projects the base SSPs into coarser components. Since we save a large range of fits and weight them by their final likelihood, we effectively smooth out our star formation histories across all of the fits, and so instead of requiring this base projection in order to get a realistic and stable combined fit we effectively sum over all possible solutions.

The mock galaxies of Cid Fernandes et al. (2005) are tuned to match SDSS data and so go down to low S/N as ours do. They test recovery of light- and mass-weighted age and metallicity, total stellar mass, stellar velocity dispersion, and dust extinction, to which they find broadly good recovery but find it difficult to resolve the individual stellar population components, compared to our approach which works well down to a S/N of 5.

We compare with the results of STARLIGHT for different datasets in Chapters 4 and 5.

STECKMAP

STECMAP/STECKMAP by Ocvirk et al. (2006b) & Ocvirk et al. (2006a) is a matrix inversion code that again use SSPs as their base and also a penalty-based method of avoiding over-fitting in a similar way to our use of the BIC. Instead of an iterative method, STECKMAP retrieves likelihoods like FIREFLY, but instead of combining a range of fits it has a smoothness requirement in its solutions that it uses to achieve robustness. This method is also capable of achieving very precise recovery of sub-populations, however seems to struggle at SDSS-like signal-to-noise of 15 or less.

Ocvirk et al. (2006b) also perform a detailed analysis for single and double burst mock galaxies, although again at mostly higher values of S/N than in our analysis; however for most of their values of S/N they find excellent parameter recovery. Since their work is much more tuned for high S/N objects, equivalent comparisons between the codes are difficult to make.

VESPA

VESPA by Tojeiro et al. (2007) & Tojeiro et al. (2009) is an iterative χ^2-minimisation full spectral fitting code. It retrieves solutions through use of age bins that are relatively much larger than our single bursts. The age bins use a combination of continuous star formation rate models and broad exponentially-declining star formation rate models. They also test dual-burst models but find them to give inferior results in general. The resolution of bins used varies depending on the number of parameters required to fit below the noise level, and thus the results obtained strongly depend on signal-to-noise of the data. This process is used to avoid over-fitting in a similar way to FIREFLY's use of the BIC. Thus the main difference between our codes is that the result of convergence in FIREFLY is to return that linear combination of SSPs, and include that in many other fits (weighted by likelihood) summed together to build a star formation history, whereas VESPA will return a combination of flux contributions from its age bins.

Additionally they convolve a constant $\sigma = 170$ km s^{-1} stellar velocity dispersion with the Bruzual & Charlot (2003) models, compared to our approach of using GANDALF to fit for σ separately; see section 3.6.

Tojeiro et al. (2007) tested mock galaxy property recovery with VESPA using exponentially-declining star formation history models (τ models) with $\tau = 0.3$Gyr^{-1} to test the effect of

using two different wavelength ranges (1000 - 9500 and 3200 - 9500 Å), two different S/N cases (20 and 50), and a range of dust values. It is of note that for this value of τ, our parameter recovery in FIREFLY is similarly very good, even for low S/N of 5. We compare our results to those of VESPA for SDSS DR7 in Chapter 4.

PCA

The PCA method is a best-fit spectral code by Chen et al. (2012) decomposes their model spectra into orthogonal components with the aim of exploiting the differences between different model templates to break degeneracy. This has the advantage of making the code very fast and gives reliable error estimates, however because the principal components are often complex mixes of parameters it can be very difficult to interpret results with meaningful physical conclusions.

Chen et al. (2012) do not use mock galaxies, but instead use 67,000 SDSS repeat spectra to quantify their uncertainties, computing a covariance matrix of errors in each of their principal components. We compare with their results of the mass distribution of BOSS galaxies in Chapter 4.

3.13 Conclusions

We have presented FIREFLY, a full spectral fitting code designed recover galaxy properties recovery as a function of input model ingredients, whilst also mapping out property degeneracies from both the inherent degeneracies in galaxy spectra and errors in the data. Differently to other full spectral fitting codes available, FIREFLY outputs a probability distribution of star formation histories, in addition to the individual stellar population property distributions. Also unique among fitting codes is the innovative method for treating the effects of dust attenuation.

Using a comprehensive suite of mock galaxies and sample of globular clusters, we have mapped out the inherent uncertainty in age, metallicity and stellar mass. Mock galaxies were made from both the simple stellar populations themselves and composite stellar populations with a set of exponentially declining star formation histories. Using globular clusters allowed us to probe the spectra of near-coeval populations of stars and explore the effect of wavelength range on the derived stellar population properties. We have analysed the effect of input stellar library used at each stage. We used Monte Carlo simulations to measure how offsets and errors

in age, metallicity and mass vary as a function of signal-to-noise, and input model parameters. We have shown that using more realistic mock galaxies with composite stellar populations do not affect these conclusions. Lastly, we have shown that a single run of FIREFLY is able to enclose correct solutions when fitting realistic model galaxies and gives reasonable errors on stellar population properties.

In the next Chapter, we run FIREFLY on two SDSS datasets, assessing the differences in the picture of galaxy evolution derived as a function of sample and model library, including effects that propagate into relations such as the mass-metallicity relation and the redshift evolution of galaxy properties.

Chapter 4

Application of Spectral Fitting to Large Galaxy Surveys

Having tested FIREFLY on many sets of mock galaxies and globular clusters, we have confidence that we can apply the code to large galaxy surveys to produce a database of detailed star formation histories and other galaxy properties. In this chapter, we run FIREFLY on two large optical galaxy surveys, SDSS DR7 (Abazajian et al., 2009), which aims for a wide range of galaxy types at $0 < z < 0.2$, and SDSS DR9-BOSS (Ahn et al., 2012), which aims for massive, passive galaxies at $0.4 < z < 0.7$. We analyse the fossil record of these passive galaxies to shed light on their mass assembly.

We produce maps of the constituent stellar population properties for each of these surveys for a range of models. Within each of these surveys, we discuss how the sample cuts in colours described in the literature affect the derived galaxy properties, and suggest methods for linking the two surveys in order to provide a consistent picture of redshift evolution. We note that, as mentioned in Chapter 3, we present the fitting results from using models with a Kroupa (2001) IMF.

4.1 The Sloan Digital Sky Survey

The Sloan Digital Sky Survey (SDSS) (York et al., 2000) is a multi-phase imaging and spectroscopic survey whose instrument is the 2.5 m Sloan telescope (Gunn et al., 2006) at Apache Point Observatory, New Mexico.

The first eight years of the survey (SDSS I/II) observed 230,000 stars in the Milky Way halo and disk (Yanny et al., 2009), measured 500 supernovae Ia lightcurves (Frieman et al. (2008), Sako et al. (2008)), imaged over 8,000 square degrees of the sky with over 1 million galaxy spectra and 140,000 quasar spectra (Abazajian et al., 2009). In section 4.3 we discuss results from using the galaxy spectra survey part of SDSS, known as ' the Data Release 7 legacy survey', or in this thesis 'DR7' for concision, with FIREFLY.

Building on the success of SDSS I and II, SDSS III observed a further 120,000 stars in the Milky Way, particularly focusing on the halo, conducted infra-red spectroscopy of 100,000 red giant stars in the Milky Way (Zasowski et al., 2013), measured 11,000 stellar radial profiles in order to detect exoplanets, and conducted optical and near-infra-red spectroscopy of a further 1.5 million galaxies, mostly aiming for more red and passive galaxies, and 150,000 quasars. In section 4.4 we discuss FIREFLY's results from fitting the galaxy survey part of SDSS-III, known as the 'Baryon Oscillation Spectroscopic Survey' (BOSS).

The current phase of SDSS is SDSS-IV, which is undertaking observations with three new surveys. One is a follow-up to the stellar IR spectroscopy survey, another is a successor to the galaxy surveys, but focussing on distant emission-bright galaxies and quasars. Lastly, an integral field unit survey, MaNGA (Bundy et al., 2015), is mapping out spectra of nearby galaxies. The results of the prototype of the MaNGA survey are discussed in Chapter 5.

In this chapter, we analyse results from the completed established galaxy surveys from SDSS I/II and SDSS III.

4.1.1 Data Release 7

The final release of SDSS-I/II, Data Release 7 (DR7) (Abazajian et al., 2009), was a galaxy survey that took photometric and spectroscopic observations. Equipped with two multi-object spectrographs, it produced spectra of more than 0.93 million galaxies in its 'Legacy' survey across a very large area of sky across a large wavelength range, covering 9380 square degrees at 3800 – 9200 Å at a spectral resolution of 3 Å, across a redshift range of $0.0 \leq z \leq 0.5$, see Figure 4.1.

The DR7 database consists of a main galaxy sample, which includes in its target selection a wide range of galaxy types, and a luminous red galaxy (LRG) subsample (Eisenstein et al., 2001), selected to give a fainter, more passive sample of galaxies than the main galaxy sample. We analyse the full set of both samples in this Chapter.

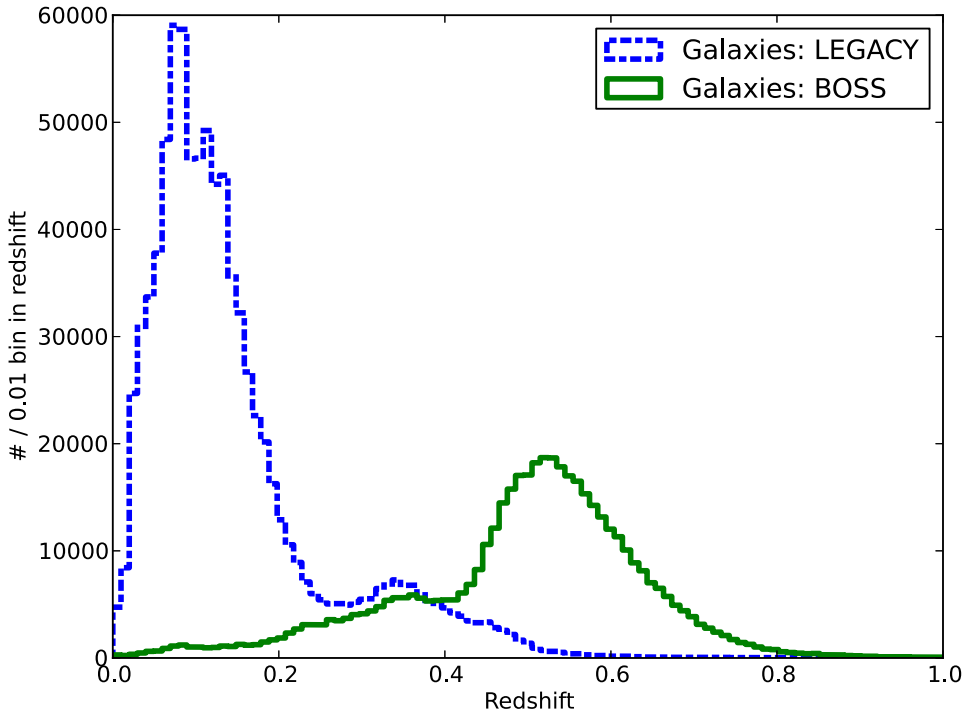

Fig. 4.1 Redshift distributions of the two SDSS galaxy surveys analysed in this chapter: SDSS I/II DR7 ('Legacy'), section 4.1.1, and SDSS III DR9 BOSS, section 4.1.2. This figure is a reprint of Figure 3 from Ahn et al. (2012).

4.1.2 Data Release 9 (BOSS)

The SDSS-III recently finished its observations in July 2014, producing Data Release 12 (DR12). It has the same observational setup as DR7 but with updated spectrographs (Smee et al., 2013), and a larger wavelength coverage of 3600 – 10400 Å, covering 3275 square degrees. To compare with the literature in our analysis we focus on analysing an earlier iteration of this survey known as Data Release 9 (DR9) (Ahn et al., 2012). This includes 0.91 million spectra from the Baryon Oscillation Spectroscopic Survey (BOSS), designed to observe a well-defined passive sample of galaxies, generally at high redshifts ($z \sim 0.7$), see Figure 4.1. As well as analysing the sample as a whole, we also analyse two subsamples of BOSS: a low-redshift sample ($z \lesssim 0.4$, known as LOWZ), which is a close analogue to the LRG subsample of DR7, and a high redshift subsample ($z \gtrsim 0.4$), named CMASS as it was studied to define a sample of galaxies with approximately similar stellar masses. Unless otherwise specified, comparisons with the literature use results from the whole sample.

4.1.3 Data Pre-processing

When analysing DR7 and BOSS SEDs, some important considerations need to be made to ensure good recovery of galaxy physical parameters. In FIREFLY, these considerations become features in the code that can make the analysis more versatile and robust. We list these considerations and features here.

We always use the velocity dispersion output by GANDALF to downgrade the resolution of our models as described in chapter 3. This routine also provides us with emission-cleaned spectra that we use to fit each of the galaxies used in this chapter. As also described in Chapter 3, we pre-process the data SEDs for Milky Way extinction by assuming a Fitzpatrick (1999) reddening law, and dereddening the data as a function of the wavelength range used.

All SDSS datasets include quality flags (known as the 'goodpixel array') on each datapoint that signify if it is untrustworthy. For example, pixels can show extreme residuals or very low signal to noise that can arise from artefacts in the data, or high amounts of sky flux. These points are removed from the analysis and shown in the spectral fits as if that part of the wavelength space had no data. Additionally, skylines from atmospheric scattering occur at 5577, 6200, and 6363 Å (in the observed frame) - these points are similarly removed with 5 Å masks to ensure they are not part of the spectral fits in their corresponding galaxy rest frame.

Occasionally, these flags can miss poorly processed fluxes, which would bias our fitting by weighting the chi-squared values obtained towards them. To prevent this, we use sigma-clipping of points at every measurement of chi-squared as used in many popular codes such as PPXF, Cappellari & Emsellem (2004).

4.2 Calculating the mass of SDSS galaxies

FIREFLY, as described in Chapter 3, outputs a set of luminosity-weighted contributions of SSPs. We also described how we can retrieve the total stellar mass of each of the galaxies by converting these luminosity-weighted contributions to mass-weighted contributions. The SDSS data fluxes are measured in [10^{-17} erg/s/Å/cm^2], meaning that the total stellar mass of an SDSS object is given by

$$\mathrm{M}^{tot}_{stellar} = \Sigma_i \mathrm{M}_{SSPi} = 4\pi D_L^2 \sum_i (w_i^L \frac{\Sigma_\lambda \phi[Data]}{\Sigma_\lambda L[SSPi]}), \tag{4.1}$$

as described in Chapter 3. Hence the total stellar mass within the fiber in which we are observing the spectra is simply given by the sum of all the SSP weightings. Note that this is for the fiber only, and not the whole galaxy. In this Chapter, we quote the above total fiber mass, apart from when combining surveys, in Section 4.5. To get an approximation for the whole galaxy we would need to compare the flux within the fiber to the flux within the whole imaging plate (and therefore we would need to assume that the stellar populations remain roughly the same when going out to radii beyond that of the fiber). This is typically done using the total imaging and fiber fluxes available in each *ugriz* band in the SDSS catalog. In our work we have matched the work of Chen et al. (2012) and used the'i'-band fluxes:

$$\mathrm{M}^{galaxy}_{stellar} \approx \mathrm{M}^{stellar}_{imaging} \approx \mathrm{M}^{stellar}_{tot} \times \frac{\phi^{i-band}_{imaging}}{\phi^{i-band}_{fiber}}. \tag{4.2}$$

4.3 Results from SDSS DR7

In this section we show the application of FIREFLY to SDSS DR7 and construct the star formation history of full DR7 dataset by summing the contributions from all the likelihood-weighted fits for each stellar population model. An example fit to a typical DR7 galaxy is

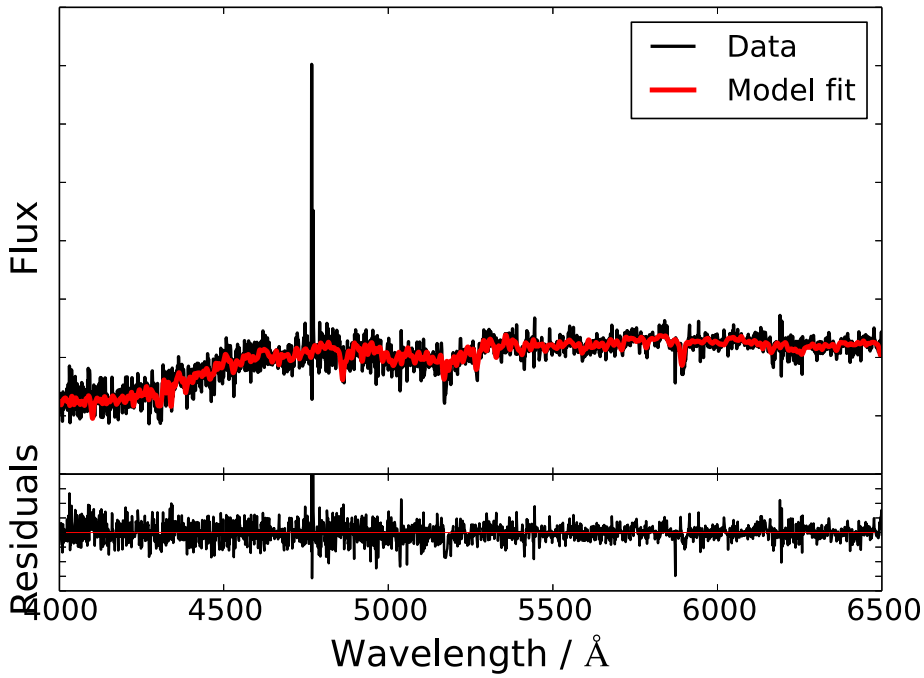

Fig. 4.2 Example fit (red) of a typical SDSS DR7 galaxy SED (black). Models used are MILES-based M11 models with a Kroupa IMF.

shown in Figure 4.2. We use the full range of age, metallicity and wavelength coverage available from each of the MILES-, STELIB- and ELODIE-based M11 models since we want to assess the ability of each of the models to recover galaxy properties to their fullest extent. The results of the complete star formation history are shown in figure 4.3. We note that we have computed a full set of stellar population properties including mass and light-weighted average ages and metallicities, dust, mass, and chi-squared as a function of stellar library, but the plots shown are representative of the full set of possible plots.

We provide mass and light-weighted stellar population properties since, as we described in Chapter 3, they are more sensitive to different stellar populations.

For all three models we see that the star formation histories of DR7 galaxies are dominanted in light-weighted SSP contributions by 1 – 12 Gyrs, half-solar metallicity solutions, with spread mainly in metallicity either side of this. In terms of the stellar mass assembly, most of the mass of DR7 galaxies are found to have formed at 10 – 12 Gyrs, at solar to half-solar metallicity. There is then a spread of solutions corresponding roughly to an exponential profile of star formation rate with decay time 4 – 5 Gyrs.

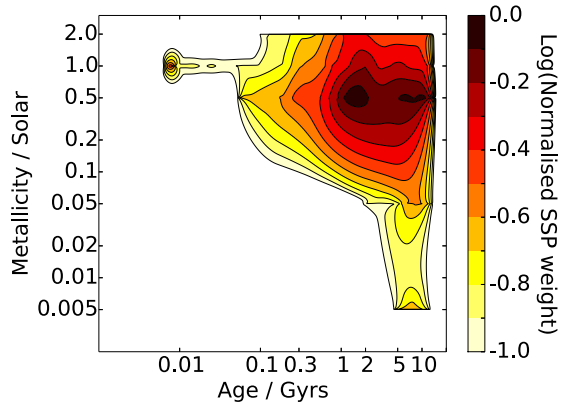

(a) Light-weighted MILES-based solutions.

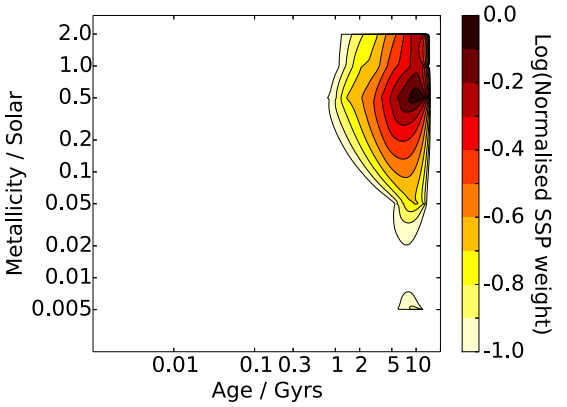

(b) Mass-weighted MILES-based solutions.

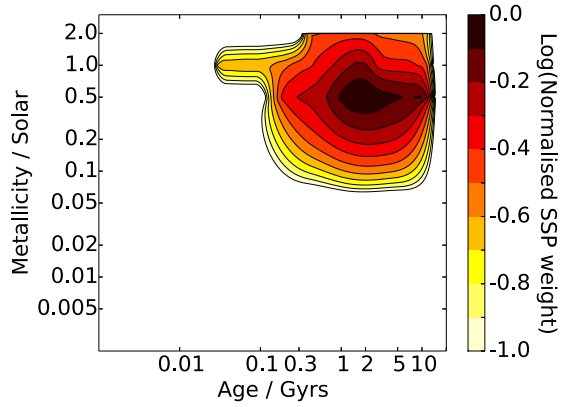

(c) Light-weighted STELIB-based solutions.

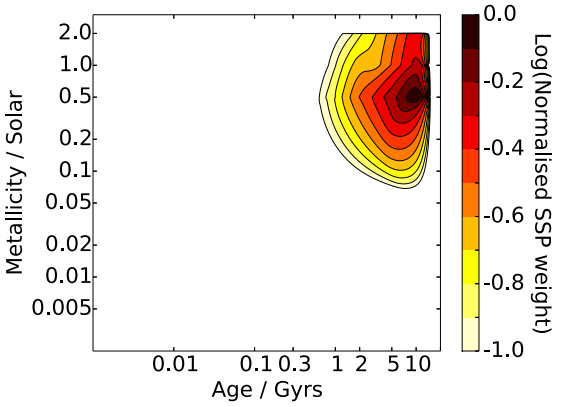

(d) Mass-weighted STELIB-based solutions.

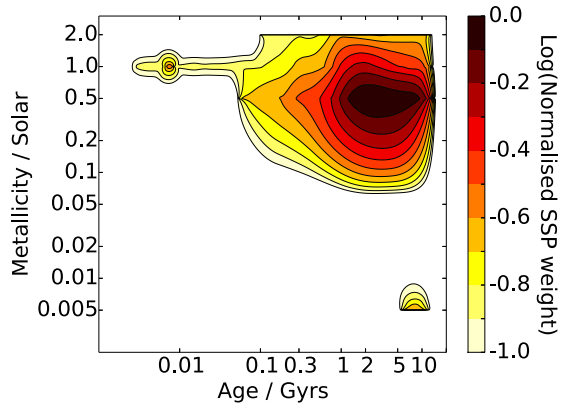

(e) Light-weighted ELODIE-based solutions.

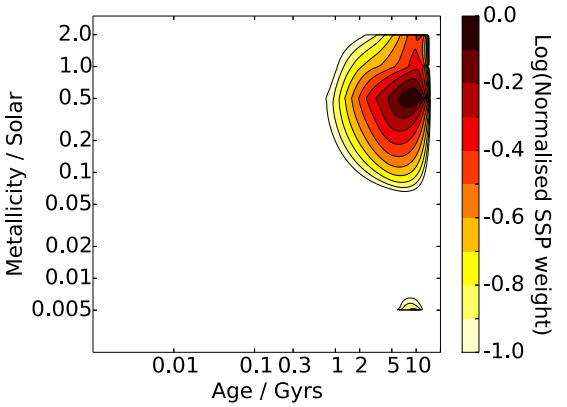

(f) Mass-weighted ELODIE-based solutions.

Fig. 4.3 The likelihood-weighted sum of all SSP contributions from all galaxies in the SDSS DR7 survey, as a function of empirical stellar library model ingredient, by light (i.e. flux) (LHS) or by stellar mass (RHS). Each contour represents the fractional weight of stellar population solutions in that part of age-metallicity space.

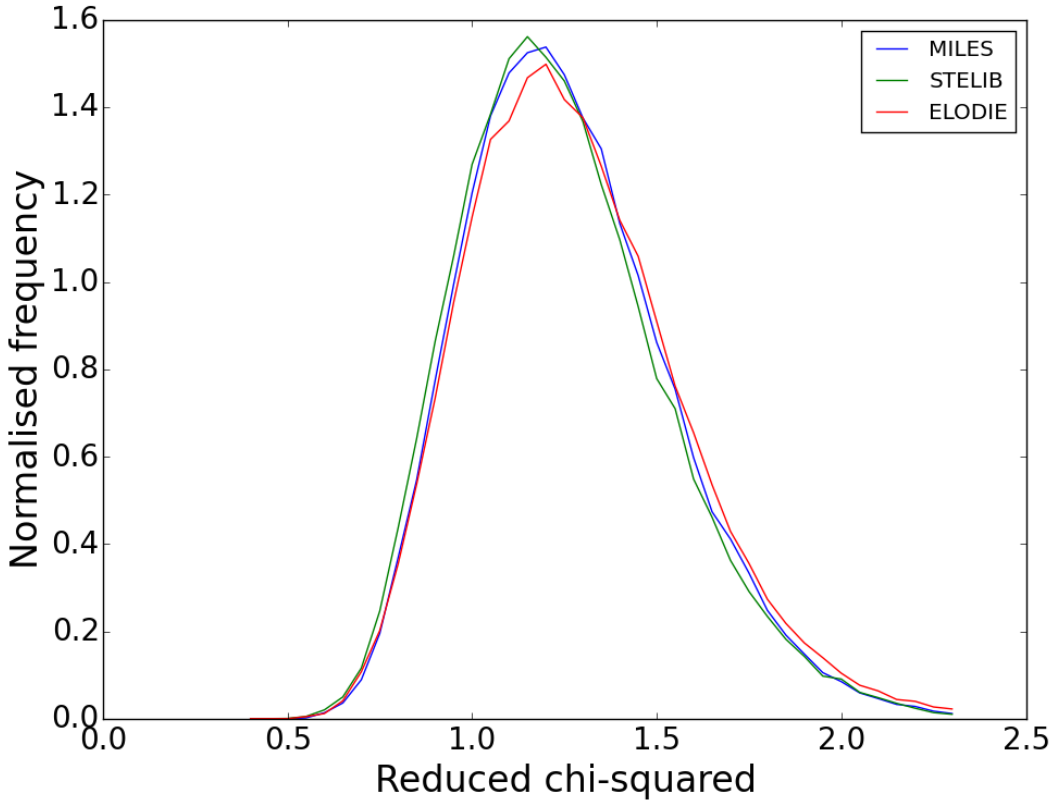

Fig. 4.4 MILES-based models.

Fig. 4.5 Reduced chi-squared distribution of fitting all DR7 galaxies with MILES-, STELIB- and ELODIE-based models, which have corresponding mean averages of 1.13, 1.10, and 1.19 respectively.

In general, the 3 different models are very consistent except for some minor differences. MILES-based models, for example, show some bimodality in the high age main solutions. STELIB-based models lacks the ultra-low metallicity and the young age parameter range, so cannot find solutions here. Instead, the solutions show a wider spread of the remaining ages, compared to the other models being more compressed towards older ages in these regions. MILES- and STELIB-based models show the greatest number of solutions with high metallicity, both at high $\sim$ 10 Gyrs and $\sim$ 2 Gyrs. ELODIE-based models show relatively little high metallicity contributions. In terms of mass-weighted contributions, these metallicity differences are somewhat less apparent. MILES also shows a tendency towards higher ages in the mass-weighted plots. Hence, we conclude that the most dominant effect of stellar library on DR7 properties are the metallicities recovered.

We plot the chi-squared distributions of the three libraries in Figure 4.5, which shows the distributions to be very similar with average reduced chi-squared values of 1.13, 1.10, and 1.19 for MILES-, STELIB- and ELODIE-based models respectively. The differences are driven by a small number of galaxies (with no clear pattern for what characterises these galaxies) fitting somewhat more poorly for ELODIE-based models compared to the others, and STELIB-based models having slightly more galaxies with reduced chi-squared of ~ 1.

4.3.1 Separating Red and Blue Galaxies

As is well discussed in the literature (e.g. Kauffmann et al. (2003a)) galaxies are found to group into two main groups; a red, passive so-called 'galaxy red sequence' and a blue, star-forming 'cloud'. With this in mind, SDSS DR7 has a set of cuts that select for a subsample of redder, generally more massive galaxies, called the LRG subsample (known in the SDSS database as the 'LRG class'). Figures 4.6 show the results of FIREFLY for two subsamples of the SDSS DR7 dataset for redshifts below 0.4. We classify an object in this dataset as a luminous red galaxy (LRG) if the following criteria on the *ugriz* magnitudes, selected from "cut I" of Eisenstein et al. (2011) and updated for DR7, are met. We state these explicitly here since we have not included star-galaxy cuts since these are made in the SDSS pipeline already.

$$r_{Petro} < 13.116 + c_{\parallel}/0.3, \tag{4.3}$$

$$r_{Petro} < 19.2, \tag{4.4}$$

$$| c_{\perp} | < 0.2, \tag{4.5}$$

where $c_{\perp} = (r-i) - (g-r)/4 - 0.177$, and $c_{\parallel} = 0.7(g-r) + 1.2[(r-i) - 0.177]$. All three conditions must be met for classification as an LRG, and condition 4.5 must be met for inclusion in our sample as a $z < 0.4$ galaxy. If condition 4.5 is met but not either 4.3 (luminosity threshold as a function of redshift) or 4.4 (flux cut), or both, the object in question is classified as 'non-LRG' for this analysis. Note we do not need a colour constraint on star-galaxy classification or on scattered light as we use the galaxy classifications provided by the DR7 database. The LRG sample provides good comparison with the SDSS III BOSS LOWZ subsmaple, which will be investigated later in this chapter. We choose to plot the light-weighted SSP contributions since these show greater spread in age and metallicity, allowing for easier

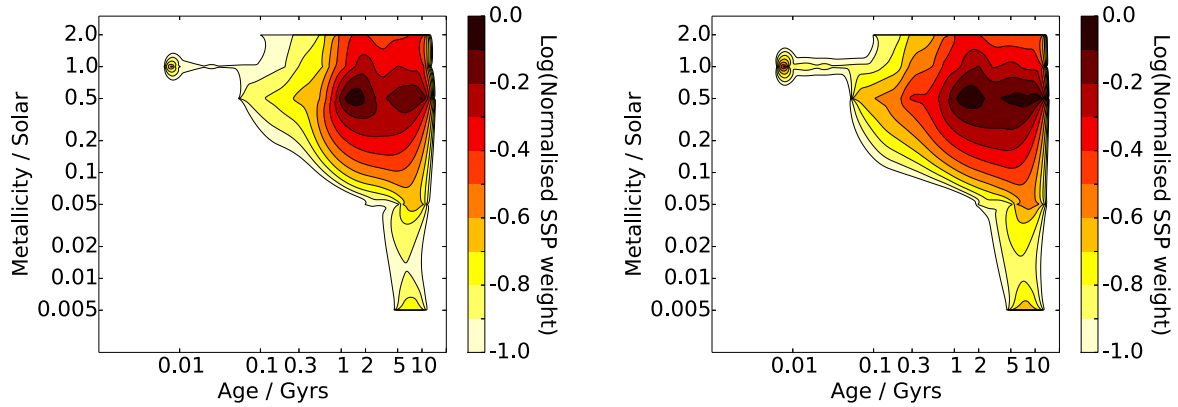

(a) Light-weighted MILES-based solutions for DR7 LRGs.

(b) Light-weighted MILES-based solutions for DR7 non-LRGs.

Fig. 4.6 As LHS of Figure 4.3, but split by classification as an LRG, or a non-LRG as defined in Section 4.3.1.

comparison between input library.

We find that the stellar library used in the model does not affect the main conclusion from making the cut, so we show only the MILES-based model results here, since they show the same information as the other models. We find that overall there is only a small effect from making the LRG cut, which is most noticeable in the middle of the range of contour values (red colours). We see that the LRG results show fewer solutions lower than 0.5 Gyr in age compared to the non-LRG galaxies, despite the non-LRGs still showing a dominant high age component. This suggests that the LRGs have somewhat shorter star formation timescales; the LRGs truncate their star formation after $\sim$ 5 Gyrs compared to the $\sim$ 7 Gyrs or more timescale of the non-LRGs. This suggests that the LRG cut is somewhat successful in selecting for more passive galaxies compared to the overall population, but some of these galaxies can still have fairly long star formation timescales, for example resembling those of massive spirals.

4.3.2 Comparisons with the literature

We compare the results of FIREFLY applied to SDSS DR7 galaxies with the results of two popular full spectral fitting codes, the methodologies of which are described in Chapter 3. These codes have publically accessible and published databases of fitting results from DR7. We note that these databases use different sets of stellar population models, so there is a degeneracy between the comparisons made between both codes and models. Nonetheless, these are useful comparisons to make.

Firstly, we compare our results to VESPA using their DR7 database (Tojeiro et al., 2009), available at http://www-wfau.roe.ac.uk/vespa/. In Figure 4.7 we show the results of summing the stellar populations found in all DR7 galaxies for the stellar population models of Maraston (2005) (M05) in VESPA with the results of FIREFLY for M11, both models of which use the same prescriptions for stellar evolution. Since they use MILES-based models with mass-weighted stellar population properties, we use the same fitting parameters in FIREFLY here. We note that M11 has greater wavelength resolution compared to M05, potentially leading to resolving greater details in galaxies' star formation histories. In addition, we note that VESPA is written to give solutions with lower resolution in parameter space than FIREFLY.

The plots clearly show the different priors made in the fitting codes. That is, since FIREFLY allows for more contributions from individual SSPs compared to VESPA's more strict allowance of introducing more complex star formation histories, we find that there is considerable extension towards lower ages in the plots produced from FIREFLY. Additionally, FIREFLY finds a small region of parameter space with high metallicity that is relatively unpronounced in VESPA's results due to the lower age resolution. Nonetheless, qualitatively the results agree on a near-solar high metallicity stellar component being dominant for the DR7 sample.

Secondly, we compare our results with the full DR7 database of STARLIGHT (Cid Fernandes et al., 2005), available at http://casjobs.starlight.ufsc.br/casjobs/. Unlike VESPA's database, a full breakdown of stellar population components is not available; instead they provide mass- and light-weighted average properties for all DR7 galaxies obtained using STELIB-based BC03 models. In Figure 4.8 we make a comparison to their age and metallicity results using STELIB-based M11 models, using light-weighted properties for the higher range of values enabling a more distinctive comparison. We plot density contours of the $\sim$ 1 million points from directly plotting STARLIGHT results against FIREFLY results.

In these plots, the main density of age and metallicity points are nearly identical between STARLIGHT and FIREFLY, being around 0.8 Gyr in age and 0.1 dex in [Z/H]. Hence for the total sample, the codes agree very well. Some differences are visible however. Firstly, in the age plot, the extension down to lower ages is flatter in FIREFLY compared to STARLIGHT, suggesting that STARLIGHT is more sensitive to star formation in the star forming galaxies in the sample. Alternatively, this could be due to the high mass components in more star forming galaxies being difficult to constrain since large age SSPs only weakly affect the total flux when there are younger ages present. Secondly, in the metallicity plot, we see a flatter profile out to low metallicity.

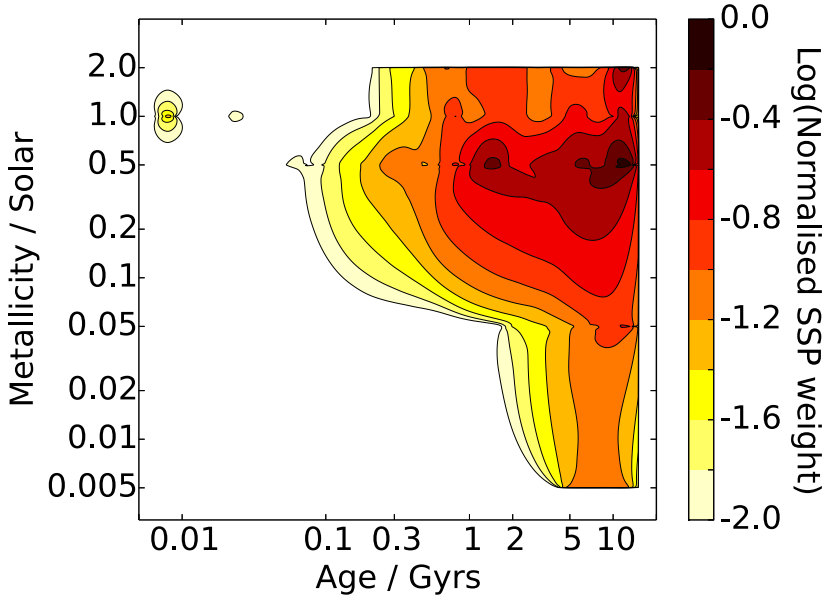

(a) FIREFLY, M11

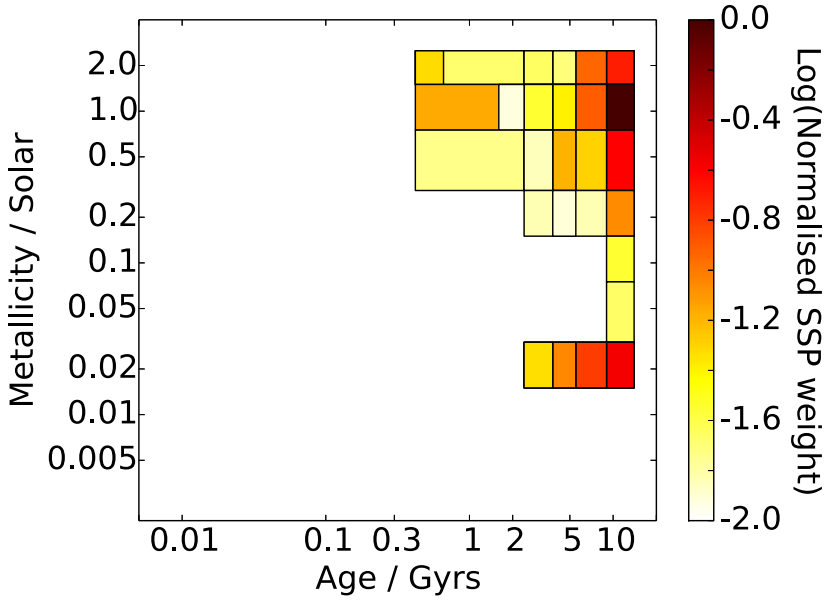

(b) VESPA, M05

Fig. 4.7 Comparison of the total stellar population mass contributions for the all DR7 galaxies between FIREFLY with M11 models (top panel) and VESPA with M05 models (bottom panel). The VESPA plot has age-metallicity bins as defined in Tojeiro et al. (2009), with the colours representing the total weighted mass in that bin, compared to FIREFLY's weights based on the total mass of SSPs in that region of the plot. Both plots are based on fitting with MILES-based models with a Kroupa IMF.

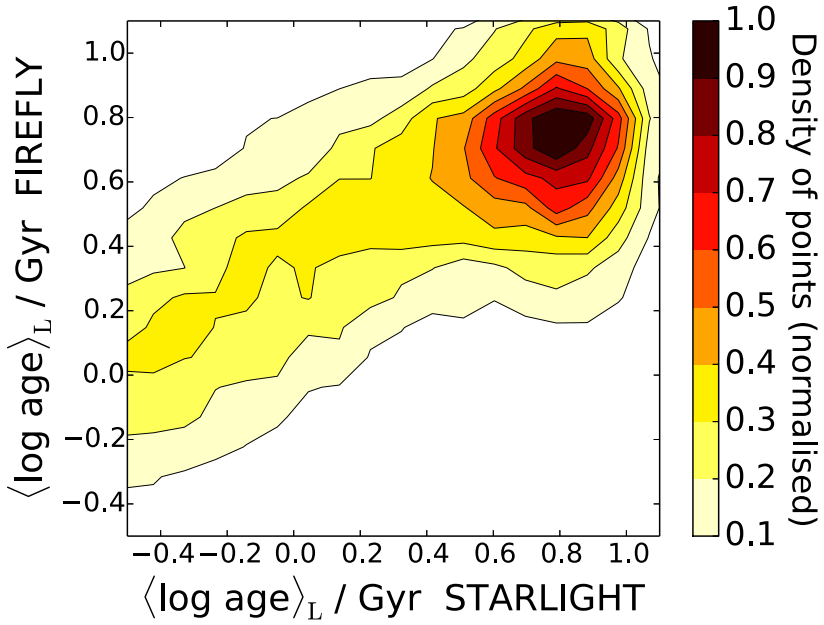

(a) STARLIGHT's light-weighted ages derived from DR7 compared with FIREFLY. Contours represent the density of points.

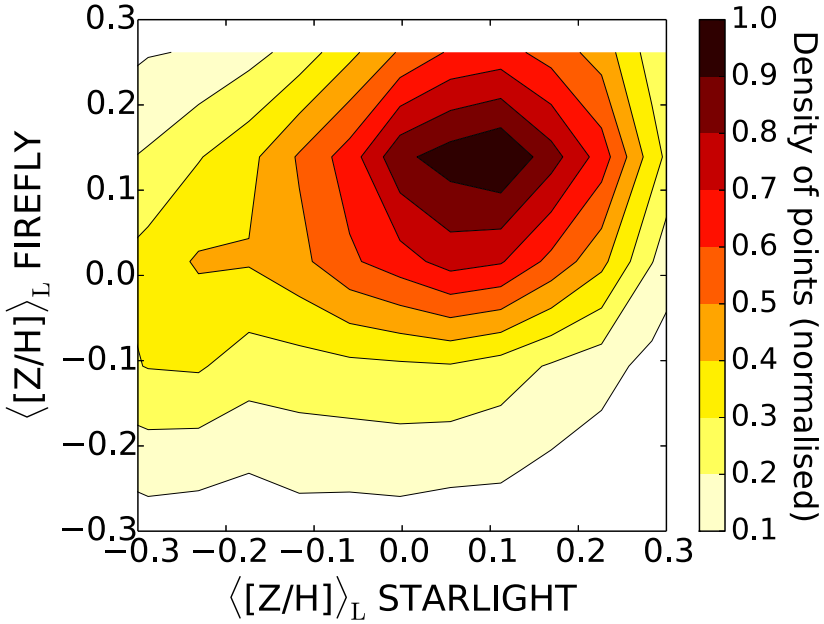

(b) STARLIGHT's light-weighted metallicities derived from DR7 compared with FIREFLY. Contours represent the density of points.

Fig. 4.8 Comparison of the light-weighted average ages and metallicities obtained with STARLIGHT and FIREFLY. STARLIGHT's results are obtained using BC03 models, and FIREFLY's are obtained with M11 models, but both models are based on the STELIB library.

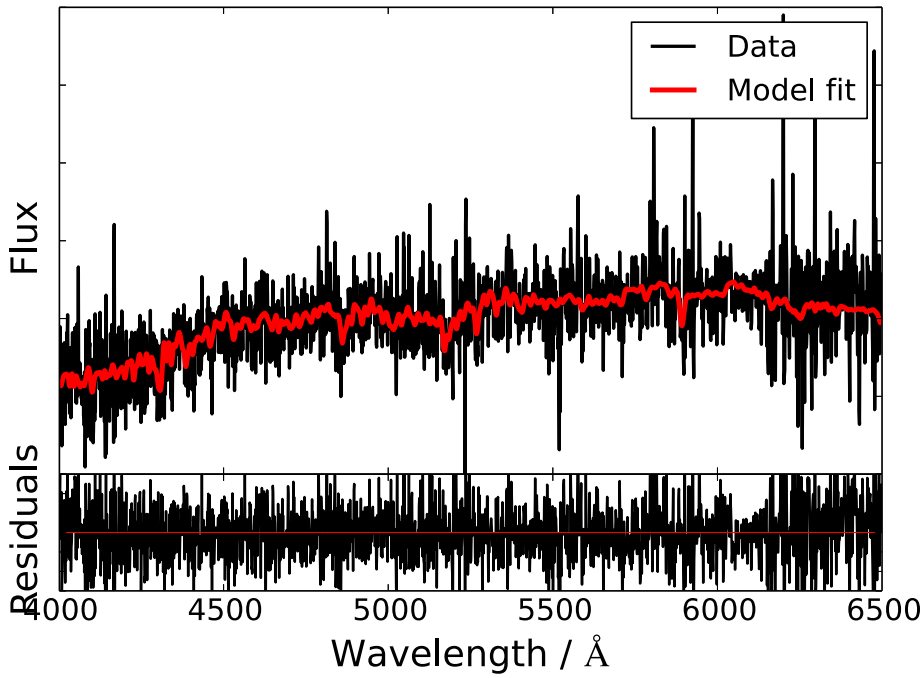

Fig. 4.9 Example fit (red) of a typical SDSS DR9-BOSS galaxy SED (black). Models used are MILES-based M11 models with a Kroupa IMF.

Despite some differences in the details of the minor stellar population components, we conclude that we have good qualitative agreement with the literature on full spectral fitting of DR7 galaxies even when different stellar population models are used.

4.4 Results from SDSS DR9-BOSS

In this section, we show the full star formation history of SDSS DR9 BOSS, presenting the results in the same way as the previous section. An example fit of a typical BOSS galaxy is shown in Figure 4.9, which shows a clear difference in signal-to-noise compared to DR7. The results of the whole sample are shown in figure 4.10 as a function of models based on different input stellar library. As before, we note that we have produced a large database of the different sets of properties obtained but again, the plots shown here are representative of the full set of possible plots.

From the light-weight plots we see that the sum BOSS star formation history is more metal-rich than the DR7 star formation history, and has a high-age (6 Gyr) twice-solar component that is dominant from fitting using all three models. There is then a spread towards somewhat

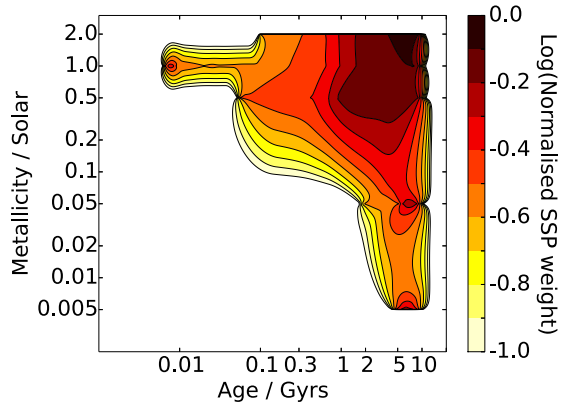

(a) Light-weighted MILES-based solutions.

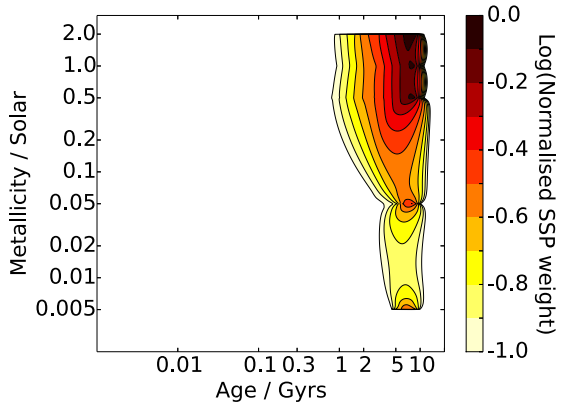

(b) Mass-weighted MILES-based solutions.

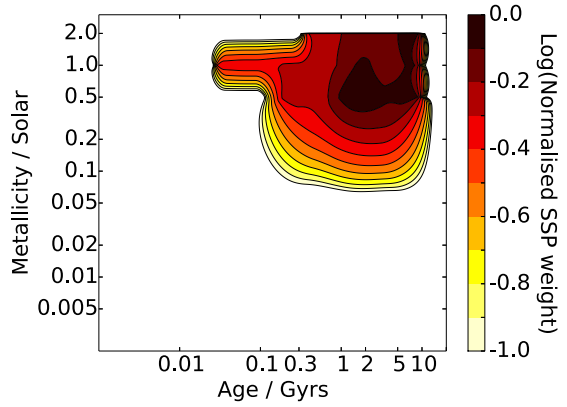

(c) Light-weighted STELIB-based solutions.

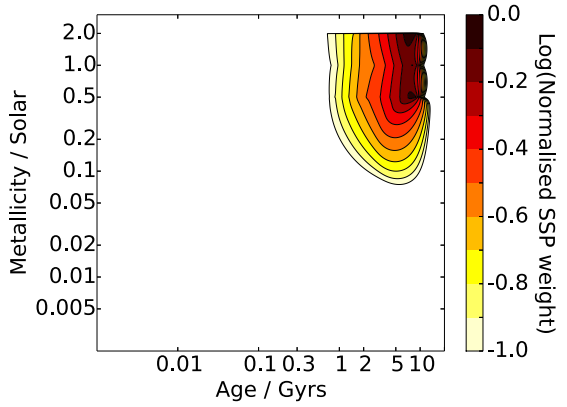

(d) Mass-weighted STELIB-based solutions.

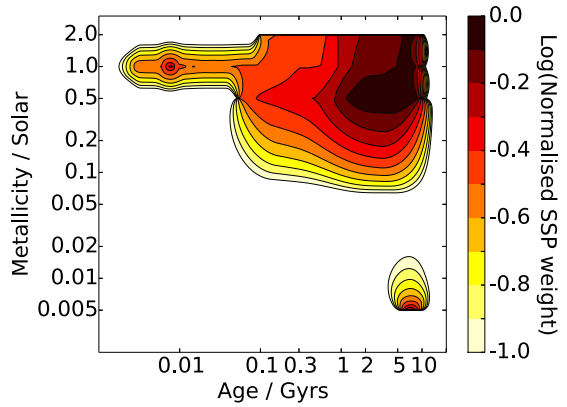

(e) Light-weighted ELODIE-based solutions.

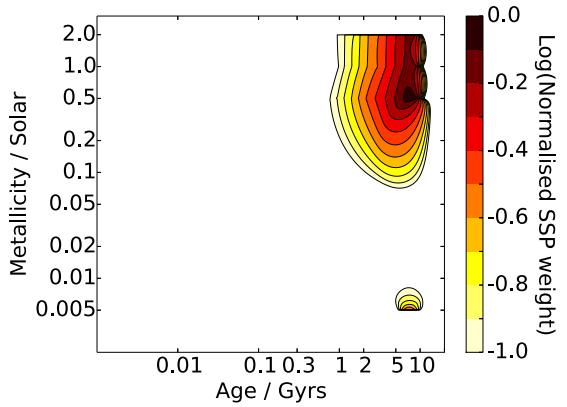

(f) Mass-weighted ELODIE-based solutions.

Fig. 4.10 The likelihood-weighted sum of all SSP contributions from all galaxies in the SDSS DR9-BOSS survey, as a function of empirical stellar library model ingredient, by light (i.e. flux) (LHS) or by stellar mass (RHS). Each contour represents the fractional weight of stellar population solutions in that part of age-metallicity space.

younger (2 - 3 Gyr) ages with solar metallicities. The mass-weighted plots show that BOSS galaxies are well represented by an old age population with a short to moderate star formation timescale proceeding that, about 3 Gyr depending on model, in agreement with Maraston et al. (2009). This timescale is shorter than that of DR7, meaning that we find that BOSS selects more passive galaxies than DR7, again in agreement with the literature.

Model differences are more pronounced in these BOSS plots compared to the DR7 plots, suggesting the models are more uncertain for these high-metallicity high-age stellar populations, or that the metallicity bins need to be more finely sampled above solar metallicities. In particular, MILES-based models prefer a much more dominant component of $\sim$ 5-7 Gyr (about the age of the Universe at these redshifts), twice solar stellar population, and in addition much more very low metallicity components, whereas in the other two models there is also a similarly weighted component at lower metallicities and lower ages. STELIB, as before, shows extension to younger ages $\sim$ 0.5 Gyr since it lacks the very low ages and metallicities that are present in other models. Chi-squared distributions are very similar to the DR7 distributions, again being very similar between the models, but have lower overall values for the BOSS sample, about 0.8 on average, so we do not plot them here. This could suggest that the the spectral errors in BOSS are overestimated compared to DR7's error estimations.

4.4.1 BOSS subsamples: CMASS and LOWZ

The database of DR9-BOSS galaxies has two different subsamples of galaxies that fulfill different survey requirements. Firstly, the LOWZ subsample, defined in Ahn et al. (2012), is made to augment the LRG cut I in DR7 with fainter, but equally passive, galaxies. Hence, we should expect good matching between these two subsamples. Secondly, the CMASS sample is selected to give a well defined near-complete sample of massive galaxies at $0.4 < z < 0.8$. Since for these plots we use both of these cuts directly as implemented in Ahn et al. (2012), we refer the reader for details there.

We use the subsamples of galaxies defined using exactly these cuts, and present their light-weighted star formation histories in Figure 4.11. As before for the DR7 cuts, the stellar libraries behave very similarly, so for brevity we show only the results from the MILES-based models.

We see that as expected the star formation history of BOSS LOWZ is similar to that of the DR7 LRGs, see Figure 4.6, except for some extension to higher metallicities. This could be

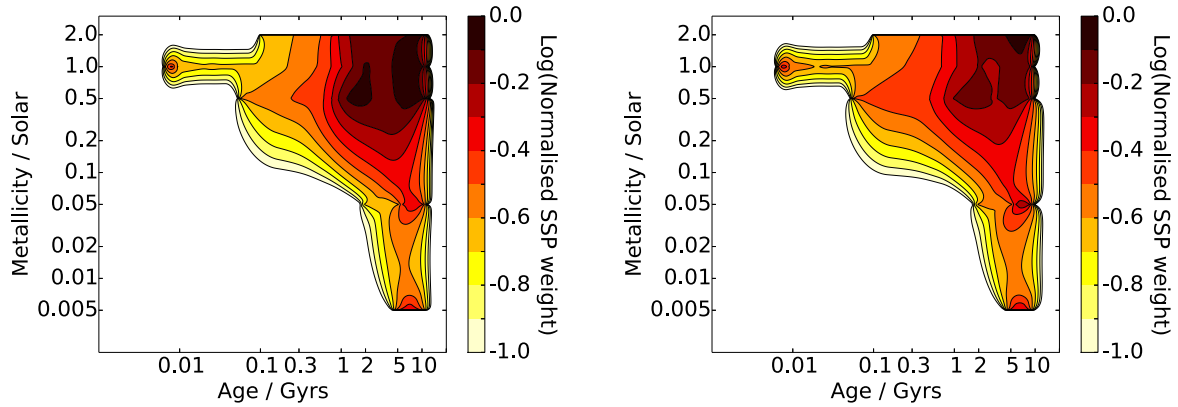

(a) Light-weighted MILES-based solutions for BOSS LOWZ galaxies.

(b) Light-weighted MILES-based solutions for BOSS CMASS galaxies.

Fig. 4.11 As LHS of Figure 4.10, but split by subsample as LOWZ, or CMASS, respectively, as defined in Ahn et al. (2012).

due to the different redshift distributions of these subsamples, so in Section 4.5 we control for this. The CMASS contours are noticeably more dominant in high age, high metallicity solutions, though not much different from the BOSS sample as a whole. This is due to the fact that the CMASS cut is not intended to be restrictive in colour to passive galaxies, containing about 73% passive galaxies (Masters et al., 2011), and so seems to be somewhat similar to the sample as a whole. The stellar mass distribution of CMASS will now discussed in the next section with comparisons with the literature.

4.4.2 Comparisons with the literature

Since BOSS aims for the most massive galaxies (> 11.5 $M^*_\odot$), and the CMASS sample is near-complete for high masses (Maraston et al., 2013), we have good motivation to compare our stellar mass results with that of the literature. With the release of BOSS data, there are two main stellar mass estimates: those from fitting after using Principal Component Analysis (PCA) on the spectra (Chen et al., 2012), and those from broad-band SED fitting. We plot both of these mass functions in comparisons with ours in Figure 4.12.

We see that FIREFLY's results lie between the two literature mass distributions, being approximately 0.05 dex higher than the photometric measurements and 0.15 dex lower than the PCA measurements. The 0.2 dex difference between PCA and broadband measurements could be due to the priors required in specifying a particular star formation history in the broadband fitting (Pforr, Maraston & Tonini, 2012), but the exact cause of the offset is currently unclear.

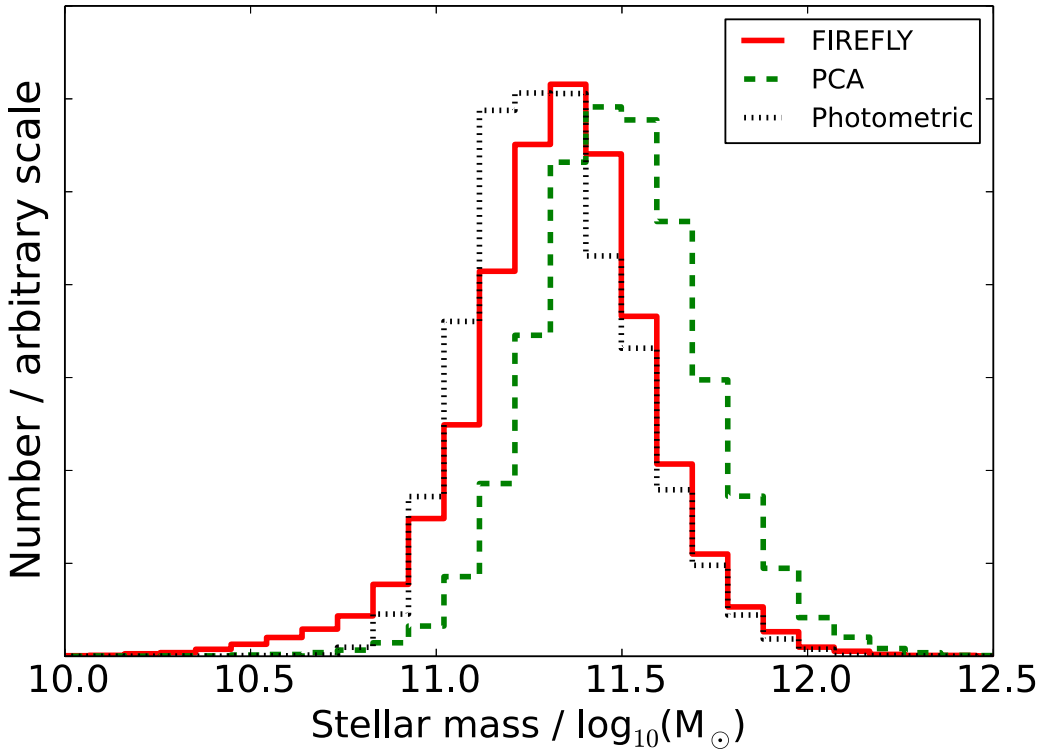

Fig. 4.12 The stellar mass distribution of the BOSS CMASS subsample, as measured through FIREFLY, PCA from (Chen et al., 2012), and broadband (photometric) SED fitting from Maraston et al. (2013). All models use a Kroupa IMF.

Using PCA on the spectra may cause offsets in the stellar masses measured PCA compared to FIREFLY, for example some principal components could be less or more sensitive to high age populations with high mass-to-light ratios. Specifically, FIREFLY's approach of summing SSPs may give a more nuanced composition of high-age populations, rather than an individual principal component which will necessarily be a grouping of proximate SSPs, such as at high age. Small offsets in these high-age components can give rise to moderately high shifts in stellar mass, giving a potential explanation of this offset. In future work, we intend to test the effect of adding priors to the range of solutions used in FIREFLY, in addition to using the code directly on broadband SEDs, to investigate this further.

4.5 Redshift Evolution of Luminous Red Galaxies

Given the variety of subsamples available in the two surveys, one can attempt to link the two surveys in order to widen the redshift range and sample size analysed. This may be difficult to accomplish because the surveys have different typical signal-to-noise and slightly different wavelength ranges. We can test the extent to which we can link them by taking an approximately equivalent subsample across each of surveys. In this section we always use MILES-based models with Kroupa IMF to produce the plots, but all conclusions hold for each of the stellar libraries and IMFs used in this thesis. Additionally we use light-weighted properties to calibrate the cuts used since these show greater property range in the contours, but all conclusions hold when using mass-weighted properties. In this section we use the term 'low redshift' to mean $z < 0.44$ and 'high-redshift' as $z > 0.44$, and we make cuts separately for these two redshift ranges to match the recommended cuts from Eisenstein et al. (2001) for a good LRG sample across a large redshift range.

To compare the low-redshift cuts, we take the LRG subsample from DR7 and the LOWZ subsample of BOSS, which in any case are very similar. However, we do not select by 'c-perp' as in Ahn et al. (2012) since this is equivalent to the redshift cut we are already making. To take an approximately proportionate amount of galaxy redshifts, we select only those galaxies with $0.25 < z < 0.35$. The number of galaxies in this range is shown in Figure 4.1 to be nearly identical for the DR7 and BOSS surveys. In the top panels of Figure 4.13 we plot the sum star formation history of all galaxies that fall into these criteria for DR7 and BOSS in this redshift range. We can see that each pair of plots show remarkable agreement in comparison to the earlier star formation history plots from this chapter.

To compare the high-redshift cuts, we take the high-z LRG subsample from DR7 (cut II in

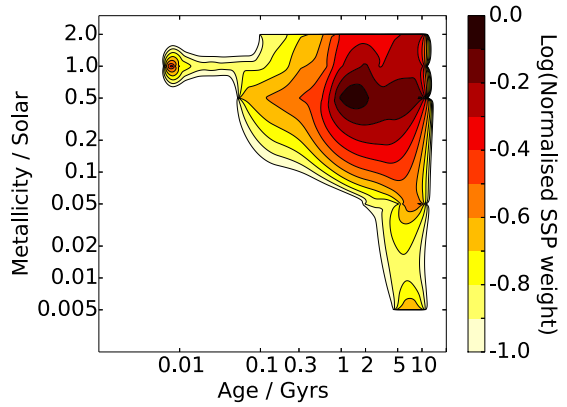

(a) Light-weighted solutions of DR7 LRGs with $0.25 < z < 0.35$.

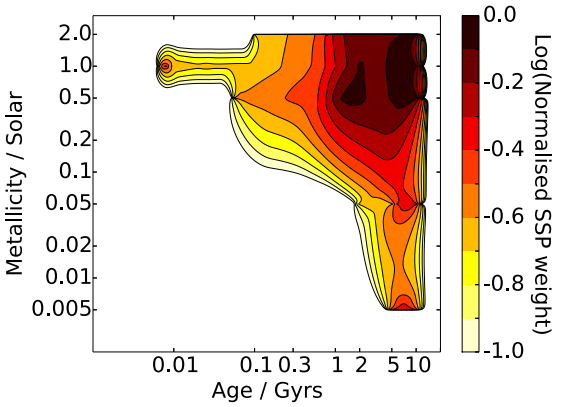

(b) Light-weighted solutions of BOSS LOWZ galaxies with $0.25 < z < 0.35$.

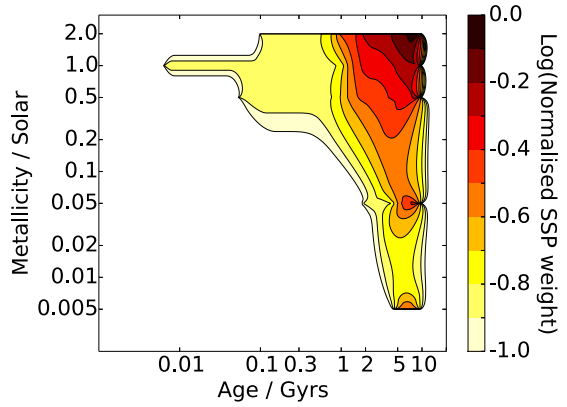

(c) Light-weighted solutions of DR7 LRGs with $0.45 < z < 0.50$ and E(B-V) < 0.2.

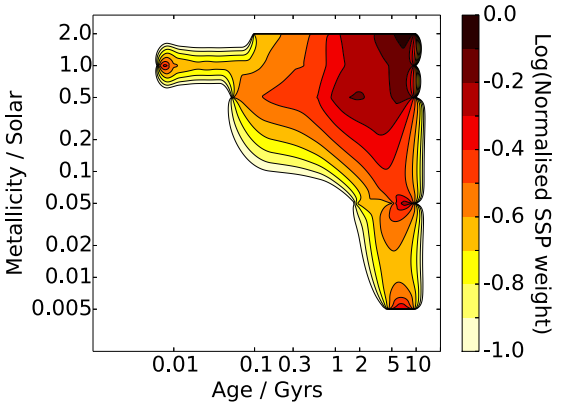

(d) Light-weighted solutions of all BOSS galaxies selected with the DR7 LRG cut with $0.45 < z < 0.50$.

Fig. 4.13 The likelihood-weighted sum of all SSP contributions for DR7 and BOSS for two different redshift ranges (low redshift, top, and high redshift, bottom) applying the LRG cuts as described in this section.

Eisenstein et al. (2011)) and the BOSS sample with the same cuts applied (except for the brightness cut, which is removed), at $0.45 < z < 0.50$. This is a smaller redshift range than before so that we do not have a significant redshift evolution within each subsample. However, due to the higher amounts of star forming dusty galaxies being bright enough to come into in the high redshift end of the LRG subsample of DR7, mimicking the colours of genuine LRGs, there ages and metallicities were somewhat lower compared to the BOSS galaxies at that redshift. This degeneracy is shown in Masters et al. (2011). Empirically, we found that by removing galaxies with dust extinction E(B-V) > 0.2 as measured from FIREFLY, we could remove these dust interlopers reliably. Therefore when using the high-redshift cut, $z > 0.44$ of DR7 LRGs we this additional dust to match better with BOSS LRGs. This cut does not need to be made across the BOSS sample, as at higher redshifts dusty star forming galaxies can still have high mean ages and metallicities (Wild et al., 2014) and thus can still reflect an LRG-like population.

As with the low-z cut, in the bottom panels of Figure 4.13 we plot the sum star formation history of all galaxies within this redshift range for DR7 and BOSS. Again we see good agreement between the two surveys. This suggests that for $z < 0.44$ we can use the LRG cut for DR7 and the LOWZ cut for BOSS, and for $z > 0.44$ use a modified version of the LRG cut for the DR7 subsample, and the BOSS galaxies selected with the DR7 LRG cut, to give a consistent LRG cut across the whole wavelength range of both surveys and combine them in this way.

Using these LRG cuts, we can now plot galaxy properties for an approximately self-similar sample as a function of redshift by adding the results from the two surveys together. In Figure 4.14 we plot mass-weighted age and metallicity, dust, and stellar mass, averaged across 50 redshift bins from 0.0 to 0.8. Overlaid on the age plot is the age of the Universe, assuming the latest cosmological parameters from Planck (Planck Collaboration et al. (2015), H_0 = 67.7, Ω_m = 0.307). Points on all plots correspond to the median value of that property in that redshift bin, and the error bars are the standard deviation of those values. We note that we have corrected for the different apertures used in the two surveys by scaling all masses to the total stellar mass estimated from the ratio of photometric magnitude to fiber magnitude as explained in Section 4.2.

From the age plot, we can see that in general the age of the galaxies follows the age of the Universe closely across the bulk of the redshift range, for most reasonable cosmological parameters. For cosmologies close to those measured in Planck Collaboration et al. (2014) (and by extension, WMAP9), the age of the LRGs differs from the age of the Universe by about

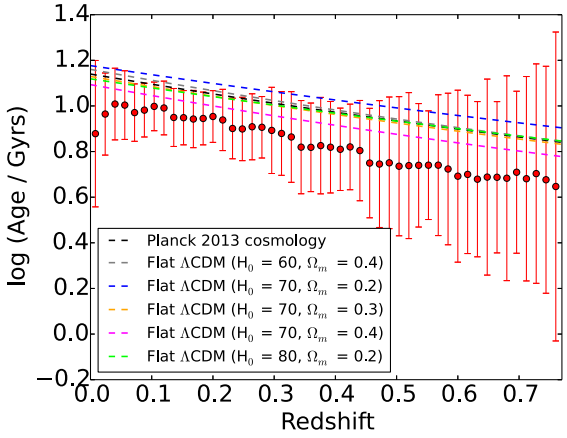

(a) Mass-weighted age, overplotted with the age of the Universe for different cosmological models (dashed lines).

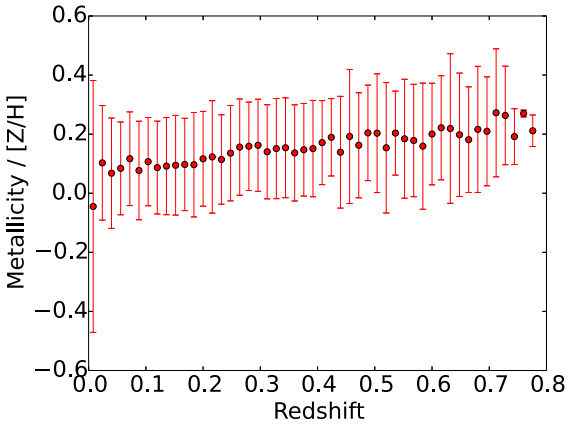

(b) Mass-weighted metallcity.

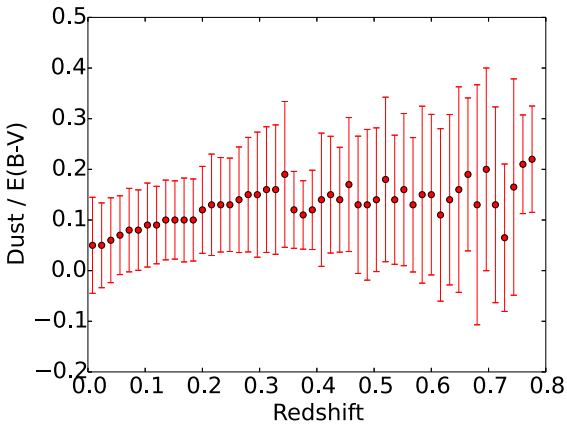

(c) Dust extinction (E(B-V)).

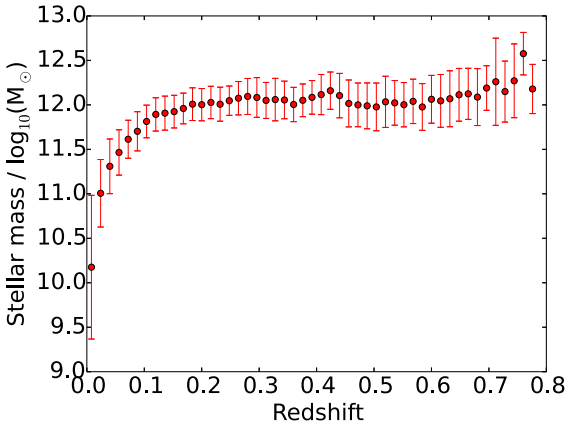

(d) Total stellar mass.

Fig. 4.14 Redshift-binned properties for the combined LRG sample of DR7 and BOSS, applying the LRG cuts as described in this section. Error bars represent the scatter of properties in each bin.

3 Gyr across the redshift range. This suggests the characteristic formation time of the LRGs used in this sample is less than 3 Gyrs from the age of the Universe, i.e. $z \sim 4$ in agreement with Thomas et al. (2010). For different cosmologies the age difference changes. For the flat ΛCDM model with H_0 = 70, Ω_m = 0.4, which is more matter-rich than other Universe cosmologies plotted, we see that the age offset is smaller, and varies across the redshift range from 1 Gyr at redshifts close to 0.0 to 2 Gyr at redshifts close to 0.7, meaning that the LRGs are no longer tracing the evolution of the Universe for this cosmology. Clearly the errors plotted make comparisons between cosmologies difficult, compared to measuring them CMB surveys or large scale structure, but this method has the potential to be used as an independent measure that traces the age of the Universe. With improvements in stellar population modelling, it could be the case in the future that these errors reduce and this method of using galaxies as independent probes of cosmology may become useful.

From the next plot, we see that the metallicity increases fairly smoothly from 0.1 dex to 0.2 dex across the whole redshift range, suggesting that more local LRGs are somewhat metal-poorer than their equivalents at higher redshift. Dust is fairly constant above $z = 0.3$, saturating at about 0.2 in E(B-V), although the low-redshift LRGs seem to be preferentially lower in dust.

This decrease in metallicity with decreasing redshift - without a clear corresponding change in the age - could be suggestive of dry, minor mergers, of small galaxies onto the LRGs with similarly high ages but significantly lower in metallicity, as observed in dwarf galaxies (Dolphin (2002), Shetrone et al. (2003), Cole et al. (2005)). Minor mergers, as mentioned in the Introduction, are a promising candidate process for explaining the size evolution of galaxies at redshifts less than 1 (Newman et al. (2012), Hilz, Naab & Ostriker (2013), van der Wel et al. (2014)), with some theoretical studies finding that the minor galaxy component could, in some configurations, become centrally concentrated and therefore in the observable footprint of single aperture surveys like SDSS (Bédorf & Portegies Zwart (2013), Welker et al. (2015)), though this evidence is currently tentative.

Similarly, the total stellar mass saturation at about $10^{12} M_{\odot}$, in a similar fashion to that observed by (Pforr, Maraston & Tonini, 2012) but at a higher mass since we scale up to the whole photometric magnitude. Between redshifts of 0.2 and 0.6 we see very little mass evolution, in good agreement with Tojeiro et al. (2012), though they use some magnitude cuts to ensure this extends to between redshifts 0.1 and 0.7. Below $z = 0.1$ there is a sharp decrease in stellar mass, in agreement with Maraston et al. (2013), where the SDSS surveys target very local objects and so are not representative of the rest of the sample.

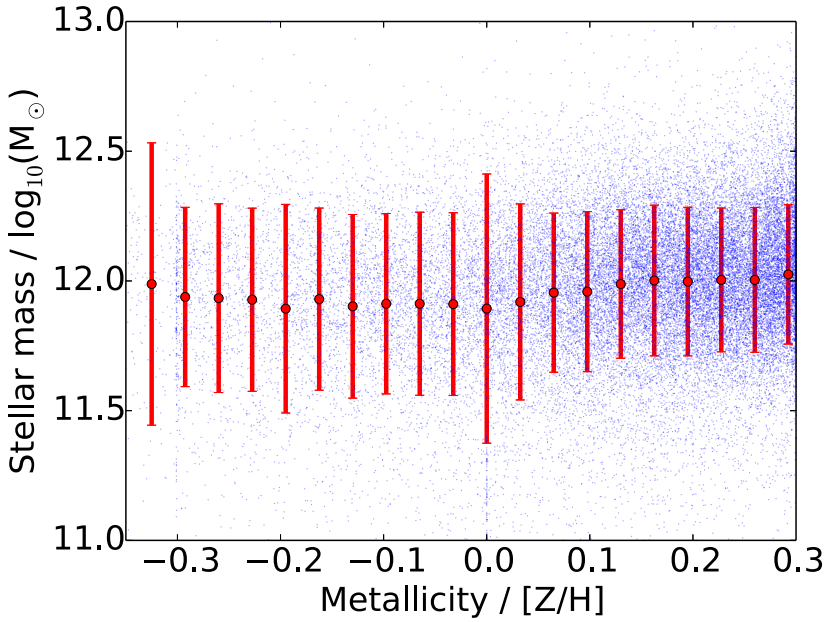

Fig. 4.15 Mass-metallicity scatterplot, overplotted with averages in metallicity bins, for the combined LRG sample of DR7 and BOSS, applying the LRG cuts as described in this section.

Figure 4.15 shows the mass-metallicity relation for the combined LRG sample. It shows a gentle increase in stellar mass from solar to super-solar metallicities, showing that the low-redshift part of the sample's low metallicity and low mass likely come from the same local galaxies. Interestingly, there is also an increase in stellar mass for very low metallicities, suggesting that some of the massive galaxies contain a sizeable fraction of stellar mass in low to ultra-low metallicity stellar populations. This could relate to the centrally-concentrated minor merger metallicity dilution discussed above, since large numbers of minor mergers could build up a galaxy mass slightly but significantly decrease the core stellar metallicity. This promising result will be investigated in future work.

4.6 Conclusions

We have presented a detailed analysis of two SDSS surveys, DR7 and DR9-BOSS, using FIREFLY. We have presented the sum star formation histories in terms of stellar population component age and metallicity, and separated each by the relevant subsamples used in the literature. We find that the sum star formation histories from these surveys is well-described by an exponentially declining star formation rate, with characteristic times of 1-3 Gyr in the most massive galaxies, down to 4-5 Gyr for the less massive galaxies in the samples. We have

also compared all results as a function of stellar library, finding good qualitative agreement but differences in the minor stellar population contributions. We have used these results to compare with publically available databases of results from both surveys, finding good qualitative agreement across all properties but with about 0.1 dex shift in some details of age, metallicity and mass. We have used the stellar population properties observed between both surveys to motivate a set of consistent LRG cuts that can be applied from redshifts $0.0 < z < 0.8$. Lastly, by using this cut to allow us to combine galaxies from both surveys to make a single sample, we have studied galaxy evolution with redshift, finding tentative clues on the role of metal-poor minor mergers on mass assembly and chemical evolution of the most massive galaxies in the Universe.

Many of results from SDSS DR7 presented in this Chapter have been written into a publication along with most of Chapter 3 as Wilkinson & Maraston (2015, submitted). The results from DR9-BOSS and the section on redshift evolution will form a large part of a future publication.

Chapter 5

Application of Spectral Fitting to Integral Field Unit Surveys: The First Spectral Analysis of Galaxies in SDSS-IV MaNGA

MaNGA (Mapping Nearby Galaxies at Apache Point Observatory) is a 6-year SDSS-IV survey that will obtain resolved spectroscopy from 3600 Å to 10300 Å for a representative sample of over 10,000 nearby galaxies. In this Chapter, we derive spatially resolved stellar population properties and radial gradients by analysing the results of FIREFLY from fitting observed galaxy spectra from P-MaNGA, a prototype of the MaNGA instrument. These data include spectra for eighteen galaxies, covering a large range of morphological type. We derive age, metallicity, dust and stellar mass maps, and their radial gradients, using high spectral-resolution stellar population models, and assess the impact of varying the stellar library input to the models. We show that the method of dust extinction described in Chapter 3 is able to give smooth stellar mass maps even in cases of high and spatially non-uniform dust attenuation.

With FIREFLY we produce detailed maps of stellar population properties which allow us to identify galactic features among this diverse sample such as spiral structure, smooth radial profiles with little azimuthal structure in spheroidal galaxies, and spatially distinct galaxy subcomponents. In agreement with the literature, we find the gradients for galaxies identified as early-type to be on average flat in age, and negative (– 0.15 dex / R_e) in metallicity, whereas the gradients for late-type galaxies are on average negative in age (– 0.39 dex / R_e) and flat in metallicity. We demonstrate how different levels of data quality change the precision with

which radial gradients can be measured. We show how this analysis, extended to the large numbers of MaNGA galaxies, will have the potential to shed light on galaxy structure and evolution.

In this chapter, section 5.2 and 5.2.1 are based on 'common text' between the P-MaNGA papers: Wilkinson et al. (2015) (from which this chapter is based), Belfiore et al. (2015), and Li et al. (2015). These have been edited between the papers during the referee process but still closely match each other to ensure consistency between them at publication. This text is a collaborative work between the architects of the MaNGA survey: Bundy et al. (2015).

5.1 Introduction to MaNGA

Large spectroscopic surveys in the past 15 years (e.g. SDSS (York et al., 2000), GAMA (Driver et al., 2011), 2dFGRS (Folkes et al., 1999)) have proved tremendously successful in deriving the physical properties of galaxies with high accuracy. Data across a range of redshift slices have been able to provide significant insight into the evolution of galaxy properties. Pairing these data with evolutionary population synthesis models (e.g. Bruzual & Charlot (2003), Maraston (1998), Fioc & Rocca-Volmerange (1997), Leitherer et al. (1999), González Delgado et al. (2005), Thomas, Maraston & Bender (2003), Vazdekis et al. (1996), Vazdekis et al. (2010), Conroy, Gunn & White (2009), Thomas, Maraston & Johansson (2011) and Maraston & Strömbäck (2011)) via a full spectral fitting method (e.g. PPXF by Cappellari & Emsellem (2004), VESPA by Tojeiro et al. (2007), fitting after using PCA, by Chen et al. (2012), STARLIGHT Cid Fernandes et al. (2005), STECKMAP by Ocvirk et al. (2006b)) , or using selected absorption lines (Thomas et al. (2005), Thomas et al. (2010)) allows the derivation of galaxy properties, such as star formation history, age of formation, metallicity and chemical content, dust content, star formation rate and stellar mass.

These large galaxy surveys - in order to collect large samples - could only perform single aperture observations per galaxy, typically across their central regions. Therefore galaxy evolution properties as a function of internal structures, such as stellar population profiles across the core, disk or halo, cannot be measured, and the global properties are very sensitive to the aperture position and coverage (Iglesias-Páramo et al. (2013)). Physical processes such as radial migration, higher level structure such as dust structure and clumped star-formation, and signatures of merging and interactions cannot be easily constrained by single-aperture observations (Gerssen, Wilman & Christensen (2012), Wuyts et al. (2012)).

In order to surpass these limitations, many modern galaxy surveys use integral field spectroscopy (IFS) (SAURON (Bacon et al., 2001), ATLAS^{3D} (Cappellari et al., 2011), CALIFA (Sánchez et al., 2012), SAMI (Croom et al., 2012), VENGA (Blanc et al., 2013), DiskMass (Bershady et al., 2010). This is a method by which multiple spectra of the same galaxy covering many 2D positions in the sky are obtained. This allows detailed internal information of each observed galaxy to be obtained.

Many of the previous IFU surveys have been limited in the number of galaxies they have observed, meaning that detailed statistics of properties of a range of galaxy types is limited. MaNGA (Mapping Nearby Galaxies at Apache Point Observatory, Bundy et al. (2015)) is designed to complement these small-sample surveys by providing spectral information for a large statistical sample of 10,000 galaxies across a range of galaxy types and morphologies, to be observed over a period of six years. MaNGA is one of the four surveys of the SDSS-IV (Sloan Digital Sky Survey IV) project. A unique feature of MaNGA with respect to other IFU surveys is its extended spectral coverage, from 3600 Å to 1μ. As is well known, the wider the spectral range the easier it is to break degeneracies such as the age/metallicity/dust degeneracies (e.g. Pforr, Maraston & Tonini (2012)). Moreover, this spectral range includes absorptions features such as the Sodium doublet and Calcium triplet, that are important diagnostics of the Initial Mass Function (IMF, e.g. Saglia et al. (2002); Conroy & van Dokkum (2012); Ferreras et al. (2013); Spiniello et al. (2014)).

MaNGA aims to answer fundamental questions about the relative importance of stellar accretion, mergers and disk instabilities to mass assembly, the formation of bulges, the regulation of star formation, and the growth of galactic disks. In order to be able to answer these questions, the MaNGA main samples are selected to achieve a uniform spatial coverage that reaches either 1.5 R_e ("Primary+," roughly ⅔ of the final sample) or 2.5 R_e ("Secondary," roughly ⅓ of the final sample), see Wake et al. (in preparation) for details. The launch of the MaNGA survey was July 1st, 2014, and the program will run for 6 years, utilizing half of the dark time available in SDSS-IV. Details on the instrumentation including the design, testing, and assembly of the fiber-IFUs are given in Drory et al. (2015). Wake et al. (in preparation) presents the sample design, optimization, and final selection of the survey. The software and data framework as well as the reduction pipeline are described in Law et al. (in preparation). A description of the commissioning, the quality of survey observations, and further operational details will be given in Yan et al. (in preparation).

In order to test the performances of the survey in advance, preliminary 'MaNGA-type' galaxy data have been obtained with a MaNGA prototype instrument called P-MaNGA (described in

detail in section 5.2). The P-MaNGA dataset contains 3D spectra (x position, y position, and wavelength) for 18 galaxies observed with a variety of IFU sizes and observational conditions. The P-MaNGA data were obtained through a generous donation of observing time by the SDSS-III Collaboration (Eisenstein et al., 2011). These data are described in detail in Bundy et al. (2015). P-MaNGA observations are used to understand and quantify the capabilities of MaNGA and help predicting the results we should expect from the full dataset.

The physical properties of galaxies are obtained by analysing spectra with stellar population models. In this Chapter we perform full spectral fitting of population models on the P-MaNGA data. We use FIREFLYto analyse the spectra and experiment with the full suite of the M11 models. We generate 2D stellar population maps and 1D radial profiles and analyse the results.

The Chapter is organised as follows. Section 5.2 describes the P-MaNGA observations, while Section 5.3 the parameters of FIREFLY and the models used in this Chapter, as well as the methodology to measure radial gradients. The analysis of individual stellar population maps and gradients is in Section 5.4. General results are in Section 5.5 where we include descriptions of tests we performed to assess the robustness of our work, and Section 5.6 presents the comparison with the other two early science P-MaNGA articles. Conclusions and discussion follow and close the Chapter.

5.2 P-MaNGA observations

MaNGA is both an instrument suite and a survey that uses the Sloan 2.5m telescope (Gunn et al., 2006). By September 2014, identical sets of MaNGA hardware were installed in six SDSS cartridges, allowing six individual plug-plates to be observed on a given night. Each MaNGA cartridge (or "cart" for short) consists of 17 science integral field units (IFUs) ranging in size from 19 fibers (12.″5 diameter) to 127 fibers (32.″5 diameter) that patrol a 3° diameter field of view. Twelve 7-fiber "mini-bundles" are used for standard star flux calibration and 92 individual fibers for sky subtraction.

All 1423 fibers have a 2.″0 core diameter and a 2.″5 outer diameter and—when the cartridge is mounted to the telescope—feed the highly sensitive BOSS spectrographs (Smee et al. (2013)) which provides continuous wavelength coverage from 3600 Å to 10,300 Å at a spectral resolution R $\sim$ 2000 (R $\approx$ 1600 at 4000 Å, and R $\approx$ 2300 at 8500 Å,) with a total system throughput of $\sim$25%. We use subsets of this wavelength range in the spectral fitting analysis of this Chapter, due to the limitations of the empirical simple stellar population models that are used, as

Survey	P-MaNGA	MaNGA
Target galaxy properties		
Sample size	18	$\sim$ 10 000
z	0.01 — 0.06	0.01 — 0.15
M_i / mag	–18.5 — –22.7	$\sim$ –17 — –23
R_e	0.7 – 3.4	1.5 (Primary) and 2.5 (secondary)
Instrument design		
Flux standard type	Single 2″fiber	Mini-bundle
Fibers used per cart	560	1423
IFU distribution	5 x N_{19} (12″), 1 x N_{61} (22″), 2 x N_{127} (32″).	2 x N_{19} (12″), 4 x N_{37} (17″), 4 x N_{61} (22″), 2 x N_{91} (27″), 5 x N_{127} (32″), 12 x N_7 mini-bundles.

Table 5.1 Summary of differences between P-MaNGA and the full MaNGA survey.

discussed in Section 5.3.1, which will be expanded in future work. Details on the MaNGA hardware are given by Drory et al. (2015). Instrument commissioning began in January 2014.

In this work, we use data obtained using the MaNGA engineering prototype instrument (P-MaNGA) in January 2013. P-MaNGA was designed to explore a variety of instrument design options, observing strategies, and data reduction algorithms. These P-MaNGA data offer a valuable look at MaNGA's potential but differ substantially from the MaNGA survey data in several ways. We summarise these differences in Table 5.1 and describe them below.

First, P-MaNGA used only 560 total fibers distributed across just one of the two BOSS spectrographs. 470 of these fibers had a 2.″0 diameter core, while 90 had either a 3.″0 or 5.″0 arcsec core and are not used for the present analysis. 410 of the 2-arcsec fibers were bundled into 8 IFUs with three sizes: 19 fibers (N_{19}), 61 fibers (N_{61}), and 127 fibers (N_{127}). The P-MaNGA IFU complement was dramatically different from the MaNGA survey instrument, with 5$\times N_{19}$ (instead of just two), 1$\times N_{61}$ (instead of 4), 2$\times N_{127}$ (instead of five), and no 37-fiber or 91-fiber IFUs. The masses and sizes of the P-MaNGA galaxies observed are therefore not representative of the final MaNGA sample.

P-MaNGA observations were obtained for 3 galaxy fields using plates 6650, 6651, and 6652 (see summary in Table 5.2). In each case, observations were obtained in sets of three 20-minute exposures dithered by roughly a fiber radius along the vertices of an equilateral triangle to provide uniform coverage across each IFU. These three fields were observed to varying depths, and in varying conditions as required by the P-MaNGA engineering tasks that they

were designed for. Although plate 6650 (Field 9) was observed to a depth comparable to what will be regularly achieved during MaNGA operations, plates 6651 (Field 11) and 6652 (Field 4) are both significantly shallower than MaNGA survey data, and plate 6651 was intentionally observed at high airmass resulting in particularly poor image quality.

Some of the P-MaNGA targets were drawn from early versions of the MaNGA sample design, but in many cases P-MaNGA targets were chosen for specific reasons. In each of the three plates, one N_{127} IFU was allocated to a galaxy already observed by the CALIFA survey (Calar Alto Large Integral Field Area, Sánchez et al., 2012) for comparison purposes, even if it would not otherwise satisfy the MaNGA selection cuts. Additionally, the non-optimal IFU complement of the P-MaNGA instrument required some targets to be selected manually. Altogether 18 P-MaNGA galaxies were observed (see Table 5.2).

The raw data was reduced using a prototype of the MaNGA Data Reduction Pipeline (DRP), which is described in detail by Law et al. (in prep). In brief, individual fiber flux and inverse variance spectra were extracted using a row-by-row algorithm, wavelength calibrated using a series of Neon-Mercury-Cadmium arc lines, and flat-fielded using internal quartz calibration lamps. Sky-subtraction of the IFU fiber spectra was performed by constructing a cubic basis spline model of the sky background flux as seen by the 41 individual fibers placed on blank regions of sky, and subtracting off the resulting composite spectrum shifted to the native wavelength solution of each IFU fiber.

Flux calibration of the P-MaNGA data is performed by fitting Kurucz (1979) (and revisions) model stellar spectra to the spectra of calibration standard stars covered with single fibers at each of the three dither positions. Such methods are shown from SDSS DR6 (Adelman-McCarthy et al., 2008) to yield median calibration errors over all plates of less than 2%. This method is preferable to observing flux-standard stars at different times from the galaxy observations, as even on the same night systematic errors (e.g. due to changing airmass) are larger than the calibration error quoted above. The flux calibration vectors derived from these single-fiber spectra were found to vary by $\sim$ 10% from exposure to exposure, depending on the amount of light lost from the fiber due to atmospheric seeing and astrometric misalignments. The flux calibration error is due to the positional error of the fibers, which can be different from plate to plate. However, error is a slowly varying function of wavelength which is absorbed by the dust method described in Chapter 3, thereby minimising the impact on the spectral fitting. While this uncertainty is acceptable for the present science purposes, the flux calibration uncertainty of the single fibers ultimately drove the design decision of the MaNGA survey to instead use 7-fiber IFU “mini-bundles” for each calibration standard star, which re-

Nickname	mangaID	Bundle	RA (J2000 degrees)	Dec	z	log M_*	M_i mag	$(g-r)$ mag	R_e "	$R_{\rm IFU}$ (R_e)	Morphological type$^\diamond$
Group α: MaNGA-like conditions and setup, has been selected for MaNGA sample.†											
p9-127B	12-131835	ma008	143.7764	+21.6277	0.013	9.1	-18.5	0.51	6.8	2.4	LTG
p9-19B	12-131893	ma005	142.7900	+22.7465	0.051	10.6	-22.2	0.86	4.0	1.6	ETG
p9-19D	12-131577	ma007	142.7878	+20.9168	0.034	10.3	-21.2	0.79	3.2	2.0	ETG
p9-19E	12-131821	ma001	145.1260	+21.2538	0.024	9.7	-20.0	0.73	2.9	2.2	ETG
Group β: MaNGA-like conditions and setup, not selected by MaNGA.											
p9-127A	12-188794	ma003	143.7400	+21.7053	0.013	10.7	-21.3	0.70	23.7	0.7	LTG
p9-61A	12-188807	ma002	144.2993	+21.6692	0.019	10.1	-20.5	1.3?	9.3	1.2	ETG
Group γ: Poorer conditions and/or setup than MaNGA, has been selected for MaNGA sample.†											
p4-19A	12-113557	ma004	165.0504	+36.3873	0.027	9.4	-19.5	0.49	2.5	2.5	LTG
p4-19B	12-113506	ma005	162.4946	+36.4150	0.023	9.5	-19.5	0.53	4.6	1.4	LTG
p4-19C	12-109657	ma006	164.0237	+36.9600	0.022	9.5	-19.4	0.72	4.8	1.3	ETG
p11-61A*	12-93688	ma002	208.0482	+13.9999	0.024	10.1	-20.7	0.77	7.3	1.5	LTG
p11-19B*	12-93551	ma005	207.2918	+13.3470	0.024	9.2	-19.4	0.42	2.4	2.6	LTG
Group δ: Poorer conditions and/or setup than MaNGA, not selected by MaNGA.											
p4-127A	12-109661	ma003	163.9803	+36.8615	0.022	10.7	-22.1	0.84	10.3	1.6	LTG
p4-127B	12-109682	ma008	163.2461	+37.6134	0.042	11.0	-22.7	0.77	13.9	1.2	LTG
p4-61A	12-113576	ma002	164.4442	+36.2827	0.030	9.7	-20.0	0.71	3.4	3.4	LTG
p11-127A*	12-196354	ma003	207.8786	+14.0922	0.024	10.9	-22.4	0.85	17.0	1.0	LTG
p11-127B*	12-196727	ma008	209.2309	+14.1423	0.016	9.4	-19.4	0.42	9.6	1.7	LTG
p11-19A*	12-196773	ma004	207.5811	+14.1407	0.062	9.5	-21.1	0.85	1.1	2.8	LTG
p11-19C*	12-93538	ma006	206.7061	+14.4005	0.021	10.0	-20.9	0.54	2.8	2.2	LTG

Table 5.2 Details of P-MaNGA galaxy sample. Galaxy nicknames are structures as p (prototype), Field number (see Table 5.3) – IFU bundle size, iterative name A/B/C. Properties are from the SDSS Data Release 8 database (Aihara et al., 2011). Stellar masses are from the 'Galspec' catalogue based on Brinchmann et al. (2004), in the Data Release 8 photometric pipeline, scaled to 3 arcsecond fiber magnitudes. These are compared to our mass estimates and other mass estimates from broad-band fitting in section 5.5.4. Starred galaxies (*) in groups γ and δ correspond to galaxies taken under very poor observational conditions and setup (plate 11, see Table 5.3), whereas other galaxies in these groups are taken with a setup that is closer to, but still poorer than, a MaNGA-like setup (plate 4, see Table 5.3).

$\diamond$ Morphologies of early-type (elliptical / lenticular) or late-type (spiral / irregular) are obtained through direct visual inspection of the corresponding SDSS images by the main author.

† P-MaNGA galaxies in these groups meet the selection criteria for either the MaNGA primary or secondary samples as described in Bundy et al. (2015), and will be observed in MaNGA.

sults in a photometric accuracy better than 2.5% between Halpha and Hbeta, and better than 7% between [NII] 6584 and [OII] 3726, 3729 for MaNGA survey data (see Yan et al., in prep).

Flux calibrated spectra from the blue and red cameras were combined together across the dichroic break using an inverse-variance weighted basis spline function. Astrometric solutions were derived for each individual fiber spectrum that incorporate information about the IFU bundle metrology (i.e., fiber location within an IFU), dithering, and atmospheric chromatic differential refraction, among other effects. Fiber spectra from all exposures for a given galaxy were then combined together into a single datacube (and corresponding inverse variance array) using these astrometric solutions and a nearest-neighbor sampling algorithm similar to that used by the CALIFA survey. For the P-MaNGA datacubes, a spaxel size of $0\farcs5$ was chosen. The typical effective spatial resolution in the reconstructed datacubes can be described by a Gaussian with FWHM $\approx 2\farcs5$. When binning the datacubes, we scale the resulting error vectors to approximately account for wavelength and spatial covariance in the P-MaNGA error cubes. The spectral resolution is given by FWHM $= 2.35\sigma$, which is a function of wavelength as described in Smee et al. (2013). In this analysis we use P-MaNGA datacubes, which have been processed through the prototype DRP and a prototype data analysis pipeline (PDAP) being developed at the Institute of Cosmology and Gravitation of the University of Portsmouth[1]. The relevant details are provided below.

5.2.1 The prototype data analysis pipeline (PDAP)

The PDAP analyses the reduced datacubes produced by the DRP to measure galaxy's physical parameters, such as kinematics and emission line fluxes. This is summarised as a flow diagram in Figure 5.1 and explained in the following paragraphs.

The first analysis block within the PDAP is to spatially bin adjacent spectra to increase the signal-to-noise (S/N) ratio. This is done by using the Voronoi Binning algorithm[2] (Cappellari & Copin, 2003). We implement optimal weighting to determine the S/N of each bin as described in section 2.1 of Cappellari & Copin (2003), in which the weighting given to each pixel is proportional to its $S/(N^2)$. Because the various galaxy's physical parameters require different minimum S/N to be measured with a desired accuracy, the PDAP performs the spatial binning three times, producing three sets of spectra binned with different S/N criteria according to the scientific needs. These three sets of spectra are processed independently in

[1] For information on the PDAP contact Daniel Thomas, daniel.thomas@port.ac.uk
[2] Available from purl.org/cappellari/software

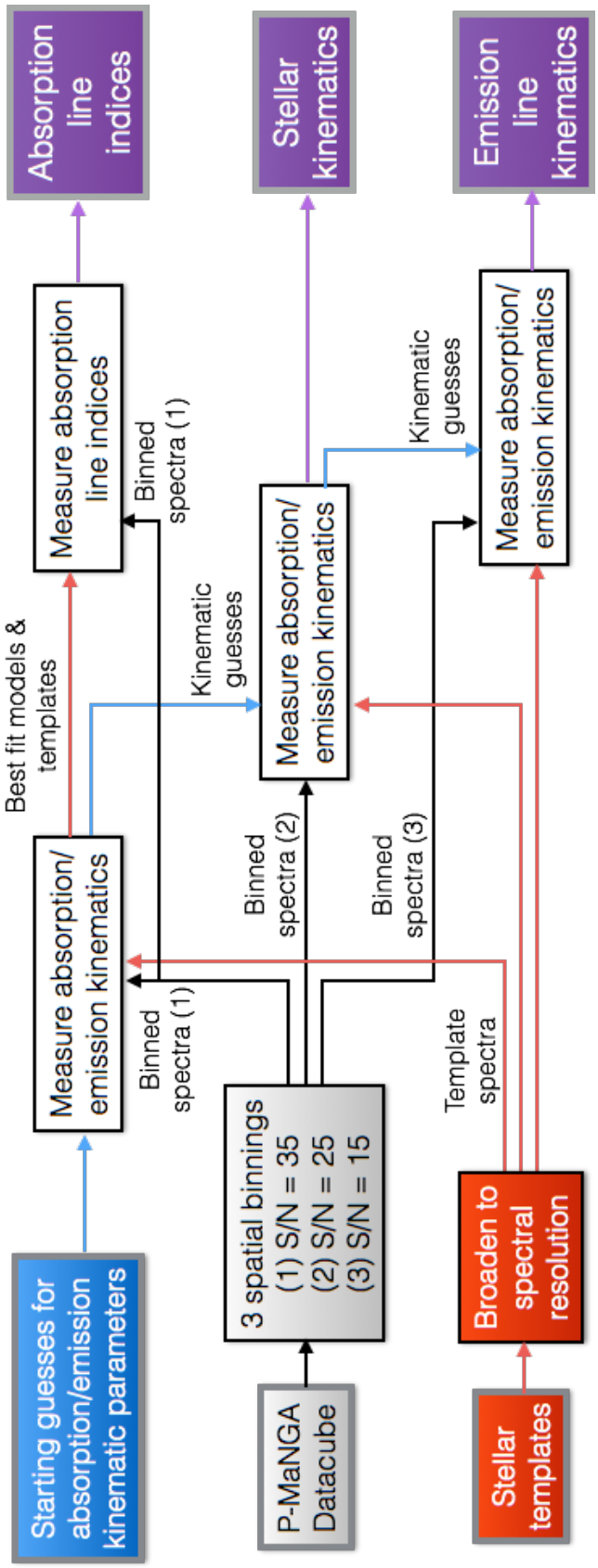

Fig. 5.1 Summary of the processes of the Prototype Data Analysis Pipeline (PDAP), used to recover the physical parameters used as input in this work in addition to the P-MaNGA datacubes. P-MaNGA datacubes are binned in three spatial schemes according to the signal-to-noise requirements of the properties extracted from the kinematic fits. Each of the processes are described in section 5.2.1. Each kinematic fit also outputs improved starting kinematic guesses for the next spatial bin.

subsequent analysis blocks, to extract the various galaxy parameters.

The S/N values quoted in the following sections are computed by calculating the median signal to noise per pixel over the wavelength range $5560 < \lambda/\text{Å} < 6942$, the wavelength range of the SDSS *r*-band (Fukugita et al., 1996), which straddles the dichroic break of the SDSS spectrograph (Smee et al., 2013), in order to better relate to the signal-to-noise measurements in SDSS photometry. However, the binned S/N values in the P-MaNGA data do not include error covariance. Hence the S/N thresholds in the following sections are empirically chosen to give reliable extraction of each of the corresponding properties.

The first spatial binning requires a minimum $S/N = 35$ per bin and is used to measure absorption line indices. This requirement is based the analysis of the errors of absorption indices as derived by Johansson, Thomas & Maraston (2012). The second spatial binning requires a minimum of $S/N = 25$ and is used to measure stellar kinematics. The requirement is derived from estimating the errors on kinematic parameters as in Cappellari & Emsellem (2004). The third spatial binning with a minimum $S/N = 15$ is used to measure the properties of the emission lines (kinematics, fluxes, equivalent widths, reddening, and Balmer decrement). This requirement is based on errors computed in Thomas et al. (2013).

The second analysis block within the PDAP fits the spatially binned spectra with a series of stellar templates and Gaussian functions. The fit is executed 3 times, one for each of the 3 groups of spatially binned spectra produced in the first analysis block.

The processes in the PDAP are applied to the full wavelength range of P-MaNGA data, however for the spectral fitting analysis with FIREFLYwe use a large portion of this wavelength range due to the limitations of the current empirical simple stellar population models used, as discussed in 5.3.1. In future work, we will expand this analysis to the full wavelength range.

The spectral fitting routine uses an implementation of the Penalized Pixel Fitting (hereafter, PPXF[3] (Cappellari & Emsellem, 2004)) and Gas AND Absorption Line Fitting (Sarzi et al. (2006)), hereafter GANDALF, and it is performed into two steps. In the first step, the galaxy's ionized-gas lines are masked, and the stellar continuum is fitted with a series of simple stellar population (SSP) models from Maraston & Strömbäck (2011), which offer a large variety of calculations for various stellar libraries. In particular, the MILES-based models, which extend to $\sim$ 7000 Å are joined with the fully theoretical M11 models based on the MARCS-stellar spectra which, by having the very high spectral resolution of 0.1 Å, makes it possible to match the required high spectral resolution of MILES (2.54 Å (Beifiori et al. (2011), Prugniel, Vauglin & Koleva (2011), Falcón-Barroso et al. (2011))) also in the near-IR (see

Section 5.3.1).[3] In this first step, stellar kinematics are measured.

In the second step, the entire (unmasked) spectrum is fitted with a series of SSP models and Gaussian functions, but the stellar kinematics are kept fixed from the measurements obtained in the first step. Gaussian functions are linked into three groups, so that each group of lines have the same velocity and velocity dispersion. The three groups are i) Balmer lines, ii) NaI absorption lines (5890–5896 Å), iii) all the other ionized-gas emission lines. Each gas line is broadened with a Gaussian function to match the instrumental FWHM at the wavelength that the specific line is detected at. Multiplicative and additive polynomials, or a dust attenuation law (following the prescriptions in Sarzi et al. (2006)) can be added to the fit procedure in these two steps.

The first execution of the spectral fitting routine (both steps as described above) is performed onto the galaxy spectra of the first spatial binning. In this execution, 6th order multiplicative polynomials are used to fit to the continuum. The best fitting model of the emission lines is then removed from the galaxy binned spectra, and the strength of absorption line indices are measured. The best fitting stellar template and the best fitting stellar template convolved by the best fitting stellar Line Of Sight Velocity Dispersion (LOSVD) are then used to correct absorption line indices for internal kinematic broadening. The best fitting stellar and gas kinematics are used as starting guesses for the next execution of the spectral fitting routine.

The second execution (both steps as above) is performed onto the galaxy spectra of the second spatial binning. Only stellar templates that have been selected in the first execution are used. In this execution, 6th order multiplicative polynomial and 3rd order additive polynomials are used for the fit. The best fitting stellar and gas kinematics will be used as starting guesses for the next execution. The best fitting stellar kinematics obtained in this step will be saved in the final output table, and will characterize the galaxy stellar kinematics.

The third execution of the spectral fitting routine (both steps as above) is performed to the galaxy spectra of the third spatial binning. Only stellar templates that have been selected in the first execution are used. In this execution, 6th order multiplicative polynomial and 3rd order additive polynomials are used in the first step, which is a fit using PPXF. Multiplicative polynomials, or a reddening extinction law if required, are used in the second step, which is fit using an adapted version (Thomas et al., 2013) of the code GANDALF (Sarzi et al., 2006). The best fitting gas kinematics (velocity and velocity dispersion) of each fitted emission line will be averaged together using the line flux as weight to characterize the mean gas kinematics

[3]These extended models as the others from M11 are available at: www.maraston.eu/M11.

Field	Groups	Conditions and setup
9	α/β	Exposure 3.0 hr, seeing $1.''7$
4	γ/δ	Exposure 2.0 hr, seeing $1.''3$
11	γ/δ	Exposure 1.0 hr, seeing $2.''0$, (airmass $\sim$1.5)

Table 5.3 Summary of observational conditions and setup

of the galaxy. Gas-subtracted galaxy spectra are de-redshifted using the stellar kinematics measured in this third execution.

In this work, we used the PDAP to bin the galaxy spectra to reach a minimum $S/N = 5$, lower than the thresholds used previously since we use full spectral fitting rather than fits to emission or absorption lines. We chose $S/N = 5$ as it seems adequate to provide well-constrained fits, based on tests done on mock galaxy spectra as shown in Chapter 3. We then fitted the binned spectra following the prescription of the third execution of the spectral fitting routine, namely to remove gas lines and to set spectra to rest-frame. The gas-free, rest-framed spectra are then analyzed, as described in Section 5.4.

5.3 Analysis Choices

5.3.1 Models

As in the rest of this thesis, we use the stellar population models of Maraston & Strömbäck (2011), hereafter M11, in order to match observed spectral energy distributions (SEDs) to physical properties of the stellar populations observed. The resulting stellar population parameter coverage is summarized in Table 1 in Chapter 2, which we reproduce here as Table 5.4 for the reader's convenience.[4]

The empirically-based models have the advantage of extending down to low ages (see Table 5.4 and M11, but unfortunately do not exploit the full wavelength extension of the P-MaNGA data, which we will pursue at a later stage when empirical SSP models with young stars with suitable resolution in the near-IR will be available. As stated in Chapter 3, we only use a Kroupa (Kroupa, 2001) initial mass function (IMF) for each of these libraries. In a separate project we plan to use MaNGA data to constrain more exotic IMFs.

[4]See www.maraston.eu/M11/README_M11.txt for details.

Model library	Wavelength coverage (min – max) / Å	Age coverage (min – max) / Myr	Metallicity coverage (Z/H)
MILES	3500 – 7429	6.5 – 15000	[0.0001, 0.001, 0.01, 0.02, 0.04]
STELIB	3201 – 7900	30 – 15000	[0.01,0.02,0.04]
ELODIE	3900 – 6800	3 – 15000	[0.0001, 0.01, 0.02, 0.04]

Table 5.4 Reproduction of Table 1 of Chapter 2 for convenience: Parameter coverage of the stellar population models as a function of input stellar library, available at www.maraston.eu/M11/README_M11.txt

5.3.2 FIREFLY Parameters

FIREFLY is ideal for analysing P-MaNGA data as it can map out inherent spectral degeneracies, work well at low S/N, compare input stellar libraries, and makes as few assumptions about the star formation histories derived as possible. The code is discussed in Chapter 3 with tests to mock galaxies and example applications to SDSS galaxies in Chapter 4.

As explained in Chapter 3, we can use the probabilities output by FIREFLY to fit a gaussian profile[5] to each of the marginal distributions of the parameters in order to estimate their averages and standard deviations. The standard deviations are used as estimates for the errors on each of the properties. We note that the error estimate using this method will include the spectral degeneracies between the stellar population properties folded into the random errors. Generally however, higher random errors taken over a large range of different stellar populations will correspond to higher error estimates. Separating out the statistical errors on the spectra from the spectral degeneracies requires careful simulation, which will be analysed in future work. The exception to this method is the dust calculation, hence degeneracies with dust are not folded into these error estimates.

We note that the errors derived in this Chapter are statistical plus degeneracy errors only. They do not include systematic errors from the modelling, fitting code or covariance between pixels. For a detailed discussion of the treatment of covariance for the SAMI IFU survey, we direct the reader to Sharp et al. (2015). However, we do quantify the size of the first two of these systematic effects in sections 5.5.5 and 5.5.6. For the effect of covariance between pixels we note that MaNGA data will have more accurate estimation of spectral errors, allowing accurate propagation through to the final datacubes from which we can construct covariance measures between pixels, but this is beyond the scope of this thesis. Hence we assume that each $2\farcs0$

[5]Since we achieve enough fits with each run of FIREFLY, these properties are generally very well fit by Gaussian profiles.

fiber is an independent observation, which with dithering will increase in area slightly, to approximately 4 square arcseconds. Thus each $0\farcs5$ spaxel the deconstructed datacube, in dependent on 15 other spaxels. Therefore when binning datacubes, for example in elliptical bins for the radial profiles, we calculate standard areas assuming that the number of independent observations is equal to the number of grid points analysed, divided by 16. We note that always applying this 1/16 factor to the variance in each radial bin means that the overall error on a single radial bin will be an overestimate, since all 16 pixels from a given fiber may not be included in each radial bin. However, this means that the covariance between bins is therefore included in the radial profiles and thus the gradient estimations. The codependence of neighbouring pixels will be analysed in more detail in future work.

We use emission-cleaned spectra, as described in Chapter 3. GANDALF, when fitting to emission lines, also has the added benefit of releasing accurate measurements of the Doppler broadening of the SEDs due to the velocity dispersion of the stars in the object, based on pPXF fits (Cappellari & Emsellem (2004)).

A particular advantage of the code when applied to P-MaNGA is the ability to map out degeneracies in age and metallicity for each individual spectrum. These effects are also explored in detail for whole-galaxy spectra in Chapter 3. The P-MaNGA data is binned spatially into Voronoi bins (see Cappellari & Copin (2003)) in order to give a target S/N per spatial bin of 5. This gives a 2D map of 1D spectra (in other words, a 3D datacube) which are then fit individually with FIREFLY for each model combination.

To derive radial gradients of stellar population properties, we bin the stellar population properties output by FIREFLY into elliptical annuli that are scaled in along the major axis such that the bins are constant in effective radius. We use the same Voronoi spectra products for consistency with the maps, and also to make sure the PDAP analysis was the same for both sets of data. From these summed properties we derive surface mass profiles, mass-weighted stellar age profiles, and mass-weighted stellar metallicity profiles. Example profiles for the galaxy p9-19B are shown in Figures 5.2.

5.4 Analysis of Stellar Population Maps

For each P-MaNGA galaxy we derive maps of stellar mass density, light-weighted and mass-weighted stellar age and metallicity in terms of [Z/H], and dust extinction in terms of E(B-V). We use the following conventions for denoting the age and metallicity properties: metallici-

ties are written as $\langle[Z/H]\rangle_L$ and $\langle[Z/H]\rangle_M$ and ages are written as $\langle age\rangle_L$ and $\langle age\rangle_M$ (or $\langle \log age\rangle_L$ and $\langle \log age\rangle_M$ for the logarithmic values) for luminosity- and mass-weighted properties respectively.

As noted above, we provide two types of stellar population maps. The first set shown in the plots are maps that are computed by weighting each stellar population component by their total luminosity across the wavelength range fitted, and find the geometric average (as standard in full spectral fitting codes, see Chapter 3) to compute 'light-weighted' properties as a function of position. The second set of maps and also the radial profiles are computed by weighting each stellar population component by their stellar mass contribution, again finding the geometric average of this to compute 'mass-weighted' properties.

In this Chapter we show both mass- and light-weighted properties since they can complement each other well to identify certain processes more clearly, as we described in Chapter 2. This is important for IFU data as, for example, a featureless $\langle age\rangle_M$ map with a steep negative $\langle age\rangle_L$ gradient can thus be interpreted as a galaxy that has most of its stars distributed uniformly across the galaxy but with some more star formation in its outer regions. We discuss case-by-case where these differences are greatest.

In all radial profile plots and analysis of gradients we use mass-weighted property values since these give insight into the mass assembly history of the galaxies. Mass-weighted properties better trace the whole evolutionary history of the galaxy, rather than being highly affected by phases contributing a high proportion of light, such as recent star formation.

In the following sections we will discuss some of the features identified in the stellar population maps by grouping galaxies by their similarity in data quality to the full MaNGA samples, both primary and secondary, and whether they would be included in the MaNGA target selection. Since in this work we do not calculate covariance between pixels due to the preliminary nature of the error estimates on the spectra, as discussed in Section 5.3.2, we calculate the statistical standard errors on the gradients obtained assuming that each pixel is dependent on 15 other pixels that in total represent a dithered $2\farcs0$ fiber observation.

After discussing each of the groups (α to δ) from Table 5.2 separately in this section, we provide summary plots in section 5.5 showing the gradients obtained across the whole sample and the statistical errors obtained on the profiles derived as a function of observational condition. We then test the stability of the results obtained as a function of stellar library. Lastly, we compare with literature values for both total stellar mass and detailed IFU stellar population information.

5.4.1 MaNGA-selected galaxies with high-quality data: Group α

Two galaxies from P-MaNGA - p9-19B (Figure 5.2) and p9-19D (for a full set of maps see the Appendix) - fall into the MaNGA primary sample selection whilst also maintaining MaNGA-like data quality with 3 hour exposures and decent ($1\farcs7$) seeing conditions. Both have been observed with the N_{19} IFU setup.

These galaxies are visually identified as early-type galaxies and indeed show a high level of radial symmetry in their age, metallicity and stellar mass density maps.

Galaxy p9-19B has a $\langle \log \mathrm{age} \rangle_L$ = 8 Gyr / $\langle \log \mathrm{age} \rangle_M$ = 10 Gyr, slightly super-solar metallicity core going down to $\langle \log \mathrm{age} \rangle_L = \langle \log \mathrm{age} \rangle_M$ = 5 Gyr with sub-solar metallicity at above 1 effective radius, and is largely dustless except for at very high radii along the minor axis. Galaxy p9-19D is similar but with a weaker age and metallicity gradient.

In both of these cases we recover extremely smooth negative stellar population profiles with very low errors on each point, with the median of errors of 0.05, 0.10 dex in age, 0.05, 0.08 dex in metallicity, and 0.03, 0.07 dex in surface mass density for p9-19B and p9-19D respectively. This results in errors on their respective gradients determined to 0.03, 0.05 dex / R_e in age and 0.05 – 0.09 dex / R_e in metallicity, which bodes well for MaNGA observations of early-type galaxies like these.

Two further galaxies from P-MaNGA fall into the MaNGA secondary sample, having wider radial coverage. The stellar population maps and profiles of these galaxies are shown and described in the Appendix.We note for both of these cases the more complex nature of the stellar populations as a function of position, coupled with the lower spatial resolution than the MaNGA primary sample, means that the uncertainties on the profiles derived are greater. Profiles are determined to a median of 0.14, 0.11 dex in age, 0.24, 0.17 dex in metallicity, and 0.10, 0.07 dex in stellar mass density, corresponding to errors on the gradients to be 0.07, 0.07 dex / R_e in age and 0.14, 0.13 dex / R_e in metallicity, for p9-19E and p9-127B respectively. This still allows recovery of significant gradients in all cases, showing that the MaNGA secondary sample should be able to find a good sample of clearly defined age gradients though may find difficulties for weak metallicity gradients. These results will form the basis of gradient comparisons in later sections.

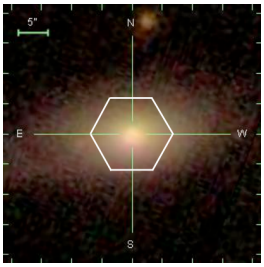

(a) SDSS image with the P-MaNGA footprint.

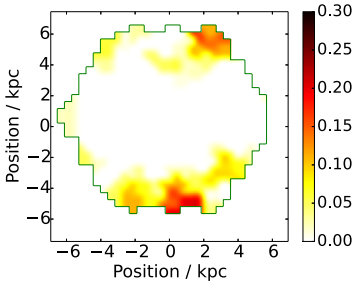

(b) Dust extinction, E(B-V).

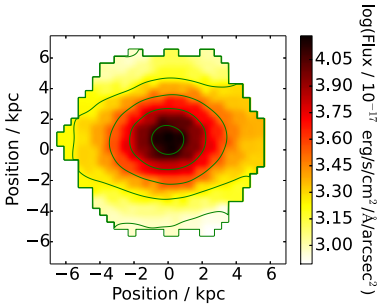

(c) Flux map with isoflux contours (green).

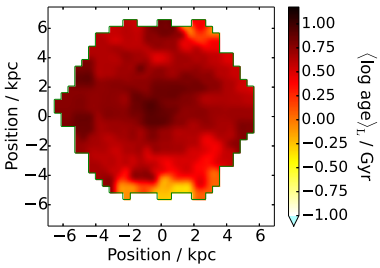

(d) Luminosity-weighted stellar age.

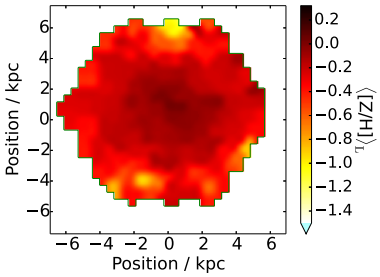

(e) Luminosity-weighted metallicity.

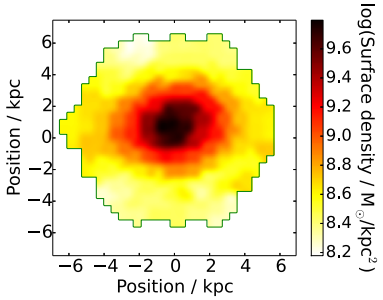

(f) Stellar mass.

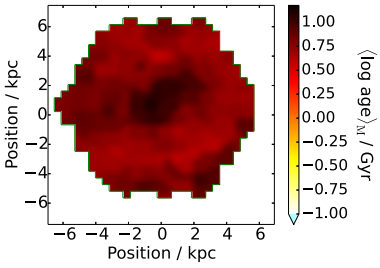

(g) Mass-weighted stellar age.

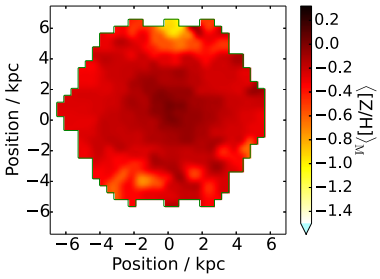

(h) Mass-weighted metallicity.

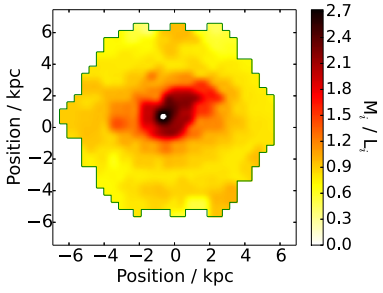

(i) Stellar mass-to-light ratio in the SDSS *i*-band.

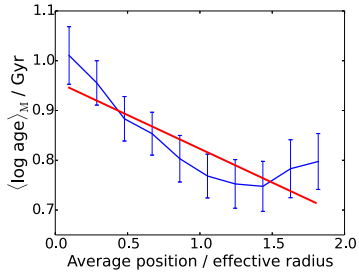

(j) Radial age profile.

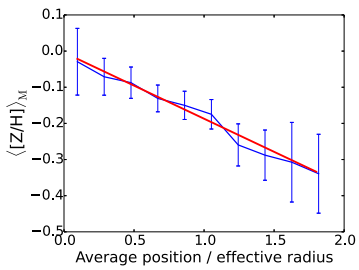

(k) Radial metallicity profile.

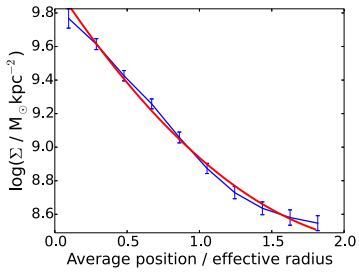

(l) Stellar mass surface density profile.

Fig. 5.2 **Group α, galaxy p9-19B** as in table 5.2. Stellar population maps and profiles analyzed using MILES-based models with their full parameter range. The radial profiles are over-plotted in red with a linear fit to the data, in the age and metallicity profiles to show the derived gradient (based on the same Voronoi data for consistency to ensure the same PDAP methods are used), and a quadratic fit in the stellar mass density profile in order to guide the eye. We use a pixel-to-pixel Gaussian filter to smooth the maps for ease of visualisation, but use a 0.5 sigma kernel in order to retain small-scale features.This galaxy has been observed with good observational conditions with a MaNGA-like exposure time and dithering, and is selected in the MaNGA primary sample. Therefore out of the P-MaNGA dataset, these observations are the most similar to the expected output of the MaNGA primary sample.

5.4.2 Non-MaNGA galaxies with high-quality data: Group β

The last two galaxies from the high-quality subsample of P-MaNGA would not be selected in the MaNGA samples, due to their low redshift and hence low radial coverage by the MaNGA IFUs. These galaxies, p9-127A (Appendix Figure A.4) and p9-61A (Figure 5.3), are observed with N_{127} and N_{61} IFUs, cover 0.7 and 1.2 R_e , and are visually identified as a face-on spiral and an early type galaxy, respectively. The high number of fibers per unit radius means that we are able to derive more detailed, but radially-limited, data than would be achievable with the full MaNGA samples.

As an example, galaxy p9-61A shows in its population maps and gradients a nearly flat metallicity profile with a ring of lower metallicities around the young central core. Its older population is shown as a 4 Gyr ring in $\langle \log \mathrm{age} \rangle_L$ around the core before becoming younger in its halo population. This is more difficult to see in $\langle \log \mathrm{age} \rangle_M$, suggesting that the mass fraction of young stars in the outer regions of the galaxy is small. The metallicity gradient is nearly flat on average, apart from the low metallicity ring causing a dip in the profile. The dust lane stretching vertically is clearly recovered in the dust attenuation map, though is quite wide across the central core. We can clearly see the effect of the dust in the age and metallicity maps too, with the dust regions corresponding to lower ages (particularly in $\langle \log \mathrm{age} \rangle_L$, very suggestive of recent star formation or a continuous star formation history) and higher metallicities.

The high spatial detail in these two cases will not be possible to recover in MaNGA due to the higher redshift, and therefore lower spatial resolution of the target galaxies. Nonetheless the radial profiles are similar in the range of errors to the group α primary galaxies, with 0.04, 0.11 dex in age, 0.05, 0.19 dex in metallicity and 0.03, 008 dex in surface mass density profiles for p9-127A and p9-61A respectively. Due to the smaller radial extent probed (0.7 and 1.2 R_e) this gives somewhat higher errors on the gradients recovered of 0.07, 0.13 dex / R_e in age and 0.09, 0.18 dex / R_e in metallicity, for p9-127A and p9-61A respectively.

5.4.3 MaNGA-selected galaxies with lower-quality data: Group γ

Five galaxies fall into the category of being selected in MaNGA, but due to testing of the P-MaNGA instrument, have lower exposure times, and/or were taken in poor observational conditions. Specifically, plate 11 and plate 4 have one and two hour exposure times respectively compared to the MaNGA exposure time of three hours, and plate 11 has the additional

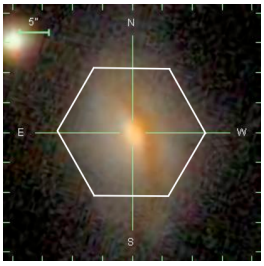

(a) SDSS image with the P-MaNGA footprint.

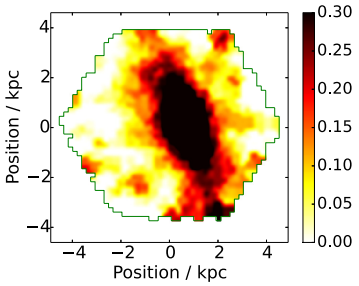

(b) Dust extinction, E(B-V).

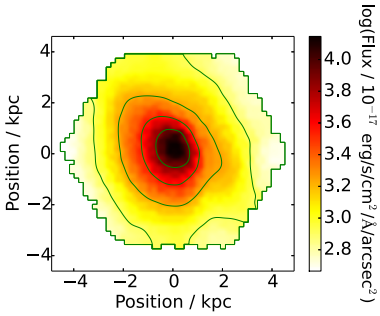

(c) Flux map with isoflux contours (green).

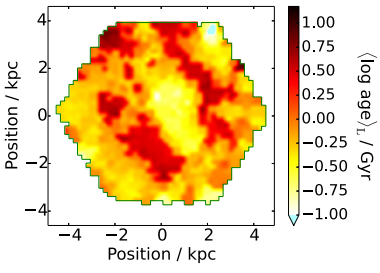

(d) Luminosity-weighted stellar age.

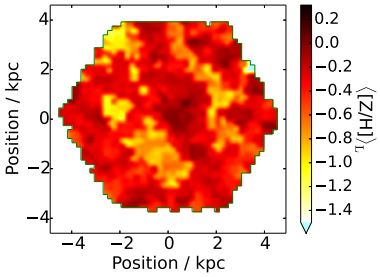

(e) Luminosity-weighted metallicity.

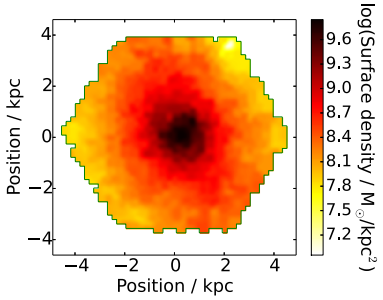

(f) Stellar mass.

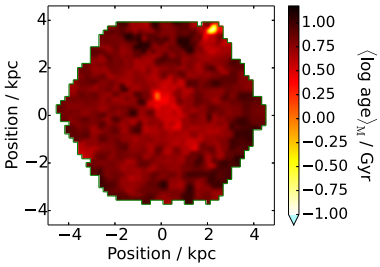

(g) Mass-weighted stellar age.

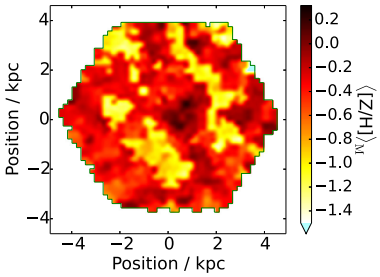

(h) Mass-weighted metallicity.

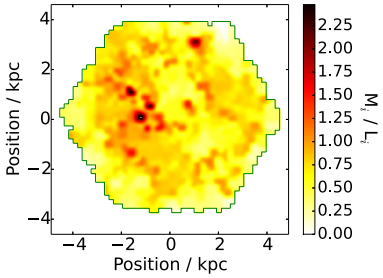

(i) Stellar mass-to-light ratio in the SDSS *i*-band.

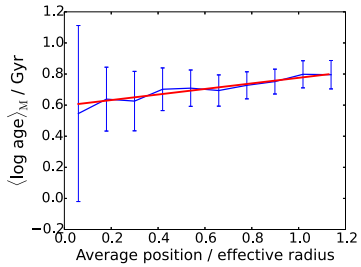

(j) Radial age profile.

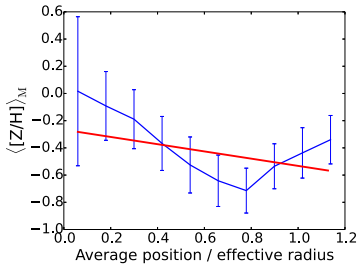

(k) Radial metallicity profile.

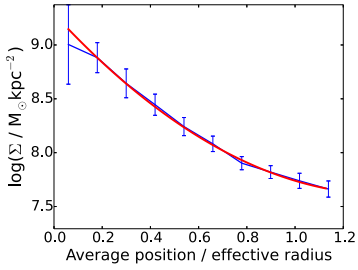

(l) Stellar mass surface density profile.

Fig. 5.3 **Group β, galaxy p9-61A** as in table 5.2. Stellar population maps and profiles analyzed using MILES-based models with their full parameter range, as described in detail in Figure 5.2. Observed under the same setup as galaxy p9-19B (Figure 5.2), except with a N_{61} IFU, and observed to a higher spatial resolution than would be targeted for the MaNGA sample.

problem of having been observing under an airmass of 1.5, see table 5.2.

We begin by looking at plate 4, which has observational conditions somewhat closer to what can be expected from the MaNGA sample than plate 11. Galaxies p4-19B (Appendix Figure A.5) and p4-19C (Figure 5.4) would fall in the primary MaNGA sample, with N_{19} IFU coverage of 1.4 and 1.3 R_e respectively. We take galaxy p4-19C as an example of galaxies in this group. It is an early-type galaxy, that from the stellar age population map has an intermediate-age (6 Gyr in both $\langle \log \mathrm{age} \rangle_L$ and $\langle \log \mathrm{age} \rangle_M$) core with a very flat gradient out to large radii. The $\langle [Z/H] \rangle_L$ and $\langle [Z/H] \rangle_M$ map shows a clear negative gradient; going from approximately half-solar metallicity to [Z/H] = – 0.5. The stellar mass density map is relatively smooth and radially symmetric.

The poorer exposure times results in somewhat poorer stellar population radial recovery than the group α and β galaxies. Errors are on the order of 0.06, 0.09 dex in age, 0.10, 0.21 dex in metallicity, and 0.06, 0.09 in stellar mass density for the profiles of p4-19C and p4-19B respectively. Stellar mass density profile errors are the least affected compared to group α which suggests that the quality of data lost by the lower exposure time affects age and metallicity determinations more significantly than surface mass density determinations. The corresponding respective errors on the gradients are 0.07, 0.11 dex / R_e in age and 0.08 – 0.21 dex / R_e in metallicity on average. Thus a 2 hour exposure, whilst giving about a factor 1.5 higher in error on the radial information obtained compared to MaNGA-like 3 hour exposures, can still give significant age gradients for many galaxies but would not be able to significantly test many metallicity gradients.

Plate 11 has two galaxies that would be selected in MaNGA, p11-61A and p11-19B, in the primary and secondary samples respectively. We do not show their stellar population maps since they represent much poorer data quality than what we expect from MaNGA, and the high pixel-to-pixel variance of the maps make them difficult to interpret. Instead we describe them briefly here.

Galaxy p11-61A is visually identifiable as an inclined disk galaxy, with N_{61} IFU coverage of 1.5 R_e , with a red core with bluer surroundings. This is matched to an older ($\langle \log \mathrm{age} \rangle_L$ = 5 Gyr / $\langle \log \mathrm{age} \rangle_M$ = 10 Gyr compared to surrounding $\langle \log \mathrm{age} \rangle_L$ = 0.5 Gyr / $\langle \log \mathrm{age} \rangle_M$ = 3 Gyr, metal-rich ($\langle [Z/H] \rangle_M$ = 0.2 dex compared to – 0.1 dex surroundings) bulge with a 1 kpc radial size, giving a strong negative age gradient. However, the stellar population maps and particularly the dust attenuation map shows a high degree of scatter that is not spatially confined to a particular region, suggesting that we are suffering from the effects of poor observational

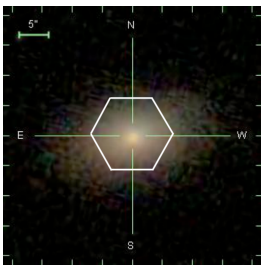

(a) SDSS image with the P-MaNGA footprint.

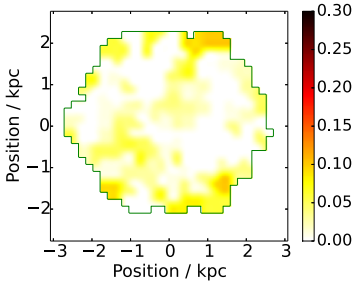

(b) Dust extinction, E(B-V).

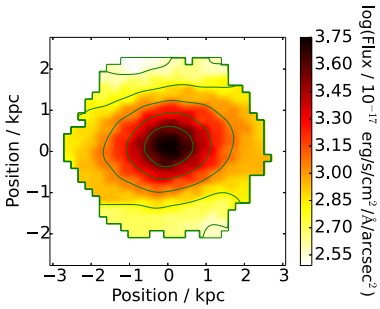

(c) Flux map with isoflux contours (green).

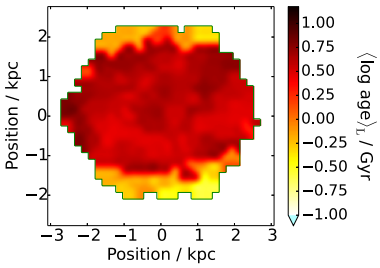

(d) Luminosity-weighted stellar age.

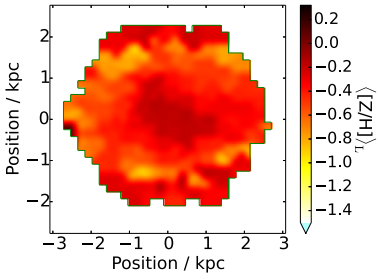

(e) Luminosity-weighted metallicity.

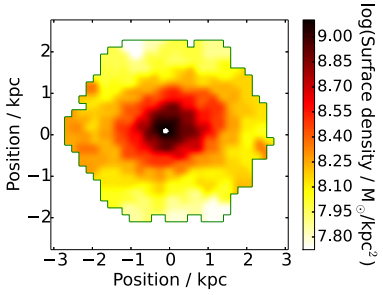

(f) Stellar mass.

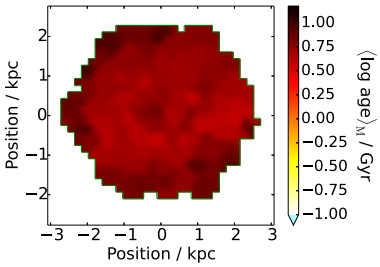

(g) Mass-weighted stellar age.

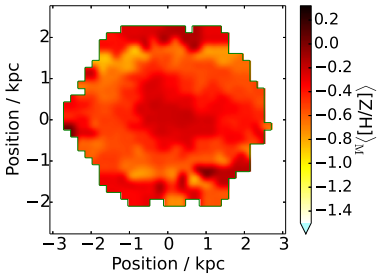

(h) Mass-weighted metallicity.

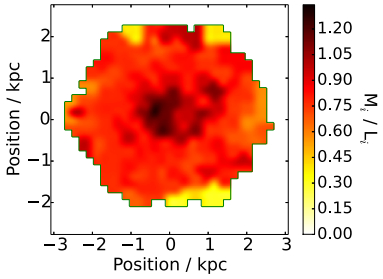

(i) Stellar mass-to-light ratio in the SDSS *i*-band.

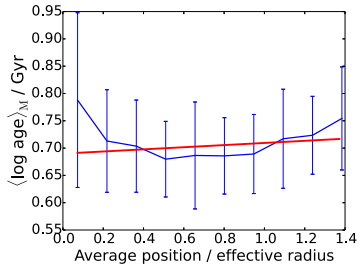

(j) Radial age profile.

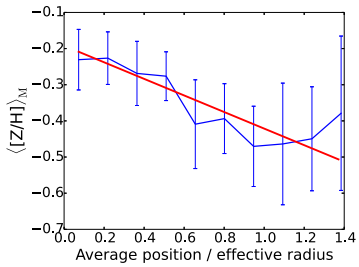

(k) Radial metallicity profile.

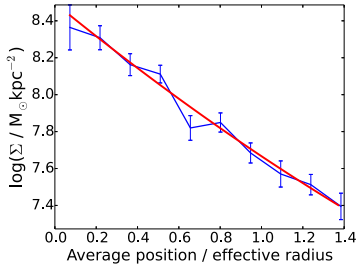

(l) Stellar mass surface density profile.

Fig. 5.4 **Group γ, galaxy p4-19C** as in table 5.2. Stellar population maps and profiles analyzed using MILES-based models with their full parameter range, as described in detail in Figure 5.2. This galaxy has been observed under poorer conditions and a lower exposure and dithering setup than expected for MaNGA. Nonetheless, we recover a simple and smooth stellar population structure with negative age and metallicity gradients.

conditions.

Similarly galaxy p11-19B, a face-on blue spiral galaxy, shows a high degree of scatter in its stellar population maps, particularly in its age map. This galaxy has an average age of 500 Myr, and also has a 2 Gyr red component in the South at the same redshift as the central galaxy visible in the SDSS image.

The stellar population radial profile recovery is somewhat better in p11-61A, despite both showing signs in their maps of artificial irregularity in their age and metallicities resulting from uncertainty in the spectral fit. This could be the result of galaxy p11-61A being a highly compact object compared to every other object in the sample and thus its fluxes on each individual fiber being higher. Since this galaxy is therefore a much brighter per unit area than other galaxies in the sample we expect errors on its gradients to be lower than the other galaxy in this subsample, p11-19B.

The radial profile errors are 0.09, 0.27 dex in age, 0.11, 0.36 dex in metallicity and 0.07, 0.16 dex in stellar mass density for p11-61A and p11-19B respectively. We note that galaxy p11-19B has a much larger radial extent than other galaxies in the sample, which could explain the larger errors on the profile, but reduces errors in the gradients. Errors on the gradients are 0.07, 0.16 dex in age and 0.11, 0.36 dex for p11-61A and p11-19B respectively.

5.4.4 Non-MaNGA galaxies with low-quality data: Group δ

This group has the highest membership of any of the identified groups above, containing seven galaxies, four in plate 11 and three in plate 4. The galaxies in this subsample are: p11-127A, p11-127B, p11-19A, p11-19C, p4-127A, p4-127B, and p4-61A. Rather than describe each galaxy in detail, we discuss some interesting features from this group. We later discuss the errors on the radial profiles for these galaxies as part of the sample as a whole and so refer the reader to section 5.5.3 for this discussion.

A feature common to p4-127A and p11-127A is the presence of a very strong dust lane across a large portion of the observation. In both cases, this feature is shown clearly in the dust attenuation maps (Figure 5.5a and 5.5b for p4-127A and p11-127A respectively) and corresponds to somewhat younger ages and, interesting, less metal-rich (approximately $\langle \log \text{age} \rangle_L = 3$ Gyr younger and $\langle [Z/H] \rangle_L = 0.2$ dex less compared to surroundings). Both of these cases give a clear interpretation of a dusty disk that has undergone more recent star formation than its surroundings from some relatively metal-poor gas. We also note that p11-127A has more vari-

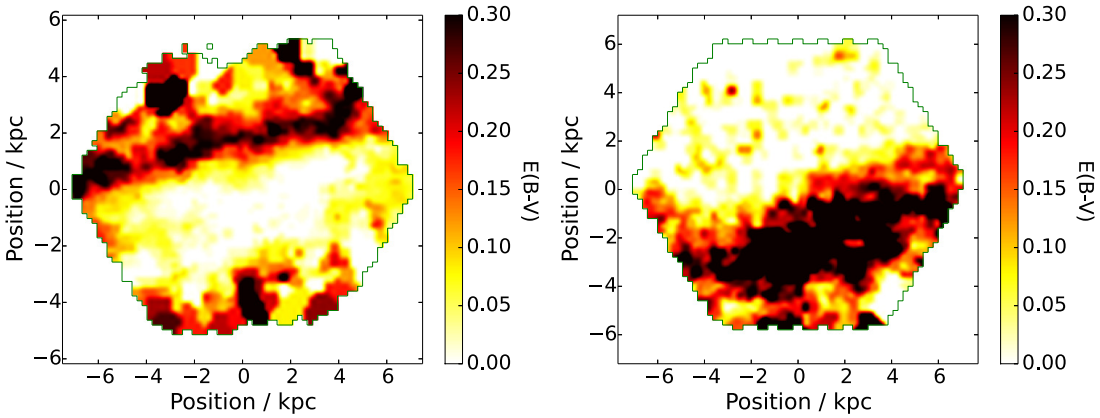

(a) Dust attenuation map of galaxy p4-127A. (b) Dust attenuation map of galaxy p11-127A.

Fig. 5.5 **Group δ galaxies p4-127A and p11-127A** as in table 5.2. These two galaxies have very clear dust lanes that show evidence of more recent star formation than their surroundings. Both of these galaxies have been observed under poorer conditions and lower exposures and dithering setup than expected for MaNGA, although p4-127A has been observed under worse conditions and setup than p11-127A, translating to a more speckled appearance in its maps.

ance in its derived stellar population properties, giving a 'speckled' appearance in the maps, compared to p4-127A, which can be attributed to the poorer observational conditions in the former case.

The observational conditions combined with the N_{19} IFU for galaxies p11-19A and p11-19C render the interpretation of stellar population maps (such as the age maps in Figures 5.6a and 5.6b) very difficult, however one can draw comparisons with the qualitatively similar galaxies in the higher-quality subsamples, galaxies p4-127A and p4-19A respectively. This gives an idea of the conclusions one might be able to draw from these galaxies if they were observed under better conditions, and conversely how much conclusions get blurred by observing galaxies in poor conditions. The variance of stellar population parameters of p11-19A and p11-19C additionally translates to poor constraints on these galaxies' radial profiles, and so this is a clear limitation of using such low (1 hour) exposure times under poor observational conditions.

The main effect of the poor observational conditions is the added Voronoi cell-to-cell variance which washes out smaller-scale structure. The identification of galaxy features such as disk structure is not possible in these cases.

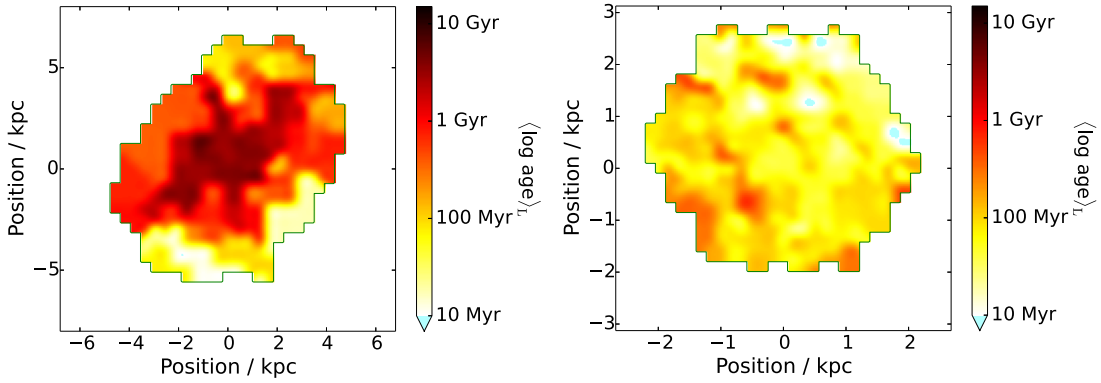

(a) Light-weighted stellar age map of galaxy p11-19A.

(b) Light-weighted stellar age map of galaxy p11-19C.

Fig. 5.6 **Group δ galaxies p11-19A and p11-19C** as in table 5.2. These galaxies have been observed under much poorer conditions and much lower exposures and dithering setup than expected for MaNGA. Both of their maps show an unclear distribution of stellar population properties, with in general high amounts of variance between neighbouring pixels.

5.5 Results

5.5.1 Radial gradients

The age and metallicity gradients for the prototype dataset are summarized in the histograms of figure 5.7. We re-iterate from the beginning of this section that all gradients and radial profiles are calculated from mass-weighted stellar population properties rather than light-weighted properties, since these more precisely trace the evolutionary history of the galaxies observed, and thus are more appropriate for assessing formation and evolutionary mechanisms.

Both age and metallicity gradients seem to draw from different distributions for spheroid / early-type galaxies and disk / late-type galaxies. Age gradients for late-types are overall strongly negative with a mean of – 0.39 dex and a wide standard deviation of 0.36 dex, compared to early-type galaxies which have a flat (mean – 0.05) age gradient and 0.24 dex standard deviation. Conversely, metallicity gradients for late type galaxies are flat (mean 0.00 dex), with 0.17 dex standard deviation, and early-type galaxies have a negative gradient of mean – 0.15 dex with a 0.14 dex standard deviation. Unfortunately these differences are only indicative of what may be produced by the full MaNGA survey in the future; a K-S test on the results finds that there are not enough galaxies to deduce a significant difference between the two samples. Future work will test the conclusions made on this result.

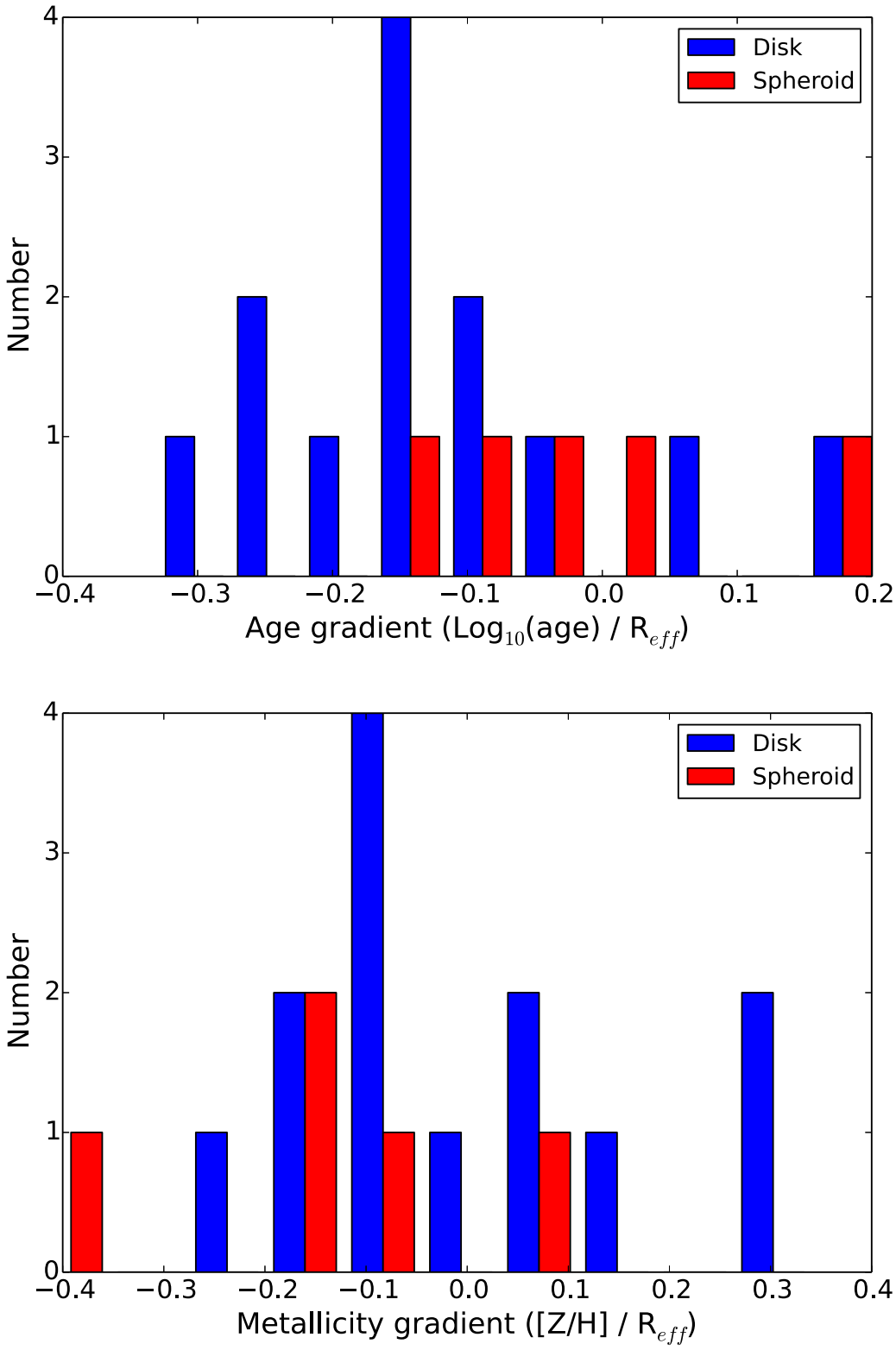

Fig. 5.7 Summary of all of the age (left) and metallicity (right) gradients deduced for the P-MaNGA dataset, using visual morphological classification from SDSS imaging data.

If we assume our results do not change significantly with sample size, our findings on metallicity and age gradients agree very well with previous analyses of early-type galaxies, such as in Kobayashi & Arimoto (1999), Saglia et al. (2000), Tamura et al. (2000), Mehlert et al. (2003), Wu et al. (2005), Annibali et al. (2007), Sánchez-Blázquez et al. (2007), Rawle et al. (2008), and Kuntschner et al. (2010), in particular the lack of a significant age gradient in early-type galaxies.

For our late-type galaxy sample we do not attempt to separate the light from the bulge and from the disk as it is beyond the scope of this work. Thus our overall gradients, particularly in age, cannot be compared directly to previous work that has done this, for example Sánchez-Blázquez et al. (2014) and MacArthur, González & Courteau (2009), and work based on local galaxies such as Williams et al. (2009) and Barker et al. (2007). However we note that our metallicity gradient estimates agree well with these literature sources in these cases. We conclude that bulge-disk separation is the main driver for the negative age gradients seen in P-MaNGA galaxies and so our conclusions agree well with the literature. For previous work assessing the age and metallicity gradients of late-type galaxies including the disk and bulge, such as Sánchez-Blázquez et al. (2011) and Yoachim & Dalcanton (2008), we find good agreement with our gradients and overall conclusions.

With our limited sample size we cannot draw significant conclusions on the relationships of stellar population gradients as a function of other physical properties. However in Figure 5.8, to compare with recent work by González Delgado et al. (2014) we plot the total stellar mass as measured in P-MaNGA against $\langle \log \mathrm{age} \rangle_\mathrm{L}$ / R_e for the late-type galaxies to see if our results are consistent. Total stellar mass estimates are calculated from u, g, r, i, z photometry following the method in Maraston et al. (2006) and Maraston et al. (2013) for SDSS-III/BOSS galaxies (Pforr et al., in preparation). 'Photometric' stellar masses do not suffer from aperture effects as will be described in Section 5.5.4. In section 5.5.4 we also test the relationships between gradients and total stellar mass.

We find that at low masses, below $\sim 10^{10}$ $\mathrm{M}_\odot$, $\langle \log \mathrm{age} \rangle_\mathrm{L}$ gradients are generally close to flat, but that above $\sim 10^{10.5}$ $\mathrm{M}_\odot$ the $\langle \log \mathrm{age} \rangle_\mathrm{L}$ gradients are very strongly negative. The correlation shown in consistent with being negative at the 90 percent level but not at 95 percent, showing that we have a reasonably strong trend in place already but stronger evidence will hope to strengthen this result further.This matches well with González Delgado et al. (2014), who find that low-mass disk galaxies show flat age gradients but at higher masses the gradients become strongly negative, with a very similar match in linear gradient. They also test early-type galaxies, but with our very small sample of early-types we are unable to see a clear

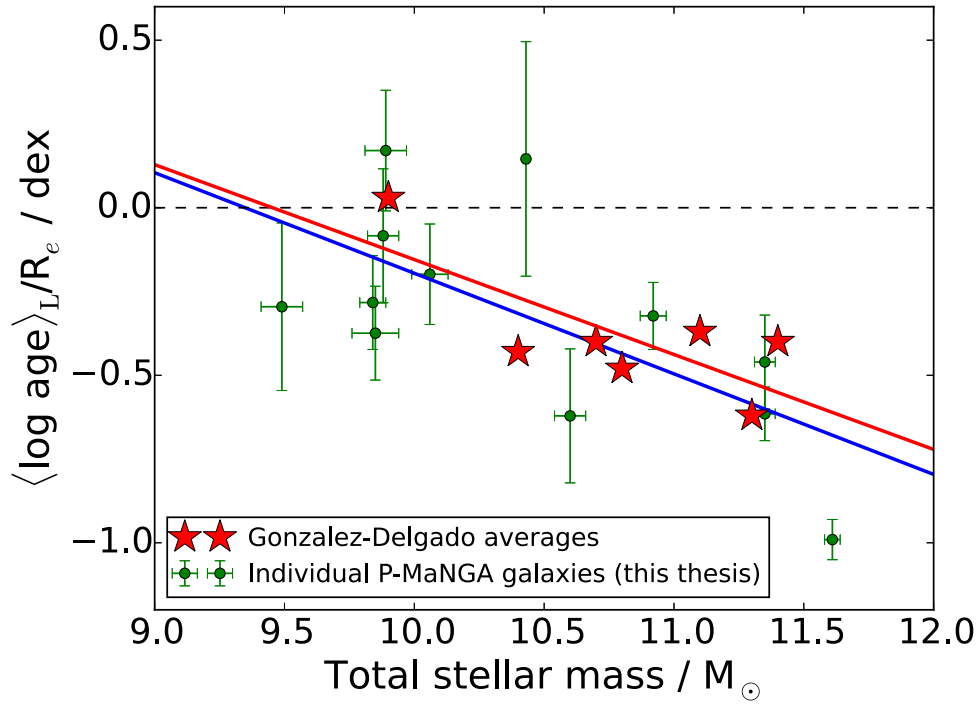

Fig. 5.8 A scatterplot showing the relation between photometric stellar masses and $\langle \log \text{age} \rangle_{\text{L}}$ / R_{e} as derived in this thesis, for the late-type galaxies in the P-MaNGA sample as listed in Table 5.2 in blue, with a best-fit linear regression line. In red we plot the results of González Delgado et al. (2014) of all their galaxies, which are averaged over a large sample as a function of mass to give the red star points, again with a linear regression line. Lastly in dashed black we show the zero gradient line.

correlation with total stellar mass so we do not pot them here. In our sample we find no clear evidence for relationships between $\langle \log \mathrm{age} \rangle_{\mathrm{M}}$, $\langle [\mathrm{Z/H}] \rangle_{\mathrm{L}}$ or $\langle [\mathrm{Z/H}] \rangle_{\mathrm{M}}$ with total stellar mass, suggesting that the main driver for the $\langle \log \mathrm{age} \rangle_{\mathrm{L}}$ — $\mathrm{M}_{\odot}$ relation is the radial transition between bulge and recent star formation in the disk.

5.5.2 Beam smearing

Results from IFU experiments can be threatened by the risk of 'beam smearing', an effect that spreads out the signal for a given pixel position into nearby pixels. Beam smearing is the combination of three observational effects: atmospheric point-spread function (PSF), sampling size of the IFU fibers, and dithering; the process of offsetting the telescope from the target by small amounts such that the fibers collectively observe whole footprint, including gaps between fibers. The effect of beam smearing should be greatest for the smaller IFUs, since there are a smaller number of fibres, meaning that the physical separation between them on the galaxy (for a given radial footprint) is larger.

Given that our largest sample of galaxies are late-type galaxies and these have generally a large range of negative gradients, we can test to see if decreasing the IFU size results in poorer age gradient recovery, for these galaxies. Metallicity gradients are not tested since there are both positive and negative gradients in the late-type sample which may be hard to separate between, and our early-type sample is too small to derive meaningful conclusions in this area.

In Figure 5.9 we plot the age gradient histograms for the late type galaxies shown in Figure 5.7, as a function of IFU size: N_{19}, N_{61} and N_{127} fiber IFUs. In the left-panel we plot the mass-weighted radial age gradients as we have plotted in Figure 5.7, where we find no correlation between mean gradient and IFU size. The mean age gradients are – 0.12, – 0.19, and – 0.13 dex for N_{19}, N_{61} and N_{127} observations respectively.

We also plot light-weighted age gradients for comparison in the right panel, since these will be more sensitive to bright stellar populations and so should be more directly related to beam smearing effects. We therefore expect larger (in magnitude) gradients to be present since small amounts of star formation in an otherwise more passive galaxy can cause large changes in the light-weighted profiles. In this case the separation is much easier to see, with N_{19} observations giving much flatter gradients (mean – 0.08 dex) than N_{127} observations (mean – 0.55 dex), and N_{61} lying in between but closer to the N_{127} observations (mean – 0.43 dex). We note that the 2 galaxies with the largest negative age gradients, around –1.0 $\langle \log \mathrm{age} \rangle_{\mathrm{L}}$ $/R_{\mathrm{e}}$,

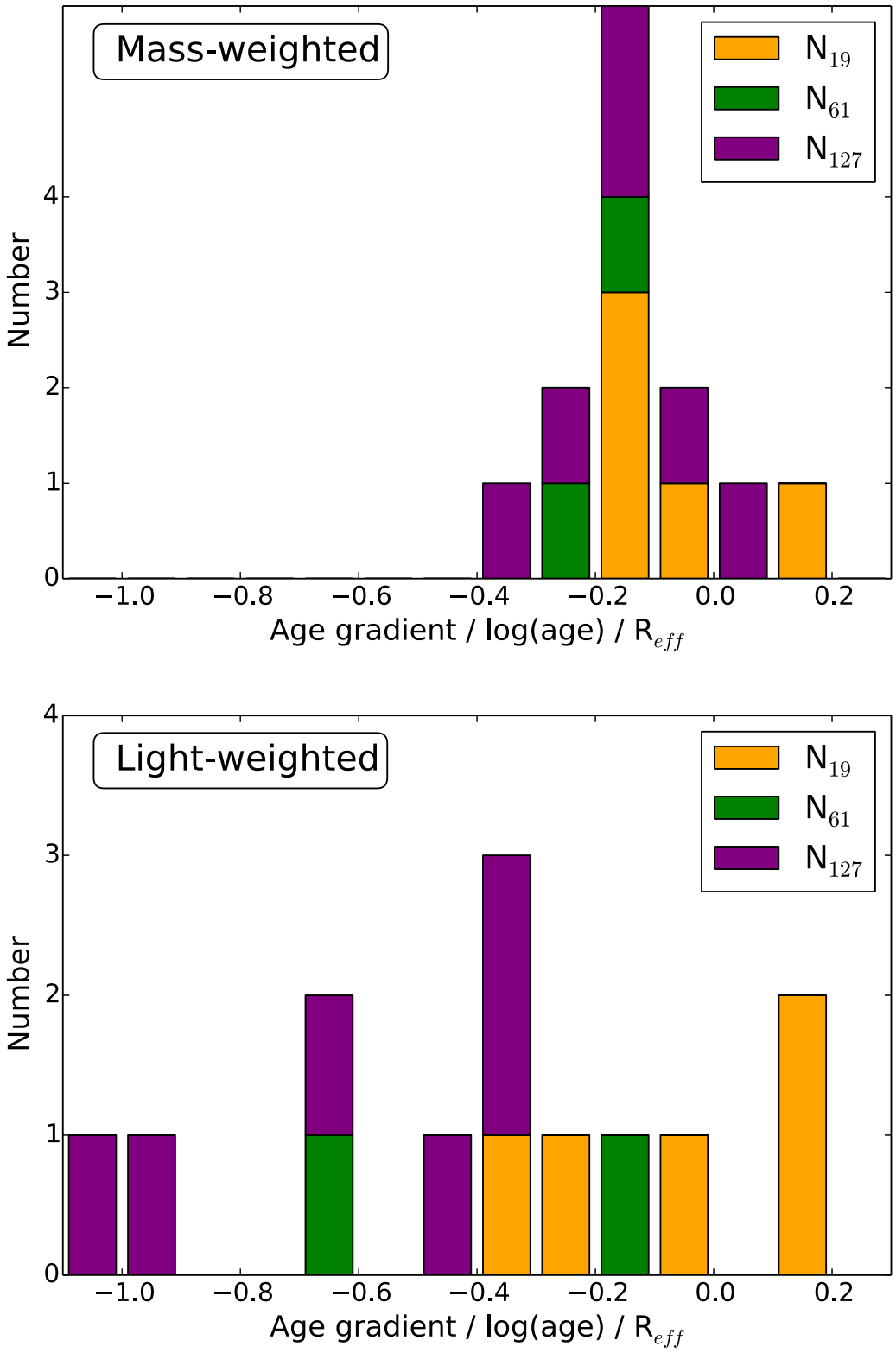

Fig. 5.9 Histograms of age gradients as in Figure 5.7, selecting only the late-type galaxies in the sample, as a function of IFU size. In the top panel we show mass-weighted age gradients as in the other profile and gradient Figures in this Chapter. In the bottom panel we show light-weighted age gradients since these will trace bright stellar populations, and thus are important for testing the effect of beam smearing.

correspond to two late-type galaxies with both spiral or disk features and very prominent bulges, p9-127A and p11-127A, clearly identifiable visually and covered within P-MaNGA N_{127} footprint. Hence it is expected that these galaxies should have very large negative age gradients in their light-weighted profiles, compared to other types of galaxies or smaller IFU sizes where the morphological features may be more difficult to separate.

We therefore conclude that beam smearing does appear to affect the lowest IFU sizes much more in the light-weighted properties, and thus is more sensitive to bright stellar populations such as from very young stars, but this effect is mitigated by calculating mass-weighted properties.

We do not go further to quantify this effect due to small sample size, and thus overlap with other effects such as radial extent and other physical galaxy properties. A detailed analysis of N_{127} MaNGA data, downgraded to the other IFU sizes, will be necessary for robust quantification, which will be subject of future work once a larger sample is available. Additionally with the much larger MaNGA sample we will be able to carry out this analysis with comparable inclinations, morphologies and colour gradients.

5.5.3 Statistical error as a function of observational conditions

In each of the P-MaNGA galaxies analysed we have derived stellar population property statistical errors on each of their pixels, as described in section 5.3, which we then propagate to standard errors on each of the elliptical bins in the radial profiles. We explore how these errors vary as a function of the observation conditions and setup used to observe each galaxy.

To measure the error on the gradient we need to find the standard error at the median radial bin. However, this decreases as a function of the number of pixels used increases, and does not include the covariance between pixels, thereby underestimating the uncertainty on the fit. In this work we do not estimate covariance between pixels due to the prototype nature of the observations. To compare these errors across each of the P-MaNGA galaxy, we therefore take the standard deviation averaged across all the pixels at each radial bin, assume the number of independent observations is equal to the number of grid points analysed divided by 16, as explained in Section 5.3.2, and find the median of this value. To be concise, we shall refer to this as the *median standard error*. This value remains constant as the number of pixels in each bin is changed, allowing us to compare this value across each galaxy directly.

Corresponding errors on the gradients are calculated from the errors on the profile points by

using bootstrap resampling of 10,000 points for each profile point recovered and recalculating the linear gradient on each resample. We note that the error calculated assumes a linear fit, hence does not describe *how linear* the radial profiles are. We assume that the errors on each point are Gaussian, which typically is an accurate approximation of the error obtained from the spectral fit with FIREFLY. We note that errors on the gradient will not directly correspond to the errors on the profile since each galaxy is observed with a different radial extent.

The upper panel of Figure 5.10 presents the median standard error for mass-weighted stellar age, metallicity and surface mass density as a function of plate, each of which corresponds to a set of observational conditions summarised in Table 5.3. We can clearly see that for all three properties, plate 9 provides the smallest errors, and plate 11 provides the highest errors, on the radial profiles. Each box plot has a high interquartile range due to the small sample size, as there are only 6 galaxies in each bin. We remind the reader that only plate 9 has been observed with MaNGA-quality conditions and setup (3 hour exposure), whereas plate 4 and plate 11 have less than MaNGA-quality observations (2 hour exposure, and 1 hour exposure with 1.5 airmass, respectively).

The corresponding errors on the age and metallicity gradients are shown in the lower panel, also summarised in Table 5.3. We note that this panel does not linearly relate to the upper panel due to each of the galaxies having different radial extents, as well as some parts of the profile being more important than others to constrain the errors on the gradient. We do not calculate stellar mass density gradients as they are not appropriate to fit with a linear profile. Again plate 9 provides the best gradient determination, with the smallest interquartile ranges in the gradient errors. We thus deduce that plate 9 galaxies provide a more stable and reliable gradient determination for both age and metallicity. There is less evidence to separate plate 4 and plate 11 galaxies in this case, other than plate 11's age gradients seeming to have a larger interquartile range and thus is provides the least stable errors estimations as a function of galaxy observed. Metallicity gradients show little separation in their median value for all three plates, despite plate 9 having a lower interquartile range, suggesting that *average* metallicity gradients are on average less sensitive to observational quality than age gradients but do become less stable with each galaxy, with worsening observations. Due to the small size of P-MaNGA's sample, we do not further separate on galaxy type, radial extent, or suggest stronger conclusions on the errors on the profiles and gradients. We summarise the errors in Table 5.5.

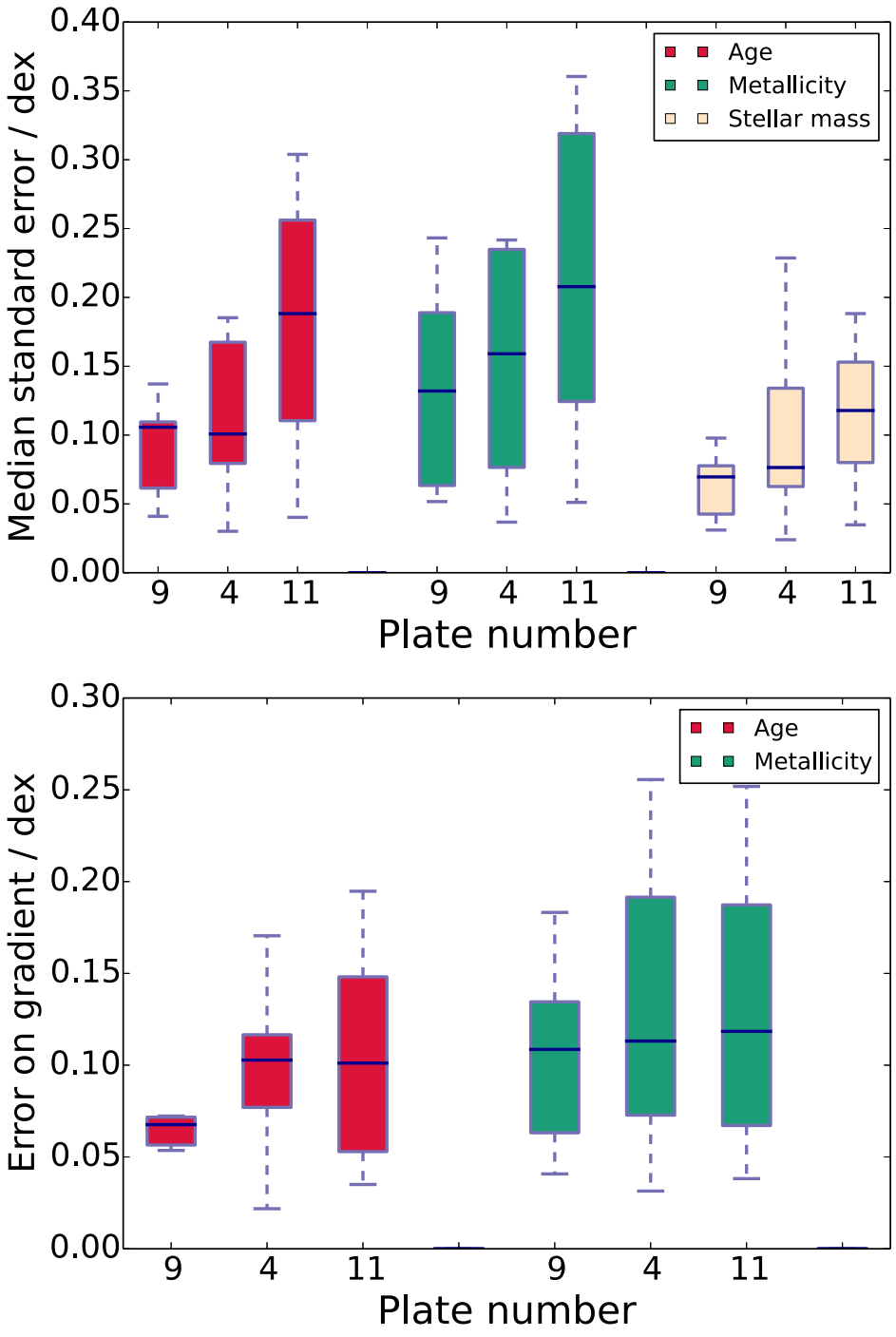

Fig. 5.10 Median standard errors (top panel), and errors in the linear gradient (bottom panel), of stellar population profiles as a function of property and observational conditions grouped by plate number, see Table 5.5. Errors in the gradient are calculated through bootstrap resampling of the median standard errors. Each box plot shows the median and interquartile range of the corresponding subsample, each of which contains the median standard error and the errors on the gradients of six galaxies. Stellar mass density gradients not shown as they are not appropriate to fit with a linear profile.

Field	Groups	Conditions and setup	Median error in profile / dex			Error on gradient / dex/R_e	
			Age	Metallicity	Mass density	Age	Metallicity
9	α/β	Exposure 3.0 hr, seeing 1.″7	0.10	0.13	0.07	0.07	0.11
4	γ/δ	Exposure 2.0 hr, seeing 1.″3	0.10	0.16	0.08	0.10	0.12
11	γ/δ	Exposure 1.0 hr, seeing 2.″0, (airmass $\sim$1.5)	0.19	0.22	0.12	0.10	0.12

Table 5.5 Summary of errors on radial profiles and gradients as a function of observational conditions and setup.

5.5.4 Stellar mass estimates

Given that FIREFLY also allows the calculation of stellar masses, we make a qualitative comparison with previous estimates for the P-MaNGA galaxies.

First we compare to the widely used 'Galspec' catalogue from the MPA-JHU group, based on Brinchmann et al. (2004) of the SDSS Data Release 8 pipeline (see Table 5.2) in Figure 5.11. These masses are based on broadband *ugriz*-filter SED fitting scaled to 3 arcsecond fiber sizes. This spatial coverage is much smaller than our P-MaNGA, which extends up to 1.5 effective radii. Hence we integrate the surface mass density only up to this radius for each galaxy. We find good overall agreement with the MPA-JHU masses with a systematic offset of about 0.1 dex and a scatter of 0.2 dex.

We note that the presence of galaxy gradients may complicate this simple scaling of the M/L ratio as this quantity depends on both age and metallicity. In addition, the stellar population modelling and fitting technique is different. The MPA-JHU masses are based on Bruzual & Charlot (2003) stellar population models and a coarser grid of ages than this work, using (unpublished) models based on the MILES stellar library and a Kroupa IMF. Hence, the stellar library and most importantly the IMF are the same, but the population models and age grids used are different. Other effects could also introduce systematics. The subtraction of stellar mass loss which is performed in our modelling, may corresponds to 30-40% by mass depending on the IMF (see Maraston (1998), Maraston (2005)) and it is not clear to us how this is accounted for in the MPA-JHU calculations.

Furthermore, masses obtained via spectral fitting may be different from those from broadband SED fit particularly when the former refer to low S/N spectra. Maraston et al. (2013) (see Appendix) find that the stellar mass of SDSS-III/BOSS galaxies at redshift $0.4-0.6$ were smaller when computed via broad band *ugriz* SED fitting by 0.25 dex compared to those obtained via PCA spectral fitting by Chen et al. (2012), as shown in Chapter 4. The hypothesis is that the spectral fitting of low S/N spectra may lead to high-ages, which have a higher M/L ratios. Chen et al. (2012) quantify this effect by applying full spectral fitting to high S/N empirical spectra and conclude in this direction.

This source of systematics is in common with the second stellar mass comparison plot in Figure 5.11, namely 'photometric'-based stellar masses calculated with the same model and fitting set up as those output of the SDSS-III/BOSS data release and pipeline (Dawson et al., 2013), as Chapter 4. In brief, these are also broad band *ugriz* SED fitting performed with the

publicly available code Hyper-Z customed with Maraston (2005) models, Kroupa IMF and our same account of mass loss. The template star formation histories encompass a range of exponentially declining τ-models, ranging from 0.1 to 3 Gyrs. No dust reddening is applied to the fitting in order to minimise the age-dust degeneracy which can lead to too young solutions which underestimate the true stellar mass (see Pforr, Maraston & Tonini (2012)). We note that a clump of galaxies in this lower-left of the plot which seem even quite far from the line are all identified as star-forming late-type galaxies in this sample, and so we expect a τ to not be able to capture these more complex star formation histories, explaining this discrepancy. Our stellar masses are on average 0.15 dex smaller than these photometric total masses. This offset will mainly come from the difference in aperture. Since P-MaNGA covers on average 1.5 R_e rather than the full extent of the galaxy as in the photometric masses, we expect our observations to cover $\sim$ 75 per cent of the light. This would give a 0.12 dex underestimate of the stellar masses, consistent with the offset we find in our comparison.

5.5.5 Effect of input stellar library

In this section we compare the results of fitting the M11 models based on the three empirical stellar libraries. We use the same example galaxy p9-127A for which we show in Figure 5.13 $\langle \log \mathrm{age} \rangle_L$ and $\langle \log \mathrm{age} \rangle_M$ maps, light-weighted age and metallicity profiles and stellar mass density profiles. In both this section and Section 5.5.6, we use light-weighted properties for the radial profiles, as these are more sensitive tracers of processes that we wish to test recovery of, such as recent star formation or very low metallicity stellar populations. However we also discuss the differences between the light- and mass-weighted age maps.

Note that in this comparison we have restricted the model parameters to be identical, hence results obtained with the MILES-based models here will be different from those obtained with the full parameter range. This corresponds to a wavelength range of 3900 – 6800 Å, ages varying between 30 Myr and 15 Gyr, and metallicities of 0.5, 1.0, and 2.0 times solar metallicity. Hence for example, the metallicity gradient for MILES-based models is somewhat positive in this case compared to the negative gradient for the same galaxy fit with the full parameter range, for which we are able to use lower metallicity stellar population components.

These plots illustrate behaviours of the model comparisons that are found among all test galaxies, namely:

– Overall distributions of stellar ages are similar in structure, however the average age values

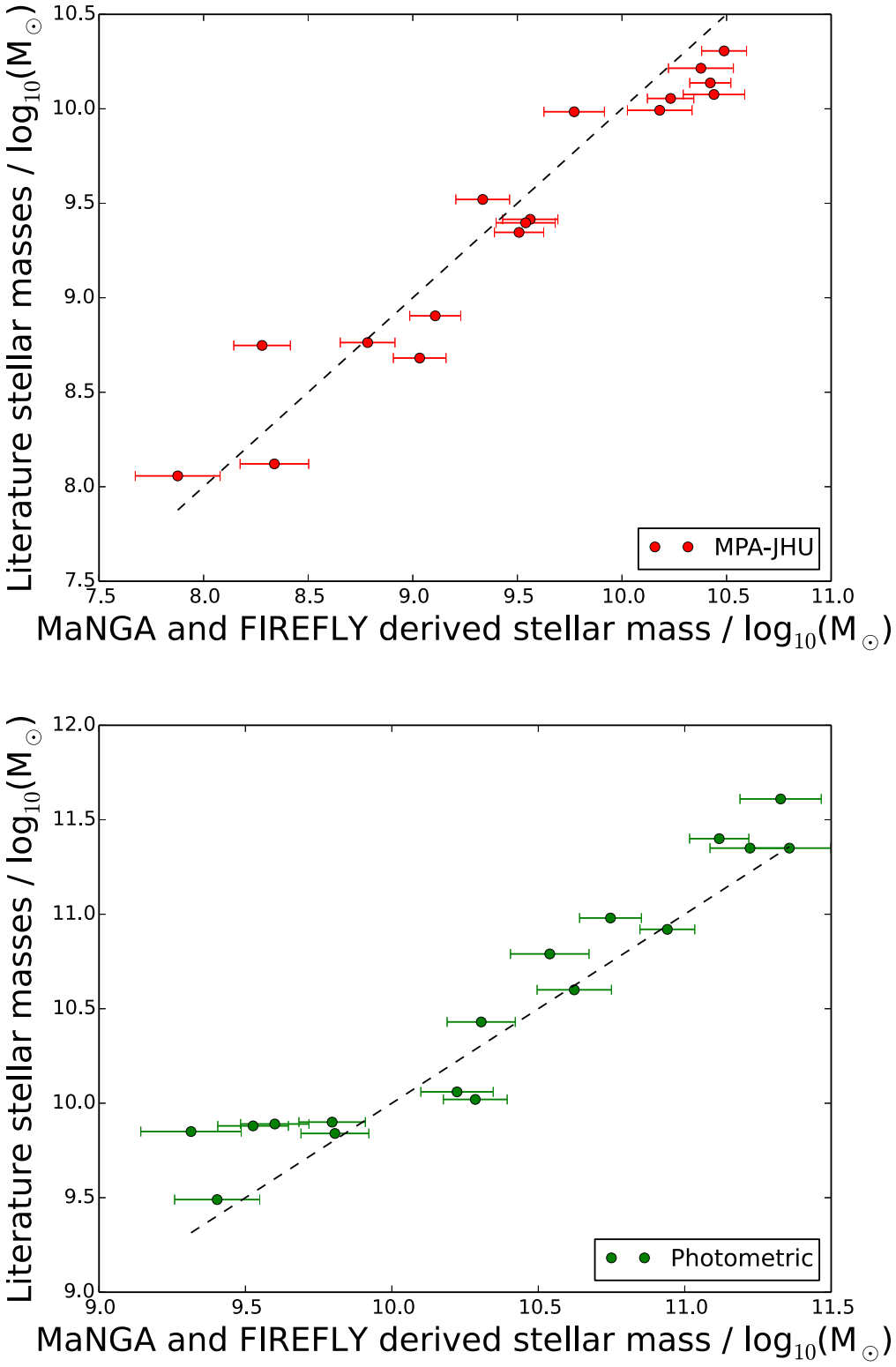

Fig. 5.11 A comparison of the total stellar mass derived for each of the P-MaNGA galaxies between this work, the 'Galspec' catalogue from the MPA-JHU group, based on Brinchmann et al. (2004) in the SDSS Data Release 8 pipeline, and the 'Photometric'-based stellar masses based on Pforr, Maraston & Tonini (2012). In black we show a one-to-one dashed line. We note that the two panels have different scales due to using a 3" aperture in the MPA-JHU comparison, but the full P-MaNGA aperture in the Photometric comparison.

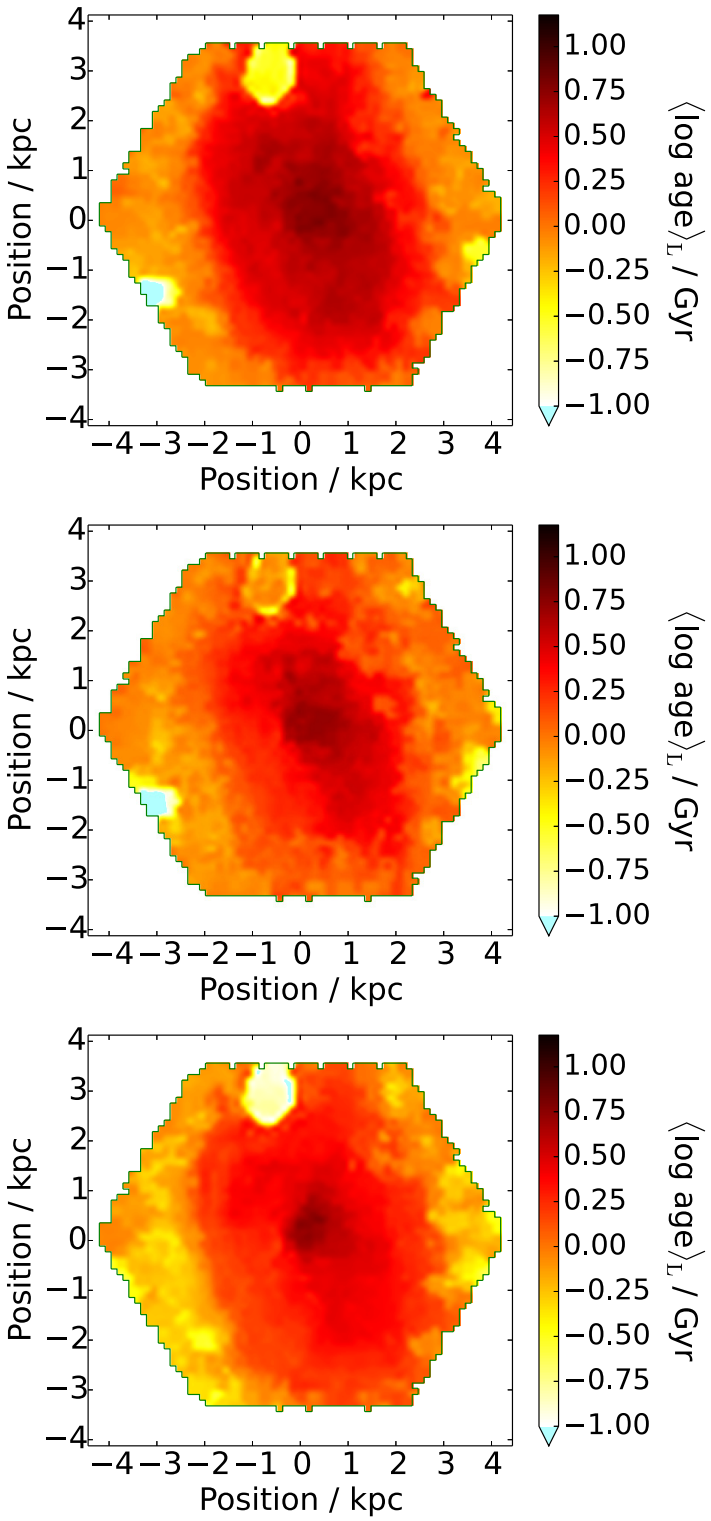

Fig. 5.12 Light-weighted age maps of p9-127A as a function of stellar library; MILES, STELIB, and ELODIE are shown in the left, middle, and right panels respectively.

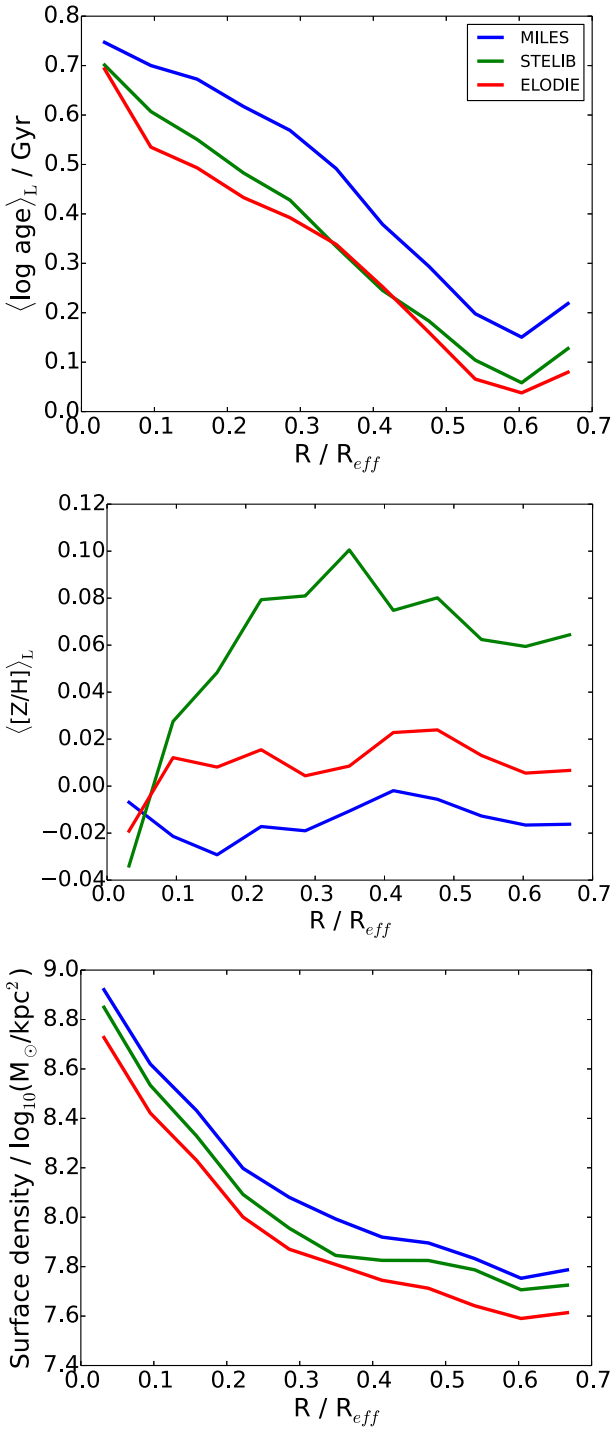

Fig. 5.13 Radial profiles of stellar age, metallicity and surface mass density respectively as a function of stellar library. Both this and the plot on the previous page show the effect on galaxy properties of the stellar library input in the stellar population model. In all cases, models were fit with identical stellar population parameter grids (see section 5.3.1). Maps are composed of Voronoi binned cells of properties, corresponding to binned spectra that cover enough sky area such that the median signal-to-noise at any given cell is as close as possible to 5. Typically this means that the outer Voronoi cells of the galaxy cover a more extended area than the inner cells. The radial properties are computed from spectra summed in annuli that have radial extent that approximately scales logarithmically, in order to give the surface mass density (right-hand side) profiles.

can vary by an order of 3 Gyr in the worst cases (see for example, the radial extent of high ages in the MILES stellar age map in Figure 5.13, compared to the other two models). Age gradients are the same for the three models.

– Metallicity maps and profiles also show very similar structures among the three models, though STELIB-based models correspond to a slight increase of 0.1 dex in [Z/H] in the outer parts of its maps compared to the other models. The metallicity gradients are flat for MILES and ELODIE-based models but the STELIB-based models have a clear increase in the inner 0.2 R_e , giving a positive metallicity gradient across the whole galaxy of 0.1 dex / R_e .

– We note that ELODIE-based models have slightly redder spectra than STELIB-based models at these approximate parameters, explaining why STELIB-based models fits for higher metallicity and slightly higher age. Age-metallicity degeneracy causes this colour offset to mix between age and metallicity offsets. This is visible in Figure 5.13 where the larger offsets in either the age or metallicity profiles at a given radius correspond to a smaller offset in the other profile.

– Stellar mass maps obtained also show very similar structure, with 0.1 dex variation between models visible in the gradients. This is interpreted as different models fitting differently according to age-metallicity degeneracy, with the older ages (as in the MILES-based models) corresponding to higher stellar mass.

These systematic effects between libraries may be important and so we provide the fitting parameters obtained for all 3 libraries used. These conclusions allow us to have estimates for systematic errors in the modelling to bear in mind when considering comparisons with other fitting codes, methods, models and surveys. A more quantitative and comprehensive analysis of this will be subject of future work based on a larger set of MaNGA galaxies.

5.5.6 Comparison with the CALIFA galaxy survey and with PPXF

In the P-MaNGA sample there are three galaxies that overlap with the CALIFA survey (Sánchez et al., 2012). Two of these lie in group δ, whose poor data quality in the P-MaNGA survey make a direct comparison between the results of the survey difficult to interpret. However, one galaxy, p9-127A, lies in group β, enabling a good opportunity to explore how MaNGA-like observations compare to CALIFA observations, even though this galaxy will not be in MaNGA due to its redshift being too low.

The fitting code used in CALIFA is STARLIGHT (Cid Fernandes et al., 2005), and the stellar population models are a blend of Vazdekis et al. (2010) and González Delgado et al. (2005) for STARLIGHT/CALIFA, based on MILES.

In the left hand panels of Figure 5.16 we plot the light-weighted stellar age and metallicity of p9-127A as measured by applying CALIFA data cubes (CALIFA 277 in Cid Fernandes et al. (2013)) but with this thesis' plotting scheme. These can be compared directly with the corresponding plots applying FIREFLY to P-MaNGA data cubes. We also compare to PPXF fits of the same P-MaNGA spectra as used in this Chapter's analysis in the middle panels of Figure 5.16, see later in this section for details of the fitting parameters used.

We find a remarkable agreement in the structures of maps between STARLIGHT/CALIFA and FIREFLY/P-MaNGA, particularly between the stellar age and stellar mass map. The CALIFA metallicity map appears to show much finer structure in its core than the P-MaNGA map, although the general high metallicity core with lobes of lower metallicity is matched in both codes and surveys. This finer structure could be artificial, arising from uncertainties in deconvolving the CALIFA fiber spectra into the datacube, since CALIFA has a lower fiber density across the P-MaNGA radial footprint analysed in this galaxy.

We look quantitively at these differences by binning the properties in elliptical annuli in the bottom panels of Figure 5.16, where we have plotted the corresponding properties from the top panel as radial profiles. Again we note remarkable agreement in stellar age (< 0.1 dex at all points), bearing in mind that the statistical errors plotted will be much lower than the systematic errors from flux calibration, covariance between pixels, and stellar population model uncertainties. We find a more complex structure, and generally higher values, in metallicity in the CALIFA profile than the P-MaNGA profile, differing by up to 0.1 dex in [Z/H]. We note that the stronger transition between high and low metallicity identified in FIREFLY and is consistent with the bulge/disk separation visible in the SDSS image of the galaxy. The agreement here is very encouraging since we use a different set of models, base stellar population components, wavelength range, fitting code and survey compared to Cid Fernandes et al. (2013).

In the middle panels of Figure 5.16 we show the $\langle \log \mathrm{age} \rangle_\mathrm{L}$ and $\langle [\mathrm{Z/H}] \rangle_\mathrm{L}$ maps extracted with the full-spectrum fitting PPXF code on the same spectra fitted with FIREFLY. For this comparison PPXF used as input a grid of SSP models from Vazdekis et al. (2010), based on the MILES stellar library. Ages were sampled with 24 models logarithmically spaced between 0.08 and 14 Gyr, while for each age metallicity was samples by 6 models with [M/H] = [-1.71,

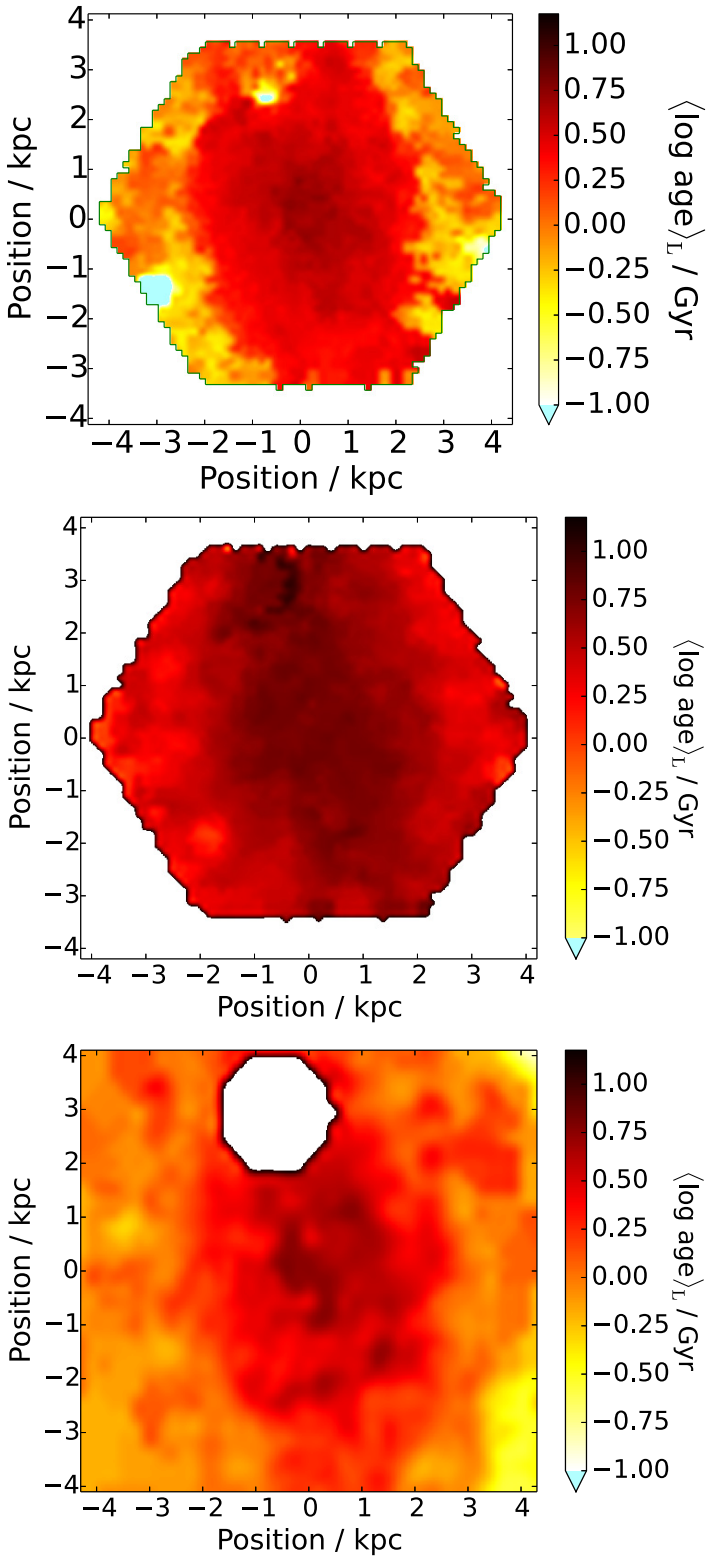

Fig. 5.14 Stellar age maps for CALIFA 277 / p9-127A. In the top panel are the results from this thesis. In the middle panel are the results from fitting to P-MaNGA with PPXF. In the bottom panel, results from fitting CALIFA data with STARLIGHT are shown as derived in Cid Fernandes et al. (2013).

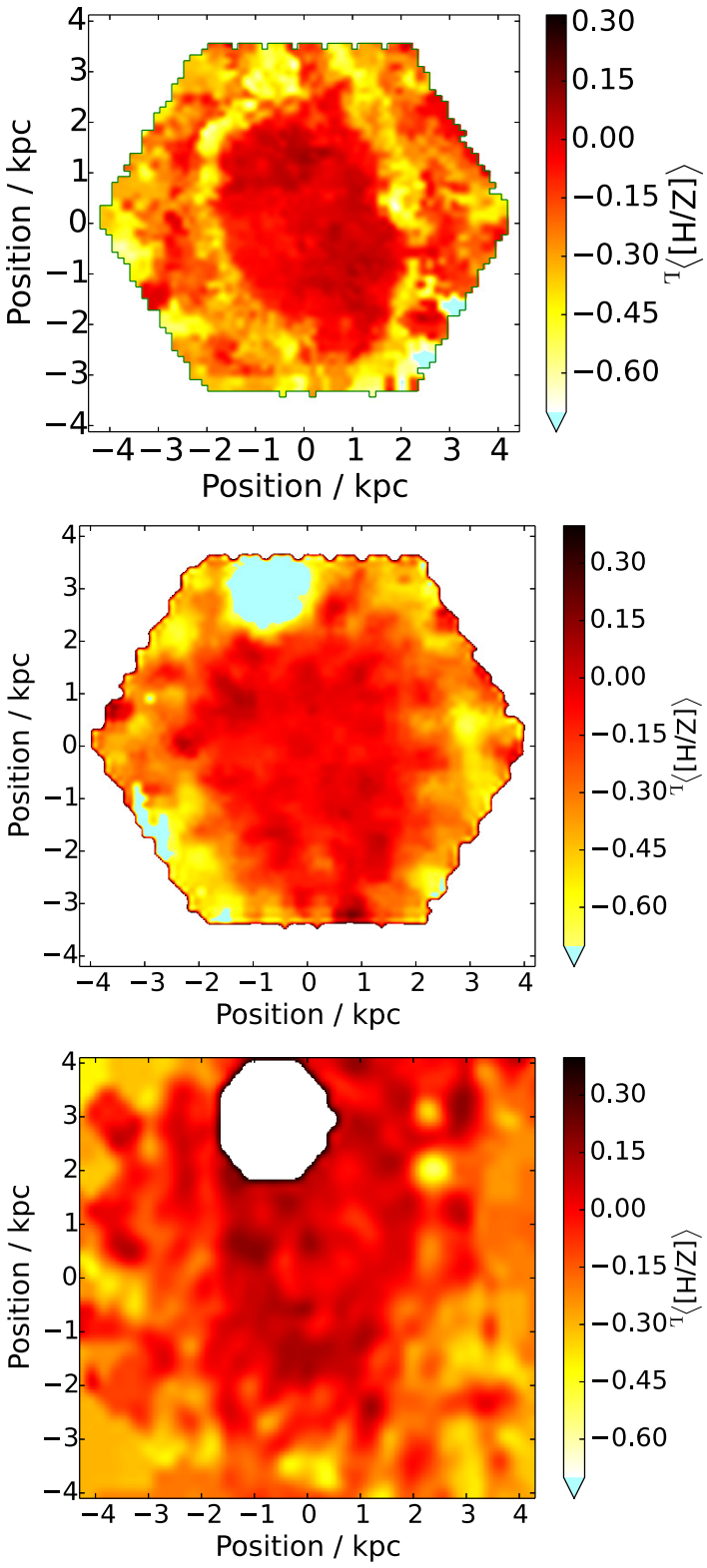

Fig. 5.15 As previous page but for metallicity.

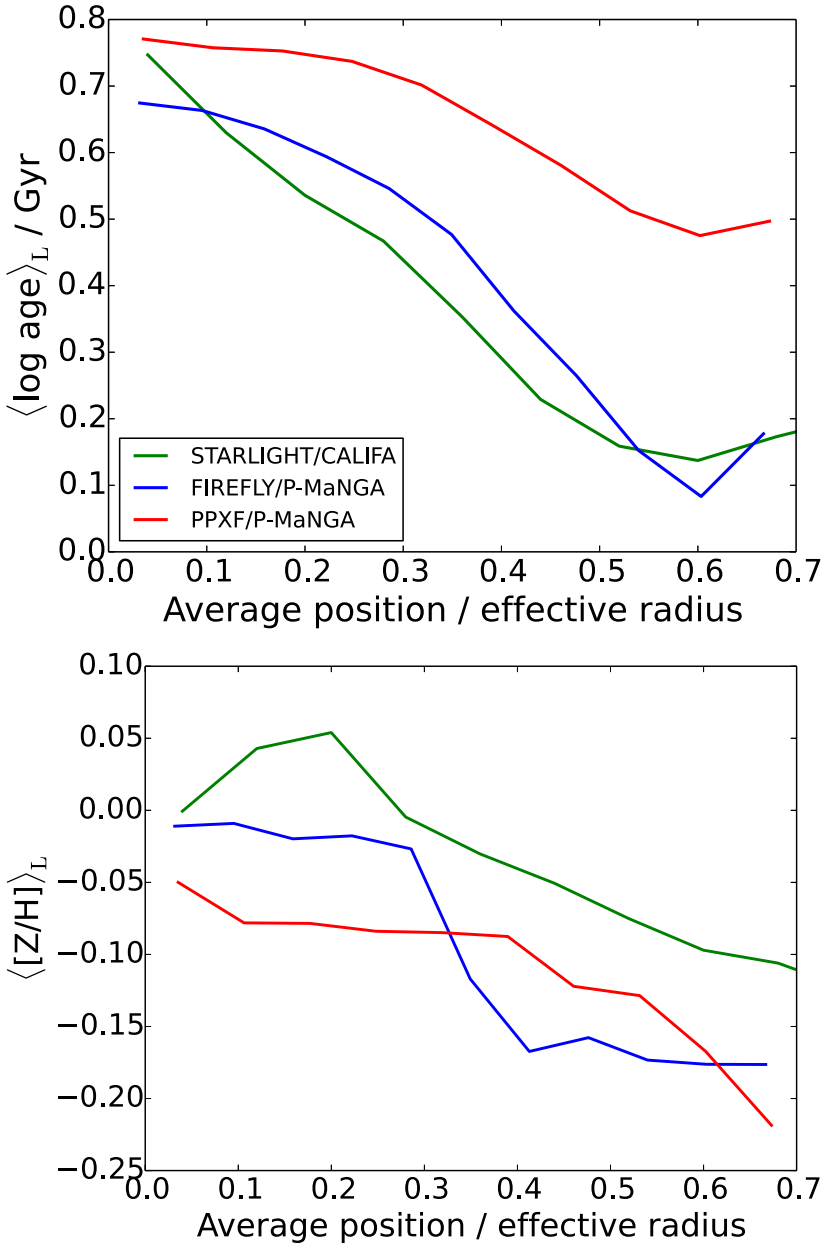

Fig. 5.16 Radial profiles of age (top panel) and metallicity (bottom panel), colour-coded by the survey and fitting code used. Together, the plots on the this and the previous 2 pages show the derived stellar population maps and profiles for CALIFA-277, known in this thesis as p9-127A, a target shared by both the P-MaNGA and CALIFA surveys at observational conditions similar to those expected for MaNGA. The galaxy as observed with CALIFA is analysed with the spectral fitting code STARLIGHT, and is compared to the results from P-MaNGA observations with both FIREFLY analysis and analysis with PPXF as described in section 5.5.6.

-1.31, -0.71, -0.40, 0.00, 0.22], for a total of 144 model templates. The fit was restricted to the wavelength range from 3600 to 7400 Å. To suppress the noise in the inferred population parameter we used linear regularization (keyword REGUL in PPXF) in the two-dimensional age and metallicity distribution. The level of regularization was chosen in such a way that the χ^2 of the regularized fit increases by $\Delta\chi^2 \approx \sqrt{2N_{\rm pix}}$ from the unregularized best-fitting χ^2. This provides the smoothest age-metallicity distribution consistent with the observed spectrum. The results are very weakly sensitive to the choice of the regularization parameter. The stellar kinematics was fitted simultaneously to the stellar population. We adopted a 6 degree multiplicative polynomial to account for possible inaccuracies in the relative flux calibration and remove the effect of dust attenuation on the continuum shape. No additive polynomials were used to avoid affecting the line strength of the SSP models.

The profiles and maps of PPXF fits find only adequate qualitative spatial agreement with FIREFLY, showing some bulge-disc separation. The systematically higher ages, by about 0.2 going out to 0.4 dex, and the greater smoothness of the age maps compared to both STARLIGHT/CALIFA and FIREFLY/P-MaNGA could arise from differences in the ages of the SSP templates used, but this is not clear how strongly this would affect the fits. For example, the other two codes include younger ages (in our case down to 6.5 Myr, see Table 5.4). The metallicity of the PPXF fits agrees with the other codes to within 0.1 dex. This suggests that the greatest sensitivity on the results obtained is from the range of SSPs used, based on this example. We will investigate these differences in detail for a larger sample in future work.

In conclusion we find an overall good, ~ 0.1 dex, agreement between the CALIFA/STARLIGHT and P-MaNGA/FIREFLY, and across all three cases consistent recovery of the spatial features of the galaxy observed, and higher differences in age are present when comparing with P-MaNGA/PPXF which may just come by construction. Matching general profiles are recovered in all three cases, but differences caused by the different analysis codes, stellar population templates used and models are significant and larger than the random errors in the analysis of detailed features.

5.6 Comparisons with other P-MaNGA analyses

In this section we compare the analyses in this thesis with other current analyses of the P-MaNGA data.

5.6.1 Emission line ratios

Emission line ratios are a powerful tool to study the state of the ionised gas in galaxies. The Baldwin-Phillips-Terlevich (BPT, Baldwin, Phillips & Terlevich (1981); Veilleux & Osterbrock (1987)) diagram, making use of the line ratios [NII] $\lambda 6584/\mathrm{H}\alpha$ and [OIII]$\lambda 5007/\mathrm{H}\beta$, is the most popular diagnostic used to distinguish ionisation due to star-formation from ionisation due to other sources, including Active Galactic Nuclei (AGN), Low Ionisation Nuclear Emission-line Regions (LINERs) and shocks. A detailed analysis of the ionised gas content of the P-MaNGA galaxies using the BPT diagram, complemented with other diagnostics, is presented in Belfiore et al. (2015). Note that in this analysis that uses [NII] we are unable to separate Seyfert galaxies from LINERs, so we classify these collectively as AGN. See Belfiore et al. (2015) for more details on these classifications.

In this section we compare the results of the BPT classification with stellar ages and metallicities derived in this thesis from full spectral fitting. We make use of the emission lines maps created by Belfiore et al. (2015) and plot in Fig. 5.17 the position of all the regions in the 14 galaxies considered by Belfiore et al. (2015) in the BPT diagram. Belfiore et al. (2015) discuss a comparison with D4000 and $H\delta$ absorption. Here we extend this analysis by directly comparing with stellar population ages and metallicities. We make use of the demarcation lines of Kewley et al. (2001) and Kauffmann et al. (2003). We refer the reader to Belfiore et al. (2015) for a careful discussion of the assumptions and caveats implicit in the use of these demarcation lines. We expect galactic regions (Voronoi bins) which lie below the demarcation Kauffmann 2003 line to harbour on-going star-formation in HII regions. This is confirmed by the study of the stellar population ages, as evident in the left-hand-side of Figure 5.17, where the regions lying below the Kauffmann 2003 line present younger stellar populations, consistently with a significant population of O and B stars, capable of ionising classical HII regions.

We wish to remark on the cluster of young points ($t \sim 100$ Myr) which lie just across the Kauffmann 2003 line: these all belong to a single galaxy (p11-19C) which is experiencing a star-burst. This galaxy is found by Belfiore et al. (2015) to be Nitrogen enriched and hence appearing to cross over into the 'Composite' region of the BPT diagram, between the two demarcation lines, although its ionisation is fully compatible with star-formation.

As we move away from the star-forming sequence in the BPT diagram towards the 'right-wing', inhabited by AGN and LINERs, we see progressively older stellar populations. There is a tantalising hint that the regions lying at higher $[\mathrm{NII}]/\mathrm{H}\alpha$, generally associated with LIN-

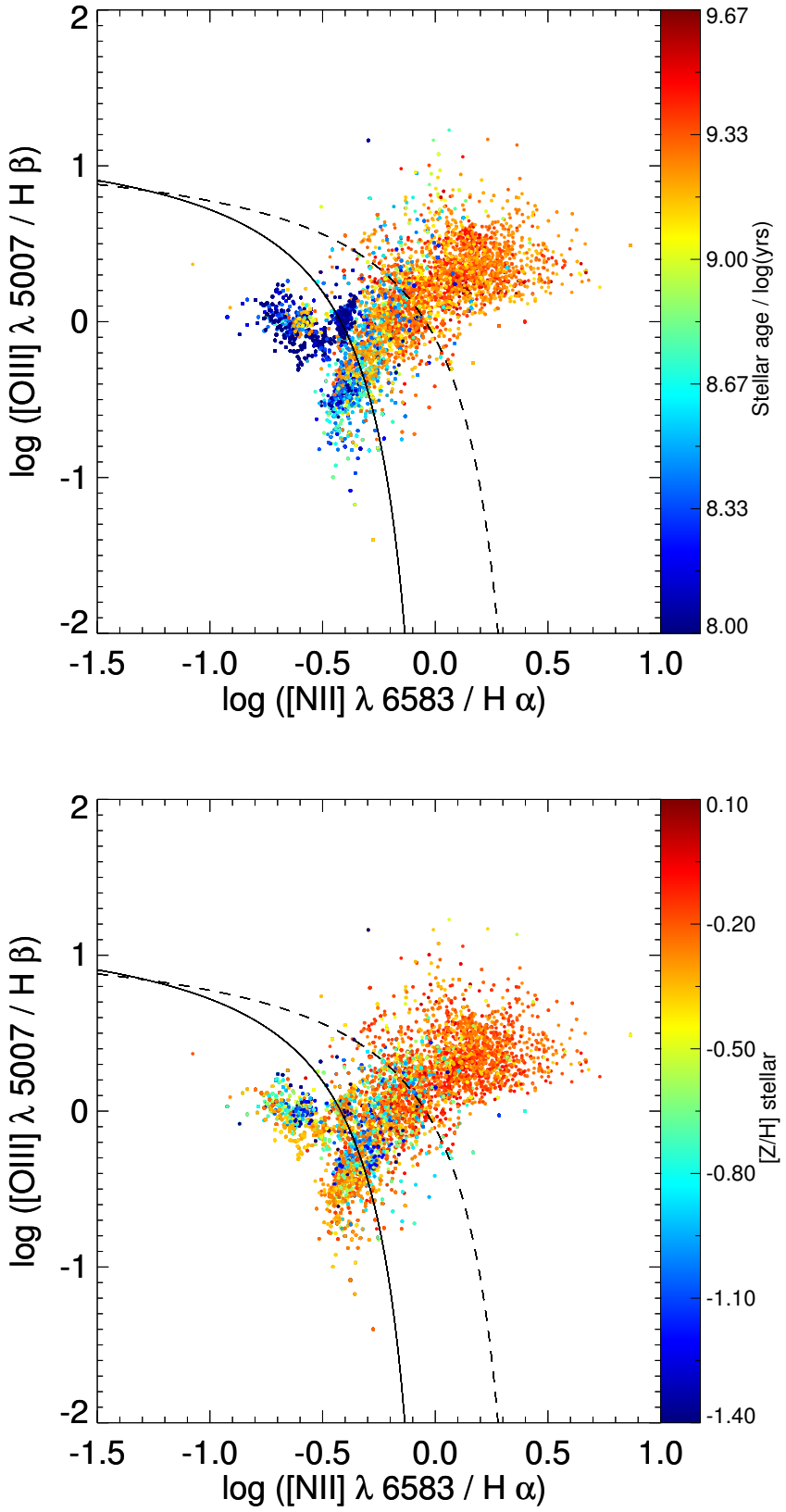

Fig. 5.17 Emission line ratios as derived in Belfiore et al. (2015) as a function of light-weighted stellar ages (top) and metallicities (bottom) as derived in this Chapter, for every galaxy showing emission. Overplotted are demarcation lines from Kewley et al. (2001) and Kauffmann et al. (2003). Each pixel from all of their subsample of P-MaNGA galaxies is plotted following the binning scheme used in Belfiore et al. (2015).

ERs, are older than the regions at lower $[\mathrm{NII}]/\mathrm{H}\alpha$, generally associated with AGN. Though, as shown in Belfiore et al. (2015), where this separation line exists is not clear. Larger statistics and a bona-fide AGN sample is needed to make further progress in the study of stellar populations of AGN and LINER hosts, but the results from these preliminary observations seem to confirm trends already observed in SDSS for the global galaxy population (Cid Fernandes et al., 2010; Kauffmann et al., 2003; Kewley et al., 2006). This analysis also confirms the more simplistic conclusions reached using stellar populations indices ($\mathrm{D_N}(4000)$ and $\mathrm{EW}(\mathrm{H}\delta_\mathrm{A})$) in Belfiore et al. (2015) and Li et al. (2015).

The bottom panel of Figure 5.17 shows BPT diagram colour-coded by stellar metallicity. We see that AGN hosts have more metal-rich stellar populations, most likely because they are more massive, which would then give a mass-metallicity relationship as described in e.g. Thomas et al. (2010). In the star forming regions, on the other hand, we see a variety of stellar metallicities from relatively metal-poor to metal-rich. The pixels with metal-poor populations are mostly found at high $[OIII]/H\beta$ ratio, coinciding with regions of low metallicity in the gas (Shields & Searle, 1978).

The picture presented in these results is consistent with the 'inside-out' galaxy formation theory, since central regions dominated by AGN-type emission are very likely to be high in metallicity compared to the outer, star-forming low metallicity regions. In addition this idea, the evidence for central AGN could be a form of star formation regulation in the cores of galaxies, also known as 'quenching', which we investigate in the next section. We direct the reader to Belfiore et al. (2015) for more details including emission line maps.

5.6.2 Absorption and emission line diagnostics

Li et al. (2015) perform emission- and absorption-line fitting to obtain 2D maps and radial gradients of the 4000 Å break and the equivalent widths of $H\delta$ absorption and $H\alpha$ emission for the P-MaNGA dataset. They categorise the dataset into two groups; 'centrally quiescent/passive', where the D_{4000} break in the central pixel of the P-MaNGA data cube of the galaxy observed is above 1.6, and 'centrally starforming', where the D_{4000} break is below 1.6. They find that their centrally star-forming galaxies generally have very weak radial variation in these diagnostics, whereas the gradients of centrally quiescent galaxies are significant.

We compare their results to the ages and metallicities obtained from spectral fitting in two sets of figures, first to assess how well their indices trace our results, and secondly to see whether

we recover similar gradients as a function of galaxy group. We note that plate 11 galaxies, identified in this Chapter as being the most difficult to recover smooth gradients from, are excluded from their analysis due to being unable to obtain reliable diagnostic measurements. Figure 5.18 shows the pixel-by-pixel $H\delta_A$ and D_{4000} as a function of this Chapter's recovered ages and metallicities.

As expected, we see a clear dependence of both D_{4000} and EW($H\alpha$) with both age (Kauffmann et al. (2003), Kauffmann (2014)) and metallicity (Davidge & Grinder (1995), Worthey & Ottaviani (1997), Maraston (2005)), as well as some scatter which could be due to other dependencies such as dust attenuation and element abundance ratios (Thomas, Maraston & Korn (2004), Sánchez et al. (2012)) as well as observational errors and statistical errors in the spectral fitting. We confirm a clear dependence on age, which becomes flatter as metallicity decreases, for both indices (see Maraston (2005)). We see that there is an approximately 0.1 in D_{4000} and 1.0 in EW($H\delta_A$) scatter.

We note that there are two branches of high metallicity, high age points in the $H\delta_A$ plot that are not visible in the D_{4000} plot. The bifurcation is due to most of the high metallicity points coming from a single galaxy in the sample, galaxy p9-127B, which is the dust lane clumpy galaxy shown in Figure 3.4. The galaxy has high metallicity (above $\langle[\mathrm{Z/H}]\rangle_\mathrm{L} > 0.05$), high age ($\langle\log \mathrm{age}\rangle_\mathrm{L} > 5$ Gyr) and high D_{4000} (> 1.8) across all of the bulge and most of the disc, except the dust lane region where these values are much lower. However, the EW($H\delta_A$) has a large asymmetry between the two sides of the core along the major axis that transitions quickly between very low (~ -2) to more moderate (~ 0) values, giving rise to the appearance of two fairly distinct branches in the $H\delta_A$ plot. The physical explanation for why this asymmetry exists in this galaxy in $H\delta_A$ and not the other properties is not currently known. Similarly the points with low metallicity at low age with relatively high D_{4000} also come from one galaxy, but again the explanation for this is unclear.

This plot also shows that though using EW($\mathrm{H}\delta_A$) to measure age is approximately as accurate for all metallicities, D_{4000} has a tighter relation with age for higher metallicities. This will need more galaxies to quantify precisely, but the relative power of the different indicators as a function of age and metallicity suggests that D_{4000} alone may give adequate errors on the estimate of stellar age, as long as the area observed is high in metallicity. Otherwise, both indicators are approximately similarly useful to assess age.

In figure 5.19 we use the same plotting and binning conventions used in Li et al. (2015), binning our properties in 0.2 effective radius annular bins and measuring the difference in age

and metallicity determined from the first bin (r_0). We use classifications based on measured D_{4000} in the central pixel of each galaxy in the upper panels, and use the same morphological classification as used in Table 5.2 in the lower panels.

Encouragingly we see that age gradients are clearly the main driver of the split between centrally quiescent and centrally star forming galaxies, with metallicity gradients showing no clear divide between the two. We emphasise that this result is not in conflict with the gradient results presented earlier. The centrally quenched galaxies in Li et al. (2015) contain a mix of different morphologies, and in particular include objects in which the combination of a passive central bulge with a star forming disc result in the age gradients measured. If we separate again by morphology as in Section 5.5.1, we recover the conclusions presented in that section as shown by Figure 5.7. We note that compared to the gradients derived in Figure 5.7, we only analyse up to 1 R_e in this figure to match Li et al. (2015), hence we do not probe the outer regions of the early type galaxies which will typically have a lower metallicity stellar component and therefore a more negative gradient.

We find that age gradients in late type galaxies are typically negative whereas the early type galaxies are typically flat. The metallicity gradients of late-type galaxies show no clear separation, while the early type galaxies have on average more negative gradients. This shows that the clear distinction in age and metallicity gradients between centrally quiescent and centrally star forming galaxies as discussed in Li et al. (2015) is mostly driven by bulge-disc transition. Such a transition will be more clearly identifiable in the full MaNGA sample.

Importantly, these also show that early-type galaxies with positive age gradients may appear star-forming in their very central regions. This result could be due to low amount of new star formation, or the accretion of younger stars, in the outer regions of the galaxy migrating towards the central region of the galaxy, perhaps due to dynamical friction effects (e.g. Lu & Wei (2003)). Tentatively, this could be evidence for somewhat young minor merging being a reasonable effect on early type galaxies, but larger sample sizes will be required to test this fully. This appears to represent similar conclusions about the importance of minor merging with Chapter 4, suggesting that assessing that chapter's conclusions on minor merging will be possible with full MaNGA and similar large statistical surveys. Similarly, late-type galaxies with large negative gradients appear to be centrally quenched, suggesting that there is little migration of fresh material onto the central bulge for these galaxies, though this is not necessarily true for late-type galaxies with less negative age gradients..

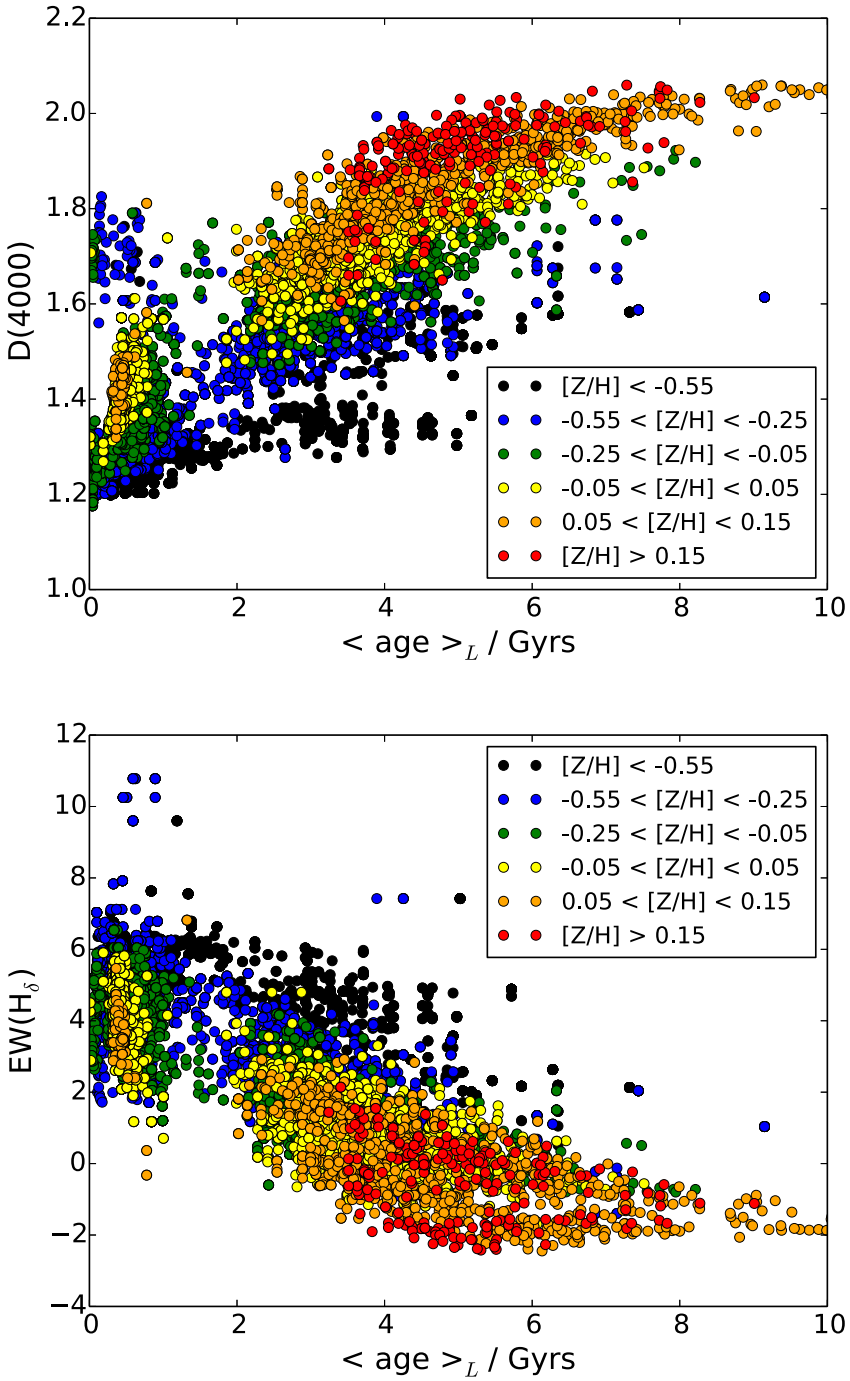

Fig. 5.18 D_{4000} and EW($H\alpha$) measurements from Li et al. (2015) as a function of the light-weighted stellar ages and metallicities (colour-coded) derived in this Chapter. Each pixel from all of their subsample of P-MaNGA galaxies is plotted following the binning scheme used in Belfiore et al. (2015).

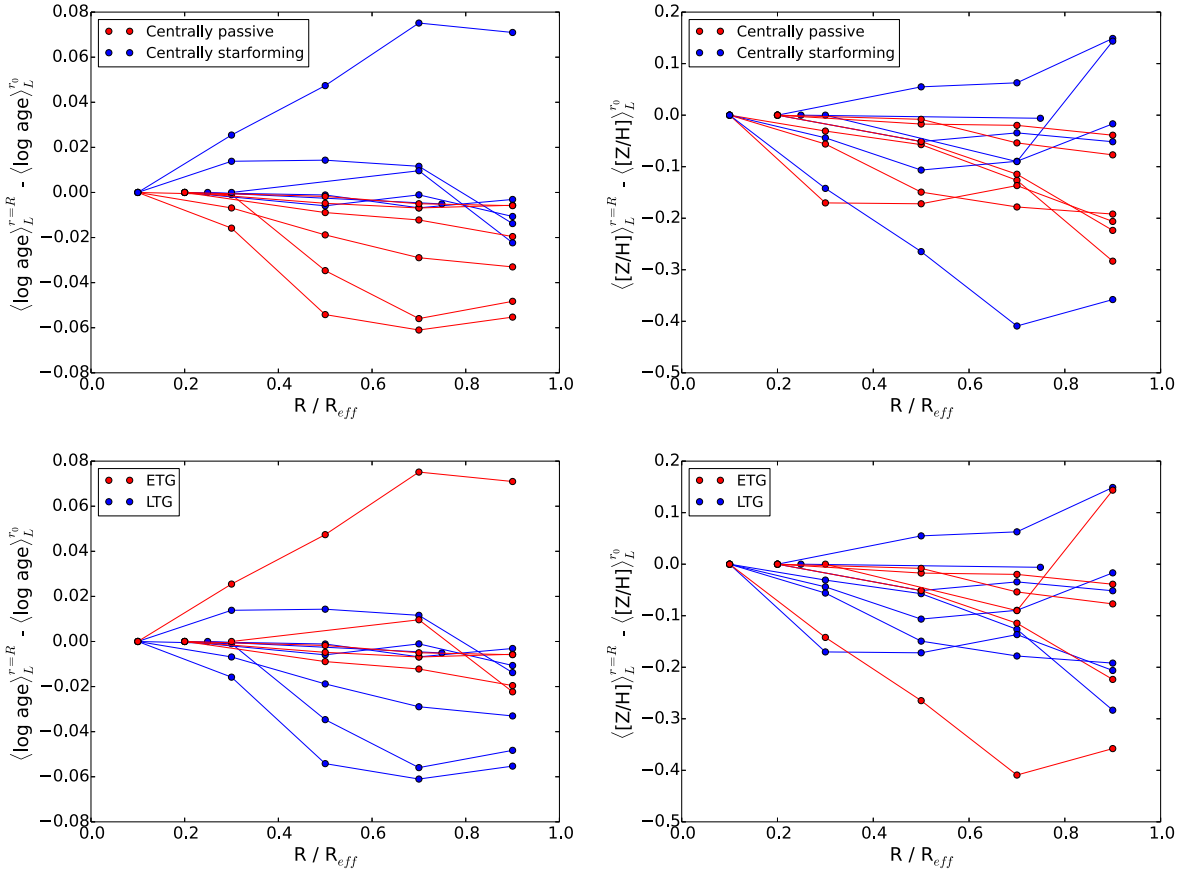

Fig. 5.19 Light-weighted age and metallicity gradients up to 1 effective radius, plotted as the change in age / metallicity from the first elliptical annular bin, where each line represents the profile from a P-MaNGA galaxy. In the upper panels we use the classifications of centrally quiescent/passive or centrally starforming as described in Li et al. (2015). In the lower panels we use the morphological classifications in this Chapter (as in Table 5.2). Bins are 0.2 effective radius in size to match Li et al. (2015) as much as possible, however we impose a condition that each bin must contain at least 10 pixels from the corresponding data cube. If this condition is not met we sample at wider bins until the criterion is met, in order to ensure a reliable mean age or metallicity at each point.

5.7 Conclusions

We have shown and discussed the first application of full spectral fitting of stellar population models to P-MaNGA galaxy data, a prototypical data release preceeding the start of the actual MaNGA IFU galaxy survey (Bundy et al. (2015)). We embarked in this work for several reasons, namely exploring the capabilities of our fitting and modelling method to unveil the physical parameters of galaxies and study our success as a function of observational conditions, exposure times, and galaxy type. As a hot spot of our approach, we show how the method to deal with dust attenuation shown in Chapter 3 removes the large scale features of spectra such as the continuum and flux calibration errors before fitting, allow us to fit unattenuated spectra and to then derive very accurate dust values. We calibrate the method by using galaxies which display dust lanes in their optical images as well as mock galaxies with known dust input. We show that we can accurately recover the dust displacement in the stellar population maps. This now allows us to calculate other stellar population properties that are more accurate and physically plausible, such as radially symmetric stellar mass maps.

We present our calculations as 2D maps of age, metallicity, dust and stellar mass and their corresponding radial profiles and gradients. Since the P-MaNGA data contain a varied selection of galaxy types, we show that we are able to recover many different features and structures in this data, such as spiral arms, additional galaxy components, clear radial profiles for spheroidal galaxies, and artefacts in the data. This will be a superlative tracer of galaxy evolution.

We derive radial profiles of age, metallicity and stellar mass for all of the P-MaNGA data. We show that the mass profiles are in general very smooth as a function of radius. Age and metallicity profiles can show unevenness, which depends on the quality of observations. We notice that the maps of poorly observed or noisy galaxies display an increased variance on the Voronoi bins which create fake structures, but most importantly erase the signature of real structures as spiral arms.

Importantly for galaxy evolution studies, we derive the radial gradients of stellar population properties. We find that metallicity gradients are negative for spheroids (– 0.15 dex / R_e), compared to the flat gradients of late-type galaxies, which is consistent with previous knowledge. Age gradients are also negative for late type galaxies (– 0.39 dex / R_e), though almost negligible for spheroids, which is again consistent with the literature. We calculate statistical errors on the radial profiles and gradients obtained as a function of observational quality, comprised of S/N, airmass and exposure times, which we will use to calibrate analysis of MaNGA

data.

Additionally we demonstrate that the stellar mass density profiles remain relatively unchanged as a function of three stellar population model input stellar spectral libraries, even if we find $\sim$ 0.1 dex differences in the age and metallicity profiles. Nonetheless the overall set of gradients for the P-MaNGA data sample is consistent across the 3 model libraries. Additionally we show that the recovery of spatial features in age and metallicity is consistent across model, fitting code, fitting parameters and the CALIFA survey.

Lastly we show how comparisons with analyses of the absorption and emission features MaNGA data can shed light on galaxy evolution questions such as inside-out growth and/or quenching, studies of AGN, and hint at assessing the relative importance of minor merging in early-type galaxies.

This work will proceed with the analysis of the full MaNGA dataset in the future, and constitutes the basis of our understanding of the performances of full spectral fitting on MaNGA-type IFU data. The work in this Chapter is presented in Wilkinson et al. (2015).

Chapter 6

Conclusions

In this thesis we have presented a new full spectral fitting code called FIREFLY. We have used it to investigate galaxy properties for a range of redshift, galaxy type, and model and observational uncertainties for both point-source and IFU statistical surveys. In Chapter 3 we explained how FIREFLY is structured, detail its many features, calibrated it with mock galaxies and globular clusters, and demonstrated its application. In Chapter 4 we applied the code to SDSS DR7 and DR9-BOSS, both point-source galaxy surveys that together span a large range in redshift. We showed how these surveys can be combined to give a self-consistent sample of LRGs across cosmic time. In Chapter 5 we applied the code to a new IFU galaxy survey called MaNGA, using prototype observations to guide future stellar population analysis for this and other IFU surveys. We also presented the uncertainties in obtaining maps and profiles of properties from IFU observations. All through this, we demonstrated how the effect of changing the stellar library as input into stellar population models presents systematic uncertainties on different types of galaxies. These studies hope to shed light on the power, but also the limitations, of a full spectral fitting approach and the clear requirement for such approaches for understanding of key galaxy evolution problems. We summarise here the conclusions from each of these chapters.

6.1 Chapter conclusions

In Chapter 3 we presented our motivations for building a new full spectral fitting code. We explained that, as shown in Maraston & Strömbäck (2011), the best-fitting solution is not necessarily one that describes the physical solution, and in fact can be quite different. This is due

to spectral degeneracies allowing multiple solutions to fit to the data that are indistinguishable, in a statistically robust way, from each other. We describe the algorithm of FIREFLY, a code first built to demonstrate these degeneracies. Rather than aiming solely for the best-fit in terms of χ^2 minimisation, it collects hundreds or thousands of solutions using an iterative approach to build up an adaptively resolved parameter-likelihood space. Our additional requirements of the code are to work well at low signal-to-noise, motivated by the typical signal to noise available in large surveys such as SDSS DR9-BOSS, run quickly, in order to process whole galaxy surveys in reasonable timeframes, make the code applicable to a diverse range of galaxy types by relying on as few priors on the star formation history as possible, and be able to test the effect of varying model ingredients such as the input stellar library. We show that since FIREFLY constructs probability distribution functions for every galaxy allows for accurate error estimates based on model degeneracies.

During the progression of the thesis, many features were added to FIREFLY in order to ensure its versatility and precision. Our tests on prototype SDSS MaNGA data motivated the need for more flexibility in dealing with the combined effects attenuation from dust and flux calibration errors. Hence we constructed a new innovative method for the treatment of dust attenuation, using of a high-pass filter in combination with our fitting approach in order to use the small wavelength features to constrain the large features. Using the approach successfully allowed the mitigation of flux calibration issues in order to obtain spatially resolved and physically realistic dust maps. This general approach then became standard in FIREFLY due to the increased versatility of the method. We also compared our methods with other popular full spectral fitting codes available in order to explain our place in the literature.

Lastly in this chapter we detailed the tests we have carried out on mock galaxies and globular clusters in order to demonstrate FIREFLY's effectiveness, finding that a set of offsets in age, [Z/H] and mass as a function of data S/N for solar metallicity, which we summarise here, where offset means recovered value – input value,:

Age offset / dex	= +1.5 / (S/N),	+0.7 / (S/N) + 0.1,	+0.2 / (S/N)
[Z/H] offset	= –0.5 / (S/N),	–0.3 / (S/N),	–0.2 / (S/N)
Stellar mass offset / dex	= +1.0 / (S/N),	+0.3 / (S/N),	+0.1 / (S/N),

for young stellar populations (< 100 Myr), intermediate age populations (1 – 3 Gyr), and all other age populations respectively. We showed how realistic mock galaxies constructed from composite stellar populations are consistent with these values. We also showed that a single

run of FIREFLY gives realistic errors that enclose correct solutions.

In Chapter 4 we applied FIREFLY to two large-number galaxy surveys from SDSS: DR7 and DR9-BOSS, which in combination involved analysing $\sim$ 2 million galaxy SEDs. We derived the full star formation histories for both surveys, but also the star formation histories of their commonly used subsamples. This is valuable since different studies will sometimes need only to analyse these particular subsamples depending on their science goals. We explained how these data are treated in order to retrieve galaxy properties, such as stellar mass.

We found the sum star formation history of DR7 to be an old population with $\sim$ 10 Gyr populations dominating in mass, but with fairly long star formation histories extending down to less than 1 Gyr. We showed that the different models can give slightly different nuances to the picture, particularly in metallicity, with MILES-based models finding DR7 galaxies to be slightly more metal-rich and ELODIE-based models the metal-poorest in comparison to STELIB-based models. These differences exist despite negligible differences in the statistical significance of their fits. We compare with two other publically available databases of DR7 galaxies, VESPA and STARLIGHT, finding good agreement.

We demonstrated that the LRG cut is successful in selecting for more passive galaxies at low redshift, although has a somewhat high incidence of dusty starforming galaxies at the upper end of its redshift range. We found that DR7 LRGs have very low amounts of light from stellar populations with ages less than 0.5 Gyr, whereas the remainder of the sample provides a much more continuous range of ages right down to the lowest end of the age range fitted. LRGs were also found to have star formation timescales on the order of 5 Gyr rather than 7 Gyr or more for the remainder of the sample, suggesting that while the LRG cut selects for more passive objects, there are still galaxies with longer star formation histories such as massive spiral galaxies contributing to the LRG sample.

We repeat the star formation history analysis for the DR9-BOSS sample, finding an overall more metal-rich, shorter star formation timescale stellar population sample than from DR7. An old population of about $\sim$ 7 Gyr dominates in this sample due to the different redshift range compared to DR7, but there is very little mass in stellar populations below 2 Gyr, suggesting a timescale of about 3 Gyr for these galaxies. Again there are some differences in the properties obtained as a function of input stellar library into the model, with MILES-based models finding older, metal-richer stellar populations, and STELIB-based models younger, compared with ELODIE-based models.

In BOSS there are two main subsamples, LOWZ and CMASS, both of which were separately

analysed in this chapter. We found that the LOWZ sample is successful in its aims of being very similar in stellar populations to that of DR7 LRGs, and CMASS retaining a largely passive stellar population sample. We constructed the stellar mass distribution function from BOSS, finding a peak of $10^{11.4}M_{\odot}$, which is in good agreement with previously derived properties from broadband SED fitting as well as principle component analysis, though there is 0.1 dex offset, the precise origins of which is still to be determined.

In Chapter 5 we applied FIREFLY to the first data from SDSS MaNGA, an IFU survey that when complete will present 2D maps of SEDs for $\sim$ 10,000 local galaxies. This prototype sample consisted of 18 datacubes of galaxies with a range of galaxy types observed under a variety of observational conditions. We produced highly spatially resolved maps, down to 0.5 arcsec in the galaxy cores in some cases, and 1D radial profiles, of stellar population properties of the whole sample.

We grouped the galaxies by the conditions they were observed under, showing how lower exposure times and higher airmass lead to higher pixel-to-pixel variance in the maps and to greater errors in the radial profiles. This makes the science case for the exposure times and the full MaNGA survey is using, since the errors under MaNGA-like conditions were approximately 0.1 dex or less in age and metallicity under these conditions.

Separating the galaxies out into early-type and late-type showed differences in the gradients of these galaxies. Early-types were found to be flat in age, and – 0.15 dex / R_e in [Z/H], whereas late-types were flat in metallicity but – 0.39 dex / R_e . These results compared well with the literature for previous studies of small numbers of resolved galaxy data.

We then demonstrated consistency of the approach as a function of stellar library, fitting code, and even observational survey used when producing these maps and gradients. Lastly, we combined our analyses with other prototype MaNGA studies, producing BPT diagrams of gas properties and measurements of absorption features. These results found that the reasons being identified as centrally passive in the sample are largely due to the bulge-disc transition for late-type galaxies, and that AGN hosts have more metal-rich, somewhat older stellar populations.

By producing this thesis we have demonstrated the versatility and effectiveness of FIREFLY, the range of results and scientific questions one can assess using it, and explained carefully the limitations of full spectral fitting and of stellar population modelling. This has resulted in two first-author publications from the author of this thesis and many other co-authored publications both published and in preparation. We hope that the code will continue to prove useful for scientific results, and in the rest of this chapter we highlight current and future work

being undertaken.

6.2 Future applications of my research

To ensure that my research continues to be useful to the astrophysics community, it is important that the codes and results from them continue to demonstrate their versatility under a range of astrophysical conditions. In the near term, work will be done to ensure that the code is as well-documented and as general as possible so that it can be released publically. As alluded to in many of the chapters of this thesis, much care must be taken to assess the priors that one is using when undertaking full spectral fitting. Hence, a future project will be to compare directly with the inner workings of many full spectral fitting codes to understand exactly what systematics one places on the results when making different choices in the fitting process. For example, a function of the code in development currently is using FIREFLY for broadband SED fitting, and testing the differences in the results obtained using the same data and models. The aim is to provide a unified picture of full spectral fitting and a detailed measurements of the systematic errors on the results from this approach.

FIREFLY is already being used in Le Cras et al. (in preparation), in order to measure stellar population properties in the Ultra-Violet both from spectra and from absorption indices for complex star formation histories. They are testing the effect of the UV upturn in passive galaxies from DR9-BOSS, currently finding that ~ 30 % of these are well-fit by old UV upturn models. Their work requires the use of spectral stacking and careful choice in the absorption indices used, and the probability distributions output by FIREFLY are useful for constraining these choices.

Another interesting use of FIREFLY would be to assess the ability of model dust attenuation model curves, since the code outputs its own measurement of attenuation which could be compared with these curves. One could measure the attenuation curve output as a function of galaxy properties to test for systematic changes.

Lastly, FIREFLY has already demonstrated its effectiveness in application to large surveys, so a natural extension to the work done on prototype MaNGA data is to run the procedure on the full set of MaNGA galaxies. In addition to improving the results from Wilkinson et al. (2015), both in terms of the stellar population properties from full spectral fitting and from combining the results with absorption and emission line studies, one could separate the MaNGA galaxies into well-defined and populous subsamples to answer fundamental questions about the role of

accretion and galaxy growth.

With many future and ongoing observational spectroscopic surveys, and developments in stellar population modelling, it is clear that taking a detailed approach to full spectral fitting and exploring the degeneracies within the process itself is essential to robustly assessing galaxy properties and processes. In this sense, it is hoped that this thesis has provided a comprehensive view of on many of the uses and challenges in this field, and their fundamental importance for galaxy evolution.

Bibliography

Abazajian K. N. et al., 2009, ApJS, 182, 543

Adelman-McCarthy J. K. et al., 2008, ApJS, 175, 297

Ahn C. P. et al., 2012, ApJS, 203, 21

Aihara H. et al., 2011, ApJS, 193, 29

Annibali F., Bressan A., Rampazzo R., Zeilinger W. W., Danese L., 2007, A&A, 463, 455

Arp H., 1962, ApJ, 135, 311

Bacon R. et al., 2001, MNRAS, 326, 23

Baldwin J. A., Phillips M. M., Terlevich R., 1981, PASP, 93, 5

Baldwin J. A., Phillips M. M., Terlevich R., 1981, PASP, 93, 5

Barker M. K., Sarajedini A., Geisler D., Harding P., Schommer R., 2007, AJ, 133, 1138

Bate M. R., 2011, MNRAS, 417, 2036

Bedijn P. J., 1988, A&A, 205, 105

Bédorf J., Portegies Zwart S., 2013, MNRAS, 431, 767

Behroozi P. S. et al., 2015, MNRAS, 450, 1546

Beifiori A., Maraston C., Thomas D., Johansson J., 2011, A&A, 531, A109

Belfiore F. et al., 2015, MNRAS, 449, 867

Belokurov V. et al., 2007, ApJ, 654, 897

Bershady M. A., Verheijen M. A. W., Swaters R. A., Andersen D. R., Westfall K. B., Martinsson T., 2010, ApJ, 716, 198

Blanc G. A. et al., 2013, AJ, 145, 138

Bloecker T., 1995, A&A, 297, 727

Bolton A. S., Schlegel D. J., 2010, PASP, 122, 248

Brainerd T. G., Blandford R. D., Smail I., 1996, ApJ, 466, 623

Bressan A., Fagotto F., Bertelli G., Chiosi C., 1993, A&AS, 100, 647

Brinchmann J., Charlot S., White S. D. M., Tremonti C., Kauffmann G., Heckman T., Brinkmann J., 2004, MNRAS, 351, 1151

Bruzual G., Charlot S., 2003, MNRAS, 344, 1000

Bruzual A. G., 1983, ApJ, 273, 105

Bryan G. L., Volk K., Kwok S., 1990, ApJ, 365, 301

Bullock J. S., Johnston K. V., 2005, ApJ, 635, 931

Bundy K. et al., 2015, ApJ, 798, 7

Bundy K., Ellis R. S., Conselice C. J., 2005, ApJ, 625, 621

Calzetti D., Armus L., Bohlin R. C., Kinney A. L., Koornneef J., Storchi-Bergmann T., 2000, ApJ, 533, 682

Cappellari M., Copin Y., 2003, MNRAS, 342, 345

Cappellari M., Emsellem E., 2004, PASP, 116, 138

Cappellari M. et al., 2011, MNRAS, 413, 813

Cassisi S., Pietrinferni A., Salaris M., Castelli F., Cordier D., Castellani M., 2006, Mem. Societa Astronomica Italiana, 77, 71

Chaboyer B., 1999, Post-Hipparcos Cosmic Candles, 237, 111

Chabrier G., 2003, PASP, 115, 763

Chapman S. C., Blain A. W., Smail I., Ivison R. J., 2005, ApJ, 622, 772

Chen Y.-M. et al., 2012, MNRAS, 421, 314

Chevallard J., Charlot S., Wandelt B., Wild V., 2013, MNRAS, 432, 2061

Chilingarian I., Prugniel P., Sil'Chenko O., Koleva M., 2007, in IAU Symposium, Vol. 241, IAU Symposium, Vazdekis A., Peletier R., eds., pp. 175–176

Cid Fernandes R., Mateus A., Sodré L., Stasińska G., Gomes J. M., 2005, MNRAS, 358, 363

Cid Fernandes R. et al., 2013, A&A, 557, A86

Cid Fernandes R., Stasińska G., Schlickmann M. S., Mateus A., Vale Asari N., Schoenell W., Sodré L., 2010, MNRAS, 403, 1036

Cimatti A., Bianchi S., Ferrara A., Giovanardi C., 1997, MNRAS, 290, L43

Coelho P., Barbuy B., Meléndez J., Schiavon R. P., Castilho B. V., 2005, A&A, 443, 735

Coil A. L., Weiner B. J., Holz D. E., Cooper M. C., Yan R., Aird J., 2011, ApJ, 743, 46

Cole A. A., Tolstoy E., Gallagher, III J. S., Smecker-Hane T. A., 2005, AJ, 129, 1465

Conroy C., Gunn J. E., 2010, ApJ, 712, 833

Conroy C., Gunn J. E., White M., 2009, ApJ, 699, 486

Conroy C., van Dokkum P. G., 2012, ApJ, 760, 71

Croom S. M. et al., 2012, MNRAS, 421, 872

Daddi E. et al., 2005, ApJ, 626, 680

Davidge T. J., Grinder M., 1995, AJ, 109, 1433

Dawson K. S. et al., 2013, AJ, 145, 10

Dole H. et al., 2006, A&A, 451, 417

Dolphin A. E., 2002, MNRAS, 332, 91

Dotter A., 2008, ApJ, 687, L21

Draine B. T., 2003, ARA&A, 41, 241

Driver S. P. et al., 2011, MNRAS, 413, 971

Drory N. et al., 2015, AJ, 149, 77

Eisenstein D. J. et al., 2001, AJ, 122, 2267

Eisenstein D. J. et al., 2011, AJ, 142, 72

Falcón-Barroso J., Sánchez-Blázquez P., Vazdekis A., Ricciardelli E., Cardiel N., Cenarro A. J., Gorgas J., Peletier R. F., 2011, A&A, 532, A95

Fall S. M., Efstathiou G., 1980, MNRAS, 193, 189

Ferraro F. R., Origlia L., Testa V., Maraston C., 2004, ApJ, 608, 772

Ferreras I., La Barbera F., de la Rosa I. G., Vazdekis A., de Carvalho R. R., Falcón-Barroso J., Ricciardelli E., 2013, MNRAS, 429, L15

Fioc M., Rocca-Volmerange B., 1997, A&A, 326, 950

Fitzpatrick E. L., 1999, PASP, 111, 63

Folkes S. et al., 1999, MNRAS, 308, 459

Frieman J. A. et al., 2008, AJ, 135, 338

Fukugita M., Hogan C. J., Peebles P. J. E., 1998, ApJ, 503, 518

Fukugita M., Ichikawa T., Gunn J. E., Doi M., Shimasaku K., Schneider D. P., 1996, AJ, 111, 1748

Fusi-Pecci F., Renzini A., 1976, A&A, 46, 447

Gallazzi A., Charlot S., Brinchmann J., White S. D. M., 2006, MNRAS, 370, 1106

Gerssen J., Wilman D. J., Christensen L., 2012, MNRAS, 420, 197

Girardi L., Bressan A., Bertelli G., Chiosi C., 2000, A&AS, 141, 371

Girardi L., Bressan A., Chiosi C., Bertelli G., Nasi E., 1996, A&AS, 117, 113

González Delgado R. M., Cerviño M., Martins L. P., Leitherer C., Hauschildt P. H., 2005, MNRAS, 357, 945

González Delgado R. M. et al., 2014, A&A, 562, A47

Gunn J. E. et al., 2006, AJ, 131, 2332

Gunn J. E., Stryker L. L., Tinsley B. M., 1981, ApJ, 249, 48

Gustafsson B., Edvardsson B., Eriksson K., Jørgensen U. G., Nordlund Å., Plez B., 2008, A&A, 486, 951

Hilz M., Naab T., Ostriker J. P., 2013, MNRAS, 429, 2924

Hubble E. P., 1926, ApJ, 64, 321

Hung C.-L. et al., 2013, ApJ, 778, 129

Iglesias-Páramo J. et al., 2013, A&A, 553, L7

Johansson J., Thomas D., Maraston C., 2012, MNRAS, 421, 1908

Kauffmann G., 2014, MNRAS, 441, 2717

Kauffmann G. et al., 2003, MNRAS, 346, 1055

Kauffmann G. et al., 2003a, MNRAS, 341, 33

Kauffmann G. et al., 2003b, MNRAS, 341, 54

Keller S. C., Wood P. R., 2006, ApJ, 642, 834

Kewley L. J., Dopita M. A., Sutherland R. S., Heisler C. A., Trevena J., 2001, AJ, 556, 121

Kewley L. J., Groves B., Kauffmann G., Heckman T., 2006, MNRAS, 372, 961

Kirby E. N., Boylan-Kolchin M., Cohen J. G., Geha M., Bullock J. S., Kaplinghat M., 2013, ApJ, 770, 16

Knapp G. R., Guhathakurta P., Kim D.-W., Jura M. A., 1989, ApJS, 70, 329

Kobayashi C., Arimoto N., 1999, ApJ, 527, 573

Koleva M., Prugniel P., Ocvirk P., Le Borgne D., Soubiran C., 2008, MNRAS, 385, 1998

Kroupa P., 2001, MNRAS, 322, 231

Kuntschner H. et al., 2010, MNRAS, 408, 97

Kurucz R. L., 1979, ApJS, 40, 1

Lançon A., Wood P. R., 2000, A&AS, 146, 217

Le Borgne D., Rocca-Volmerange B., Prugniel P., Lançon A., Fioc M., Soubiran C., 2004, A&A, 425, 881

Le Borgne J.-F. et al., 2003, A&A, 402, 433

Lee S.-K., Ferguson H. C., Somerville R. S., Wiklind T., Giavalisco M., 2010, ApJ, 725, 1644

Leitherer C. et al., 1999, ApJS, 123, 3

Li C. et al., 2015, ApJ, 804, 125

Liddle A. R., 2007, MNRAS, 377, L74

Longhetti M., Saracco P., 2009, MNRAS, 394, 774

Lu Y., Wei J.-Y., 2003, CJAA, 3, 395

MacArthur L. A., González J. J., Courteau S., 2009, MNRAS, 395, 28

Maraston C., 1998, MNRAS, 300, 872

Maraston C., 2005, MNRAS, 362, 799

Maraston C., Daddi E., Renzini A., Cimatti A., Dickinson M., Papovich C., Pasquali A., Pirzkal N., 2006, ApJ, 652, 85

Maraston C. et al., 2013, MNRAS, 435, 2764

Maraston C., Pforr J., Renzini A., Daddi E., Dickinson M., Cimatti A., Tonini C., 2010, MNRAS, 407, 830

Maraston C., Strömbäck G., 2011, MNRAS, 418, 2785

Maraston C., Strömbäck G., Thomas D., Wake D. A., Nichol R. C., 2009, MNRAS, 394, L107

Marigo P., Girardi L., Bressan A., Groenewegen M. A. T., Silva L., Granato G. L., 2008, A&A, 482, 883

Masters K. L. et al., 2011, MNRAS, 418, 1055

Mathis J. S., 1990, ARA&A, 28, 37

Matteucci F., 1994, A&A, 288, 57

Matteucci F., Greggio L., 1986, A&A, 154, 279

Mehlert D., Thomas D., Saglia R. P., Bender R., Wegner G., 2003, A&A, 407, 423

Meneux B. et al., 2006, A&A, 452, 387

Mihalas D., Auer L. H., Mihalas B. R., 1978, ApJ, 220, 1001

Moustakas L. A. et al., 2004, ApJ, 600, L131

Nelan J. E., Smith R. J., Hudson M. J., Wegner G. A., Lucey J. R., Moore S. A. W., Quinney S. J., Suntzeff N. B., 2005, ApJ, 632, 137

Nelson E. J. et al., 2012, ApJ, 747, L28

Newman A. B., Ellis R. S., Bundy K., Treu T., 2012, ApJ, 746, 162

Nomoto K., Thielemann F.-K., Wheeler J. C., 1984, ApJ, 279, L23

Nomoto K., Thielemann F.-K., Yokoi K., 1984, ApJ, 286, 644

Nordstroem B., Andersen J., Andersen M. I., 1997, A&A, 322, 460

Ocvirk P., Pichon C., Lançon A., Thiébaut E., 2006a, MNRAS, 365, 74

Ocvirk P., Pichon C., Lançon A., Thiébaut E., 2006b, MNRAS, 365, 46

Palla F., Stahler S. W., 1992, ApJ, 392, 667

Pannella M. et al., 2009, ApJ, 701, 787

Panter B., Jimenez R., Heavens A. F., Charlot S., 2007, MNRAS, 378, 1550

Percival W. J. et al., 2001, MNRAS, 327, 1297

Perlmutter S. et al., 1999, ApJ, 517, 565

Petty S. M. et al., 2013, AJ, 146, 77

Pforr J., Maraston C., Tonini C., 2012, MNRAS, 422, 3285

Piotto G. et al., 2012, ApJ, 760, 39

Planck Collaboration et al., 2014, A&A, 571, A16

Planck Collaboration et al., 2015, ArXiv e-prints

Press W. H., Schechter P., 1974, ApJ, 187, 425

Prugniel P., Soubiran C., Koleva M., Le Borgne D., 2007, ArXiv

Prugniel P., Vauglin I., Koleva M., 2011, A&A, 531, A165

Rawle T. D., Smith R. J., Lucey J. R., Swinbank A. M., 2008, MNRAS, 389, 1891

Reimers D., 1975, Memoires of the Societe Royale des Sciences de Liege, 8, 369

Reimers D., 1977, A&A, 61, 217

Renzini A., Buzzoni A., 1986, in Astrophysics and Space Science Library, Vol. 122, Spectral Evolution of Galaxies, Chiosi C., Renzini A., eds., pp. 195–231

Renzini A., Fusi Pecci F., 1988, ARA&A, 26, 199

Renzini A., Voli M., 1981, A&A, 94, 175

Roškar R., Debattista V. P., Stinson G. S., Quinn T. R., Kaufmann T., Wadsley J., 2008, ApJ, 675, L65

Rubin V. C., Burstein D., Ford, Jr. W. K., Thonnard N., 1985, ApJ, 289, 81

Ryder S. D., Dopita M. A., 1994, ApJ, 430, 142

Saglia R. P., Maraston C., Greggio L., Bender R., Ziegler B., 2000, A&A, 360, 911

Saglia R. P., Maraston C., Thomas D., Bender R., Colless M., 2002, ApJ, 579, L13

Sako M. et al., 2008, AJ, 135, 348

Salpeter E. E., 1955, ApJ, 121, 161

Sánchez S. F. et al., 2012, A&A, 538, A8

Sánchez-Blázquez P., Forbes D. A., Strader J., Brodie J., Proctor R., 2007, MNRAS, 377, 759

Sánchez-Blázquez P., Ocvirk P., Gibson B. K., Pérez I., Peletier R. F., 2011, MNRAS, 415, 709

Sánchez-Blázquez P. et al., 2006, MNRAS, 371, 703

Sánchez-Blázquez P. et al., 2014, A&A, 570, A6

Sandage A., 1958, ApJ, 127, 513

Sandage A., 2005, ARA&A, 43, 581

Sandage A., Cacciari C., 1990, ApJ, 350, 645

Sandberg Lacy C. H., Torres G., Claret A., Charbonneau D., O'Donovan F. T., Mandushev G., 2010, AJ, 139, 2347

Sarajedini A., Dotter A., Kirkpatrick A., 2009, ApJ, 698, 1872

Sarzi M. et al., 2006, MNRAS, 366, 1151

Schaller G., Schaerer D., Meynet G., Maeder A., 1992, A&AS, 96, 269

Schiavon R. P., Rose J. A., Courteau S., MacArthur L. A., 2005, ApJS, 160, 163

Schlegel D., White M., Eisenstein D., 2009, in astro2010, Vol. 2010, astro2010: The Astronomy and Astrophysics Decadal Survey, p. 314

Schlegel D. J., Finkbeiner D. P., Davis M., 1998, ApJ, 500, 525

Sharp R. et al., 2015, MNRAS, 446, 1551

Shetrone M., Venn K. A., Tolstoy E., Primas F., Hill V., Kaufer A., 2003, AJ, 125, 684

Shields G. A., Searle L., 1978, ApJ, 222, 821

Smee S. A. et al., 2013, AJ, 146, 32

Smoot G. F. et al., 1992, ApJ, 396, L1

Spergel D. N. et al., 2003, ApJS, 148, 175

Spiniello C., Trager S., Koopmans L. V. E., Conroy C., 2014, MNRAS, 438, 1483

Stothers R. B., 1991, ApJ, 383, 820

Tamura N., Kobayashi C., Arimoto N., Kodama T., Ohta K., 2000, AJ, 119, 2134

Thomas D., Greggio L., Bender R., 1998, MNRAS, 296, 119

Thomas D., Maraston C., Bender R., 2003, MNRAS, 339, 897

Thomas D., Maraston C., Bender R., Mendes de Oliveira C., 2005, ApJ, 621, 673

Thomas D., Maraston C., Johansson J., 2011, MNRAS, 412, 2183

Thomas D., Maraston C., Korn A., 2004, MNRAS, 351, L19

Thomas D., Maraston C., Schawinski K., Sarzi M., Silk J., 2010, MNRAS, 404, 1775

Thomas D. et al., 2013, MNRAS, 431, 1383

Tinsley B. M., 1972, ApJ, 178, 319

Tinsley B. M., 1980, Fundam. Cosmic Phys., 5, 287

Tinsley B. M., Gunn J. E., 1976, ApJ, 203, 52

Tojeiro R., Heavens A. F., Jimenez R., Panter B., 2007, MNRAS, 381, 1252

Tojeiro R. et al., 2012, MNRAS, 424, 136

Tojeiro R., Wilkins S., Heavens A. F., Panter B., Jimenez R., 2009, ApJS, 185, 1

Tollerud E. J., Bullock J. S., Graves G. J., Wolf J., 2011, ApJ, 726, 108

Tremonti C. A. et al., 2004, ApJ, 613, 898

Tremonti C. A., Moustakas J., Diamond-Stanic A. M., 2007, ApJ, 663, L77

Trujillo I., Conselice C. J., Bundy K., Cooper M. C., Eisenhardt P., Ellis R. S., 2007, MNRAS, 382, 109

Trumpler R. J., 1930, PASP, 42, 214

van den Bosch F. C., 2001, MNRAS, 327, 1334

van der Wel A. et al., 2014, ApJ, 788, 28

van Dokkum P. G. et al., 2008, ApJ, 677, L5

VandenBerg D. A., Stetson P. B., 2004, PASP, 116, 997

Vazdekis A., Casuso E., Peletier R. F., Beckman J. E., 1996, ApJS, 106, 307

Vazdekis A., Sánchez-Blázquez P., Falcón-Barroso J., Cenarro A. J., Beasley M. A., Cardiel N., Gorgas J., Peletier R. F., 2010, MNRAS, 404, 1639

Veilleux S., Osterbrock D. E., 1987, AJ Suppl. Ser., 63, 295

Welker C., Dubois Y., Devriendt J., Pichon C., Kaviraj S., Peirani S., 2015, ArXiv e-prints

White S. D. M., Rees M. J., 1978, MNRAS, 183, 341

Wild V. et al., 2014, MNRAS, 440, 1880

Wild V., Charlot S., Brinchmann J., Heckman T., Vince O., Pacifici C., Chevallard J., 2011, MNRAS, 417, 1760

Wilkinson D. M. et al., 2015, MNRAS, 449, 328

Williams B. F., Dalcanton J. J., Dolphin A. E., Holtzman J., Sarajedini A., 2009, ApJ, 695, L15

Willson L. A., 2000, ARA&A, 38, 573

Wilson E. B., Hilferty M. M., 1931, Proceedings of the National Academy of Sciences, 17, 684

Worthey G., Faber S. M., Gonzalez J. J., Burstein D., 1994, ApJS, 94, 687

Worthey G., Ottaviani D. L., 1997, ApJS, 111, 377

Wu H., Shao Z., Mo H. J., Xia X., Deng Z., 2005, ApJ, 622, 244

Wuyts S. et al., 2012, ApJ, 753, 114

Yanny B. et al., 2009, AJ, 137, 4377

Yi S. K., 2003, ApJ, 582, 202

Yi S. K., Kim Y.-C., Demarque P., 2003, ApJS, 144, 259

Yoachim P., Dalcanton J. J., 2008, ApJ, 683, 707

York D. G. et al., 2000, AJ, 120, 1579

Yoshii Y., Tsujimoto T., Nomoto K., 1996, ApJ, 462, 266

Zapata L. A., Palau A., Galván-Madrid R., Rodríguez L. F., Garay G., Moran J. M., Franco-Hernández R., 2015, MNRAS, 447, 1826

Zasowski G. et al., 2013, AJ, 146, 81

Zoccali M., Cassisi S., Frogel J. A., Gould A., Ortolani S., Renzini A., Rich R. M., Stephens A. W., 2000, ApJ, 530, 418

Zwicky F., 1937, ApJ, 86, 217

Appendix A

Supplementary P-MaNGA Galaxies

In this Appendix we provide the stellar population maps and radial profiles of the P-MaNGA galaxies described briefly in the Results section of Chapter 5, but not shown there to avoid disrupting the flow of the thesis with detail about individual galaxies. As in the Results section, we split our analyses by groups as described in Table 2 of Chapter 5.

A.0.1 Additional maps: Group α

Galaxy p9-19D (Appendix Figure A.1) has been observed with MaNGA-like data quality with 3 hour exposures, decent (1“.7) seeing conditions, and is in the MaNGA primary sample selection. It is an early-type galaxy that has been observed with the N_{19} IFU setup. We see a high level of radial symmetry in the age, metallicity and stellar mass density maps. It has a $\langle \log \mathrm{age} \rangle_L$ = 6 Gyr / $\langle \log \mathrm{age} \rangle_M$ = 8 Gyr, somewhat super-solar metallicity core going down to $\langle \log \mathrm{age} \rangle_L = \langle \log \mathrm{age} \rangle_M$ = 5 Gyr with approximately solar metallicity at above 1 effective radius, and shows little signs of dust. It therefore has quite clear, albeit weak, negative age and metallicity gradients.

Galaxies p9-19E (Appendix Figure A.2) and p9-127B (Appendix Figure A.3) have N_{19} and N_{127} IFU observations covering 2.2 and 2.4 effective radii respectively. The early-type galaxy p9-19E shows a much flatter age and metallicity profile and is considerably younger in $\langle \log \mathrm{age} \rangle_L$ than the primary-selected early-type galaxies, though similar $\langle \log \mathrm{age} \rangle_M$ to other galaxies in the sample, with evidence of a possibly younger core in the population maps that is washed out with the intermixed older population in the radial profile. This suggest recent star formation

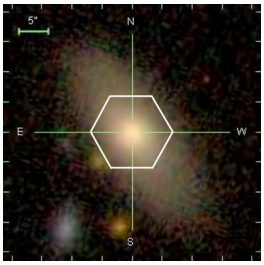

(a) SDSS image with the P-MaNGA footprint.

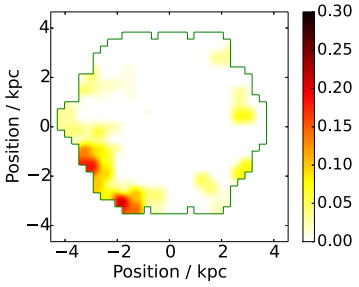

(b) Dust extinction, E(B-V).

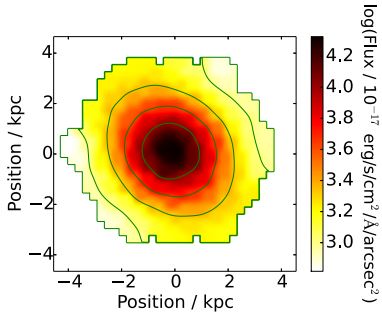

(c) Flux map with isoflux contours (green).

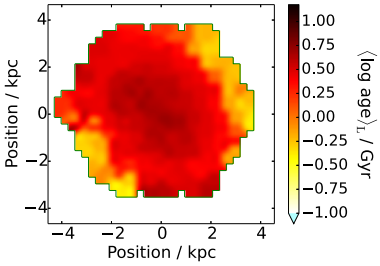

(d) Luminosity-weighted stellar age.

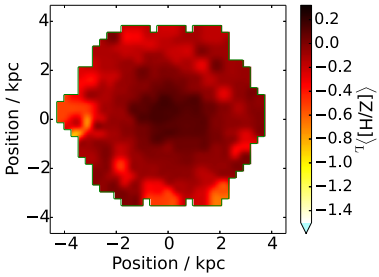

(e) Luminosity-weighted metallicity.

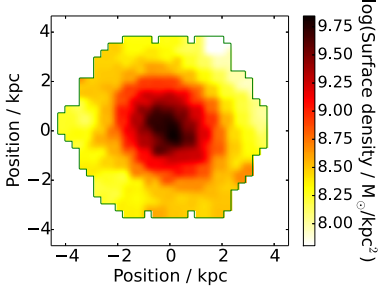

(f) Stellar mass.

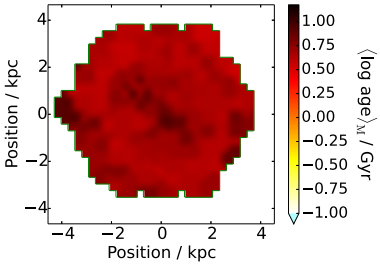

(g) Mass-weighted stellar age.

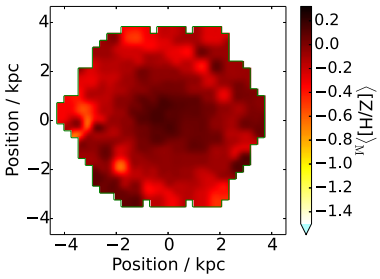

(h) Mass-weighted metallicity.

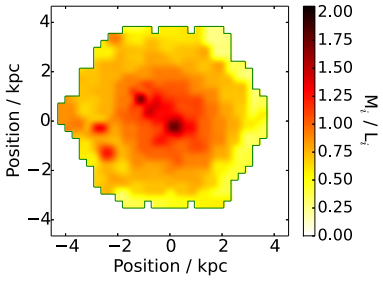

(i) Stellar mass-to-light ratio in the SDSS *i*-band.

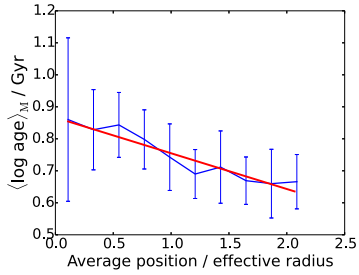

(j) Radial age profile.

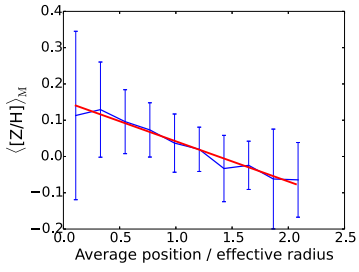

(k) Radial metallicity profile.

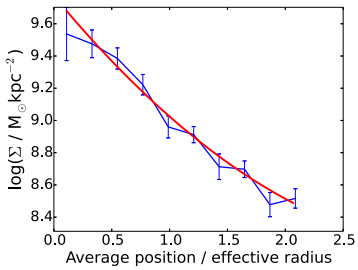

(l) Stellar mass surface density gradient profile.

Fig. A.1 **Group α, galaxy p9-19D** as in table 5.2. Stellar population maps and profiles analyzed using MILES-based models with their full parameter range, as described in detail in Figure 5.2. This galaxy, like p9-19B in Figure 5.2, has been observed with good observational conditions with a MaNGA-like exposure time and dithering, and is selected in the MaNGA primary sample. Therefore out of the P-MaNGA dataset, these observations are the most similar to the expected output of the MaNGA primary sample.

is well-mixed within most of the galaxy, giving the maps a clumpy structure.

Conversely, galaxy p9-127B (Appendix Figure A.3) is an edge-on late-type galaxy with a very clumpy structure, as evidenced clearly in the dust attenuation map. The galaxy as a whole is relatively young ($\langle \log \mathrm{age} \rangle_\mathrm{L}$ = 0.8 Gyr / $\langle \log \mathrm{age} \rangle_\mathrm{M}$ = 2 Gyr on average), but also has some regions of older populations, on average 1 Gyr older and more metal-poor (–0.50 dex or less) in a ring around the central kpc core. This is visible in the radial profiles in both age and metallicity as a peak and a dip respectively in these properties at low radius. In age this trend turns over to give a negative gradient but in metallicity it rises again at 1.0 R_e to give a positive gradient on average.

A.0.2 Additional maps: Group β

Galaxy p9-127A (Appendix Figure A.4) is identified very clearly in the light-weighted population maps as a galaxy with an old (8 Gyr) metal-rich ([Z/H] = 0.2) core with a younger (1-2 Gyr) and less metal-rich ([Z/H]= – 0.2) outer population, which matches in position with the imaging data as corresponding to the inner part of the spiral arm structure. The mass-weighted properties shows a flatter structure across the galaxy, suggesting that the star formation in the spiral arms are the main driver of the structure in the light-weighted properties. As mentioned earlier, the large difference between mass-weighted and light-weighted age indicates a more continuous star formation history, consistent with spiral arm star formation histories. This spiral structure is also traced in the dust attenuation maps. We note the presence of a foreground star on top of the image, which we mask over in the radial profiles by applying a recessional velocity cut in the data before fitting.

A.0.3 Additional maps: Group γ

Galaxy p4-19B (Appendix Figure A.5) is a late-type galaxy with a fairly complex structure in its stellar population maps. We see a band of $\langle \log \mathrm{age} \rangle_\mathrm{M} = \langle \log \mathrm{age} \rangle_\mathrm{L}$ = 1 Gyr stretching across the maps from North-East to South-West. This band is visible in the other maps as having low $\langle [\mathrm{Z/H}] \rangle_\mathrm{L}$ and $\langle [\mathrm{Z/H}] \rangle_\mathrm{M}$, but high $\langle \log \mathrm{age} \rangle_\mathrm{M}$ compared to the background halo. This combination is suggestive an intermediate age disk population with a background old halo and/or disk population, with a high contribution of star formation in the outer disk regions of the galaxy giving a significant negative age gradient in $\langle \log \mathrm{age} \rangle_\mathrm{L}$ or a flat gradient in $\langle \log \mathrm{age} \rangle_\mathrm{M}$.

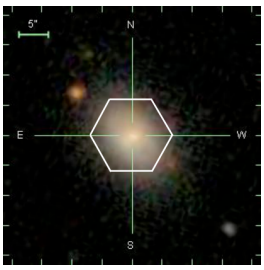

(a) SDSS image with the P-MaNGA footprint.

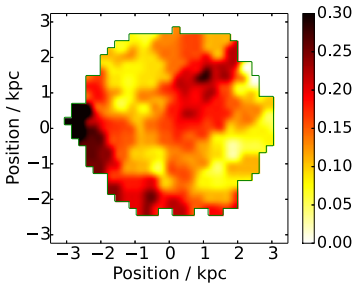

(b) Dust extinction, E(B-V).

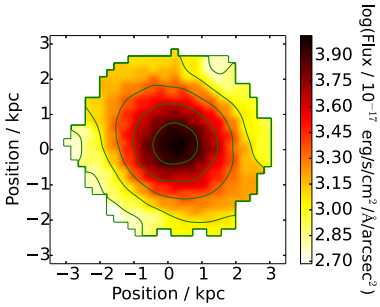

(c) Flux map with isoflux contours (green).

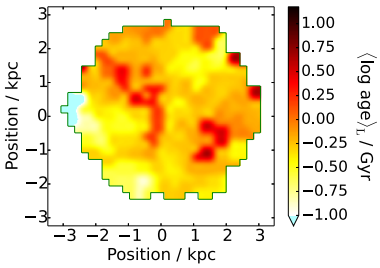

(d) Luminosity-weighted stellar age.

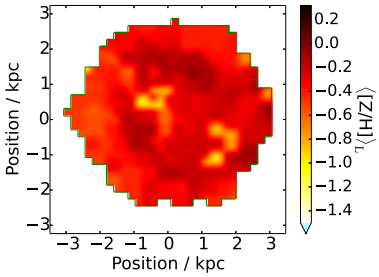

(e) Luminosity-weighted metallicity.

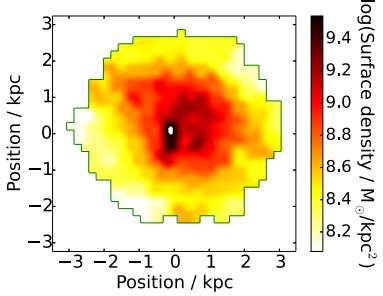

(f) Stellar mass.

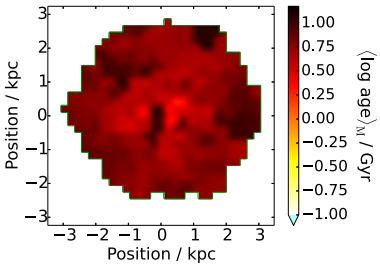

(g) Mass-weighted stellar age.

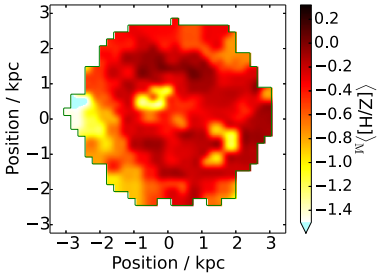

(h) Mass-weighted metallicity.

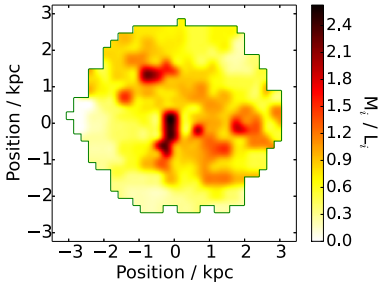

(i) Stellar mass-to-light ratio in the SDSS *i*-band.

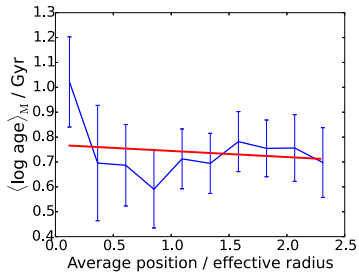

(j) Radial age profile.

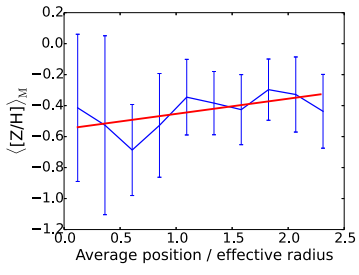

(k) Radial metallicity profile.

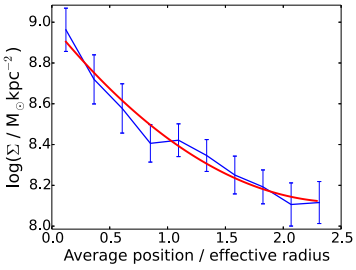

(l) Stellar mass surface density gradient profile.

Fig. A.2 **Group α, galaxy p9-19E** as in table 5.2. Stellar population maps and profiles analyzed using MILES-based models with their full parameter range, as described in detail in Figure 5.2. This galaxy has been observed under good observational conditions with MaNGA-like exposure time and dithering, but covers a larger radial extent than would be targeted in the MaNGA primary sample. However it is selected by the MaNGA secondary sample.

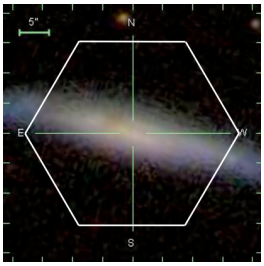

(a) SDSS image with the P-MaNGA footprint.

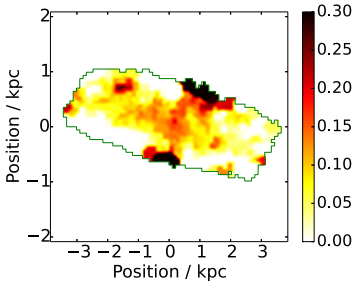

(b) Dust extinction, E(B-V).

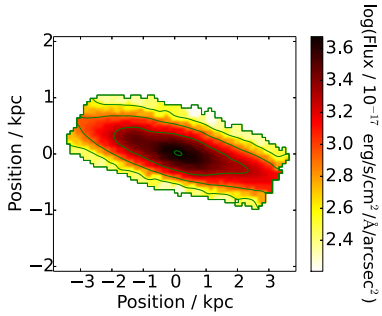

(c) Flux map with isoflux contours (green).

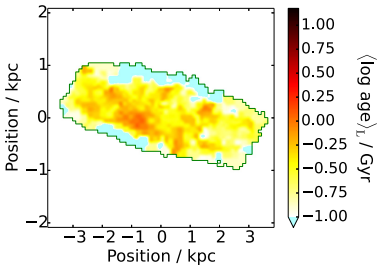

(d) Luminosity-weighted stellar age.

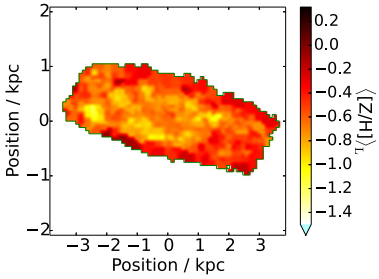

(e) Luminosity-weighted metallicity.

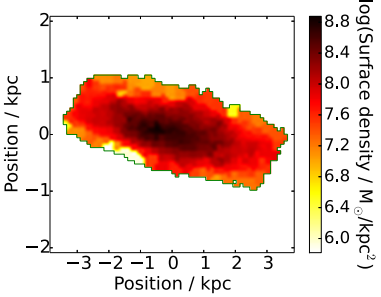

(f) Stellar mass.

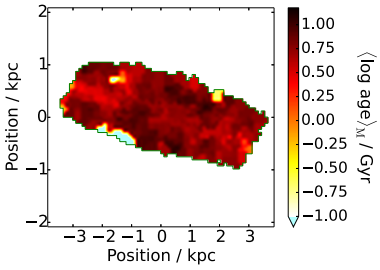

(g) Mass-weighted stellar age.

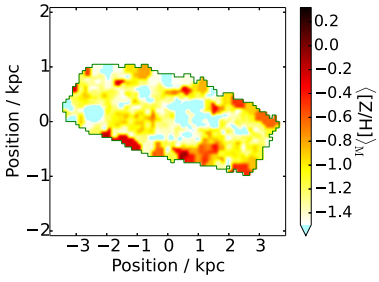

(h) Mass-weighted metallicity.

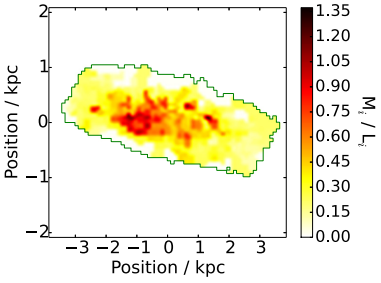

(i) Stellar mass-to-light ratio in the SDSS *i*-band.

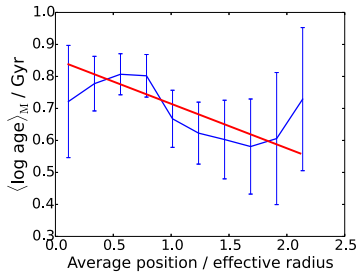

(j) Radial age profile.

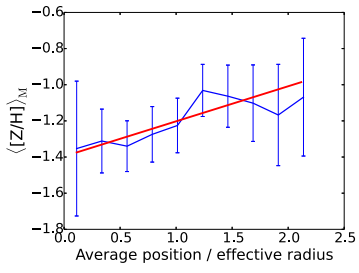

(k) Radial metallicity profile.

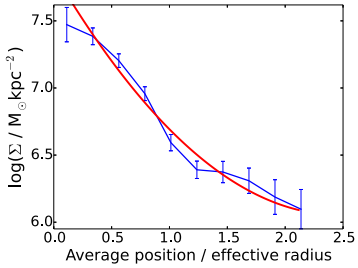

(l) Stellar mass surface density gradient profile.

Fig. A.3 **Group α, galaxy p9-127B** as in table 5.2. Stellar population maps and profiles analyzed using MILES-based models with their full parameter range, as described in detail in Figure 5.2. This galaxy has been observed under good observational conditions with MaNGA-like exposure time and dithering, but covers a larger radial extent than would be targeted in the MaNGA primary sample, like galaxy p9-19E (Figure A.2), and is selected by the MaNGA secondary sample.

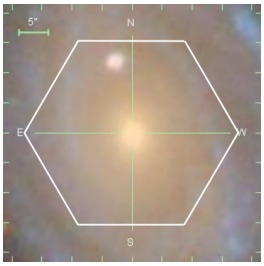

(a) SDSS image with the P-MaNGA footprint.

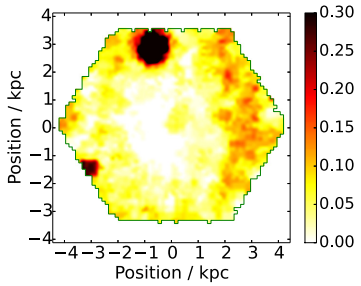

(b) Dust extinction, E(B-V).

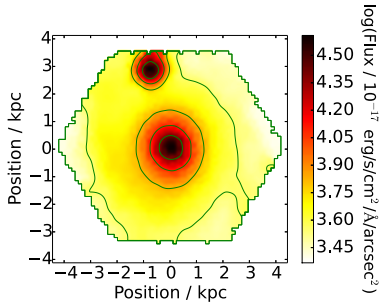

(c) Flux map with isoflux contours (green).

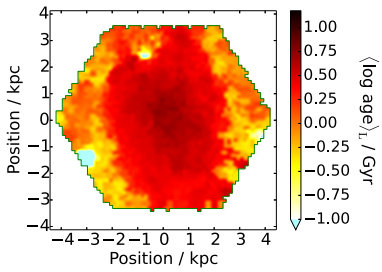

(d) Luminosity-weighted stellar age.

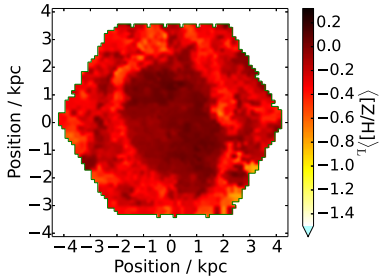

(e) Luminosity-weighted metallicity.

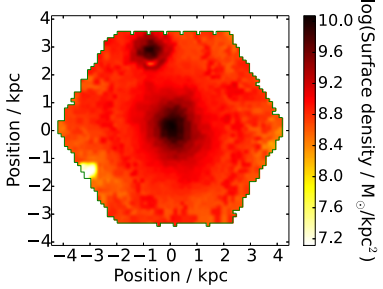

(f) Stellar mass.

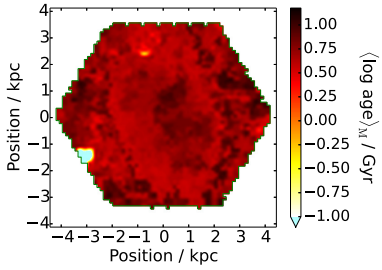

(g) Mass-weighted stellar age.

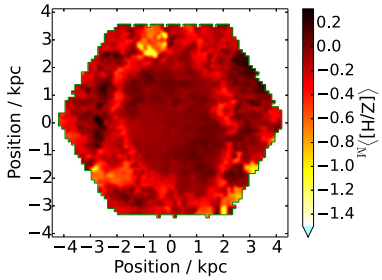

(h) Mass-weighted metallicity.

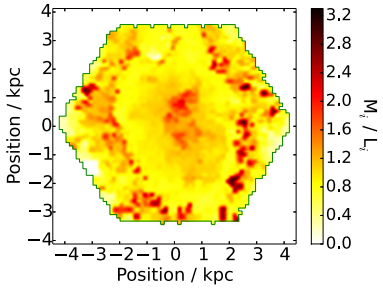

(i) Stellar mass-to-light ratio in the SDSS *i*-band.

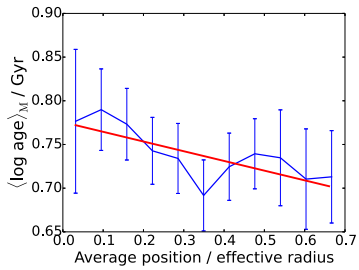

(j) Radial age profile.

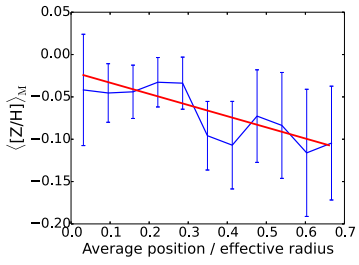

(k) Radial metallicity profile.

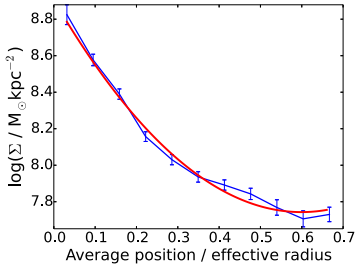

(l) Stellar mass surface density gradient profile.

Fig. A.4 **Group β, galaxy p9-127A** as in table 5.2. Stellar population maps and profiles analyzed using MILES-based models with their full parameter range, as described in detail in Figure 5.2. This galaxy is taken under MaNGA-like observational conditions and setup, but is not targeted in the main MaNGA samples due to its low redshift, and therefore radial coverage by MaNGA IFUs. Hence this galaxy is observed with a higher amount of structural detail then we should expect to observe with MaNGA.

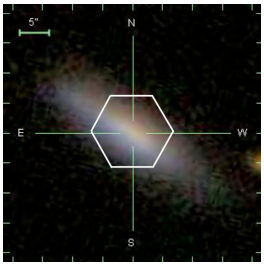

(a) SDSS image with the P-MaNGA footprint.

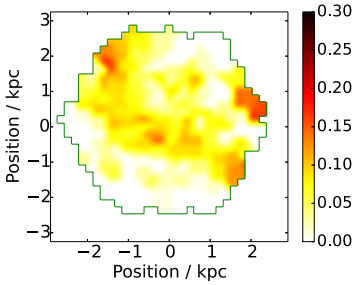

(b) Dust extinction, E(B-V).

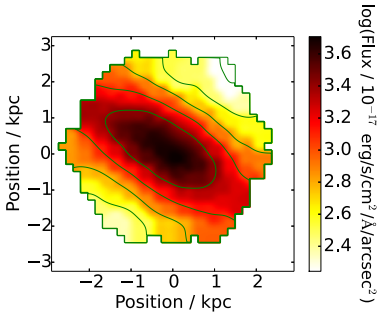

(c) Flux map with isoflux contours (green).

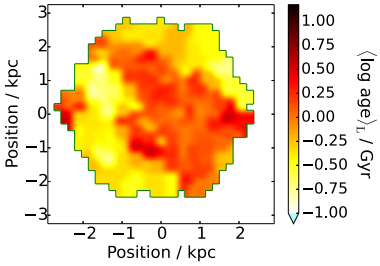

(d) Luminosity-weighted stellar age.

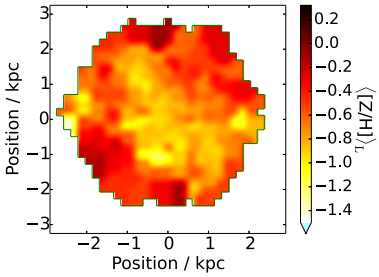

(e) Luminosity-weighted metallicity.

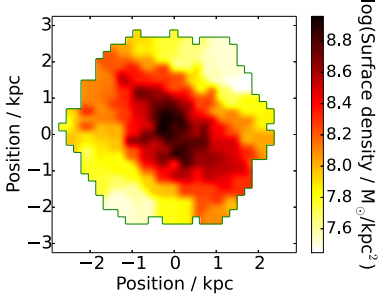

(f) Stellar mass.

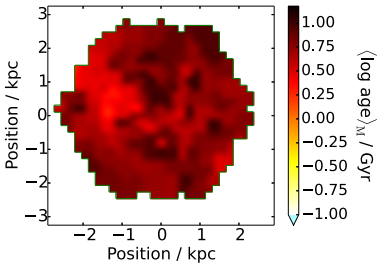

(g) Mass-weighted stellar age.

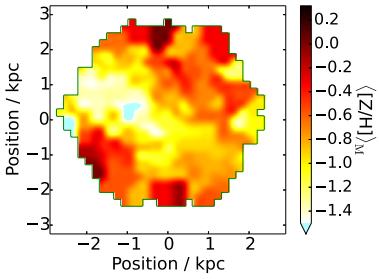

(h) Mass-weighted metallicity.

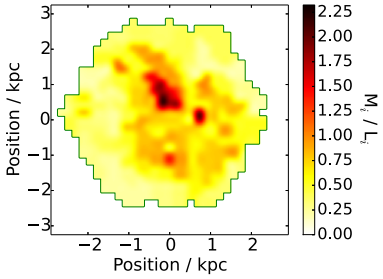

(i) Stellar mass-to-light ratio in the SDSS *i*-band.

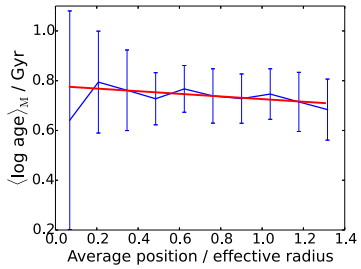

(j) Radial age profile.

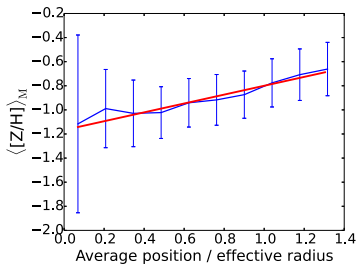

(k) Radial metallicity profile.

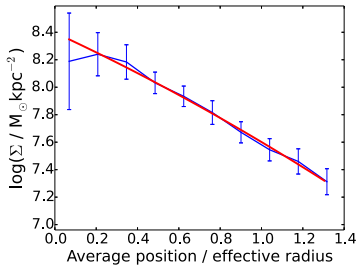

(l) Stellar mass surface density gradient profile.

Fig. A.5 **Group γ, galaxy p4-19B** as in table 5.2. Stellar population maps and profiles analyzed using MILES-based models with their full parameter range, as described in detail in Figure 5.2. This galaxy has been observed under poorer conditions and a lower exposure and dithering setup than expected for MaNGA. Unlike galaxy p4-19C (Figure 5.4), we resolve a more complex stellar population structure that reflects the asymmetric colour distribution seen in the SDSS image.

FORM UPR16

Research Ethics Review Checklist

University of Portsmouth

Please include this completed form as an appendix to your thesis (see the Postgraduate Research Student Handbook for more information

Postgraduate Research Student (PGRS) Information			**Student ID:**	**641893**
PGRS Name:	**David Mark Wilkinson**			
Department:	**ICG, Technology**	**First Supervisor:**	**Claudia Maraston**	
Start Date: (or progression date for Prof Doc students)		**1 Oct 2011**		
Study Mode and Route:	**Full-time**	**PhD**		

Title of Thesis:	Full Spectral Fitting of Stellar Population Models for Studies of Galaxy Evolution
Thesis Word Count: (excluding ancillary data)	39,258

If you are unsure about any of the following, please contact the local representative on your Faculty Ethics Committee for advice. Please note that it is your responsibility to follow the University's Ethics Policy and any relevant University, academic or professional guidelines in the conduct of your study

Although the Ethics Committee may have given your study a favourable opinion, the final responsibility for the ethical conduct of this work lies with the researcher(s).

UKRIO Finished Research Checklist: (If you would like to know more about the checklist, please see your Faculty or Departmental Ethics Committee rep or see the online version of the full checklist at: http://www.ukrio.org/what-we-do/code-of-practice-for-research/)	
a) Have all of your research and findings been reported accurately, honestly and within a reasonable time frame?	**YES**
b) Have all contributions to knowledge been acknowledged?	**YES**
c) Have you complied with all agreements relating to intellectual property, publication and authorship?	**YES**
d) Has your research data been retained in a secure and accessible form and will it remain so for the required duration?	**YES**
e) Does your research comply with all legal, ethical, and contractual requirements?	**YES**

Candidate Statement:		
I have considered the ethical dimensions of the above named research project, and have successfully obtained the necessary ethical approval(s)		
Ethical review number(s) from Faculty Ethics Committee (or from NRES/SCREC):		Certificate number (attached on next page): CA81-FDC6-4E78- 56F4-74C0 -93AD-E779-IDE3
If you have *not* submitted your work for ethical review, and/or you have answered 'No' to one or more of questions a) to e), please explain below why this is so:		
N/A		
Signed *(PGRS)*:	D. Wilkinson	**Date:** 1 Sept 2015

University of Portsmouth

Certificate of Ethics Review

Project Title:	Full Spectral Fitting of Stellar Population Models for Studies of Galaxy Evolution
User ID:	510590
Name:	David Wilkinson
Application Date:	09/04/2015 23:47:17

You must download your certificate, print a copy and keep it as a record of this review.

The chair person of the Technology Faculty Ethics Committee is John Williams.

It is your responsibility to adhere to the University Ethics Policy and any Department/School or professional guidelines in the conduct of your study including relevant guidelines regarding health and safety of researchers and University Health and Safety Policy.

It is also your responsibility to follow University guidance on Data Protection Policy:

- General guidance for all data protection issues
- University Data Protection Policy

You are reminded that as a University of Portsmouth Researcher you are bound by the UKRIO Code of Practice for Research; any breach of this code could lead to action being taken following the University`s Procedure for the Investigation of Allegations of Misconduct in Research.

Any changes in the answers to the questions reflecting the design, management or conduct of the research over the course of the project must be notified to the Faculty Ethics Committee. **Any changes that affect the answers given in the questionnaire, not reported to the Faculty Ethics Committee, will invalidate this certificate.**

This ethical review should not be used to infer any comment on the academic merits or methodology of the project. If you have not already done so, you are advised to develop a clear protocol/proposal and ensure that it is independently reviewed by peers or others of appropriate standing. A favourable ethical opinion should not be perceived as permission to proceed with the research; there might be other matters of governance which require further consideration including the agreement of any organisation hosting the research.

GovernanceChecklist
A1-BriefDescriptionOfProject: Computer analysis of galaxy data and models.
A2-Faculty: Technology
A5-AlreadyExternallyReviewed: No
B1-HumanParticipants: No
HumanParticipantsDefinition
B2-HumanParticipantsConfirmation: Yes

C6-SafetyRisksBeyondAssessment: No
D2-PhysicalEcologicalDamage: No
D4-HistoricalOrCulturalDamage: No
E1-ContentiousOrIllegal: No
E2-SociallySensitiveIssues: No
F1-InvolvesAnimals: No
F2-HarmfulToThirdParties: No
G1-ConfirmReadEthicsPolicy: Confirmed
G2-ConfirmReadUKRIOCodeOfPractice: Confirmed
G3-ConfirmReadConcordatToSupportResearchIntegrity: Confirmed
G4-ConfirmedCorrectInformation: Confirmed